NASA/TM—2017–219848

Marshall Space Flight Center Faculty Fellowship Program

N.F. Six, Program Director
Marshall Space Flight Center, Huntsville, Alabama

R. Damiani, Compiler
The University of Alabama in Huntsville, Huntsville, Alabama

December 2017

The NASA STI Program…in Profile

Since its founding, NASA has been dedicated to the advancement of aeronautics and space science. The NASA Scientific and Technical Information (STI) Program Office plays a key part in helping NASA maintain this important role.

The NASA STI Program Office is operated by Langley Research Center, the lead center for NASA's scientific and technical information. The NASA STI Program Office provides access to the NASA STI Database, the largest collection of aeronautical and space science STI in the world. The Program Office is also NASA's institutional mechanism for disseminating the results of its research and development activities. These results are published by NASA in the NASA STI Report Series, which includes the following report types:

- TECHNICAL PUBLICATION. Reports of completed research or a major significant phase of research that present the results of NASA programs and include extensive data or theoretical analysis. Includes compilations of significant scientific and technical data and information deemed to be of continuing reference value. NASA's counterpart of peer-reviewed formal professional papers but has less stringent limitations on manuscript length and extent of graphic presentations.

- TECHNICAL MEMORANDUM. Scientific and technical findings that are preliminary or of specialized interest, e.g., quick release reports, working papers, and bibliographies that contain minimal annotation. Does not contain extensive analysis.

- CONTRACTOR REPORT. Scientific and technical findings by NASA-sponsored contractors and grantees.

- CONFERENCE PUBLICATION. Collected papers from scientific and technical conferences, symposia, seminars, or other meetings sponsored or cosponsored by NASA.

- SPECIAL PUBLICATION. Scientific, technical, or historical information from NASA programs, projects, and mission, often concerned with subjects having substantial public interest.

- TECHNICAL TRANSLATION. English-language translations of foreign scientific and technical material pertinent to NASA's mission.

Specialized services that complement the STI Program Office's diverse offerings include creating custom thesauri, building customized databases, organizing and publishing research results…even providing videos.

For more information about the NASA STI Program Office, see the following:

- Access the NASA STI program home page at <http://www.sti.nasa.gov>

- E-mail your question via the Internet to <help@sti.nasa.gov>

- Phone the NASA STI Help Desk at 757–864–9658

- Write to:
  NASA STI Information Desk
  Mail Stop 148
  NASA Langley Research Center
  Hampton, VA 23681–2199, USA

NASA/TM—2017–219848

Marshall Space Flight Center Faculty Fellowship Program

N.F. Six, Program Director
Marshall Space Flight Center, Huntsville, Alabama

R. Damiani, Compiler
The University of Alabama in Huntsville, Huntsville, Alabama

National Aeronautics and
Space Administration

Marshall Space Flight Center • Huntsville, Alabama 35812

December 2017

Acknowledgments

All are grateful to those who, through their diligence, brought the 2017 NASA Marshall Space Flight Center Faculty Fellowship program to completion. These professionals include Steve Cash, Todd May, Preston Jones, Jim Turner, John Honeycutt, and Richard Burt, along with Jerry Karr, Rachael Damiani, Mona Miller Katie Hayden, Tina Atchley, Deborah Nielson, Judy Drinnon, and Tammy Rowan.

TRADEMARKS

Available from:

NASA STI Information Desk
Mail Stop 148
NASA Langley Research Center
Hampton, VA 23681–2199, USA
757–864–9658

This report is also available in electronic form at
<http://www.sti.nasa.gov>

EXECUTIVE SUMMARY

The 2017 Marshall Faculty Fellowship Program involved 21 faculty in the laboratories and departments at Marshall Space Flight Center. These faculty engineers and scientists worked with NASA collaborators on NASA projects, bringing new perspectives and solutions to bear. This Technical Memorandum is a compilation of the research reports of the 2017 Marshall Faculty Fellowship program, along with the Program Announcement (Appendix A) and the Program Description (Appendix B). The research affected the following six areas:

(1) Materials
(2) Propulsion
(3) Instrumentation
(4) Spacecraft systems
(5) Vehicle systems
(6) Space science

The materials investigations included composite structures, printing electronic circuits, degradation of materials by energetic particles, friction stir welding, Martian and Lunar regolith for in-situ construction, and polymers for additive manufacturing. Propulsion studies were completed on electric sails and low-power arcjets for use with green propellants. Instrumentation research involved heat pipes, neutrino detectors, and remote sensing. Spacecraft systems research was conducted on wireless technologies, layered pressure vessels, and two-phase flow. Vehicle systems studies were performed on life support—biofilm buildup and landing systems. In the space science area, the excitation of electromagnetic ion-cyclotron waves observed by the Magnetospheric Multiscale Mission provided insight regarding the propagation of these waves. Our goal is to continue the Marshall Faculty Fellowship Program funded by Center internal project offices.

Faculty Fellows in this 2017 program represented the following minority-serving institutions: Alabama A&M University and Oglala Lakota College.

TABLE OF CONTENTS

TABLE OF CONTENTS (Continued)

2017 Marshall Faculty Fellows

From Left to Right:

Back Row – Gerald Karr, Frank Six, Amanda Smith, Robert Amaro, Amin Aknoukh, Chih-Hao Wu, Douglas McRoberts, Daniel Harris, Rachael Damiani

Middle Row – Jichun Zhang, Carlos Montalvo, Chihdar Yang, Gennady Miloshevsky, Charlotte Marr de Vries, Cameron Coates, Baek-Young Choi, Christine Stagnetto-Zweig

Front Row – David Gross, Robert McTaggart, Aaron Adams, Andre Denham, Hunain Alkhateb

Not Pictured – Trevor Moeller, Nickolas Solomey

Ionic Polyimides: New High-Performance Polymers for Additive Manufacturing

A.Adams[1]
Alabama A &M University, Department of Mechanical and Civil Engineering, Normal, AL 35762

E. West [2]
The Florida and Agricultural and Mechanical University, Department of Physics, Tallahassee, FL 32310

and

E. Jackson.[3]
NASA, Marshall Space Flight Center, Alabama, 35812

Nomenclature

3D	=	Three dimensional
6FDA	=	*4,4'-(Hexafluoroisopropylidene)dipthalic anyhydride*
ABS	=	Acrylonitrile Butadiene Styrene
APL	=	1 - (3-Aminopropyl) imidazole
ATR	=	attenuated total reflectance
BPADA	=	4,4'- (4,4'-isopropylidenediphenoxy) bis (phthalic anhydride)
DSC	=	Differential scanning calorimetry
FDM	=	Fused Deposition Modeling
FT-IR	=	Fourier transform infrared spectroscopy
ISS	=	International Space Station
M-dichloroxylene	=	α,α' – dichloro-m-xylene [m-dichloroxylene]
MSFC	=	Marshall Space Flight Center
MWCNT	=	multi-walled carbon nanotubes
NASA	=	National Aeronautics and Space Administration
P-dichloroxylene	=	α,α' – dichloro-p-xylene [p-dichloroxylene]
PMDA	=	pyrometallic dianhydride
(poly(ILs))	=	Polyimides and polymeric ionic liquids
SiC	=	Silicon carbon
Tg	=	Glass Transition
Tm	=	Melting Temperature

I. Introduction

Additive manufacturing or 3D printing is a technology that has been vastly researched since the early 1990s. It is a technology that allows a three-dimensional object to be produced from a digital file. Sometimes referred to as "additive manufacturing," because the process consists of adding one layer of material on top of another until it formed into a three-dimensional object. The rise of popularity of this technology and its flexibility to manufacture complex parts with high degree complexity without molds has sparked NASA's interested and is currently being utilized on the International Space Station (ISS). NASA material scientists and engineers have been conducting intensive research on improving acrylonitrile butadiene styrene (ABS) plastics. This has been done with functionalized and non-functionalized multi walled carbon Nanotubes (MWCNT), Silicon carbon (SiC) whiskers, and other material modification. ABS plastic exhibits improved mechanical properties that make it ideal for human spaceflight operations, but due to some ABS's inherent limitations such as limited weathering resistance, moderate heat, moisture, and chemical resistance and are flammable, thus making it an unattractive choice for certain applications gives rise to the development of other engineering polymers. Additive manufacturing of custom components will require a much

[1] Assistant Professor, Mechanical and Civil Engineering, Alabama A&M University Normal, AL 35762
[2] PhD Candidate, Department of Physics, Florida A&M University, Tallahassee, FL 32310
[3] Aerospace Polymeric Engineering, Materials and Processes Lab, EM22, MSFC, Al 35812

larger array of polymers, especially those with physical, thermal, chemical, and mechanical properties that can be tailor-made. The development of 'Ionic Polyimides' offers a solution to this shortage by combining the well-understood and widely accepted properties of conventional polyimides, with a new approach to polymer synthesis. Polyimides and polymeric ionic liquids (poly(ILs)) are at the forefront of advanced polymer materials, each with their own set of advantages and disadvantages. This research will focus on additive manufacturing to develop in-space manufacturing capabilities for space exploration. Unlike any material currently available for 3- D printing, ionic polyimides retain the robust nature of polyimides while displaying the processability and conductivity of poly(ILs). This unique combination of properties is not found in conventional polyimides or other engineering polymers. In addition, the use of these materials will allow for potential aerospace applications such as valves, O-rings, seals, and gears. Researchers have already demonstrated that the first-generation of ionic polyimides can be extruded, made into pellets, and molded at approximately 220°C, which is ideal for use in typical 3-D printers. While it is clear more types of polymer materials are needed for fused deposition modeling (FDM) additive manufacturing, there is a need to explore these unprecedented classes of materials. Using a synthesis process developed at the University of Alabama allows full control over polymer structure, nanostructure, and thermal, electrical, and physical properties making them a prime candidate for use in the additive manufacturing process. Furthermore, the new process allows us to tailor-make a high strength polymer that can be used to fabricate filament feedstock instead of pellets for 3D printing. Five ionic polyimides synthesized by the University of Alabama were received analyzed by differential scanning calorimetry (DSC) and a Fourier transform infrared-spectroscopy (FT-IR) on all eight building blocks polyimides to determine the thermal properties of each sample, and the relative abundance of the elements/molecules in each sample

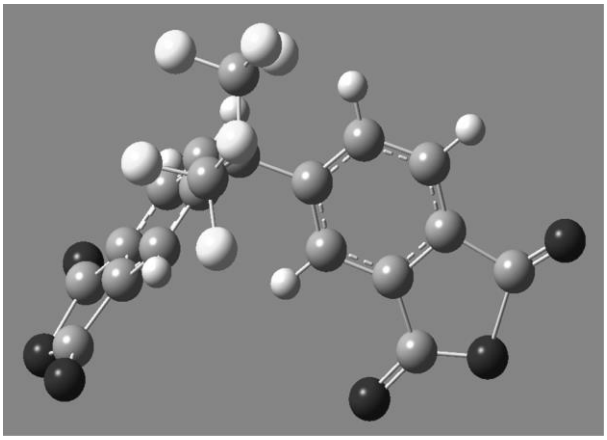

Figure 1 *Molecular representation of building block 6FDA*

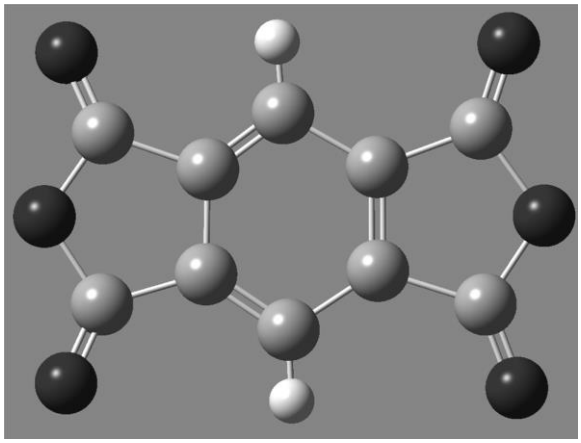

Figure 2 *Molecular representation of building block PMDA*

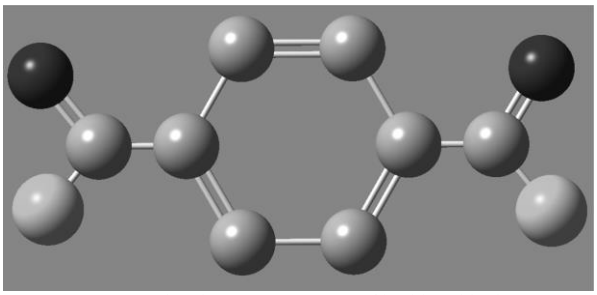

Figure 3 *Molecular representation of building block TC*

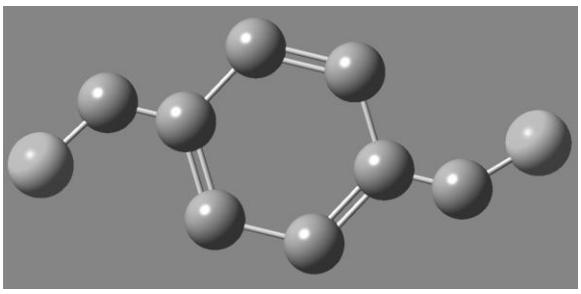

Figure 4 *Molecular representation of building block P-Dichloroxylene*

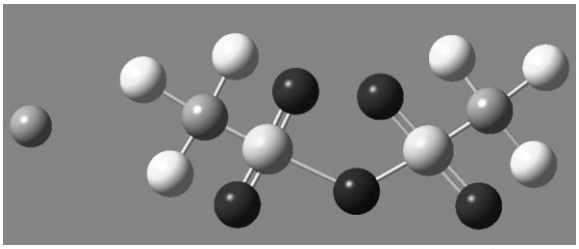

Figure 5 *Molecular representation of building LiTf2N*

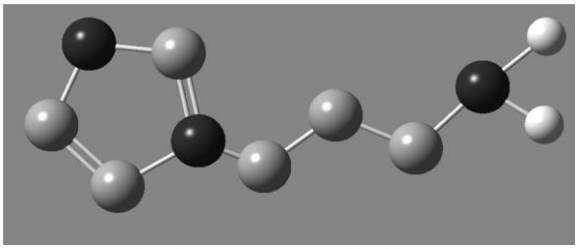

Figure 6 *Molecular representation of building APL*

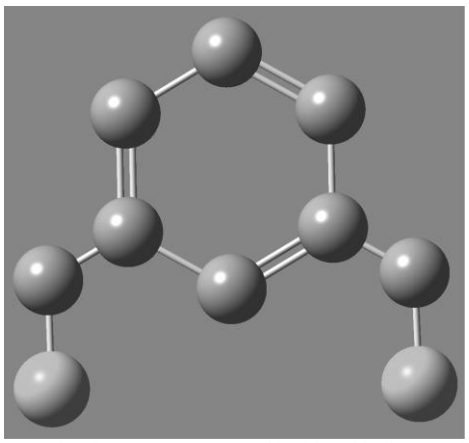

Figure 7 *Molecular representation of building block P- Dichloroxylene*

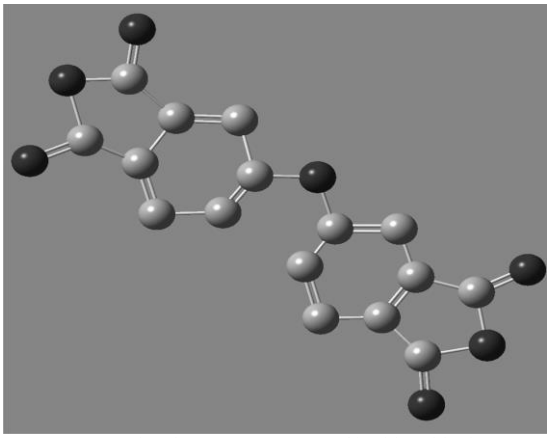

Figure 8 *Molecular representation of building block BPADA*

This experimental data will be used to develop and validate a Gaussian 16 simulation that will grant the ability to rapidly identify viable ionic polyimide configurations (i.e. polyimides with the correct thermal, chemical, and physical properties for 3D printing). Our deliverables are a set of relationships between molecular structure and polyimide properties (e.g. Tg/Tm relative to different ionic polyimide structures) ultimately, this database can be used to develop proof-of-concept materials for additive manufacturing, and to guide the development of next generation materials. Government agencies, universities, non profit organizations and commercial aerospace entities are currently developing new research efforts that involve sophisticated hybrid materials. These hybrid materials would ideally be able to withstand environmental impacts and improved performance not realized in known compounds. The improved technology has become an intriguing concept for NASA, as the technology can be used to potentially create a combination of materials that can support a diverse amount of material properties. The additive materials can be designed to have localized, specific values of selected physical characteristics, making parts tailored for performance under various structural load and temperature conditions such as an artifact's hardness, rigidity, and/or electrical and thermal conductivities. To form a resolution that would expand 3D printing, with respect to additive manufacturing, the limitations of current additive manufacturing materials must be addressed.

II. Experimental Setup

The data was collected using the Differential scanning calorimetry (DSC) technique. Differential scanning calorimetry is the most widely used of the thermal analysis techniques and is widely accepted in the research and development community for the quality of the results that are produced. DSC has the following capabilities which are used for collecting data for this study, identifying substances, measuring phase diagrams, and determining the degrees of crystallinity. DSC advantages over conventional calorimetry are its dynamic mode of operation ("scanning"). This allows reactions or processes to be investigated that can be thermally activated and has high sensitivity to anomalies of the temperature-time function. The DSC measurements taking over large temperature range on the building blocks samples. Performing this over a board temperature range showed the thermal effects of the samples. Another benefit of using DSC in that relevant temperatures and characteristic caloric values can be obtained by only using a few mg of material which is very desirable due to the limited amount of building blocks produced the Bara group at the University of Alabama.

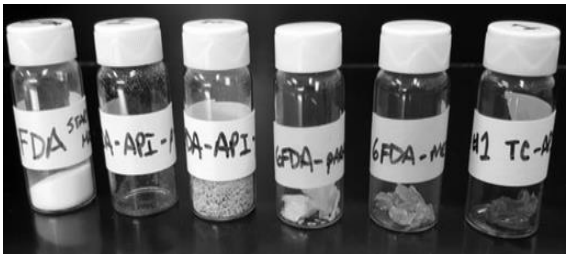

Figure 9 *Ionic Polyimides build blocks supplied for the BARA group at the University of Alabama*

The measured properties the will be obtained on the building blocks will be heat capacities, heats of transitions, kinetic data, sample purity, and temperatures of glass transitions. TA Instruments DSC model 2920 was used to perform the

following experiments, it works by measuring the temperature difference between the sample and a reference specimen as a function of temperature and time. The DSC 2920 model operation is detailed in figure 9 below. DSC can be used to measure specific heat (Cp) in two ways the first outlined in ASTM E1269 requires three separate experiments for baseline, calibration, and sample analysis. The second method is to modulate a DSC experiment where modulation of the sample temperature permits the heat flow to be split into two components, one thermodynamic that is dependent upon the sample's specific heat (Cp) and the other kinetic reflecting nonreversible changes to the material. A typical DSC transitions are shown in figure 10 below: Theses samples which are approximately 10-15 mg, are loaded into aluminum pans which were approximately 0.25 in diameter, with a depth of 0.0625 and loaded into the DSC 2920 to perform the desired test. The DSC heat flow is given by the following equations.

$$\frac{dH}{dt} = Cp\left(\frac{dT}{dt}\right) + f(T,t)$$

Where dH/dT = DSC heat flow signal
Cp = Sample Heat capacity
dT/dt = Heating rate
f(T,t) = Heat flow that is a function of time at an absolute temperature (kinetic)

The initial condition were entered into the computer, for this experiment the parameters were 10 C per minute from a temperature range of 30 C to 40 C. The figure below shows the DSC aluminum sample disk that were used in this experiment.

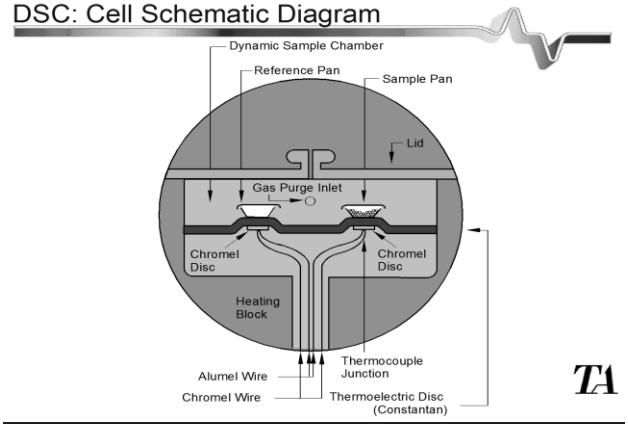

Figure 10 *Instruments 2920 Differential Scanning Calorimeter (DSC) measures heat flow into or out of a sample (right), and measures that heat relative to a reference (left) as a function of temperature and time. A steady flow of purge gas (nitrogen, argon, air or oxygen) goes through the cell. [7]*

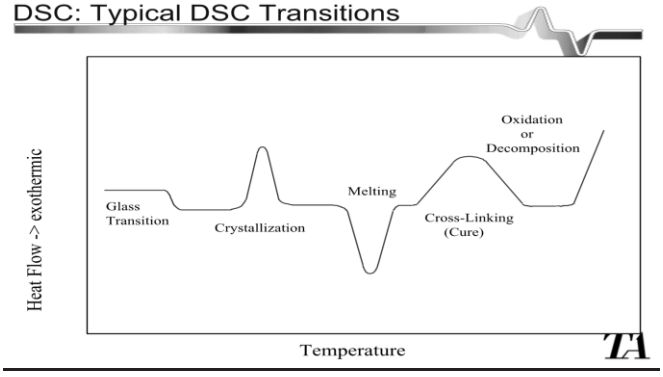

Figure 11 *DSC schematic of a plot of heat flow vs. temperature showing often observed molecular transitions in a material sample. Glass transition temperature (T_g) is a glassy-to-rubbery transition upon heating at a controlled rate. Crystallization and cross linking are exothermic transitions, and melting is an endothermic transition [7]*

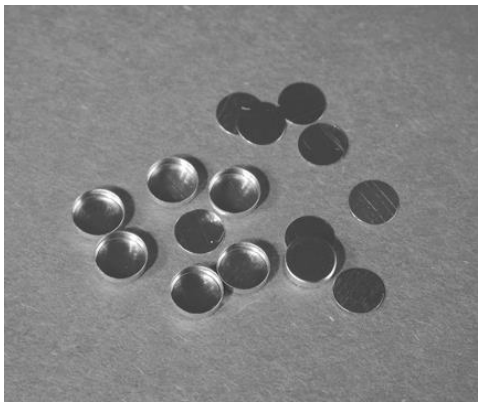

Figure 12 *DSC standard aluminum sample pans. Each ≈ 0.25 in. diameter pan has a bottom ≈ 0.0625 in. deep that contains the sample (≈ 10-15 mg), with a matching flat disk lid. A tool is used to manually crimp the sample between the pan bottom and lid. [7]*

Before the test could begin a baseline had to be established for the DSC instrument, this is used calculated the baseline drift and the initial bias for the heat flow data for an ideal reference of zero heat flow. A straight line fit of the raw signal of temperature difference (ΔT in μV) between -135 and 150°C determines the baseline slope and offset necessary to return the curve to the ideal reference for a heat flow of zero. Two baseline calibrations were performed at these conditions and the following values calculated. For baseline calibration 1 the slope was recorded at -0.015 and the offset were -3.152. For baseline calibration 2 the slope was recorded at -0.013 and the offset were -2.886. a graphical representation is shown in figure 13.

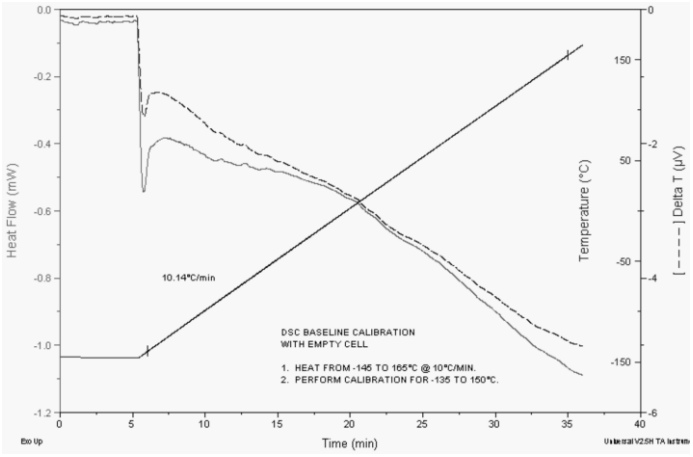

Figure 13 *The DSC baseline calibration determines the baseline drift and bias by calculating of the heat flow data for an empty cell heated from -145 to 165°C at a controlled rate of 10°C/min with an argon gas purge of ≈ 55 ml/min. A straight line fit between -135 and 150°C determines the baseline slope and offset necessary to return the curve to the ideal reference for a heat flow of zero.[7]*

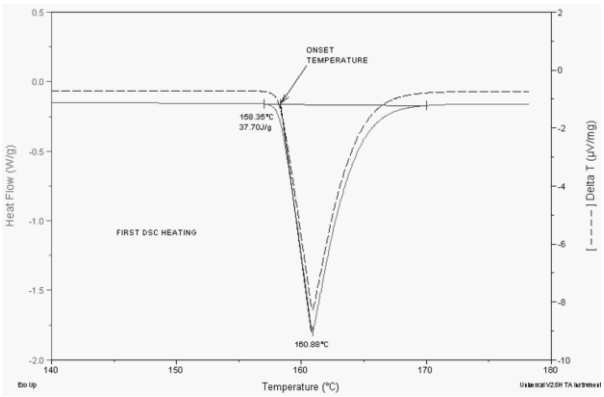

Figure 14 *Indium, a soft, malleable metal, is most frequently used for DSC temperature and cell constant calibrations because it has a sharp, well-defined melting transition. An indium sample of 19.5 mg was heated at 10°C/min. from 25 to 180°C. The onset melting temperature and heat of fusion of 158.4°C and 37.7 Joules/gram (J/g), respectively, were not in very good agreement with accepted values of 156.6°C and 28.71 J/g.[7]*

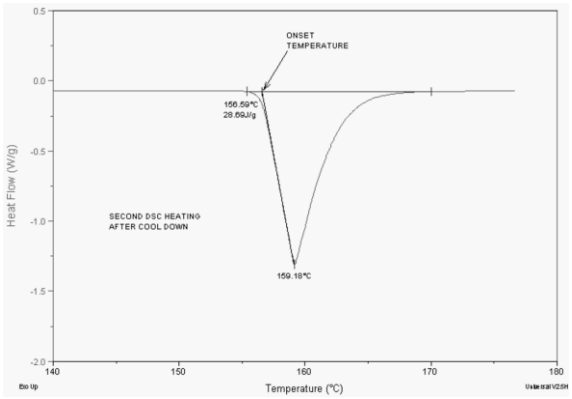

Figure 15 *The second DSC heating scan--at the same heating conditions—on the indium sample shown in Fig. 14. The second scan, soon after cool down from the first scan, allows better heat transfer between the aluminum pan and sample after an initial melting. The measured onset melting temperature and heat of fusion were very close to accepted values. [7]*

DSC has been used by several researchers to study thermal transitions in several metallic standards, including indium, as a function of sample mass from 0.57 to 20.90 mg, and heating rates from 4 to 324°C/min.

- For indium, both the onset melting temperature and heat of fusion were found to be mostly linear with increasing DSC heating rate from 4 to 36°C/min.
- For a range of DSC sample mass most often used at MSFC (9.10 to 20.90 mg), the relationships were also mostly linear.
- A sample mass of 9.10 mg and heating rate of 9°C/min. appeared to yield the best agreement between measured and accepted values of onset melting temperature and heat of fusion.

The provided building block samples were also analyzed the provided using a mid-range infrared spectrometer and a technique referred to as single-bounce attenuated total reflectance (ATR). The ATR consists of an infrared transparent germanium crystal with a pressure device located above the crystal surface, the latter intended for the collection of solid sample infrared spectra. A sample is placed on the crystal surface, the pressure applied and the infrared signature collected from the crystal contact side of the sample. This is largely considered a surface-based analysis as the infrared penetration is equivalent to only a few microns, and thus independent of sample thickness in general. Spectra collected by this method are sensitive to the amount of pressure applied, with increasing pressure translating into primarily greater peak heights. The pressure device being used for this testing has a locking mechanism that ensures a constant pressure, such that a semi-quantitative comparison between samples is possible under most conditions.
The provided samples for the Bara group had to be altered to accommodate the crystal surface dimensions. For the ribbon sample, this included hard-rolling a portion to present a flattened surface to the crystal. The remaining samples required using a scalpel blade to remove material for analysis. The samples were tested under the varying resolution, scan rates and wavenumber ranges to reach optimal, reproducible test parameter conditions. Finally deciding on a resolution 4 $cm^{-1,}$ 32 scans, and range 4000-700 cm^{-1}) after several iterations.

III. Results

These experimental results offer a better understanding of the complex parameter that are involving in the process of adding characterization to new ionic building blocks for the propose of defining their thermal and mechanical properties. Figures 16 through 18 show DSC graphs of building block 6FDA-META and the accompanying table 1 shows the results for the heat of fusion and melting point the averages for those values and the standard deviations. Figures 19 through 21 show the DSC graphs for the building block PMDA-API-P-XYL and the accompanying table 2 shows the results for the heat of fusion and melting point the averages for those values and the standard deviations. The other building blocks were also tested and characterized and the results are in tabulated form in the appendix.

Table 1: Building block 6FDA-META DSC results

Test #	Onset Temperature #1 (°C):	Heat of Fusion #1 (J/g):	Melting Point #1 (°C)
1	97.99	4.691	102.52
3	96.67	5.481	105.85
4	108.97	4.54	117.48
	Average Onset Temp #1 (°C):	Average Heat of Fusion #1 (J/g):	Average Melting Point #1 (°C):
	101.21	4.904	108.6166667
	Standard Deviation OT #1	Standard Deviation HF #1	Standard Deviation MP #1
	6.752688354	0.505368183	7.854376699

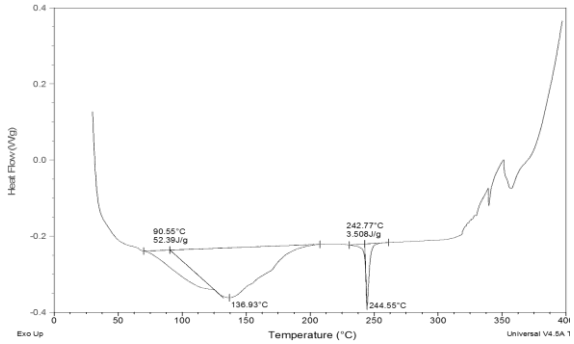

Figure 16 *6FDA-META results of sample test number1*

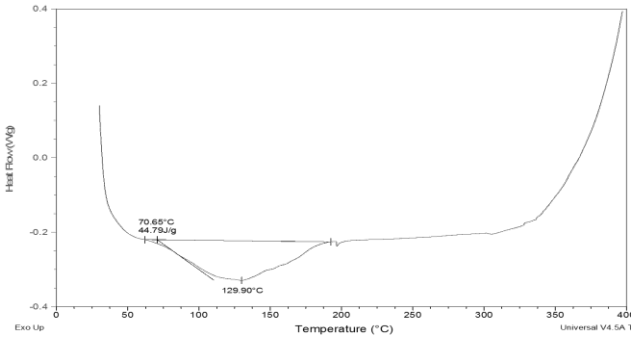

Figure 17 *6FDA-META results of sample test number 2*

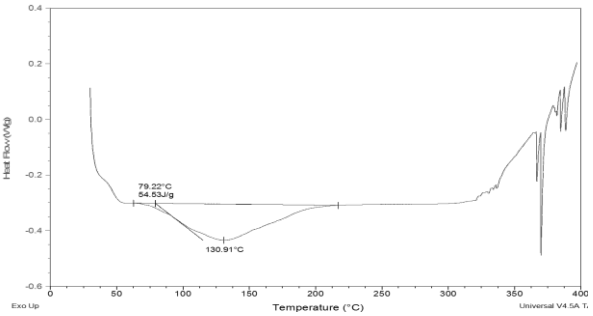

Figure 18 *6FDA-META results of sample test number 3*

Table 2: Building block PMDA-API-P-XYL DSC results

Test #	Onset Temperature #1 (°C):	Heat of Fusion #1 (J/g):	Melting Point #1 (°C)	Onset Temperature #2(°C):	Heat of Fusion #2 (J/g):
1	161.56	21.91	194.56		
2	176.19	21.81	194.29		
3	161.02	20.81	192.44		
	Average Onset Temp #1 (°C):	Average Heat of Fusion #1 (J/g):	Average Melting Point (°C)	Average Onset Temp #2 (°C):	Average Heat of Fusion #2 (°C):
	166.2566667	21.51	193.7633333		
	Standard Deviation OT #1	Standard Deviation HF #1	Standard Deviation MP #1	Standard Deviation OT #2	Standard Deviation HF #2
	8.606755099	0.608276253	1.153964182		

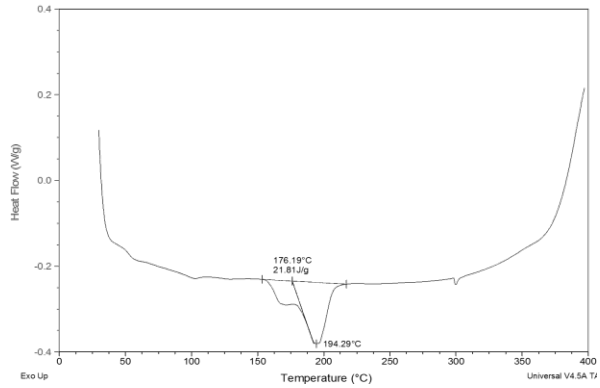

Figure 19 *PMDA-API-P-XYL results of sample test number1*

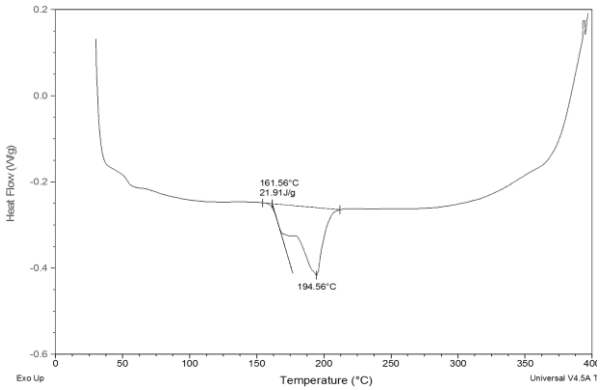

Figure 20 *PMDA-API-P-XYL results of sample test number2*

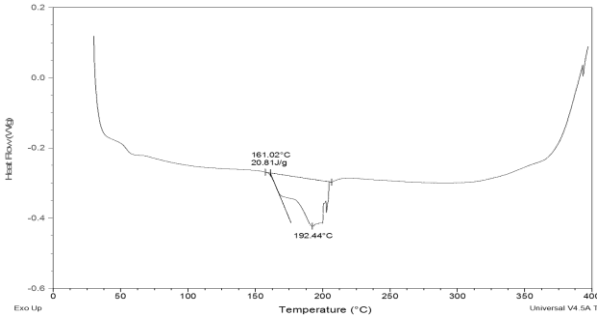

Figure 21 *PMDA-API-P-XYL results of sample test number3*

The styrene component of this ABS in the supplied samples provides the majority of Fourier transform infrared spectroscopy (FT-IR) peaks observed, although there are specific locations where the butadiene and acrylonitrile can co-locate with the styrene. The peak at ~2237 is attributed to the acrylonitrile (C-N triple bond) whereas the peak at ~966 is likely associated with a –CH bending vibration associated with the butadiene carbon-carbon double bond. There is also a peak ~1738 as mentioned in previous literature where carbonyl (C=O) has been discussed. Polystyrene also exhibits multiple resonance peaks from 2000-1700 wavenumbers that do not have defined functional groups assigned but it does appear that the intensity of this peak represents other than these undefined groups. Examination of the laboratory commercial database ABS spectra shows a similar peak profile to the collected spectra in this location. The broad peak associated with O-H stretching vibrations 3500-3000) was largely undetectable. Liquid water, which has a secondary O-H vibration at ~1638, was not observed. There is additional information that can be gathered from these spectra, mostly regarding molecular bond locations and substitutions, but the above I think represents a reasonable starting point. Regarding the ability to determine moisture absorption differences, we would ideally want to test materials of known difference to assure the instrument is as sufficient sensitivity to detect this. Alternatively, as briefly mentioned in conversation before, samples could be analyzed using a combined thermogravimetric-infrared analyzer. Samples are heated under controlled temperature conditions and as chemical groups evolve they are transferred to a gas cell IR for functional group analysis. The observed weight loss can be correlated (and quantified) to specific evolving groups, in this case evolving water. This would take place well below the temperature required for decomposition of the ABS. Using this method and another program a "database" of material spectra has been established, allowing us to maintain a chemical fingerprint profile for comparison to new materials lots.

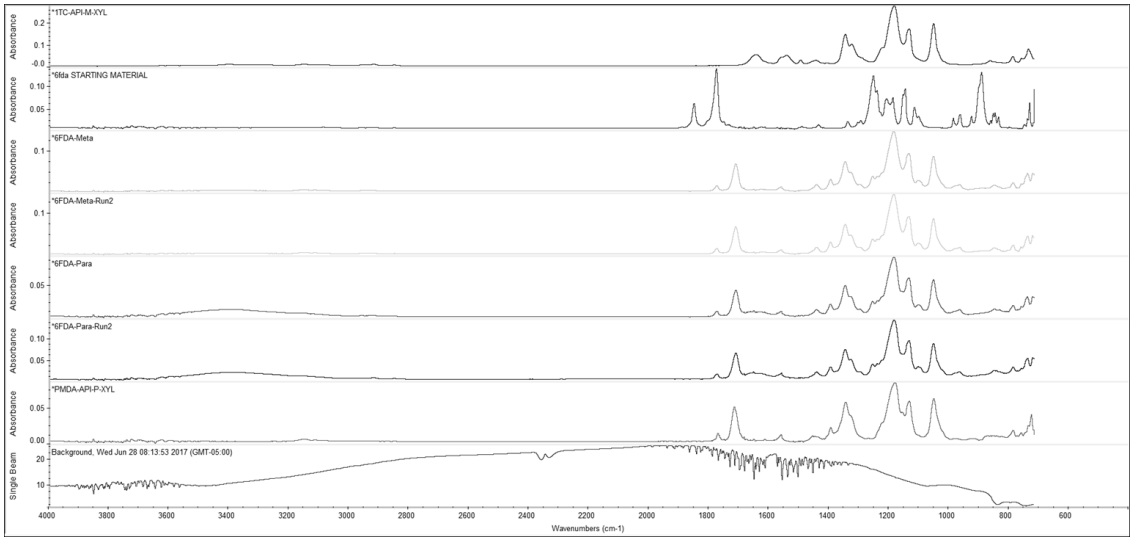

Figure 22 *Shows ATR results for all the Buiding blocks tested*

IV. Conclusion

The concept of integrating polyimides and ILs represents a new direction in the design of polymer materials for use in additive manufacturing. This report has provided preliminary experimental data to help construct and validate a Gaussian 16 simulation model that will be used as a guide to help develop the next iteration of ionic polyimides that can be syntheses to produce a feedstock that can be used in 3-D. The development of 'Ionic Polyimides' offers a solution to this shortage by combining the well-understood and widely accepted properties of conventional polyimides. Much like ILs, the possible combinations of precursors that can be used means that there are thousands of unique ionic polyimide structures possible. Further work on ionic polyimides is clearly warranted, and we believe that the next logical steps are to extend conduct more experiments on other dianhydrides (e.g., 6-FDA) and their thermos properties. This work clearly lays the ground work for future studies to expand the experimental data, as well as continue to build and strengthen confidence in the Gaussian 16 simulation model.

Appendix

Table 3: Building block 6FDA DSC results

Test #	Onset Temperature #1 (°C):	Heat of Fusion #1 (J/g):	Melting Point (°C)
1	244.12	101.9	246.36
2	244.29	109.5	246.12
3	244.35	103	246.42
	Average Onset Temp #1 (°C):	Average Heat of Fusion #1 (°C):	Average Melting Point (°C)
	244.2533333	104.8	246.3
	Standard Deviation OT #1	Standard Deviation HF #1	Standard Deviation MP
	0.119303534	4.107310556	0.158745079

Table 4: Building block Sample TC

Test#	Onset Temperature #1 (°C) :	Heat of Fusion #1 (J/g):	Melting Point #1 (°C):	Onset Temperature #2(°C):	Heat of Fusion #2 (°C):	Melting Point #2 (°C):
1	67.95	8.776	70.62	82.12	102	86.99
2	67.24	10.02	69.11	81.62	112.1	84.23
3	67.66	9.27	70.09	81.37	113.7	83.97
	Average Onset Temp #1 (°C):	Average Heat of Fusion #1 (°C):	Average Melting Point #2 (°C):	Average Onset Temp #2 (°C):	Average Heat of Fusion #2 (°C):	Average Melting Point #2 (°C):
	67.61666667	9.355333333	69.94	81.70333333	109.2666667	85.06333333
	Standard Deviation OT #1	Standard Deviation HF #1	Standard Deviation MP #2	Standard Deviation OT #2	Standard Deviation HF #2	Standard Deviation MP #2

	0.356978057	0.626374755	0.766093989	0.381881308	6.343763342	1.673598917

Table 5: Building block 6FDA-PARA

Test #	Onset Temperature #1 (°C):	Heat of Fusion #1 (J/g):	Melting Point #1 (°C):	Onset Temperature #2(°C):	Heat of Fusion #2 (J/g):	Melting Point #2 (°C):
1	90.55	52.39	136.93	242.71	3.508	244.55
2	70.65	44.79	129.9	N/A	N/A	N/A
3	79.22	54.53	130.91	N/A	N/A	N/A
	Average Onset Temp #1 (°C):	Average Heat of Fusion #1 (J/g):	Average Melting Point #1 (°C)	Average Onset Temp #2 (°C):	Average Heat of Fusion #2 (°C):	Average Melting Point #2 (°C):
	80.14	50.57	132.58			
	Standard Deviation OT #1	Standard Deviation HF #1	Standard Deviation MP #1	Standard Deviation OT #2	Standard Deviation HF #2	Standard Deviation MP #2
	9.981848526	5.118710775	3.800907786			

Table 6: Building block Sample TC-API-M-XYL

Test #	Onset Temperature #1 (°C):	Heat of Fusion #1 (J/g):	Melting Point (°C):	Onset Temperature #2(°C):	Heat of Fusion #2 (J/g):	Melting Point #2 (°C):	Onset Temperature #3(°C):	Heat of Fusion #3 (J/g):	Melting Point #3 (°C):
1	139.59	5.925	150.82	320.07	0.1092	321.18	347.76	0.2082	348.26
2	134.99	4.54	145.25	323.55	0.4459	327.16	336.97	0.0779	337.47
3	142.89	7.113	157.04	N/A	N/A	N/A	338.16	0.06333	338.71
	Average Onset Temp #1 (°C):	Average Heat of Fusion #1 (J/g):	Average Melting Point #1 (°C):	Average Onset Temp #2 (°C):	Average Heat of Fusion #2 (J/g):	Average Melting Point #2 (°C):	Average Onset Temp #3 (°C):	Average Heat of Fusion #3 (J/g):	Average Melting Point #3 (°C):
	139.1566667	5.859333333	151.0366667	321.81	0.27755	324.17	340.9633333	0.116476667	341.48
	Standard Deviation OT #1	Standard Deviation HF #1	Standard Deviation MP #1	Standard Deviation OT #2	Standard Deviation HF #2	Standard Deviation MP #2	Standard Deviation OT #3	Standard Deviation HF #3	Standard Deviation MP #3
	3.967786957	1.287756318	5.897985532	2.460731599	0.238082853	4.228498551	5.9160826	0.079768093	5.904295047

Table 7: Building block Sample 6FDA-Starting Material

Test #	Onset Temperature #1 (°C):	Heat of Fusion #1 (J/g):	Melting Point #1 (°C):	Onset Temperature #2(°C):	Heat of Fusion #2 (J/g):	Melting Point #2 (°C):
1	244.47	87.71	246.49			
2	244.53	103.3	246.87			
3	244.43	105.8	246.53			
	Average Onset Temp #1 (°C):	Average Heat of Fusion #1 (J/g):	Average Melting Point #1 (°C):	Average Onset Temp #2 (°C):	Average Heat of Fusion #2 (J/g):	Average MP #2 (°C):
	244.4766667	98.93666667	246.63			
	Standard Deviation OT #1:	Standard Deviation HF #1:	Standard Deviation MP #1:	Standard Deviation OT #2:	Standard Deviation HF #2:	Standard Deviation MP #2:
	0.05033223	9.802603396	0.20880613			

Table 8: Building block Sample BPADA-APT-P-XYL

Test #	Onset Temperature #1 (°C):	Heat of Fusion #1 (J/g):	Melting Point #1 (°C)	Onset Temperature #2(°C):	Heat of Fusion #2 (J/g):
1	124.1	25.86	143.91		
2	129.49	24.73	136.35		
3	134.52	11.27	146.7		
	Average Onset Temp #1 (°C):	Average Heat of Fusion #1 (J/g):	Average Melting Point #1	Average Onset Temp #2 (°C):	Average Heat of Fusion #2 (J/g):

	129.37	20.62	142.32		
	Standard Deviation OT #1	Standard Deviation HF #1	Standard Deviation MP #1	Standard Deviation OT #2	Standard Deviation HF #2
	5.211036365	8.117025317	5.355063025		

Acknowledgments

This work was done at NASA Marshall Space Flight Center and has been supported by the MSFC's Dr. Frank Six, director of the Office of University Affairs, Dr. Surendra Singhal director EM, Dr. Wayne Gamwell, Mrs. Erin Richardson, EM division. The United States Government retains, and by accepting the article for publication, the publisher acknowledges that the United States Government retains, a non-exclusive, paid-up, irrevocable, worldwide license to publish or reproduce the published form of this work or allow others to do so, for United States Government purposes.

The primary author would like to give a special thank you to the co-authors Dr. Enrique Jackson, Mrs. Erica West, and Tim Huff. I would also like the thank the entire staff of NASA MSFC building 4602 and 4601, for providing their expertise and access to their facilities, raw material, and equipment used in this study.

References

[1] Jones, R, *Mechanics of Composite Materials*, 1nd ed., McGraw–Hill, Washington D.C., 1983,

[2]Committee on Space-Based Additive Manufacturing, *3D Printing in Space*, The National Academics Press, Washington D.C., 2014,

[3] G. Postiglione, G.Natale, G.Griffini, M.Levi, and S.Turri ., "*Conductive 3D microstructures by direct 3D printing of polymer/carbon nano tube nanocomposites via liquid deposition modeling*," Journal of Composites, 2014 pp. 110-113.

[4]R.D. Goodridge, M.L. Shofner, R.J.M. Hague, M. McClelland, M.R. Schlea and R.B. Johnson, C.J. Tuck., "*Processing of a Polyamide-12/carbon nanofiber composite by laser sintering," Journal of Polymer Testing Composites*, 2011 pp. 94-100.

[5]C. I. Braga, et al., "Methodology for DSC calibration in high heating rates," *J. Aerosp. Technol. Manag.*, 3(2), May-Aug. 2011, 179-192.

[6] Bara, J. E.; Camper, D. E.; Gin, D. L.; Noble, R. D. Room-Temperature Ionic Liquids and Composite Materials: PlatformTechnologies for CO2 Capture. Acc. Chem. Res. 2010, 43, 152−159.

[7] Wingard, D NASA Techinal Breifing, 12-11-14

Optimization of Concrete Mixes using Martian and Lunar In-Situ Resources for Additive Construction

Amin K. Akhnoukh[1]
East Carolina University, Greenville, NC

Hunain Alkhateb[2]
The University of Mississippi, University, MS, 38655

Jennifer Edmunson[3] and Michael Fiske[4]
Jacobs Technology NASA-MSFC, Huntsville, AL, 35806

And

John Fikes[5]
NASA –MSFC, Huntsville, AL, 35812

NASA's anticipated date to send humans to an asteroid is 2025 and to Mars is 2030s which requires the preparation of habitats on space for human accommodation. Due to the high cost of shipping construction materials to space, it is required to utilize in-situ materials available on space for the development of standard concrete mixes that fit the construction process and the potential technology to be used in spatial construction, including 3-D printing. In this research, cement matrix using regular Portland cement, stucco, and cement replacement as multi-wall carbon nano-tubes will be tried. In addition, Martian and Lunar regolith will be utilized as aggregate (filling materials) due to their high availability in space in lieu of sending terrestrial aggregates for concrete production. Utilized aggregates were sieved and grouped into different sizes in an effort to find the optimum aggregate size for concrete properties. Research findings proved that smaller regolith particles tend to produce concrete mixes with higher strength due to the improved packing order attained and minimal voids available in the mix. The findings of this research presents a step forward into producing economic concrete mixes, using local spatial materials for the development of habitats on the surface of the moon and mars.

---

[1] Associate Professor, Construction Management Department, East Carolina University, Greenville, NC
[2] Assistant Professor, Civil Engineering, NIRG, The University of Mississippi, , University, MS 38655.
[3] Geologist, In-Space Manufacturing Engineer, Building 4201, Room 228A, Jacobs Technology Inc., NASA Marshall Space Flight Center, AL 35812.
[4] Principal Investigator, Building 4201, Room 230 Jacobs Technologies Inc., NASA/Marshall Space Flight Center, AL 35812
[5] ACME Project Manager, Building 4201, Room 224A, NASA/Marshall Space Flight Center, AL 35812

Nomenclature

ACME = Additive Construction Using Mobile Emplacement
AM = Additive Manufacturing
Fc' = Compressive Strength
CNT = Carbon Nano-Tubes
CNO = Carbon Nano-Onions
MWCNT = Multi-Wall Carbon Nano-Tubes
SCM = Supplementary Cementitious Materials
W/CM = Water-Cement Ratio

I. Introduction

High strength concrete has been produced using terrestrial resources for more than two decades, and was successfully used in special construction projects, high-rise buildings and highway applications. Due to the successful launching of missions to outside space, the demand has risen in the past few years to build space habitats for the accommodation of humans on the outside space. The main impediment to the widespread of spatial construction is the high cost of shipping standard construction materials to outside space. Thus, several research programs are currently working on the investigation of using lighter materials with higher strength, in addition to the utilization of the in-situ spatial resources for the production of economic construction material. In this research, the developed concrete mixes were produced using the following procedures:

1- Supplementary cementitious materials (SCMs) are used in partial replacement of regular Portland cement in an attempt to produce higher strength and better long term performing mixes using lighter weight materials.
2- In situ aggregates, mainly Martian and Lunar Regolith are used as filling materials in lieu of normal fine and coarse aggregate used in today's construction market. Due to the high cost of regolith, simulants with comparable properties are used. The used simulant was sieved into individual sizes to be used in developing various mixes, and investigate the effect of regolith size on the concrete final properties.
3- Water-Cementitious materials ratio (W/CM) are highly controlled to attain a mix suitable for use with the 3-D printing technique to be used in space habitat construction

The focus of this report will be on the potential effect of multi-wall carbon nano-tubes (MWCNT) on the performance of the cement paste, and the effect of different regolith size on the final properties of the concrete produced. In this study, the main property used for the evaluation of the concrete mix performance will be 1) mix flowing ability for fresh mixed concrete, 2) compressive strength (fc') at 7 day, and 3) compressive strength of the concrete mixes at 28 days.

II. Innovation

In today's construction market, additive manufacturing and concrete pouring using 3-D printing techniques are still in its infancy. Few construction projects were poured using 3-D printing technology, mainly in Dubai, China, and the United States. Currently, the largest 3-D printer used in the industry is located in China and used in building furniture. It was successfully used in printing a low rise five story building. Examples of completed 3-D projects are shown in Figures 1 and 2.

Figure 1: 3-D Printed Villa – China

Figure 2: Carbon Fiber Studio – Chicago, USA

The use of additive construction requires to monitor concrete properties to accomplish the construction project on earth or in space construction. The five main critical challenges facing additive construction projects are: flowabilility, extrudability, buildability, set time including initial and final setting and interlayer adhesion. Main challenges are shown in in Figure 3.

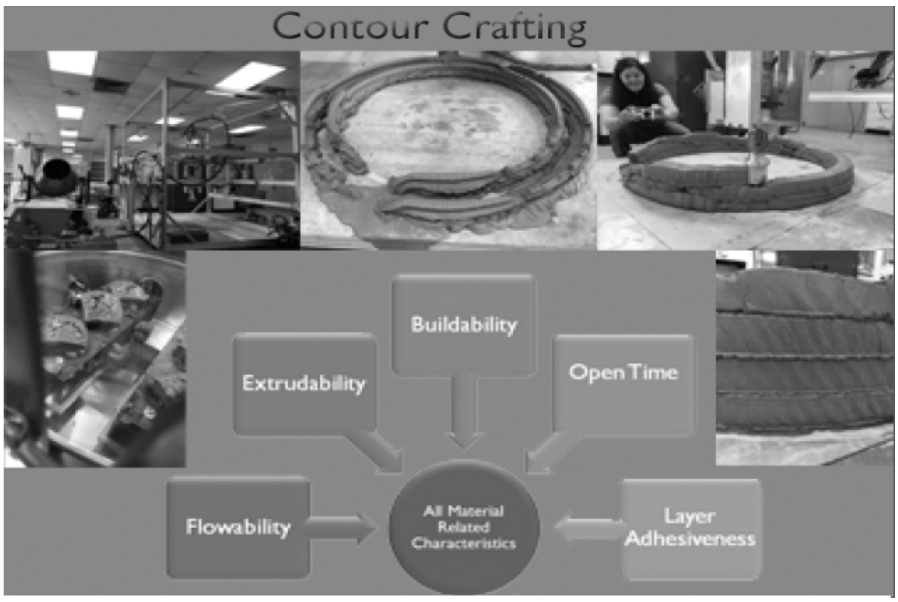

Figure 3: Main Challenges for Concrete Contour Crafting

The use of in-situ resources for habitat construction will expedite the progress of NASA space programs and increase the economic feasibility of space missions. First, the shipment of materials to space will be less frequent, which will reduce the final budget of any project. In addition, the availability of local material reduce the life cycle cost in case of any need to maintenance or repair activities. Finally, a sustained supply for construction materials presents a guarantee to the continuity of construction activities, and minimizes the critical path activities along the project duration. Due to this crucial demand for local construction materials, there is a critical need to understand the transformation of in-situ materials from extraterrestrial destinations such as Martian regolith and any respective atmospheric constituents into revolutionary superior construction materials[1]. Also, a need exists to a better comprehend the relationship between potential research/settlement sites and the available in-situ resources as construction materials at those locations, which will result in optimal composites. Along with the formulation several magnesia-based composite mixes, developing these materials will require intensive multiscale/multifunctional characterization and fundamental modeling and validation of autonomous contour crafting.[2]

III. Materials

Different materials are identified to be used in this research projects. Additional attention was given to materials with superior characteristics that may potentially increase concrete compressive strength, while reducing the final weight of the produced concrete (high strength to weight ratio is extremely beneficial for economic purposes). In-Situ aggregates are also tried as the sole aggregates in concrete manufacturing to minimize freight expenditure. Table 1 Shows the materials used in concrete production:

Table 1: Materials Used and their Main Properties

Material	Property
Portland Cement – Type I/II	Strength requirement meet Type I and composition meet requirement of type II as specified in ASTM C 150[3]
Multi Wall Carbon Nano Tubes	It comprises particles of diameter upto 30 nm. Very large specific surface and high water absorption
Stucco	Containing 25% of its weight cement
Lunar Simulant	With different particle size composition, as shown in the

	following section
Martian Simulant	With different particle size composition, as shown in the following section

IV. Experimental Investigation

The experimental investigation in this research project is divided into two phases. Phase (1) included the sieving of Lunar and Martian simulant to obtain individual sizes to be used in concrete production, and Phase (II) where concrete mixes were batched into standard 2 inch cubes to be tested for compressive strength at ages of 7 and 28 days.

A. Phase I

During phase I, Lunar and Martian simulant samples were analyzed using sieve analysis procedure. According to sieve analysis results, Martian simulant was classified into 8 different sizes using sieve openings ranging from 4 opening per lineal inch to 120 openings per lineal inch, while Lunar simulant was classified into 5 different siezs using sieve openings ranging from 18 openings per lineal inch to 230 openings per lineal inch. Based on Phase (I) sieve analysis results 9 standard concrete mixes were poured for Martian simulant including the 8 different simulant particle sizes and the general non-sieved simulant particle. Similarly, 6 standard concrete mixes were poured for Lunar simulant including the 5 different simulant particle sizes, in addition to the general non-sieved Lunar simulant. (See Table A.1 in Appendix for the nominal sieve opening sizes)

B. Phase II

The different simulant sizes obtained from Phase I were used in mixing 15 different standard concrete mixes to investigate the effect of simulant size on the compressive strength properties of the concrete. In addition to simulant size variation mixes, additional batches of concrete were produced using the non-sieved simulant using MWCNT added as a SCM for the concrete mixes. MWCNT were added by different percentages ranging from 0.25% up to 0.5% of the cement weight in the mix.

Concrete batches using Martian and Lunar simulant were produced by preblended dry granular materials including Type I/II Portland cement, stucco, Martian or Lunar simulant for 2 minutes. Once a homogeneous dry blended powder is attained, mixing water and chemicals are added to the mix for wet mixing. Average wet mixing procedure duration ranged from 3 to 5 minutes (until sufficient mix is attained). Each concrete mix were used to produce 6 2-inch cubes for testing in compression at 7 and 28 days of age. 3 cubes were tested in compression at each age[4]

V. Results

The outcomes of the compressive strength test were recorded for Day 7 and Day 28 for Martian simulant and for Day 7 for Lunar simulant and MWCNT mixes. Additional testing for Lunar simulant and MWCNT specimen at 28 day will be concluded for future research reports. Results for Martian specimen compressive strength are shown in Table 2 and Figure 4, while lunar simulant and MWCNT results are shown in Tables 3 and 4 respectively. Each mix was named to reference the material ingredients and a shortened phrase was given in the results section whereas a detailed list for the materials in each abbreviated legend displayed in Table A.2 in the Appendix.

Table 2: Results of Compressive Strength Testing for Martian Simulant Mixes

Size	Day 7	Day 28	% Increase
General	3311	3536	6.80
PTM004	2950	4673	58.41
PTM005	3067	5161	68.28
PTM010	3207	4739	47.77
PTM018	3094	4861	57.11
PTM035	3183	5168	62.36

PTM060	3717	4627	24.48
PTM120	4032	4979	23.49
PTM230	3472	4346	25.17

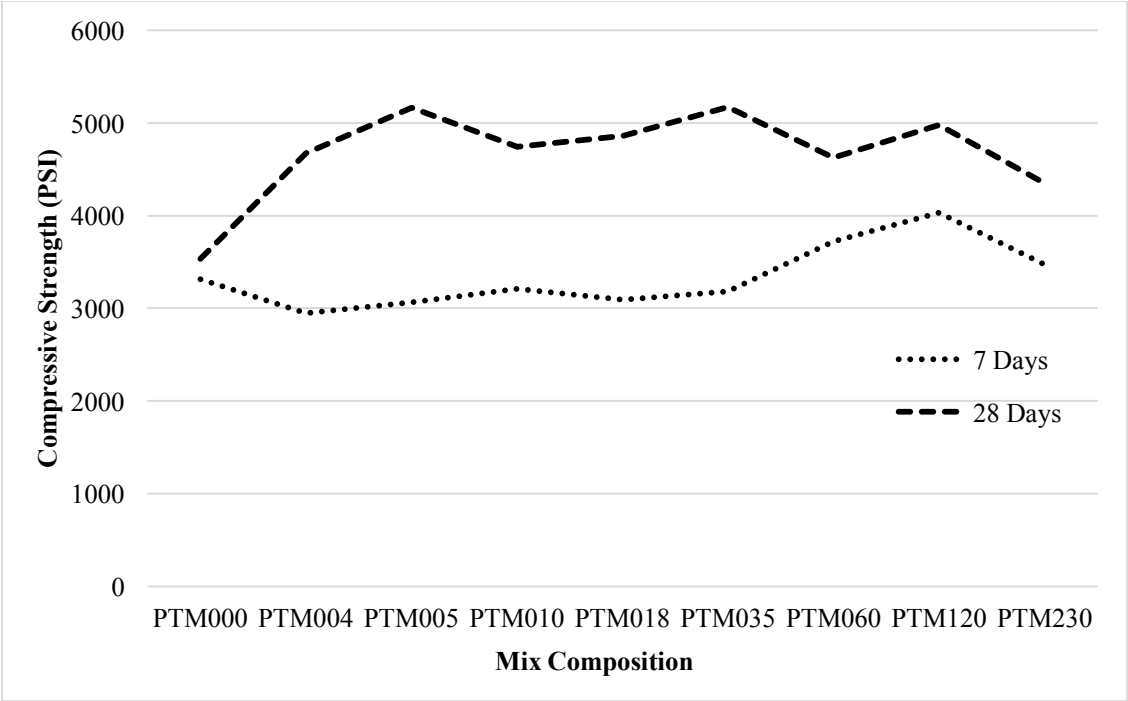

Figure 4: Martian Simulant Mixes Compressive Strength Test Results

As shown from Table 2 and Figure 4, there is a general trend in for the gained compressive strength in the Martian simulant mixed specimens. The results displayed show that Martian simulants have on average a higher strength gain (>38%) for the 7days compared to the 28 days compressive strength. In addition, the optimum simulant size is shown to be sieve #120, the smaller the particle size the higher the compressive strength. It would be very valuable to conclude on this by carrying further chemical and physical testing validations; which will be done in near future.

Table 3: Results of Compressive Strength Testing for Lunar Simulant Mixes

Size	Day 7
PTL000	4031
PTL018	2981
PTL035	3587
PTL060	3059
PTL120	4035
PTL230	4259

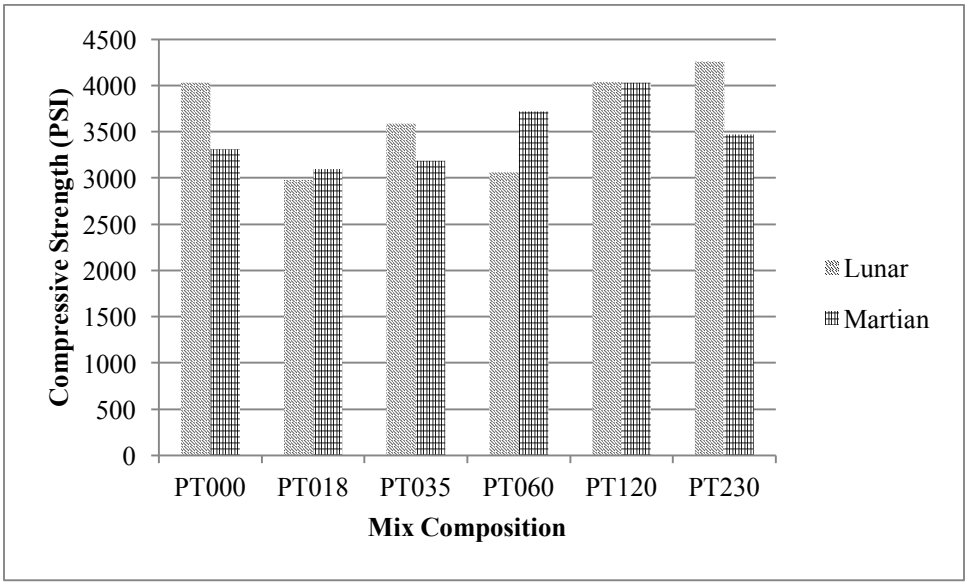

Figure 5: Comparison Between the Martian and the Lunar Simulants Particle size on Compressive Strength

The Lunar simulant particle size aging compressive strength was not completed by the time this report has been submitted. It is anticipated that the Lunar simulant will follow a similar trend compared to the Martian, however the average gained strength is still unknown. It is anticipated that the average gained strength will be higher compared to the results shown in Table 2, due to the physical interlocking enhancement. However a comparison for the effect of the Martian simulant vs the Lunar simulant particle size distribution on the compressive strength is shown in Figure 5. As displayed in Figure 5, the trend in the Martian simulant is more obvious compared to the Lunar, and the optimum particle size is not the same for both simulants; it is #120 (Martian) and #230 (Lunar), further investigation is needed to address these variations. On the other hand, the researchers have recognized the necessity to step back and characterize the simulant themselves, in terms of mineralogy, chemical reactivity, specific gravity, and absorption capacity, ..etc to better understand the simulants effect on OPC mixes.

Table 4: Results of Compressive Strength Testing for MWCNT Mixes

Mix Composition	Day 7
PTN(0.4)M004A	1562
PTN(0.4)M004B	2813
PTN(0.25)M000A	3112
PTN(0.25)M000B	2341
PTN(0.5)M000	1588
PTN(0.25)L000	2784
PTN(0.25)M120	1399
PTN(0.25)L120	3210
PTN(0.4)M000A	1363
PTN(0.4)M000B	1202
PTN(0.4)L000	2663

Table 5: Results of Compressive Strength Testing for MWCNT Mixes

Composition	7 Days	28 Days	% Increase
PTN(0.4)M004A	1562	2847	82.31
PTN(0.4)M004B	2813	4608	63.79
PTN(0.25)M000A	3112	3994	28.35
PTN(0.25)M000B	2341	3545	51.47
PTN(0.5)M000	1588	2473	55.79
PTN(0.25)L000	2784	4095	47.09
Average	2367	3594	54.80

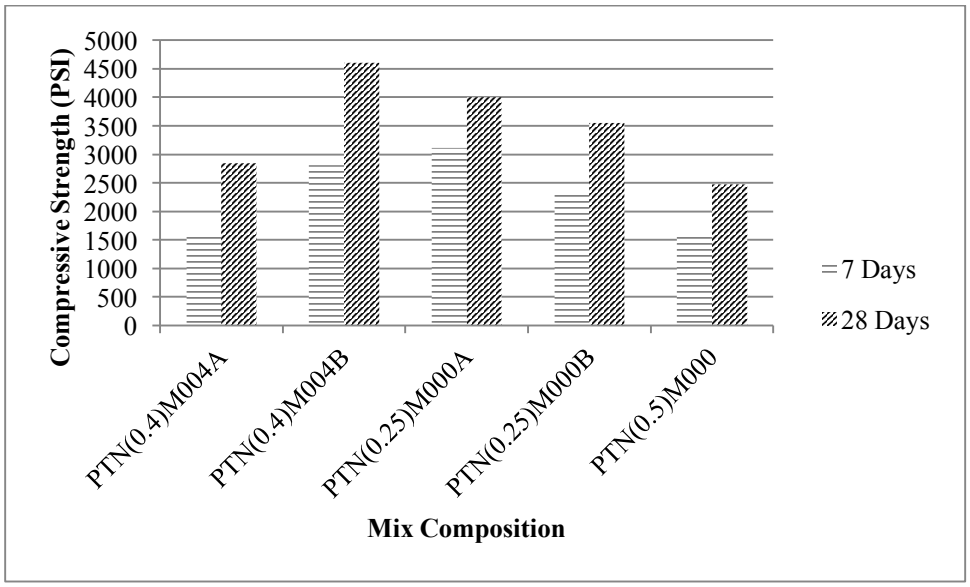

Figure 6: Results of Compressive Strength Testing for MWCNT Mixes @ 7 and 28 Days

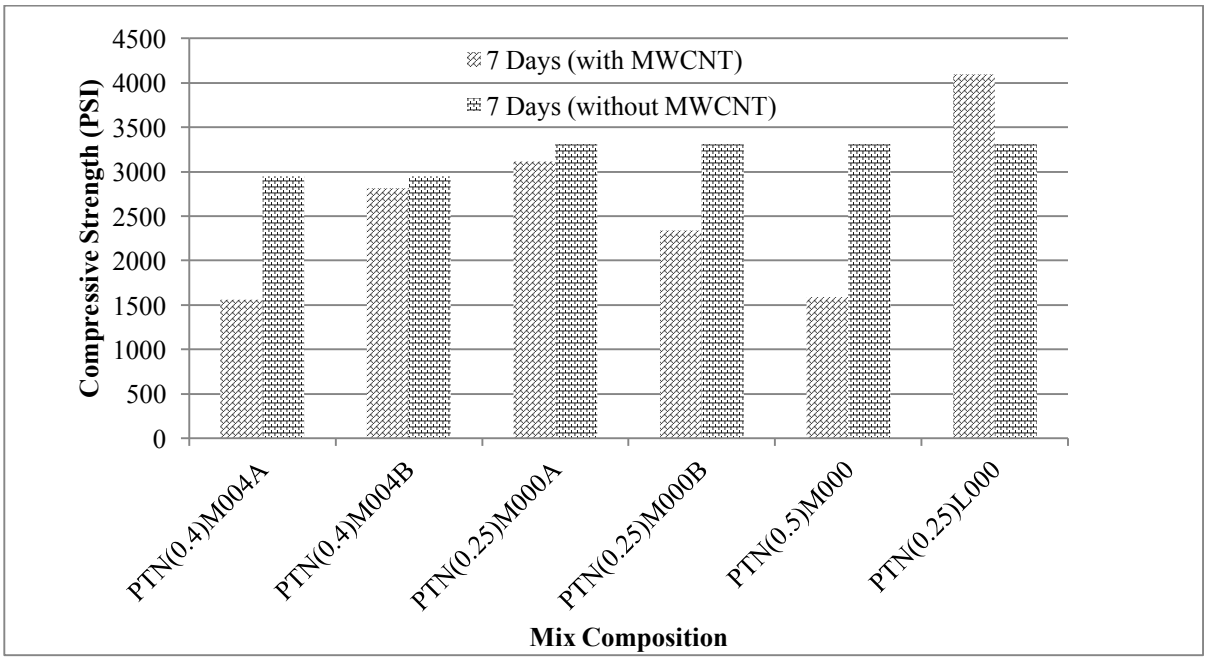

Figure 7: Results of Compressive Strength Testing for MWCNT effect @ 7Days for Martian and Lunar Simulant

VI. Conclusion

Supplementary cementitious materials are detrimental to the success of high strength concrete mixing. However, the use of MWCNT particles with superior quality didn't result in added value in this research due to the relatively high dosage of MWCNT (up to 0.5% of cement weight). Higher dosage of MWCNT resulted in lower flowing ability and increased voids within the concrete mix, which reduced the measured compressive strength at age of 7 and 28 days. Additional research findings showed that Lunar and Martian Regolith can be successfully used in pouring concrete mixes with relatively high strength. Simulant particle sizes have a direct effect on cube final compressive strength. The research results showed that smaller particle sizes typically result in higher concrete strength due to the reduced voids in poured cube.

The authors highly recommend the use of additional types of SCMs for future research as fly ash, micro-silica, nano-silica, quartz flour, and carbon nano-onions. In addition, different types of fibers should be used for improving mix tensile strength and long term characteristics.

Appendix

Table A.1: Particle Size Conversion

Mesh (Sieve Designation)	Nominal Sieve Opening (µm)	
	Martian	Lunar
004	5000	
005	4000	
010	2000	
018	1000	1000
035	500	500
060	250	250
120	125	125

230	63	63
000	Unsieved	Unsieved

Table A.2: Legend Abbreviations

Abbreviation	Material
P	Portland Cement
Mg	MgO based Cement
Na	Sodium Silicate
G	Geopolymer
S	Silica Fume
F or C	Fly ash
N	Carbon nanotubes
T	Stucco
M	Martian Simulant
L	Lunar Simulant

A. Phase 1 Mixing Procedure

1. All dry ingredients were mixed together (OPC, Stucco, and Regolith)
2. Water with half of the superplacterizer were mixed together
3. Liquid mixture in step 2 was added to the dry ingredients in step 1 and mixed thoroughly
4. The rest of the superplacterizer was added to the mortar mix and blended well together
5. Mortar was tested for followability and poured into the compressive strength molds

B. Phase 2 Mixing Procedure

1.MWCNT were ultrasonicated, to ensure dispersion, for 4-6 hours, depending on the MCWNT % in 0.5 of the water measured for the mix
2. Dry ingredients were mixed together (OPC, Stucco, and Regolith)
3. Water with half of the superplacterizer were mixed together
4. Liquid mixture in step 2 was added to the dry ingredients in step 1 and mixed thoroughly
5. The rest of the superplacterizer was added to the mortar mix and blended well together
6. Mortar was tested for followability and poured into the compressive strength molds

Acknowledgments

The authors would like to acknowledge the funding received for the Additive Construction with Mobile Emplacement Project from the United States Army Corps of Engineers Engineer Research Development Center – Construction Engineering Research Lab and the National Aeronautics and Space Administration Space Technology Mission Directorate Game Changing Development Program. The research team would like to acknowledge the contribution of Dr. Alex. Biris at the University of Arkansas at Little Rock for his scientific guidance, Mr. Tom Strickland for his material donation, and Engineer Katherine Bell for her support and help during the compressive strength testing of concrete cubes.

References

[1]NASA Technology Roadmaps TA 6: Human Health, Life support, and Habitation Systems, 2015.

[2]Cesaretti, G., Dini, E., Kestelier, X. D., Colla, V., and Pambaguian, L. "Building components for an outpost on the lunar soil by means of a novel 3D printing technology" *Acta Astrunautica* Vol. 93, 2014, pp. 430-450.

[3] ASTM C150, "Standard Specifications for Portland Cement," American Society for Tetsing and Materials, 2012

4 ASTM C 109, " Standard Test Method for Compressive Strength of Hydraulic Cement Mortars," American Society for Testing and Materials, 2016

Failure and Fatigue Analysis of Self-Reacting Friction Stir Welding Pin Tools

Robert L. Amaro[1]
University of Alabama, Tuscaloosa, AL,35487. Formerly with Colorado School of Mines, Golden, CO, 80401

The self-reacting friction stir welding (SR-FSW) process is used extensively in the construction of the Space Launch System (SLS) launch vehicle at NASA. The solid-state welding process is performed by use of three primary tool components: the crown shoulder, the root shoulder, and the pin. The welding tool is responsible for both heating and mixing of the materials being joined. The tool experiences large loads during steady state welding, as well as impulse-like excursions during weld start up. Furthermore, a-typical welding procedures have been shown to impart sufficient loads upon the pin as to either break the pin from singular overload events, or shorten the fatigue life of the pin. This work characterizes the SR-FSW pin tool's life and load capabilities for single event excursions, as well as for fatigue life, when welding 0.625" thick 2219-T87 aluminum.

I. Introduction

Self-reacting friction stir welding is a solid-state joining technique in which the parent material is mechanically stirred by use of a cylindrical pin tool and two disk-like shoulders, placed at the top (crown shoulder) and bottom (root shoulder) surface of the joint being bonded. The pin tool and shoulders are spun at the same prescribed rotational speed, ω. The crown shoulder and root shoulder apply pinch-like forces to the bond joint. The pinch forces are prescribed and can be independent from each other. The spinning of the pin-tool and shoulder assembly creates frictional heating at the crown, root, and center of the bond. During the SR-FSW start-up procedure, the welding tool assembly is brought up to a desired rotational speed, shoulder pinch loach are then applied, and the weld process proceeds by traversing the welding tool along the bond joint-line at a prescribed translational speed, V.

The welding tool assembly experiences transient forces and torques during the start-up procedure, as well as steady state forces and torques during the welding process. Furthermore, it has been shown that impulse-like loads that are

[1] Assistant Professor, Mechanical Engineering, Box 870276, Tuscaloosa, AL 35487-0276.

detrimental to the weld tool life may be applied to the weld tool assembly during weld tool assembly qualification. The SR-FSW pin-tool has been found to be the weak link in the weld tool assembly when welding 2219-T87 aluminum, such that the pin-tools have failed during small-scale weld tests, as well as large-scale production welds. An analysis was performed to estimate the static and fatigue life of the SR-FSW pin tool as a function of boundary conditions, input forces and torques, and pin tool material properties. The analysis may be used for life estimation of existing pin-tool designs and welding processes, as well as design of new pin-tools.

II. SR-FSW Pin-Tool Material

The current SR-FSW pin-tools utilized at NASA to join aluminum are made from the nickel-cobalt based alloy MP-159. The MP-159 alloy chemical composition and mechanical properties are listed in Table 1 and Table 2.

Table 1 Alloy MP-159 nominal chemical composition (weight percent) [1]

Ni	Co	Cr	Fe	Mo	Ti	Nb (Cb)	Al
25.5	35.7	19.0	9.0	7.0	3.0	0.6	0.2

Table 2 Alloy MP-159, work strengthened and aged, quasi-static and fatigue properties [2,4]

Temp. (F)	*UTS* (ksi)	$\sigma_{y\_0.2}$ (ksi)	$\varepsilon_{2''}$ (%)	*E* (10^3 ksi)	$Sf_{N=1M}$, *R*=-1 (ksi)	$Sf_{N=10M}$, *R*=-1 (ksi)
70	279.5	276.0	6.3	33.3	110	95
800	238.0	232.3	5.8	30.2	110	80
1200	222.5	212.3	5.0	26.3	110	80

Given the material's stable quasi-static and fatigue response between room temperature and 1000° F, the MP-159 alloy appears to be a good candidate for SR-FSW pin tool material

III. Loading and Boundary Conditions

The general SR-FSW tool geometry is provided in Figure 1. The pin tool, crown shoulder, and root shoulder are all labeled for clarity. One should note that the pin tool extends the entire length of the tool assembly, and that the crown and root shoulders are located along the pin tool length.

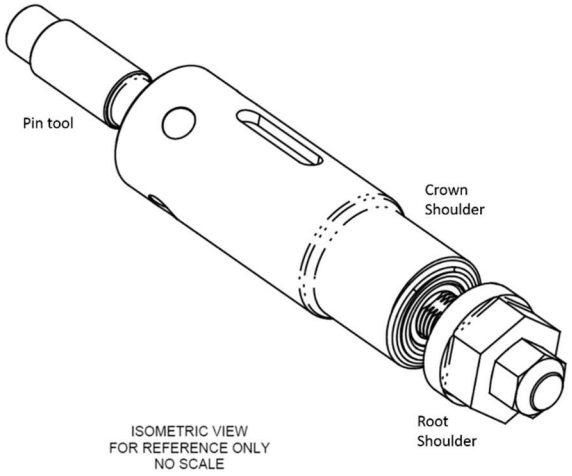

Fig. 1 Generic SR-FSW tool assembly

The SR-FSW pin tool experiences forces from three ortho-normal directions (X, Y, Z), a torque with respect to its longitudinal axis (defined as Z), as well at temperatures on the order of 350° F. The X-direction force, *Fx*, is a direct resultant of the applied weld traverse speed, *V*. The Y-direction force, *Fy*, as well as the torque with respect to the Z-axis, *Tz*, are resultants of the stirring dynamics produced by the pin tool rotational speed, ω. The Z-direction force, *Fz*, is applied to the weld joint by the application of the root shoulder pinch load. A free-body diagram of the loads applied to the welding tool assembly is provided in Figure 2. One will note that there are threads on the pin tool that will cause stress concentrations for all stresses associated with the loads applied.

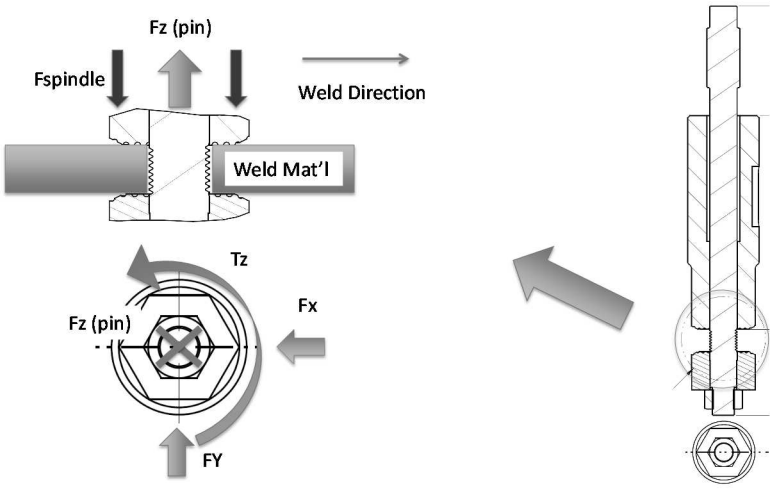

Fig. 2 SR-FSW tool free-body diagram

IV. Static Failure Analysis

As a starting point for the pin tool life analysis, one should determine the static factor of safety (FOS) for each potential combination of load incursions that the pin may experience. This would include viewing the welding start-up transients as well as the steady state welding loads as if they occurred at a single instant in time (i.e. not repeated or fatigue loaded). If the tool fails due to yielding from either of these fatigue events when viewed as a static load application, a fatigue analysis would not be worthwhile. Furthermore, one of the common methods to extract the pin tool from the base material has the potential to apply large torques (*Tz*) and extraction forces (*Fz*) on the pin in a quasi-static manner. Four potential pin loading scenarios are detailed in Table 3.

Table 3 Static welding pin tool load cases

Load Case	*Tz* (lbf-ft)	*Fx* (lbf)	*Fy* (lbf)	*Fz* (lbf)
Extraction (measured)	40	0	0	9000
Extraction (worst-case)	84	0	0	9000
Start-up	84	3800	2900	5000
Steady State	65.3	2150	2050	5000

The torque and force values in the load cases titled Extraction (measured), Start-up, and Steady State all result from measurements taken from representative SR-FSW equipment at NASA while performing welding or pin tool extraction on 0.625" thick 2219-T87 aluminum. The load case titled Extraction (worst case) couple the worst case measured extraction force in the Z-direction, and the worst case measured start-up torque, as it is conceivable that these two conditions could be inadvertently coupled during pin tool extraction.

The torque applied to the pin, *Tz*, is applied in equal magnitude over the entire circumference of the pin. This torque will also be amplified by the static stress concentration factor *Kts*. The force *Fx* is applied to the pin in the X-direction. This force results from the pin tool traversing the weld at a speed *V*. As a first-order analysis it is assumed here that the force distribution is equal as a function of material depth, and therefore the resultant of the force distribution will occur at the centroid of the force distribution in the X-direction. This assumption is depicted graphically in Figure 3a and the implications of this assumption will be explored later in this work. The force *Fy* is applied in the Y-direction (normal to *Fx*) and results from the dynamic mixing resulting from the tool rotational speed, ω. The resultant force vector, *Fy*, is also applied at the centroid of an assumed equal force distribution as a function of material depth. The location of the assumed force vectors *Fx* and *Fy* is critical as these forces result in a bending

stress that is proportional to the distance from the point of load application and the point of interest. In this case, the point of interest is located at the thread in the pin tool just below the crown shoulder. As such, a static stress concentration factor, *Kt1*, is applied to the stresses resulting from these forces.

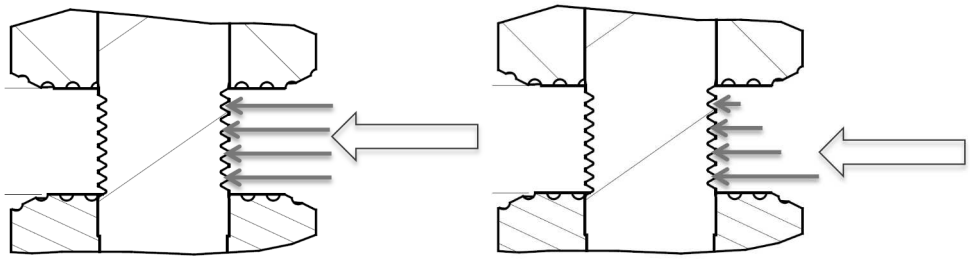

a) b)

Fig. 3 Zoomed section of SR-FSW tool. See figure 2 for reference.

The tensile force, *Fz*, results in a tensile stress within the pin tool. The maximum stress will occur at the root of each pin tool thread and therefore must be modified by a separate stress concentration factor, *Kt2*. Given that the forces *Fx* and *Fy* are applied normal to each other, there is a single location within the pin tool that experiences the entirety of the shear stress resulting from *Tz* and the normal stress resulting from *Fz*, as well as 70.7% of the bending stresses resulting from each of the forces *Fx* and *Fy*. This work will focus on that worst-case location.

The magnitude of the stress at the worst case location is determined by use of the Von Mises effective stress. The equation along with the necessary modifications for loading and boundary conditions is as follows:

$$\sigma_{VM} = \sqrt{\frac{(\sigma_{x\prime}-\sigma_{y\prime})^2+(\sigma_{x\prime}-\sigma_{z\prime})^2+(\sigma_{y\prime}-\sigma_{z\prime})^2+6\tau_{\prime}^2}{2}}, \quad (1)$$

where each of the individual stress components are defined in Eq's 2 through 5.

$$\sigma_{x\prime} = 0.707 \cdot Kt1\frac{Fx \cdot d \cdot c}{I} \quad (2)$$

$$\sigma_{y\prime} = 0.707 \cdot Kt1\frac{Fy \cdot d \cdot c}{I} \quad (3)$$

$$\sigma_{z\prime} = Kt2\frac{Fz}{A_t} \quad (4)$$

$$\tau = Kts\frac{Tz \cdot r}{J} \quad (5)$$

The variable *d* is the distance between the applied *Fx* and *Fy* loads and the point of interest (taken to be half the material thickness in this first order analysis), *c* is the distance from the neutral axis of the pin to the point of interest (outer fiber of pin), *I* is the area-moment of inertia, A_t is the tensile area of the pin tool, *r* is the radius of interest, and

J is the polar moment of inertia of the pin tool. Given that the pin tool is cylindrical, and that maximum bending and torsional stresses occur at the outer fiber, the variables *c* and *r* take on the value of the minor radius (*rt*) of the threaded section. Finally, as a worst-case assumption, the stress intensity factors (*Kt1*, *Kt2* and *Kts*) are all set to the theoretically largest numerical value of 3. The values of all the variables used in Eq's 2 through 5, for a 5/8"-18 threaded pin tool are provided in Table 4.

Table 4 Values of variables used in fist-order analysis for 5/8"-11 UNF pin tool

dt- minor diameter (in)	*I*- area moment of inertia (in4)	A_t- tensile area (in2)	*rt*- minor radius (in)	*J*- polar moment of inertia (in4)
0.5528	0.0046	0.2560	0.2764	0.0092

The worst-case Von Mises effective stress experienced by the pin tool, for each of the four static load cases detailed in Table 3, along with the factor of safety against yielding are provided in Table 5. The materials 0.2% offset yield strength was taken as 270 ksi.

Table 5 Pin tool Von Mises stress and static factor of safety against yielding for the four load cases in Table 3

Load Case	*Tz* (lbf-ft)	*FX* (lbf)	*FY* (lbf)	*Fz* (lbf)	*VM* (psi)	$FOS\_\sigma y_{0.2}$ (-)
Extraction (measured)	40	0	0	9000	129530	2.08
Extraction (worst-case)	84	0	0	9000	189892	1.42
Start-up	84	3800	2900	5000	177692	1.52
Steady State	65.3	2150	2050	5000	125391	2.15

One will note that the welding pin tool is loaded to a static FOS of 1.5 during welding start-up transients. Furthermore, the pin tool is loaded to a static FOS of 1.4 when the worst-case extraction load coupled with the worst case start-up torque are coupled. A similar load condition was further explored by determining the combinations of *Fx* and *Fy* that would cause yielding when coupled with start-up torque and axial force values. The results are provided in Figure 4. The data in Figure 4 indicates that a single *Fx* or *Fy* load of 4250 lbf, when coupled with the *Fz*=5000 lbf and *Tz*=84 lbf-ft, would cause the pin tool to yield.

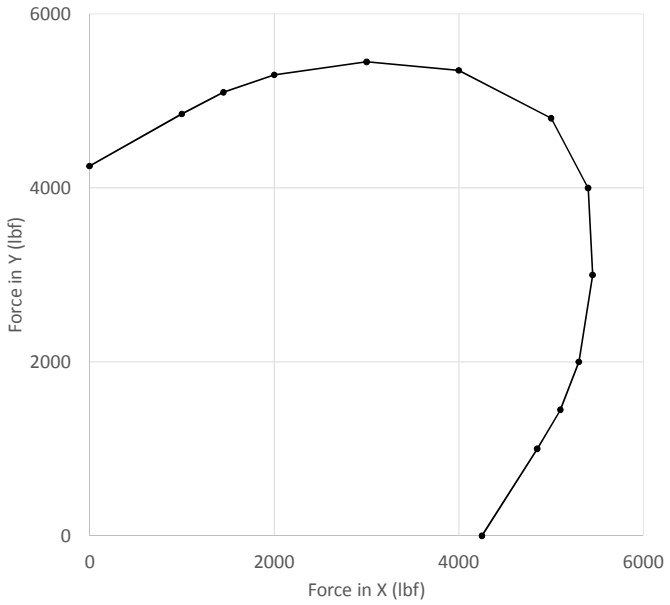

Fig. 4 Pin tool failure locus in *Fx* and *Fy* for *Fz*=5000 lbf and *Tz*=84 lbf-ft

The preceding analysis assumed that the *Fx* and *Fy* loads were evenly distributed as a function of depth within the material, i.e. the resultant force vector occurs at the center of the material being welded. Two other scenarios are explored here. First, if the resultant force distribution behaved as a pressure head, as indicated in Figure 3b, then the distance to the point of interest for Eq's 2 and 3 would be two-thirds the material thickness. Second, if the pin tool or material being welded took on some slag/flash from the welding process and the load was transferred to the pin tool at the bottom of the material, the distance of interest would be the full material thickness. The resulting FOS, for each of the four load cases discussed above, are provided in Table 6.

Table 6 Pin tool Von Mises stress and static factor of safety against yielding for the four load cases in Table 3

	d=0.3125"		*d*=0.416"		*d*=0.625"	
Load Case	*VM* (psi)	*FOS_σy0.2* (-)	*VM* (psi)	*FOS_σy0.2* (-)	*VM* (psi)	*FOS_σy0.2* (-)
Extraction (measured)	129530	2.08	129530	2.08	129530	2.08
Extraction (worst-case)	189892	1.42	189892	1.42	189892	1.42
Start-up	177692	1.52	202586	1.33	269391	1.00
Steady State	125391	2.15	133911	2.02	164484	1.64

The analysis indicates that a bur at the bottom of the weld start-up location, or an unclean pin tool could lead to yielding during start-up transient loading.

V. Fatigue Failure Analysis

The start-up and steady-state Load Cases were analyzed for fatigue life by use of a high-cycle fatigue, or S-N approach. Given that the applied load ratio, $R=\sigma_{min}/\sigma_{max}$, is not full reversed, the fatigue factor of safety for infinite life ($N=10^6$ cycles) is estimated by use of the Modified Goodman relationship provided in Eq's 6 through 10 (Modified Goodman analysis) [3].

$$\sigma'_{m@s} = \frac{UTS(Sf^2 - Sf\sigma'_a + UTS\sigma'_m)}{Sf^2 + UTS} \quad (6)$$

$$\sigma'_{a@s} = \frac{-Sf(\sigma'_{m@s})}{UTS} + Sf \quad (7)$$

$$ZS = \sqrt{(\sigma'_m - \sigma'_{m@s})^2 + (\sigma'_a - \sigma'_{a@s})^2} \quad (8)$$

$$OZ = \sqrt{(\sigma'_a)^2 + (\sigma'_m)^2} \quad (9)$$

$$FOS = \frac{OZ+ZS}{OZ} \quad (10)$$

The values for *Sf* and *UTS* are provided in Table 2, σ'_m is the fully corrected Von Mises mean stress, and σ'_a is the fully corrected Von Mises alternating stress, as provided in Eq's 12 and 13, respectively.

$$\sigma'_{VM\_max} = \sqrt{\frac{(\sigma_{x'\_max} - \sigma_{y'\_max})^2 + (\sigma_{x'\_max} - \sigma_{z'\_max})^2 + (\sigma_{y'\_max} - \sigma_{z'\_max})^2 + 6\tau'^2_{max}}{2}} \quad (11)$$

$$\sigma'_m = \sqrt{\frac{(\sigma_{x'\_mean} - \sigma_{y'\_mean})^2 + (\sigma_{x'\_mean} - \sigma_{z'\_mean})^2 + (\sigma_{y'\_mean} - \sigma_{z'\_mean})^2 + 6\tau'^2_{mean}}{2}} \quad (12)$$

$$\sigma'_a = \sigma'_{VM\_max} - \sigma'_m \quad (13)$$

The individual stress components in Eq's 11 through 13 are defined in Eq's 14 through 17.

$$\sigma_{x'_{max/mean}} = 0.707 \cdot Kfm1 \frac{Fx_{max/mean} \cdot d \cdot c}{I} \quad (14)$$

$$\sigma_{y'_{max/mean}} = 0.707 \cdot Kfm1 \frac{Fy_{max/mean} \cdot d \cdot c}{I} \quad (15)$$

$$\sigma_{z'_{max/mean}} = Kfm2 \frac{Fz_{max/mean}}{A_t} \quad (16)$$

$$\tau'_{max/mean} = Kfms \frac{Tz_{max/mean} \cdot r}{J} \quad (17)$$

The variables *Kfm1*, *Kfm2*, and *Kfms* are the mean fatigue stress concentration factors for the specific loading and boundary conditions analyzed in Eq's 14 through 17. They are each determined by use of Eq's 18 and 19.

$$Kf = 1 + q(Kt - 1), \textit{ and} \quad (18)$$

$$Kfm = \frac{\sigma_{y\_0.2} - Kf \cdot \sigma'_{a\_nom}}{|\sigma'_{m\_nom}|} \quad (19)$$

The variable q is the notch sensitivity factor and is taken as q=0.65 here. The stress values σ'_{a_nom} and σ'_{m_nom} are the uncorrected alternating and mean Von Mises stresses provided in Eq's 12 and 13. Specifically, in order to determine the uncorrected values one would solve Eq's 14 through 17 by setting *Kfm1*, *Kfm2*, and *Kfms* equal to 1.

In order to estimate the number of cycles to failure for the operational load cases (start-up and steady state), the traditional S-N approach is used (S-N analysis). First, the non-fully-reversed alternating stresses resulting from the Load Cases must be converted to an equivalent fully-reversed alternating stress, σ'_{ar}. This was done by use of the Smith-Watson-Topper relationship provided in Eq 19 [4].

$$\sigma'_{ar} = \sqrt{\sigma'_{VM\_max} \cdot \sigma'_a} \quad (19)$$

Once the corrected alternating stress is determined, it may be used in conjunction with a fully-reversed S-N curve for the MP-159 material to determine the cycles to failure, N_f, located in Table 2. The results of the Modified Goodman analysis and the S-N analysis are provided in Table 7 for the start-up and steady state load cases.

Table 7 Fatigue Factor of Safety at 10^6 cycles and cycles to failure for given load cases

	d=0.3125"	
Load Case	$FOS_{N=1M}$	N_f
Start-up	0.005	8700
Steady State	0.020	49000

VI. Conclusion

The analysis performed as part of this work indicates that the current pin tool has a small static factor of safety with respect to weld start-up transients (FOS=1.5). The static factors of safety calculated here are a first-order analysis based upon the known measured loads placed upon the pin tool. Having said that, any excursions outside of the known loading scenarios have the propensity to permanently damage the pin tool. Furthermore, the fatigue cycles to failure for steady state operation calculated here are based upon a pin tool having not experienced prior yielding. If the pin tool were loaded to yield and then subsequently used for production welding, the cycles to failure would be drastically reduced.

Acknowledgments

The author would like to thank Vann Bradford and Jeff Sowards for their support on this work.

References

[1] Latrobe Specialty Steel Company, "MP159 Alloy, High Temperature, Ultra High Strength, High Ductility, Corrosion Resistance," Advertising Technical Report, 2007.

[2] Battelle, "Engineering Data on New Aerospace Structural Materials," AFML Technical Report AFML-TR-11-198, 1977.

[3] Norton, R. L., *Machine Design an Integrated Approach*, 3rd ed., Pearson Prentice Hall, New Jersey, 2006.

[4] Dowling, N. E., "Mean Stress Effects in Stress-Life and Strain-Life Fatigue," SAE Technical Paper 2004-01-2227, 2004.

Software-Defined Wireless Communication: Toward Reliable and Energy Efficient Wireless Sensing for Space and Extreme Environments

Baek-Young Choi*
University of Missouri - Kansas City, MO 64110

Reliability is the critical challenge of wireless sensing in space systems operating in extreme environments. Energy efficiency is another concern for battery powered wireless sensors. Considering the physics of wireless communications, we propose an approach called Software-Defined Wireless Communications (SDC) that dynamically decide a reliable channel(s) avoiding unnecessary redundancy of channels, out of multiple distinct electromagnetic frequency bands such as radio and infrared frequencies. We validate the concept with Android and Raspberry Pi sensors and pseudo extreme experiments. SDC can be utilized in many areas beyond space applications.

I. Introduction

Sensing is integral for any space mission applications such as space vehicles, satellites and payloads, surface explorations, ground systems, and space habitats. Sensing data is the basis of monitoring and operation of the space missions. Sensing is also vital for exhaustive ground testings. Examples of various kinds of sensing needs are

- Physical sensing: temperature, humidity, pressure and radiation inside or around modules of a rocket, crew capsule, or habitat
- Chemical sensing: air quality and water quality of environment control and life support systems
- Biological sensing: mold, mildew or other airborne bacteria
- Crew health monitoring: vital signs and sleep behavior
- Ground testing: structure tolerance of test articles under stress from vibrations, physical strain, cryogenic and high temperatures

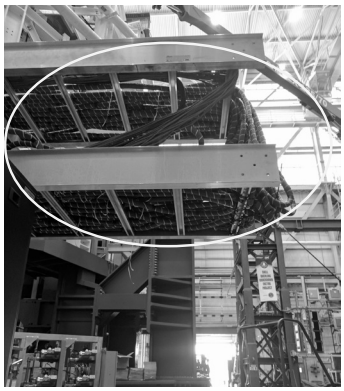

Figure 1: NASA Testing facility: bulky and heavy cables

While there are some internal efforts being made to utilize wireless technologies for sensing, most sensing data transfer in space-related projects is currently done through wireline communication, as in Figure 1. It is because the space environment poses unique and extreme challenges such as radiations from solar events and cosmic rays, extremes temperatures, both hot and cold, depending its location relative to the Sun and due to absence of the insulating atmosphere of the Earth. In the midst of the harsh operational environment, *reliability* is a primary concern of NASA's missions, like the well-known quote, *'failure is not an option'*.[1] Furthermore, a sensor's limited battery life is another challenge to stay operational for the duration of a mission.

On the other hand, for applications of the general public, there exists an enormous body of studies on wireless sensor networks including the issues of sensing coverage, routing, and architecture in the context of ad-hoc networks.[2] With the advancement of embedded systems and the prevalence of communication technologies, numerous Internet-of-Things (IoT) objects in everyday life are wirelessly connected to each other and

*Associate Professor, Computer Science Electrical Engineering, University of Missouri - Kansas City, MO 64110

through the Internet. The benefits of *wireless* sensors in space applications are tremendous and clear. The potential advantages of wireless sensing over wired counterparts include

- Reduced weight of spacecraft
- Easy and fast deployment
- Flexible sensor placement and data gathering from challenging area where wiring is difficult, hazardous or impossible
- Changes in location of sensors and data collectors
- Changes in the number of sensors and data collectors
- Reduced cost and better area usage without cables

We propose a reliable and energy efficient wireless communication mechanism for sensors of space applications. We name the approach, *Software-Defined Wireless Communication (SDC)*. The idea stems from the rationale that redundancy is the fundamental approach at any level for reliability. While there have been many diversity mechanisms proposed for wireless communications, the focus has been limited to Radio Frequency (RF) spectrum at small frequency range levels. Considering the extreme conditions in space, we propose to exploit multiple different electromagnetic (EM) spectrum that exhibit different physical characteristics such as RF, infrared (IR), visible lights (VL), etc. Through software mechanisms, the quality of each channel is monitored in a light-weight manner for reliability and energy efficiency, and the best channel is to be dynamically selected for data transmission depending on the environment channel conditions. To the best of our knowledge, this is the first work that dynamically uses diverse EM spectrum bands of different characteristics beyond RF.

The rest of the paper is organized as follows: In Section II, we provide a background of space system environments. We discuss the physics of wireless communication in Section III. We summarize a review of related technology areas in Section IV. Section V presents our approach with preliminary experimental results. Finally, Section VI concludes the paper and briefly discusses future directions.

II. Background

In this section, we discuss the challenges of space environments and the processes required for electronic systems to be used in space.

A. Challenges of Space Environments

Space poses the challenges of diverse and extreme environments including vibration, high and low temperatures, temperature variations and radiation.

Along with extremely loud sound waves, significant vibrations occur during the launch and in-space propulsions for multi-stage rockets. Collisions with celestial bodies would also create shaking of spacecraft. A spacecraft is also subject to extreme temperatures, both hot and cold, when it is located above the insulating atmosphere of the Earth. Extreme high and low temperatures can be experienced when a spacecraft is facing the Sun (i.e., day, high temperature) and behind a planet (i.e., night, low temperature) in space without the shield of the atmosphere that provides heat conduction and convection.

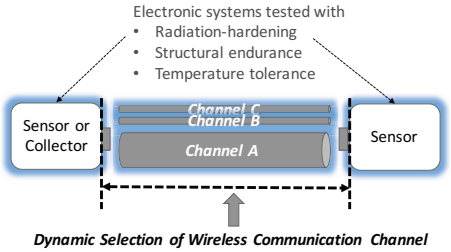

Figure 2: Focus of this study: dynamic selection of wireless communication channel

The temperature of the Sun ranges from 4,000 degrees Celsius (7,300 degrees Fahrenheit) to 2 million degrees Celsius (3.5 million degrees Fahrenheit) around the corona. As the corona cools, matter is blown off as the solar wind, emitting heat and radiation. When it is not in the presence of a heat source in space, the temperature of cosmic background is as low as -200 degrees in Celsius (-455 degrees Fahrenheit). In order to be used in space environments, hardware materials and structures should be carefully designed and thoroughly tested for such extreme vibration and temperature conditions. They simulate the conditions of launch using the vibration table and acoustic chamber at NASA Centers or ESA's European Space Technology Center.

Another significant space condition is *radiation* that is transmission of energy in the form of waves or particles either in vacuum or through a material medium.

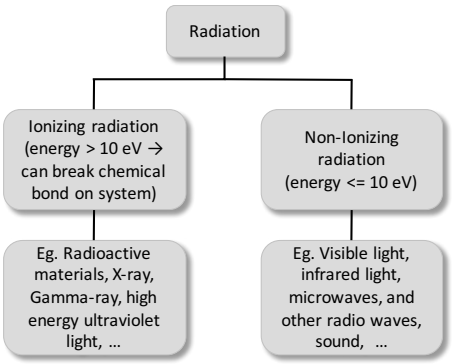

Figure 3: Classification of radiation based on energy level

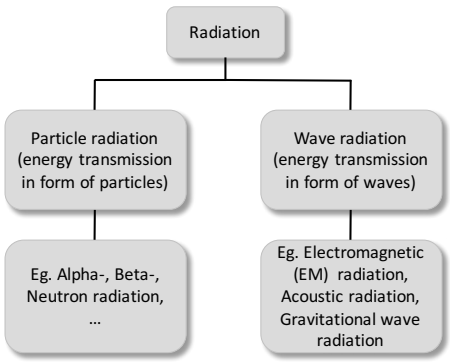

Figure 4: Classification of radiation based on form of transferred energy

Radiation in space is usually from the Sun but also comes from other celestial bodies. Depending on the amount of energy emitted, radiation can be classified as ionizing radiation and non-ionizing radiation (see Figure 3). Ionizing radiation carries more than 10 eV[a] which is strong enough to ionize atoms and molecules, and thereby break chemical bonds in living organisms. Damages from high energy ionizing particle radiation can be caused by space nature due to solar particle events, cosmic rays, Van Allen radiation belts (trapped radiation surrounding Earth)[3] and secondary particles (also called as air shower), as well as by human induced environments such as particle accelerators used in high energy physics. Ionizing radiation may also occur from natural radioactive materials such as radon and radium. Non-ionizing radiation includes visible light, infrared light, microwaves, other radio waves, and sound.

Radiation can be also classified based on its form of energy transfer, either through particles or waves. (see Figure 4). In fact, due to the wave-particle duality, all moving particles also have characteristic of waves. Higher energy particles exhibit particle characteristics more, while lower energy particles exhibit more wave characteristics. The examples of particle radiation include alpha (α) radiation, beta (β) radiation, and neutron radiation that are basically ionizing radiation. Wave radiations can be further classified as electromagnetic radiation (eg. radio waves, microwaves, visible light, x-rays, and gamma (γ)-rays), acoustic radiation (seismic waves, sound, and ultrasound), and recently discovered gravitational radiation.[4] While non-ionizing, wave radiations may be used for data communication, ionizing particle radiations are not only harmful to humans but also disrupt a semiconductor's crystal structure causing malfunction or physical damage of electronic systems. In the next subsection, we summarize the techniques for making electronic systems to be resistant to such radiation.

B. Radiation Hardening of Electronic Systems

Radiations are encountered not only in outer, deep space, but also during high-altitude flights, around particle accelerators and nuclear reactors, during nuclear plant accidents, and even possibly in factory chip packaging materials.[5] Most chips will fail due to leakage associated with the charging of insulators. For some electronic systems that are very close to a reactor, neutrons could create even physical damage to the semiconductor crystal. Electronic systems do not function properly when the operating voltage shifts outside of the limited range that they are designed for. Therefore, it is important for any electronic systems to be radiation hardened to be qualified as *space-grade*.

The technology and procedure countering radiation damages on electronic systems is called *radiation hardening*, and the electronic components are vulnerable to damage by radiations have to be *radiation hardened*. Radiation hardening process is to produce the electronic systems or components resistant to malfunction or damage done by ionizing radiation - either electromagnetic radiation or particle radiation of high energy. There are two types of radiation hardening techniques i) physical hardening and ii) logical hardening. Physical hardening techniques include production of electronic components by insulating substrates like silicon on sapphire and silicon on insulator. ICs, RAMs and shielding packages are radiation hardened in this way. Logical radiation hardening techniques are redundant elements, hardened latches, parity check-

[a] eV, electron-volt is a unit of energy equal to approximately 1.6×10^{-19} joules (J).

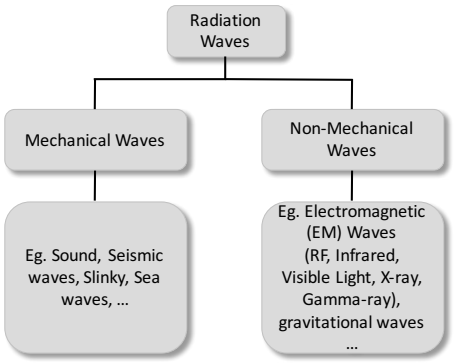

Figure 5: Classification of radiation waves

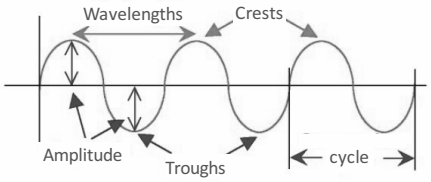

Figure 6: A wave structure

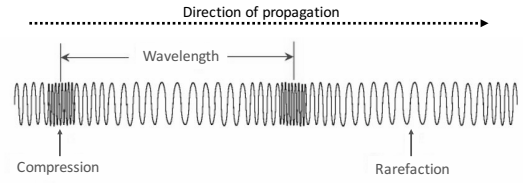

Figure 7: Mechanical wave

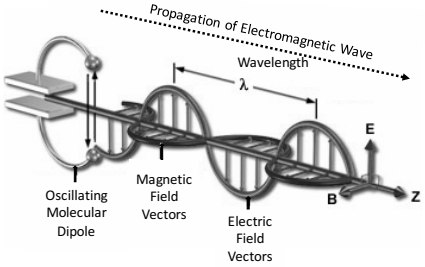

Figure 8: Electromagnetic wave (Adapted from)

ing, and watchdog timer for reducing radiation impact on electronic components. Then, radiation hardened electronic components are integrated with the rest of the non-hardened components with some design and manufacturing variations in order to reduce the vulnerability to radiation damage. Thus exhaustive testing has to be carried out. Example of the tests used typically for radiation-hardened products testing include Total Ionizing Dose (TID), Single Event Effects (SEE), Enhanced Low Dose Rate Effects (EDLRS), and proton and neutron displacement charge. Since developments and and extensive tests of the radiation hardened electronic devices are highly expensive and time consuming, radiation hardened electronic chips tend to lag behind in new developments. However, the rising demand in various space and defense applications is strongly driving the market of radiation hardened electronics markets.[6]

Most tolerance and reliability schemes against space and extreme environments such as radiation and extreme temperatures have been focused only on the physical electronic devices rather than the data path, wireless communication schemes. The focus of this work is on the wireless communication scheme between two nodes, a sender (or transmitter) and a receiver, (sensors or data collectors),[b] rather than the tolerance of electronic system end points themselves, as depicted in Figure 2. To the best of our knowledge this is the first study that addresses the issue of wireless communication channel for space and extreme environments.

III. Physics of Wireless Communication

In this section, we discuss the types of radiation waves and their physical characteristics that provide insight into designing wireless communication systems.

A. Waves

Any wireless communication method relies on propagation of wave radiation. A wave can be described as a disturbance of energy that travels from one location to another location. Waves have different shapes

[b]We use the term sender and transmitter interchangeably, as we discuss both at the physical layer and link layer of wireless communication in this paper.

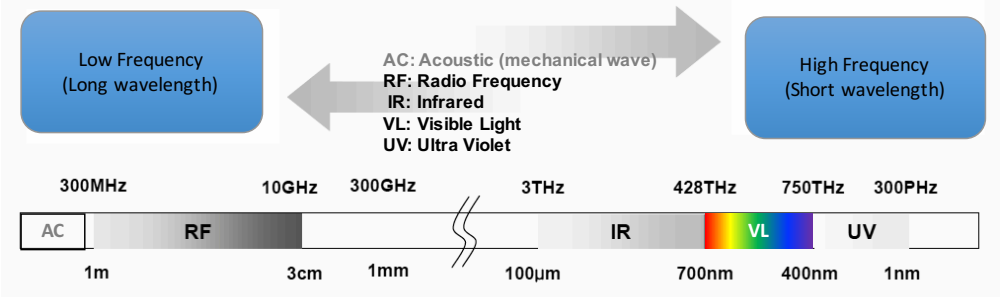

Figure 9: Electromagnetic spectrum range

and forms, and can be categorized based on fundamental characteristic properties and behaviors. Waves can be categorized based on their ability or inability to transmit energy through a vacuum. There are two categories on the basis, namely mechanical waves and non-mechanical waves, as illustrated in Figure 5. A wave consists of successive troughs and crests, and the distance between two adjacent crests or troughs is called the wavelength (see Figure 6). Frequency is inversely proportional to wavelength, according to the equation, $v = \lambda f$, where λ is the wavelength, f is the frequency, and v is the speed of the wave. The speed of electromagnetic waves through a vacuum is $c = 3.0 \times 10^8 m/s$, and decreases when passing through a medium. As waves cross boundaries between different media, their speeds change but their frequencies remain constant.

Mechanical waves take place due to the periodic motion of particles in the medium about their mean position. Mechanical waves are not capable of transmitting its energy through a vacuum and require some medium such as air or water. Sound, seismic, slinky waves are some examples. Sound is transmitted through gases, plasma, and liquids, and have been used for wireless data communication either underwater[7,8] or areal[9–11] environments. When air is the medium, sound waves transmit by the compression and expansion of air gas through decreasing and increasing particle densities. Humans can hear sound waves with frequencies between about 20 Hz and 20 kHz. Sound above 20 kHz is called ultrasound.

Electromagnetic (EM) waves are produced by the vibration of charged particles. For instance, EM waves that are produced on the Sun subsequently travel to Earth through the vacuum of outer space. Without the ability of EM waves to travel through a vacuum, there would be no life on Earth. Electromagnetic waves can be generated by a variety of methods, such as a discharging spark or by an oscillating molecular dipole, and EM radiation is a transverse wave where the oscillations of the waves are perpendicular to the direction of energy transfer and propagation. EM waves exhibit oscillating electric and magnetic fields whose amplitudes and directions are represented by vectors that undulate in phase as sinusoidal waves in two mutually perpendicular (orthogonal) planes. EM waves can be further classified based on their range of frequencies and manifested characteristics, such as radio, infrared, visible light, ultraviolet, x-ray and gamma-ray. The majority of wireless data communication protocols relies on EM waves, particularly RF such as WiFi, Bluetooth, Zigbee, cellular, and satellite communications. Figures 7 and 8 illustrate mechanical and non-mechanical, electromagnetic waves, respectively.

B. Physical Characteristics of Wireless Communications

In this subsection, we discuss physical characteristics of that are significant and unique in wireless communication, namely i) fading and ii) interferences.

Wireless signal fades as it travel toward a receiver. The fading wireless signal is not only significant in its extent and but also in tis diverse characteristic behaviors that are very different from those of wireline communication. Fading of a wireless communication channel is typically characterized by three main factors, i) path loss, ii) small scale fading often represented by Raleigh or Rician models, and iii) large scale fading or shadowing, often modeled as a lognormal distribution. Figure 10 illustrates the effect of these components on a wireless signal strength over time. Path loss is the signal power attenuation of a wave as it propagates over distance and is a major component in the design and analysis of the channel budget of a communication system.

Small scale fading describes rapid fluctuation of amplitude of a signal over short distance and time. The small scale fading concern with multipath effects by reflecting objects on the path, dynamic relative speed

between a transmitter and a receiver (random frequency modulation due to different Doppler shifts), faster speed of surrounding objects (than a receiver) and signal bandwidth being smaller than coherence bandwidth.

Multipath propagation effect (or simply, multipath) is the phenomenon where signals reach the receiving antenna by two or more paths at different frequency and times (see Figure 11 from matlab simulation). This causes phase shifting of the signal and dispersion thus fading. The causes of multipath include atmospheric ducting, ionospheric reflection and refraction, and reflection from objects such as walls and buildings. Thus, it is not a significant issue in free space in general, but could be notable inside a spacecraft made of reflective metallic enclosure. The magnitudes of the signals arriving by the various paths can be statistically modeled, using Rayleigh fading or Rician fading (see Figure 13 for Rayleigh modeling). The techniques for mitigating multipath fading are mostly at a hardware level such as equalizers, RAKE receivers, OFDM (Orthogonal Frequency-Division Multiplexing), and other channel diversity methods, in order to minimize the interference between different signals, called Inter-Symbol Interference (ISI).

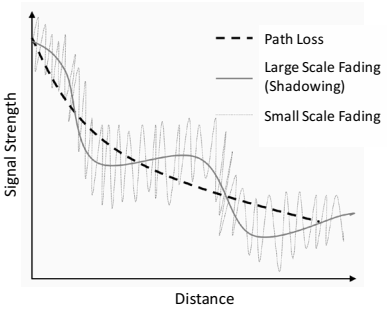

Figure 10: Effects of path loss, shadowing and small scale fading on a signal (Figure adapted from[12])

When a sender moves toward the direction of a receiver during the transmission, the received frequency increases causing positive Doppler shift, and vice versa. The broadened spectrum in response to an impulse signal due to Doppler shift is depicted in Figure 12. When the transmission signal frequency bandwidth (Hz) is larger than Doppler spread, Doppler effect becomes insignificant in communication.

Slow fading occurs when a large obstruction such as a hill or mountain obscures the main signal path between the transmitter and the receiver, and when the coherence time of the channel is large relative to the delay requirement of the application. The received power that is faded due to the slow fading can be modeled using a log-normal distribution with a standard deviation according to the log-distance path loss model.

Interference is the superposition of two or more waves resulting in a mixed wave pattern. *Electromagnetic interference (EMI)* causes increased bit level error rate or total loss of data packet on the communication 'path or channel', while it may degrade the performance of the circuit or cause malfunctioning of 'electronic systems' if it is not radiation hardened.

Natural EMI sources that generate changing electrical currents and voltages include the solar radiation, northern lights, thunderstorms. When solar storms or other bad space weather events such as a meteor shower happen,[13,14] they can cause interference to space communications, GPS satellites, or even Earth's ground RF communications.[15] Human-made EMI includes usages on competing EM frequencies such as malicious RF jamming, Electromagnetic Pulse (EMP) attack, and among microwave ovens, Bluetooth, Zigbee and WiFi devices (all operating around around 2.4 GHz EM frequency).

We point out that interference is the main issue of wireless communication in the space environments. While vibrations or extreme temperatures could be threats for electronic systems, the physical characteristics

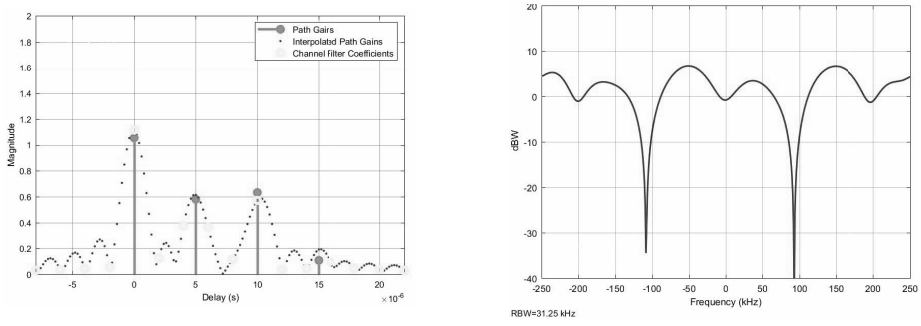

Figure 11: Multipath effects on time and frequency of a received signal

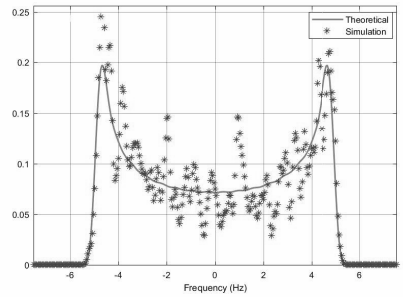

Figure 12: Doppler spectrum spread due to relative speed

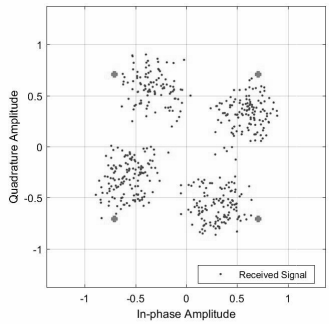

Figure 13: Received signal after Rayleigh fading modeling (QPSK)

do not directly impact the wireless communication channel, unless it is manifested as interference of the signal wave. For instance, vibration may accompany loud noise at the launch that may interfere only with acoustic communication (i.e., similar frequency). Furthermore, we recognize that there is little relevance between temperatures and EM performance unless it is presented as interference in the frequency band. Particularly, heat is not necessarily generated by infrared signal, and infrared signal doesn't necessarily generate heat. Even when high temperature is caused by infrared heater, it would interfere with infrared data signal only if their EM frequency bands overlap with each other. We validated the impact (or lack of impact) of radiation interference and temperatures under pseudo extreme conditions, and a partial result is shown in Section V.

Another point to note is that interference at a 'receiver's side' is critical rather than at a sender's. Figure 14 shows a scenario of the so called 'Hidden Node Problem'. Two senders A and C do not interfere with each other as they are outside of each other's transmission range (hidden from each other), but interference or signal collision may occur at the receiver B when they transmit at the same time. As shown in Figure 14b, the signals received at B from A and C are competitively strong and B would not discern any of them, while A and C would only observe their own signal and not find other signal(s) strong enough. On the other hand, Figure 15 shows a scenario where even if there are interferences around the sender, the receiver may not experience it. Note that WiFi resolves the issues of the Hidden and Exposed Node Problems through short reservation control messages of CTS/RTS, and Bluetooth uses a polling mechanism to avoid collisions.

The physical layer of a wireless system considers the fading characteristics in designing transmitters and receivers (transceivers), and the link layer wireless protocol design mainly addresses the signal interference (or so called 'collision)' issue.

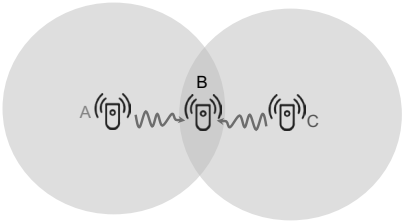

(a) Interference at receiver B

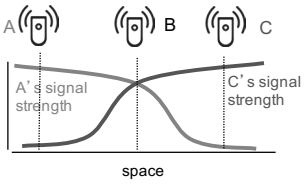

(b) Received signal strength at receiver B

Figure 14: Signal interference at receiver B (Hidden Node: A-C)

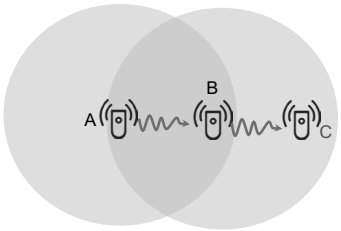

Figure 15: *No* signal interference at receiver C (Exposed Node: B)

IV. Related Work

In this section, we discuss various existing strategies for wireless communication reliability including diversity mechanisms, SDR and DTN.

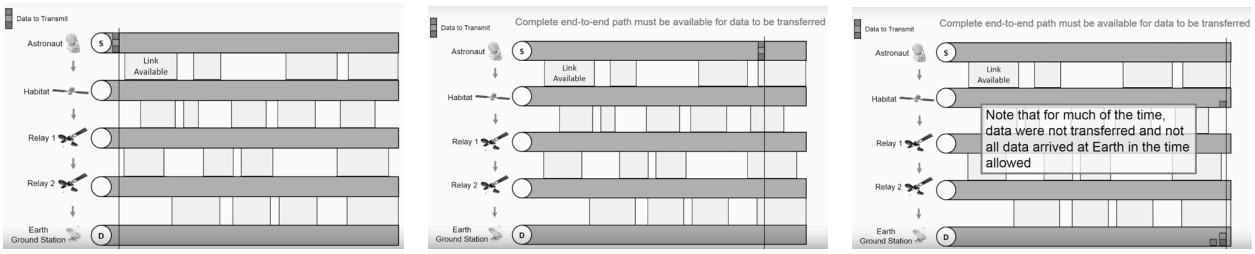

Figure 16: Sample Scenario of Using Traditional TCP/IP (Courtesy of NASA)

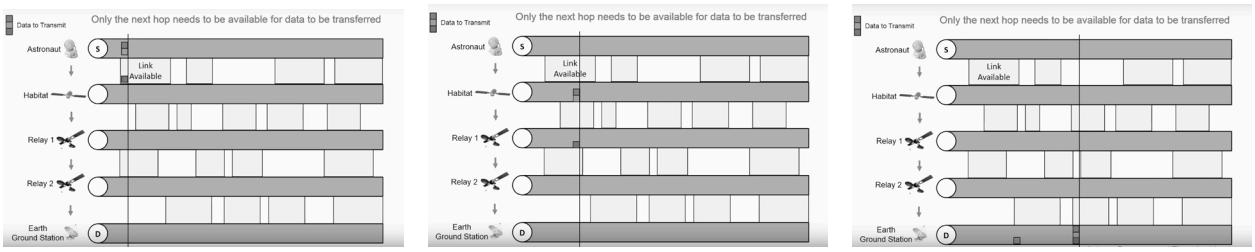

Figure 17: Sample Scenario of Using DTN Capable Nodes (Courtesy of NASA)

A. Wireless Diversity Mechanisms

There have been numerous technologies developed that adopt redundancy for improving the reliability of a wireless signal by using two or more communication channels with different RF bands. They exploit the diversities of time, frequency, space, multiuser, cooperation, or polarization. Due to space limitation, we only present the types of approaches in diversity methods for wireless communication. However, they all fundamentally address signal fading issues particular of wireless protocols of certain limited RF bands, and do not address interference issue of a large EM band.

B. Software-Defined Radio (SDR)

Software-Defined Radio (SDR) is a software approach to adaptively select and control appropriate communication radio frequency and corresponding physical layer modules such as detectors, filters, amplifiers, and modulators that have been traditionally implemented in hardware. Due to its software programmability, SDR can bridge multiple standards as well as legacy and future systems, and provides wireless communication capability that is interoperable with various communication devices operating on different RF band. It is particularly useful in scenarios where multiple organizations that use different communication protocols have to cooperate together such as military operations when Army, Air Force and Navy are involved, and public safety operations where the fire department, police department, and emergency responders from local and federal government have to collaborate.

SDR devices such as USRP[16] are relatively costly, depending on the ranges of RF spectrum observable and the options of configurable modules. While it may provide an appropriate radio channel dynamically, however, SDR is still limited only for a narrow scope of spectrum within RF range and does not cover acoustic or infrared range of EM spectrum.

C. Delay and Disruption Tolerant Networking

As a strategy to enable *end-to-end* communication in the midst of intermittent link availability, Delay or Disruption Tolerant Networking (DTN) utilizes the concept of *custody transfer* within the network where a data packet is held in custody until a network node becomes available.

The traditional TCP/IP Internet incurs much delay to initiate data transfer and exhibits poor throughput. As illustrated in Figure 16 a traditional TCP/IP network requires a complete end-to-end path to be available for communication to start the transfer. When a partial path becomes unavailable later, all the previous data transfer is wasted. Even while the end-to-end session is alive, poor link quality makes TCP significantly

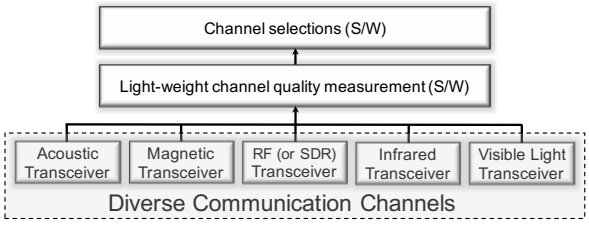

Figure 18: The Concept of Software Defined Wireless Communication (SDC)

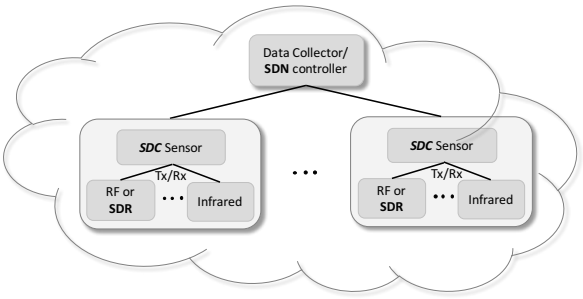

Figure 19: Software-Defined Wireless Communication (SDC): Its relationship with SDN and SDR

reduce its amount of data sent at a time (congestion window) and lead TCP not to fully utilize its available bandwidth.

High latency and high error links are common space communications. For example, at the speed of light ($3 \times 10^8 m/s$), one-way propagation time from the Earth to the moon incurs a delay of 1.7 seconds and one-way propagation time to Mars incur a minimum delay of 8 minutes. The problem of latency for interplanetary links is exasperated with increased Bit Error Rate (BER) or packet loss due to radiations from solar events and galactic cosmic ray. In addition, the celestial bodies are in constant motion, which can block the required line-of-sight between transmit and receive antennas, resulting in links that at best are only intermittently connected.[15]

DTN achieves message reliability by employing *store-and-forward*, where data can be stored or held in a buffer until the next hop becomes available to receive it. As depicted in Figure 17, the fundamental idea of DTN for reliable delivery is accomplished on a hop-by-hop basis instead of an end-to-end basis which is impractical over high latency links. DTN offers a set of protocols to operate in diverse and heterogenous network environments (eg. low-propagation delay and high-propagation delay). NASA's Space Communications and Navigation (SCaN) has contributed and deployed DTN protocols for its long distance space networks.[17] DTN also provides security services for environments where a portion of the network might become compromised posing the usual security challenges related to confidentiality, integrity and availability. Note that DTN improves end-to-end availability and throughput, but does not increase *link* reliability that is the focus of this study.

V. Software-Defined Wireless Communication (SDC) for Reliable and Energy Efficient Wireless Communication

The fundamental idea of Software Defined Wireless Communication (SDC) is to utilize multiple different EM bands that exhibit different physical characteristics such as one or more RF bands, Infrared (IR), and visible lights (VL). Acoustic or magnetic communication methods may potentially be used as well, depending on type and location of sensing (eg. liquid fuel sensing[18]). The quality of each channel is monitored in a light-weight manner in software (eg. periodic probing) where the quality can be defined based on the need of application, such as reliability, energy efficiency or their combinations. The quality of channels would vary dynamically subject to the channel environment conditions, and the best channel or top k channels would be selected for data transmission. The rationale of choosing one or a few channels rather than the entire available ones is not to waste energy unnecessarily, and to cause unnecessary interference among sensors of the application. The concept is illustrated in Figure 18. To put in a relative perspective, SDC can utilize Software-Defined Radio (SDR) as one of its potential channel, and may be deployed in a Software-Defined Network (SDN) and/or in a network that uses Delay/Disruption Tolerance Network (DTN), as depicted in Figure 19.

As a proof-of-concept implementation, we have used an Android smartphone and a Raspberry Pi 3 (see Figure 20). Raspberry Pi 3 comes with Bluetooth and WiFi built-in, and we have it connected with IR sensor for infrared communication. Samsung smartphone Note 4 comes with equipped with RF (Bluetooth and WiFi) and Infrared emitter. We have developed infrared communication physical layer protocol similar to[19] and implemented an application that enables communications through either Bluetooth and/or IR (see

Figure 20: Raspberry Pi 3 with IR sensor

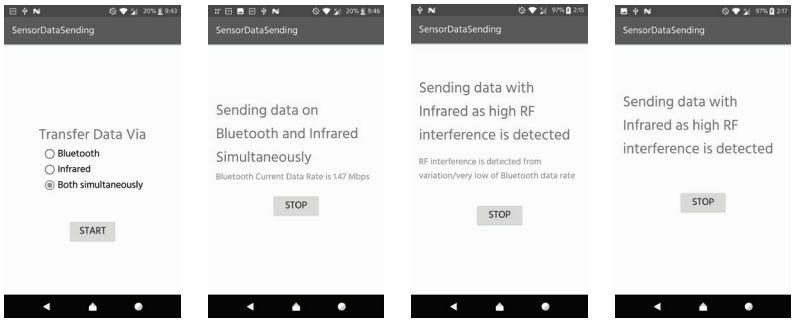

Figure 21: Experiment UIs of Samsung Android smartphone

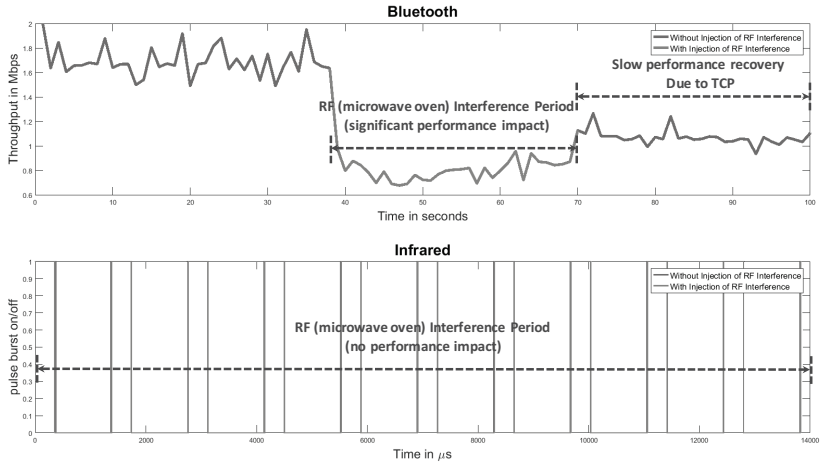

Figure 22: Impact of RF Interference (Microwave oven, 2.4 GHz): Bluetooth vs. IR

Figure 21). First, we have evaluated the performance of communication under pseudo extreme conditions – radiation interference (through microwave oven), high temperature (electric range oven and Infrared heater), and cold temperature (freezer) with the operating bounds of the electronic systems (-4 degrees and 122 degrees in Fahrenheit). Due to space limitation, among many evaluations conducted, we only show the interference of RF (microwave oven interferes with Bluetooth on 2.4 GHz) in Figure 22. It clearly shows that the performance of Bluetooth drops significantly during the interference interval, while IR does not experience any impact at the same scenario. It is interesting to find that Bluetooth throughput performance does not get restored immediately after the interference is stopped. It is due to the mobile data transfer application uses TCP where its congestion window is slow to recover to its available bandwidth.

VI. Conclusion and Future Work

Despite extreme space weather conditions, reliability is a primary concern of space applications. Energy efficiency is also critical for longevity of wireless sensors. In order to address those issues, we proposed a software approach, named Software-Defined Wireless Communications (SDC) that dynamically decide on a reliable channel(s) in an energy efficient manner. Unlike SDR that covers continuous RF bands only, SDC employs out of multiple distinct EM bands. We implemented the proposed SDR using a Raspberry Pi and a smartphone and validated the concept. SDR approach can be used in many areas beyond space applications where reliability is critical such as military applications. Many further issues can be explored and improved such as channel quality measurement and decision algorithms. Pertaining to wireless sensor systems, we also plan to investigate the sensing capacity (such as sampling and data rate) analysis and planning in an wireless sensing application.

Acknowledgments

The author is grateful for the insightful technical discussions with and guidance from DeLisa Wilkerson and Darren Boyd at the Electronic Systems Branch of NASA MSFC. She also thanks Kaushik Ayinala at the University of Missouri - Kansas City for the Android and Raspberry Pi implementations, and Chris Dail, Jason de Jongh, Bert Gangl, Bill Hopkins, Tim Kall, Garrick Merrill, Jay Perry, Scott Tashakkor, Kosta Varnavas, Peter Weber, and Andy Young at NASA MSFC for their illuminating discussions. This work was funded by the NASA Summer 2017 Faculty Fellowship Program. Many thanks to Drs. Frank Six and Gerry Karr for their great program support.

References

[1]Kranz, G., *Failure Is Not an Option: Mission Control From Mercury to Apollo 13 and Beyond*, Simon and Schuster Publishing, 2000.

[2]Razi, A., Afghah, F., and Abedi, A., "Channel-Adaptive Packetization Policy for Minimal Latency and Maximal Energy Efficiency," *IEEE Transactions on Wireless Communications*, Vol. 15, March 2016, pp. 2407–2420.

[3]"Van Allen radiation belt," https://en.wikipedia.org/wiki/Van_Allen_radiation_belt.

[4]"Solar radiation blasts radio communication," https://www.space.com/31900-gravitational-waves-discovery-ligo.html, 2016.

[5]Baston, P., "Unsafe At Any Speed? Looking under the hood at Sun's 2001 server engine problems," http://www.sparcproductdirectory.com/artic-2002-jan-pb.html, 2002.

[6]"Radiation Hardened Electronics Market - Global Industry Analysis, Size, Share, Growth, Trends and Forecast 2016 - 2024," http://www.transparencymarketresearch.com/radiation-hardened-electronics-semiconductor-market.html.

[7]Stojanovic, M. and Preisig, J., "Underwater acoustic communication channels: propagation models and statistical characterization," *IEEE Communications Magazine*, Vol. 47, 2009, pp. 84–89.

[8]Akyildiz, I. F., Pompili, D., and Melodia, T., "Underwater acoustic sensor networks: research challenges," *Ad Hoc Networks*, Vol. 3, 2005, pp. 257âĂŞ279.

[9]Lopes, C. V. and Aguiar, P. M., "Acoustic modems for ubiquitous computing," *IEEE Pervasive Computing*, Vol. 2, 2003, pp. 69–71.

[10]Madhavapeddy, A., Sharp, R., Scott, D., and Tse, A., "Audio networking: the forgotten wireless technology," *IEEE Pervasive Computing*, Vol. 4, 2005, pp. 55–60.

[11]Lee, H., Kim, T. H., Choi, J. W., and Choi, S., "Chirp signal-based aerial acoustic communication for smart devices," *Proc. of IEEE INFOCOM*, 2015.

[12]ĀŪzge Kaya, A., "Small and Large Scale Fading, Co-channel Interference, Modulated Signals," http://www.winlab.rutgers.edu/ narayan/Course/Wless/Lectures05/lect5.pdf, 2005.

[13]"NOAA (National Oceanic and Atmospheric Administration) Space Weather Prediction Center," http://www.swpc.noaa.gov/.

[14]"Space Weather: News and Information about the Sun-Earth Environment," http://www.spaceweather.com/.

[15]"Solar radiation blasts radio communication," http://www.santacruzsentinel.com/article/zz/20141007/NEWS/141008933/, 2014.

[16]Research, E., "Universal Software Radio Peripheral (USRP^{TM})," https://www.ettus.com/.

[17]Communications, N. S. and (SCaN), N., "Disruption Tolerant Networking," https://www.nasa.gov/directorates/heo/scan/engineering/techno 2016.

[18]Merrill, G., "Cryogenic Applications for Wireless Power and Data using Magnetics," *Proc. of IEEE International Conference on Wireless for Space and Extreme Environments (WISEE)*, 2015.

[19]Dhondge, K., Ayinala, K., Choi, B.-Y., and Song, S., "Optical Wireless Unlocking For Smart Door Locks Using Smartphones," *IEEE 12th International Conference on Mobile Ad-hoc and Sensor Networks (MSN)*, Hefei, China, December 2016.

Weep Hole Flow Rates and Gapping within Layered Pressure Vessels

Cameron W. Coates[1]
Armstrong State University, Savannah, GA, 31419

ABSTRACT

Weep hole flow rates due to interlayer gap flow generated by an external pressure source are measured experimentally for an AO Smith Layered Pressure Vessel (LPV) at the NASA Marshall Space Flight Center. A Computational Fluid Dynamics (CFD) model of the flow through the interlayer gaps is also done to provide further insight regarding flow behavior. The objectives of this project were: (i), to devise and conduct a suitable experiment that accurately measures weep hole flow rates based on pressure input at a single weep hole, and (ii), to interpret the data and provide recommendations regarding the management of potential leaks or failures of these LPVs. CFD predictions and experimental results both indicated that weep hole flow rates increase with increasing numbers of available layer gaps and increasing pressure. The highest flow rates occurred between weep holes that were longitudinally aligned, with the shortest path between them having no curvature. Flow rate results were not symmetric for weep holes located on opposite sides of any curved path. Results indicate that the proximity of weep holes to longitudinal welds appears to have a significant influence on flow symmetry, and that weep hole flow measurement may be a good indicator of localized gapping and inconsistent layer concentricity.

[1] Professor and Engineering Studies Program Coordinator, Engineering Studies Program, Armstrong State University, Savannah, GA 31419.

I. Introduction

Layered Pressure Vessels (LPV's) have been in service for the oil, gas, agricultural and aerospace industries since the 1950's and 60's. The layered design serves to eliminate or substantially diminish the effects of certain failure modes: any crack growth within a single layer will be limited to that layer only and external impact damage will be restricted to the outer layer only. Despite these fail safe concepts, some LPV's within the oil, natural gas and agricultural industries have still failed catastrophically, resulting in mass evacuations, loss of life, environmental damage and destruction of adjacent systems and property. In 1980, an LPV installed on the National Aeronautics and Space Administration's (NASA) Launch Complex 36 (LC-36), Cape Canaveral Air Force Station (CCAFS). Florida, developed an audible blowing leak from one of its weep holes while pressurized to 6000 psig with gaseous helium (GHe). The investigation concluded that the leakage resulted from a cyclic fatigue fracture along the edge of a longitudinal high stressed area of the weld in the inner layer.[1]

The NASA Marshall Space Flight Center has over 160 LPV's in service as of June 2017. These LPVs are not within American Society of Mechanical Engineers (ASME) Boiler and Pressure Vessel Code (BPVC) due to their early manufacturing dates, which preceded ASME's acceptance of specific layered fabrication techniques as an acceptable construction methodology[2]. Their material, fabrication and inspection techniques were also deviant from existing BPVC at the time of manufacture. Consequently, these LPV's also do not satisfy Occupational Safety and Health Administration (OSHA) requirements for federal agencies. The availability of these LPV material property data, particularly those related to fracture (Charpy, fracture toughness etc.), is also limited as this information was proprietary at the time of manufacture in many cases. The LPVs at NASA MSFC have also been manufactured by several different manufacturers, using different fabrication techniques and materials. The layered design renders conventional structural inspection techniques (ultrasound, acoustic emission, x-ray, dye penetrant etc.) ineffective or severely limits the extent of their application. However, Furr[3] showed that Phased Array Ultrasonics (PAUT) was able to successfully detect flaws within head to shell and shell to shell welds for layered metal plates has been recently demonstrated.

NASA and its partners have conducted several investigations that sought to characterize the various LPV materials, understand and predict crack growth in LPV's, develop feasible inspection techniques, assess risk and recommend risk mitigation procedures. Hudson et al[4] conducted successful experimental tests in order to determine fracture toughness, fatigue-crack growth, sustained-load flaw growth, and impact properties for three pressure vessel steels: A.O. Smith VMS 5002 and VMS 1146A, and ASTM A-225 Gr. B. More recently, Southwest Research Institute (SwRI)[5] conducted Fatigue Crack Growth (FCG) testing and fractographic analysis for an 1146a section from an A.O. Smith LPV previously used in service at the NASA Ames facility. FCG testing was performed at a load ratio, R, (ratio of minimum to maximum load) of 0.15 and at room temperature.

Prosser's[6] technical report documents a comprehensive assessment of NASA's current LPVs. The scope of this assessment included the formulation of a consensus draft proposal for the development of additional testing and analysis methods to establish the technical validity, and any limitation thereof, of these vessels for continued safe operation. However, this assessment did not include the establishment of the current safety of these vessels, or their safety for continued operations for any period into the future. The assessment team identified near-term actions that if enacted could reduce either the risk of or consequences from catastrophic LPV failure resulting from their continued use. The team also recommended that the Agency formulate and support an Agency-wide team to continue efforts to assess and reduce risks associated with LPVs and to develop a centralized database of information on the design, fabrication, materials, operation, inspection, maintenance, and repair of LPVs. NASA MSFC followed up on these recommendations with several internal studies as well as joint projects with its partners. Most recently, Coates[7] evaluated leakage rates through the weep holes of A.O. Smith LPV's based on through crack sizes within the inner layer.

This current work seeks to experimentally obtain volumetric flow rates at a weep hole based on external pressure input (above ambient) at an adjacent weep hole. Results are compared with predictions from a Computational Fluid Dynamics (CFD) model of the interlayer gap flow. The volumetric flow rate magnitudes obtained and relationships discovered increase the potential to accurately predict flow rates through LPV weep holes based on through crack size

(inner shell) and internal pressure magnitude. Other potential benefits include an improved understanding of the characterization of the flow through interlayer gaps (friction, roughness, laminar/turbulent), improved understanding regarding the variation of flow properties (pressure, velocity, density) as the fluid flows through an interlayer gap or gaps as well as the effect of the number of layers on the aforementioned phenomena. These results may also provide valuable information for the development of a Structural Health Monitoring (SHM) system based on volumetric flow rate at the LPV weep holes. Initial testing was performed on an AO Smith LPV V0031 at the NASA MSFC. V0031 was removed from service for experimental testing and evaluation, as well as to support the development of analytical or computational approaches for LPV crack growth and life assessment evaluations. The working fluid for this type of vessel may be air, gaseous nitrogen (GN_2) or gaseous hydrogen (GH_2).

II. LPV Properties

Most of the vessel description below can also be found in reference 7, a report by this author, which provides a theoretical approach for the determination of weep hole flow rates for the same vessel. The AO Smith vessel is composed of an inner cylindrical shell and concentric layers of thin plates wrapped around the inner shell with longitudinal welds. The AO Smith LPV inner and outer shell are made from AO Smith 1146a steel, while the head is made from ASTM A225 Grade B Firebox steel. Geometric and Material Properties are provided in Tables 1 and 2, respectively. Full penetration welds (i.e. welds which fuse all layers together) connect a layered section to either the solid vessel heads (head-to-shell weld) or to an adjacent shell section (shell-to-shell weld). V0031 has a single circumferential shell to shell weld joining two cylindrical shell sections of equal size. Each shell section has a single longitudinal weld and four weep holes. Two weep holes are located approximately 1.5" from the longitudinal weld along the circumferential direction and approximately six inches from each circumferential weld along the longitudinal direction. The other two weep holes are located on the opposite side of the LPV, 180 degrees from the first two. Each of the four weep holes extend from the second interlayer gap layer to the outer layer. There are additional weep holes within the LPV; these are not aligned with the aforementioned four. These holes extend from the first interlayer gap, located above the inner shell, to the second interlayer gap.

Table 1. Vessel V0031 Geometric Properties

Shell:	
Length	14.125 ft. (tangent to tangent)
Shell Inside Diameter	20 in
Inner Shell Thickness	0.5 in.
Layers	5
Layer Thickness	0.25 in.
Outer Shell Thickness	1.250 in.
Total Thickness	1.750 in.
Head:	
Radius	10 in.
Thickness	1.438 in.
Corrosion Allow.	0.00 in.

Table 2. Vessel V0031 Material Properties

Property	Inner (1146a)	Outer (1146a)	Head (ASTM-225)
UTS (ksi)	105	105	75
YS (ksi)	75	75	43
S (ksi)	35	35	25
Fracture Toughness $\left(ksi\sqrt{in}\right)$*	82	82	76
Young's Modulus(ksi)	30	30	**

*Ref. 4

III. Method and Materials

The general setup is shown in Fig. 1; several component details have not been included to reduce complexity. These additional components will be included in the more detailed procedural description to follow. Within a single cylindrical shell (4 weep holes), an external pressure source was connected to one weep hole, a flowmeter connected to another weep hole, while the remaining two weep holes were plugged. The LPV was not internally pressurized. The external pressure input at a single weep hole was then incrementally varied between 30psig and 100psig; the resulting volumetric flow rate through the remaining open weep hole was then measured. This process was then repeated for all possible combinations of input/output locations. Prior to the experiment, the potential for inner shell buckling due to external applied pressures was checked using the PV Elite software[8] as well as an existing Finite Element model. The maximum allowable external pressure was determined to be approximately 433psi.

Fig. 2 shows a schematic of a longitudinal planar section through two weep holes (longitudinally aligned), the various fitting positions are shown at the pressure input hole. Since the first interlayer gap is not used in this research, gaps are numbered one through four starting from the second interlayer gap. At the flowmeter weep hole connection, fittings of different lengths were used such that flow would only be allowed through specific interlayer gaps. Three different fitting lengths were used. For example, to obtain the flow through the interlayer gap #1 and #2 only, the male end of the pressure input (bulkhead) fitting extended across interlayer gaps #3 and #4 (See Fig. 2).

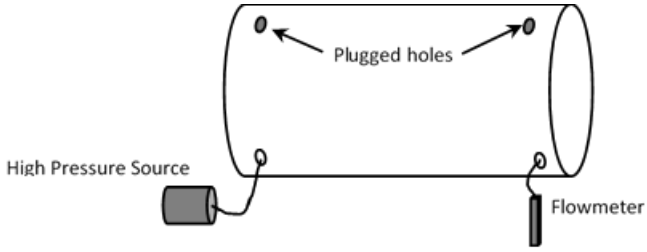

Figure 1. General Set Up Schematic

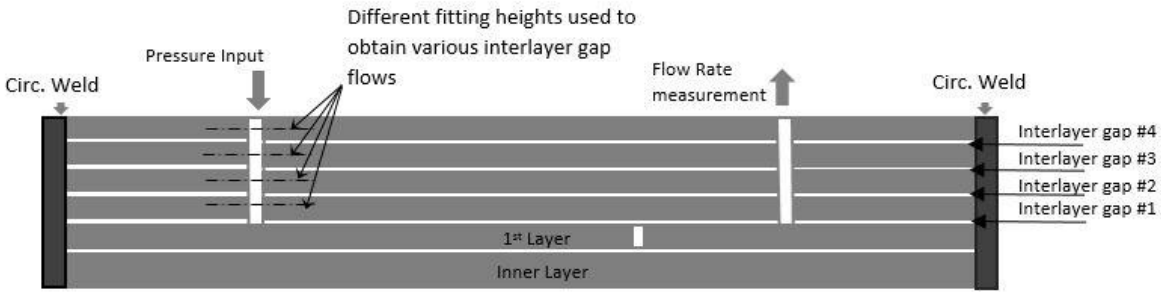

Figure 2. Pressure Input, Flow output schematic

A. Detailed Procedure

The 0.25" diameter weep hole depths were measured with a Vernier Caliper and found to range from 1.030 to 1.080 inches. These holes were then bored and tapped in order to accommodate fittings for pressurized flow input and output. The pressure vessel was placed on wooden mounts and rotated about its axis so that two longitudinally aligned holes lay in a vertical plane. A magnetic drill was mounted on a thin flat metal horizontal panel which was tangential to the vessel. Levels were used to ensure accurate orientation. This set up is shown in Figure 3a. A ¼" drill bit was initially used to verify alignment. A reamer pilot port tool (MS33649) was then used to create a flat surface at the top of the hole for the accommodation of a bulkhead fitting. The hole was then drilled with a 3/8" drill bit, followed by a 25/64" drill bit. An AN4 tap was then used to create $7/16 \times 20$ threads, followed by an AN4 bottom tap for the creation of threads at the bottom of the hole, a depth of approximately 1 inch. Compressed air and cutting fluid were

intermittently applied throughout the process in order to remove metal shavings and maintain cutting efficiency respectively. The finished hole is shown in Figure 3b. The bulkhead fitting male-male connector used at all hole connections, has an O-ring which serves as an air seal between its head and the weep hole's flat surface; this is shown in Figure 3c. The longer male end of three bulkhead fittings was cut to depths of 0.25", and 0.375", 0.675" to be interchanged at the inlet for a given pressure input (refer to Figure 2). The longer male end of one bulkhead fitting was cut to a depth of "0.25" to be used at the output end (flow rate measurement).

The input line was attached to an existing NASA high pressure line, using air as the working fluid. A pressure regulator, thermocouple and pressure transducer (Honeywell Sensotec TJE/0708-15TJ) were connected to the input line as shown in Figure 4. The output line was connected to a thermocouple, variable area flow meter (Brooks® Sho-Rate TM 3700 Series) and hand valve as shown in Figure 5. The thermocouples and pressure transducer outputs were measured with digital calibrators, a Doric 600 series and a Beckman Industrial Model 621 Strain Gage 90-132 VAC. All instrumentation used were within NASA specified re-calibration intervals.

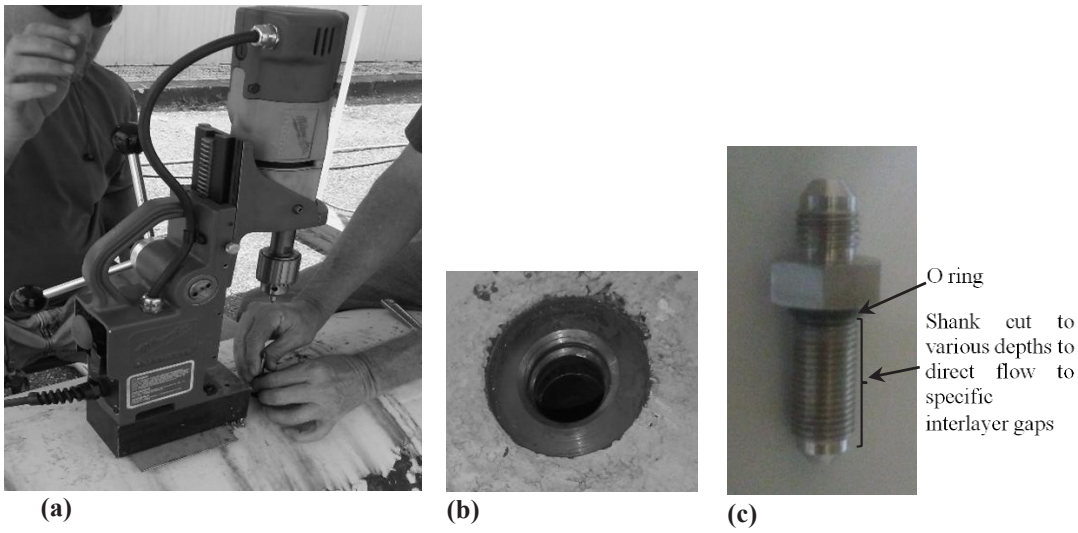

Figure 3. (a) Hole preparation, (b) finished hole, and (c) bulkhead fitting

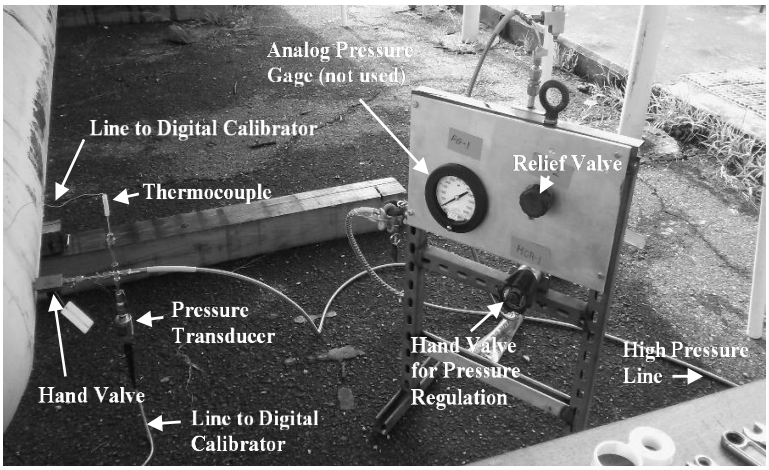

Figure 4. Instrumentation at Pressure Input Location.

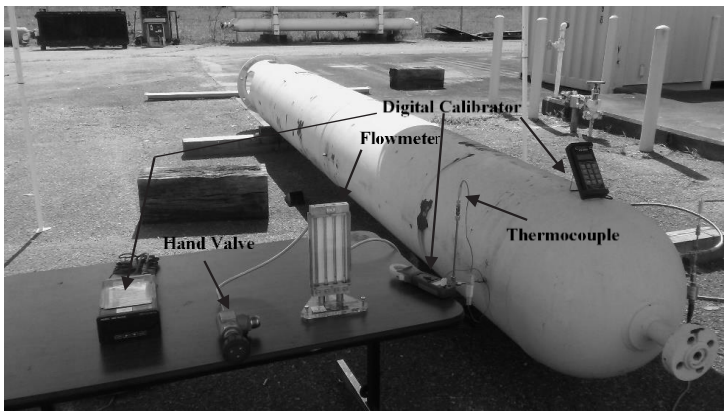

Figure 5. Weep Hole – Output Flow Measurement Connection

With two weep holes plugged, the pressure input was varied at 30, 50, 75 and 100psig. For each pressure input and bulkhead fitting length (inlet only), the inlet temperature, outlet temperature and volumetric flow rate at the remaining weep hole were measured. The flowmeter user's manual (Sho-Rate TM) provides tables that correlate flow rate values for ranges of flowmeter height readings. The volumetric flow rate was therefore determined by linearly interpolating the values provided in the tables. The process was repeated for all possible input/output combinations on the continuous cylindrical panel. Therefore, for any one input weep hole, there were four pressure values, three bulkhead fitting depths and three output weep holes, yielding $4 \times 3 \times 3 = 36$ pressure/flow rate pairs. Plugged holes were also checked for leaks each time a bulkhead fitting size was changed. Additionally, Teflon tape was applied to the threaded portion of each fitting prior to insertion in the inlet. During bulkhead fitting swaps, the hole was cleaned with a wire brush.

IV. Computational Fluid Dynamics (CFD) Model

There are a number of fabrication and physical factors that introduce complexity for modeling flow through interlayer gaps. The longitudinal welds introduce additional localized gapping, whose geometry will not be consistent among different interlayer gaps. The concentricity of each wrapped layer is also not necessarily consistent due to imperfect rolling, this results in non-uniform gap heights for a particular interlayer gap.[9] Heat transferred to the vessel from the environment will affect fluid flow parameters as well the geometry of the flow path (thermal expansion/contraction). We seek to understand where data trends in the experiment are influenced by these phenomena. Differences between observed trends in experimentally obtained data and those trends predicted from a geometrically similar CFD model which excludes the aforementioned phenomena will assist with experimental data interpretation. Therefore, a CFD model of the continuous cylindrical panel (with four weep holes), which ignore fabrication and thermal effects, was developed using SolidWorks[9] software. Table 3 summarizes the model geometry and features. Isometric and transverse cross sectional views of the CFD model are shown in Figures 6a and 6b respectively. A longitudinal weld was modeled in a single location as shown in Fig. 6b. Longitudinal weld seams are actually offset from one another for adjacent layers.

Table 3. Summary of LPV interlayer gap CFD model features.

Model	Description or Selected Value
Vessel Geometry	Three concentric cylindrical layers 0.25", interlayer gap 0.035", inner radius 10", length 7'
Boundary Conditions	Input Pressure 25 to 40 psi at weep hole depths 0.25", 0.375", 0.625", 0.875"; ambient pressure at output weep hole
Mathematical Model	Laminar and Turbulent flow
	Adiabatic Walls Surface Roughness = 0
Convergence Criterion	5.000000e-001 on flowrate at exit
Type of mesh	Immersed, Cartesian-based, Automatic
Cell Type	Cuboid
Number of cells	223,502

The boundary conditions were chosen to emulate the experimental conditions, so the inlet was pressurized above ambient while the exit remained at ambient pressure. The model allowed for laminar or turbulent flow and ignored thermal effects. Input pressure was varied from 15 to 40 psig at the same depths chosen in the experimental effort. The CFD model input pressure was limited to 40 psig due to processing hardware constraints. SolidWorks uses an immersed-body mesh in which mesh creation starts independently from the geometry itself, and the cells can arbitrarily intersect the boundary between solid and fluid.[11]

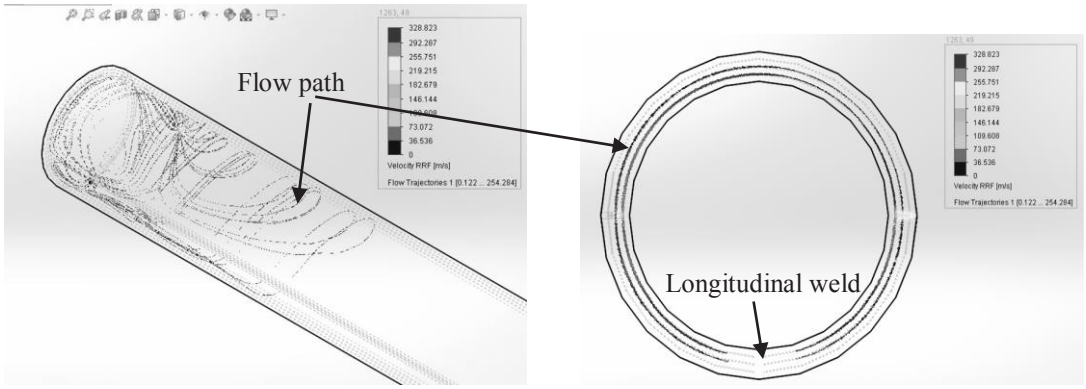

Figure 6. CFD model of flow through interlayer gaps (a) Isometric view (b) transverse view *Weep holes shown are in the same transverse plane*

V. Results

A 3D plot of CFD predicted flow rates (scim-standard cubic inches per minute) vs pressure (psig-pound-force per square inch gauge) vs number of Interlayer gaps is shown in Figure 7. The height of the surfaces represents the array of flow rates at varying pressures and depths for specific pressure input-flow rate output locations. The input-output location and flow direction are defined using the numbering scheme shown in the upper right corner of Fig.7. For example, 1-2 represents a pressure input at weep hole 1, and a flowrate measurement at weep hole 2. Note that weep holes 1 and 2 were located 1.5" circumferentially from the longitudinal weld. Fig. 8 provides a 3D plot for input-output locations 3-2, 3-1 and 3-4. Figs. 9 and 10 provide 3D plots for input-output reversal locations, 1-4, 4-1 and 4-3, 3-4, respectively.

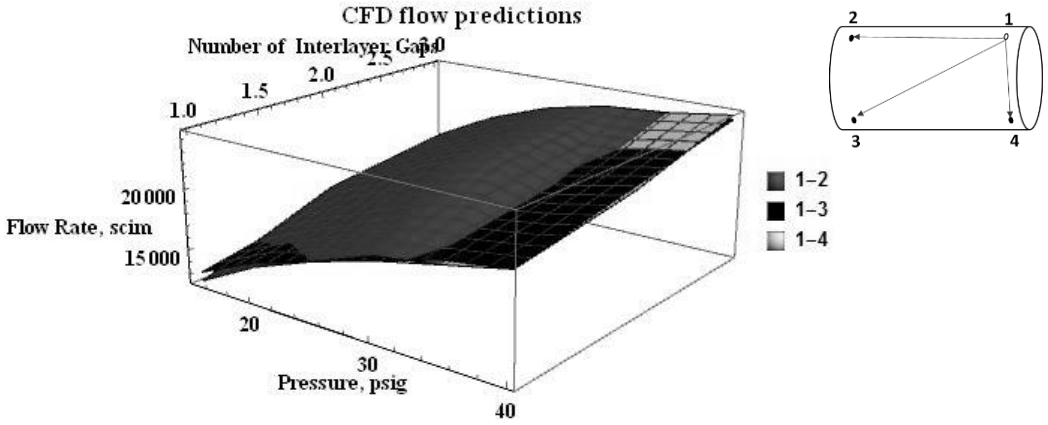

Figure 7. 3D Surface Plot based on CFD predicted values: *Pressure (psig) vs Number of Interlayer Gaps vs Flow Rate, Input-Output: 1-2, 1-3, 1-4*

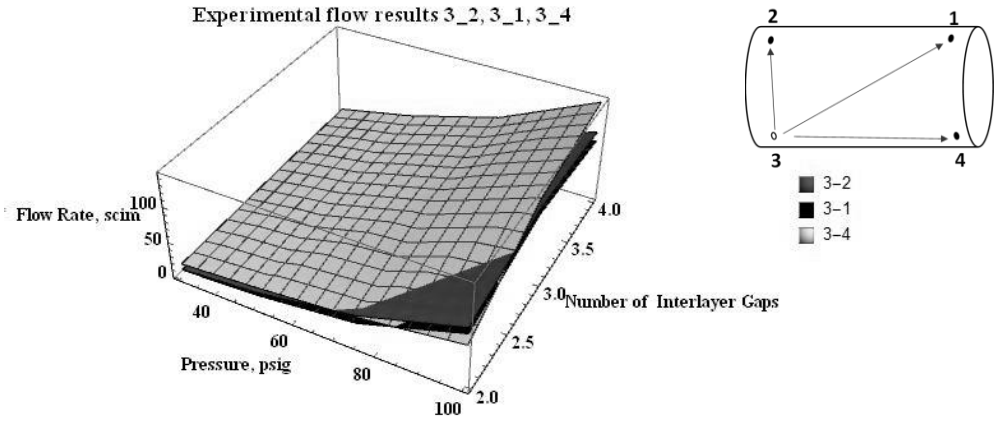

Figure 8. 3D Surface plot based on experimental results. *Pressure versus Number of Interlayer Gaps vs Flow Rate, Input-output: 3-2, 3-1 and 3-4.*

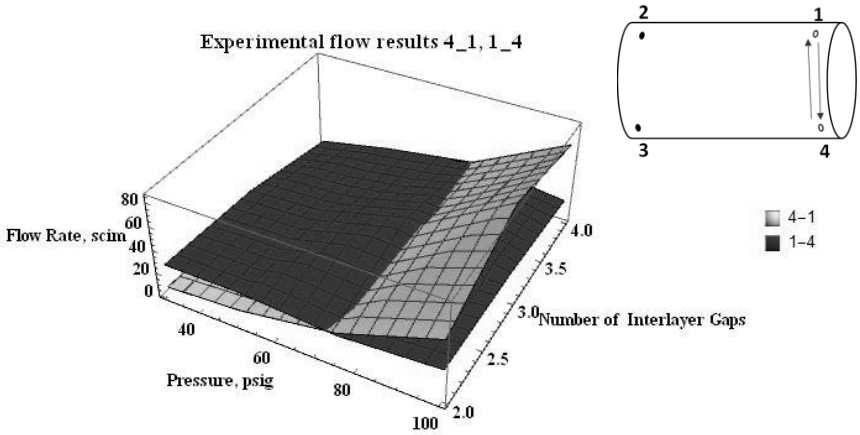

Figure 9. 3D Surface plot based on experimental results. *Pressure versus Number of Interlayer Gaps vs Flow Rate, Input-output: 4-1 and 1-4.*

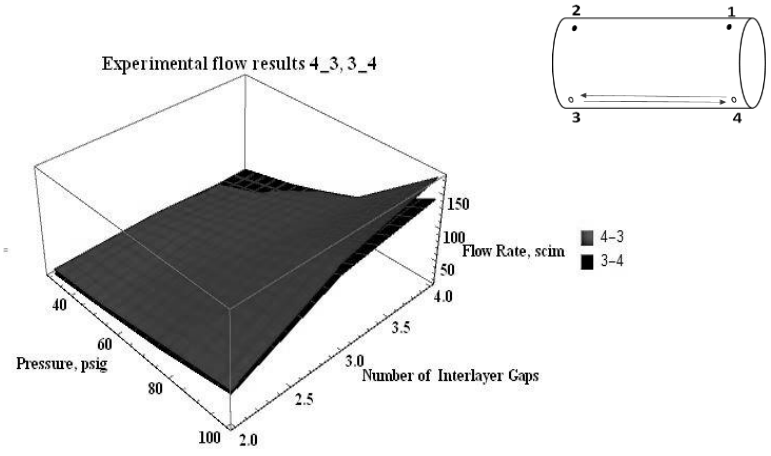

Figure 10. 3D Surface plot based on experimental results. *Pressure versus Number of Interlayer Gaps vs Flow Rate, Input-output: 4-3 and 3-4*

VI. Discussion

Figs. 7 and 8 indicate that quantitatively, the CFD predictions and experimental results differed in orders of magnitude (≈ 2). The estimated interlayer gap size based on pie tape measurements was one order of magnitude smaller than that used in the model. The estimated gap size was not used because the software crashed when this smaller size was input, likely due to CPU processing capability. Note however that the localized gaps due to longitudinal welds have been found to range from 0.03 to 0.08". The CFD model excluded surface roughness as well as the fabrication and thermal effects previously mentioned. Recall however that a quantitative comparison was never the goal. CFD predicts that the rate of change in the flow rate with pressure decreases as pressure increases while experimentally, this rate increases as pressure increases.

Similar physically intuitive trends can however be observed from both plots. Flowrates are observed to be proportional to pressure as well as the number of interlayer gaps available for flow. Both approaches also generally predicted that flow rates between longitudinally aligned weep holes on the same side were highest and flow rates between weep holes aligned such that the shortest distance between them have the greatest curvature (circumferentially aligned weep holes) were lowest. There are a relatively small set of pressure, interlayer gap number pairs for which the flow rates between circumferentially aligned weep holes were dominant. Fig. 9 demonstrates that flow rates are not symmetric for reversed paths between holes on opposite sides and opposite ends, ex. 1-4, 4-1. This phenomenon was also observed for the reversed path for input-output 3-1 and 1-3. However, Fig. 10 shows a relatively small difference in flow rates when the paths are reversed for holes that are longitudinally aligned on the same side. Two phenomena can be identified that may be responsible for the non-symmetry of the flow rates observed in Fig. 9. The different curvatures among adjacent layers due to an imperfect wrapping process and localized gapping due to the longitudinal weld. In an earlier investigation, sister vessel V0032 was dissected and gap sizes were measured.[12] The gap spacing reported ranged from 0.005" to 0.05", with gap widths ranging from 1" to 7". Fig. 11 shows an example of localized gapping due to a longitudinal weld in the fourth layer, obtained from this previous investigation.

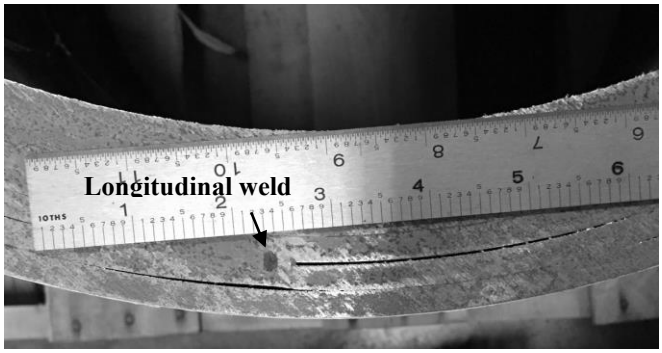

Figure 11. Localized gapping due to longitudinal weld.

With pressure input at weep hole 1 at a 0.25" depth, and flow rate measured at weep hole 3, the flow can be expected to direct itself through all interlayer gaps, however a localized longitudinal gap (due to the longitudinal weld) considerably larger than the interlayer gap height will be present at the fifth interlayer gap. So the majority of the flow can be expected to move longitudinally along this gap until it reaches the opposite end of the panel, encountering the circumferential weld. This flow would then move circumferentially towards weep hole number 3. Consider the reverse process where there is pressure input at weep hole #3 at a depth of 0.25" and the flow rate measurement at weep hole 1. The fifth layer longitudinal weld is not the closest longitudinal weld to weep hole 3. The majority of the flow would likely direct itself to the interlayer gap closest to a largest available localized gap, i.e. some other longitudinal

weld seam in either the 4th, 3rd or 2nd interlayer gap. The flow therefore is unlikely to be symmetrical where curved paths exist between weep holes. The flows observed in Fig. 10 are more likely to be symmetrical as weep holes 3 and 4 are circumferentially equidistant from their closest longitudinal welds at all depths.

VII. Conclusion

An experimental program for the determination of weep hole flow rates of an LPV due to externally applied pressure (at a weep hole) was successfully developed and executed. Results provided insight on the effect of the number of interlayer gaps through which the flow occurs, proximity to longitudinal weld seams and curvature. Flow rates were observed to increase with increasing pressure and the number of interlayer gaps available for flow. Additionally, flow rates were fastest between weep holes that are longitudinally aligned on the same side. Non-symmetry of the flow rates resulting from flow path reversal infer that the proximity of the weep hole to a longitudinal weld may have substantial influence on the flow. These trends however cannot be assumed to be definitive as the number and geometry of localized gapping, as well as inconsistent layer concentricity's varies between LPVs.

VIII. Recommendations for Future Work

Flow rate results may provide information regarding the extent of localized gapping. It is recommended that data be collected for the other half of vessel V0031. Those results would provide an excellent comparison for current results; this would allow refinement of current observations and inferences. The vessel was not pressurized in this investigation. The application of internal pressure would result in gap height narrowing with increasing pressure. Since vessels are pressurized during service, it is recommended that the current experiment be repeated at incrementally increasing pressures. The majority of LPV's on the NASA MSFC facility are substantially larger than V0031. A subsequent experiment on a larger vessel would provide an understanding on the scalability of current results and more realistic ranges regarded expected field data. A significant concern regarding LPV's at NASA MSFC is that the size of a crack in the inner layer which can be reliably detected through the weep holes is unknown. There is scant information in the peer reviewed/professional literature regarding the stability of such a crack, as well as the consequences of an unstable crack. An experiment in which an artificial crack is placed in the inner shell of an LPV and then flow rates measured at the weep holes as internal pressure increases would also provide valuable flow rate data.

The CFD model should be incrementally refined to include fabrication and thermal effects previously mentioned, as well as smaller interlayer gap heights and higher pressures. The longitudinal weld locations in each layer should be included as well as inconsistent concentricity among layers. The experimental and CFD results can then be used to refine existing closed form solutions. Weep hole flow rates as a function of inner shell crack size may be predicted with closed form methods.

Once additional weep hole flow rate data becomes available such that observed trends discussed in this report are repeated and verified, a Structural Health Monitoring method that utilizes simple mechanical devices should be strongly considered. For example, weep holes on LPV's in the chemical processing industry have been fitted with caps. These caps would remain closed but only open due to additional pressure from flow through the inner layer gaps from an inner shell through crack. As the flow rates may be indicative of the extent of localized gapping, the weep hole flow rate data itself may be used to monitor the structural health of the vessel. Greater discrepancies in path reversal flow may be indicative of increased localized gapping. Periodical measurement of weep hole flow data would allow the identification of deviant or outlier data. Vessels falling in this category could then be taken out of service and replaced. Currently no inspection techniques exist which are able to assess LPV quality of manufacture with respect to the tightness of wrapping and gaps along longitudinal welds. If gap flow data is collected for the entire fleet, there is a strong potential for the development of quantitative measures for this type of quality.

Acknowledgments

The author is grateful to the NASA MSFC Summer 2017 Faculty Fellowship program for supporting this research. The author also acknowledges and thanks Mr. Paul Dunbacher, MSFC-ET10 mechanical engineer; Mr. Ralph Keller, lead technician NASA MSFC High Pressure Test facility (bldg. 4648); Mr. Cully Cantrell, Mr. Danny Lemaster, and Mr. Danny Holland, technicians in MSFC-ET10. Their contribution to the experimental program was invaluable. Undergraduate engineering student, Mr. Diego A. Garcia, conducted a variety of CFD simulations, whose results were important first steps. The author is also grateful to MSFC:ET01 Flight Systems Test Area Deputy Manager, Mr. John "Matt" Hammond who served as the project collaborator on this fellowship. MSFC-EM21 Materials Engineers, Mr. Brian Stoltz and Mr. Joel Hobbs also shared important insights and ideas regarding the experiment.

References

[1] Welch, P.J., "Malfunction Investigation of a 6000psig Laminated Pressure Vessel," The Pressure Vessels And Piping Conference And Exhibit Orlando, Florida June 27-July 2,1982.

[2] "ASME Boiler and Pressure Vessel Code, Section VIII – Pressure Vessels," Division 1, current edition.

[3] Furr, P., "NASA MSFC – Layered Vessel Demonstration Block," Davis NDE Inc., Contract: Bastion-BPO-140096-CO1, 2015.

[4] Hudson, C.M., Newman, J.C. Jr., and Lewis, P.E., "An Investigation of Fracture Toughness, Fatigue-Crack Growth, Sustained-Load Flaw Growth, And Impact Properties of Three Pressure Vessel Steels," NASA TMX-3316, NASA Langley Research Center, Hampton, VA 1975.

[5] Cardinal, J.W., Popelar, C.F., and Page, R.A., "Multilayer Pressure Vessel Materials Testing and Analysis NASA/CR2014-218157," Southwest Research Institute , San Antonio, Texas, 2014.

[6] Prosser, W.H., "Evaluation of Agency Non-code Layered," NASA/TM2014-218505/Volume I, NESC-RP-13-00852, Langley Research Center, Hampton, VA, 2014.

[7] Coates, C., "Determination of Leakage Rates and Crack Growth Rates in a Layered Pressure Vessel," NASA/TM2017-21823, Marshall Space Flight Center, Huntsville AL.

[8] PVElite software, Ver. 2016, CADworks & Analysis Solutions, Houston TX

[9] Rasty, J. and Sabbaghian, M., "Effect of Imperfect Contact between Adjacent Layers on The Integrity of Wrapped Vessels," *Journal of Pressure Vesssel Technology,* vol. 110, no. 3, pp. 247-254, 1988

[10] Solidworks Floworks Simulation, Ver. 2017 SP2.0, DS SolidWorks, Waltham, Massachusetts, USA.

[11] Sobachkin, A and Dumnov G., Numerical Basis of CAD-Embedded CFD, NAFEMS World Congress 2013, Salzburg, Austria, June 9-12, 2013.

[12] Tillotson, M., Stoltz, B., "Gapping Measurements and Observations," NASA MSFC-EM21 internal report, Dec. 2016.

Limit Biofilm Build-Up in the UPA through the use of Predatory Bacteria

Charlotte M. de Vries[1]
Penn State Behrend, Erie, PA, 16509

In the current Water Recovery System (WRS), urine is recycled into potable water through the Urine Processor Assembly (UPA) and the Water Processor Assembly (WPA). The primary method of bactericide and fungicide is through use of a highly toxic brine (pH level of 1), but there have still been biofilm build-ups. Biofilm within the UPA can cause pressure drop within the system and damage to valves. Biofilm growth will become more of an obstacle during the cislunar missions when the WRS must stay dormant for months at a time. Currently, the study of predatory bacteria is focused on medical applications: developing bacteria for use within the human body as an antibiotic that can prey on super bacteria. To safely use it in the human body, this bacteria must be controlled so that it does not cause harm. The challenges of using therapeutic predatory bacteria within the human body are extremely complex due to the need to keep these bacteria alive. Using predatory bacteria within a mechanical system would provide its own challenges, but if successful, could be simpler all around. This study proposes testing predatory bacteria as secondary measure to mitigate biofilm levels within the UPA. At this point, due to the low TRL of this concept, the main focus will be to identify if using predatory bacteria decreases the size of biofilm components, causing less pressure drop and damage to the UPA. Proving the benefits of using predatory bacteria requires the design and building of a test chamber that will mimic the dormant running stages of the UPA. The test will run with prey bacteria alone, predatory bacteria alone, and the combination of prey and predatory bacteria. Ideally the predatory bacteria will not grow in the absence of prey bacteria, and it will be able to break apart the biofilm of the prey bacteria without adding to the problem.

Nomenclature

BSL	=	Biosafety Level
CIF	=	Center Innovation Funding
CFU	=	Colony Forming Unit
DA	=	Distillation Assembly
ECLSS	=	Environmental Controls and Life Support Systems
ISS	=	International Space Station
MSFC	=	Marshall Space Flight Center
ORU	=	Orbital Replacement Units
QD	=	Quick Disconnects
TRL	=	Technology Readiness Level
UPA	=	Urine Processor Assembly
WPA	=	Water Processor Assembly
WRS	=	Water Recovery System

I. Introduction

IN order for a human to survive in any environment, they must have access to clean air and water. The technology that has been used in to keep astronauts alive in space has developed over the last 50 years. The objective of the summer research was to identify several projects and research areas that have potential to significantly improve the

[1] Assistant Professor, Department of Mechanical Engineering, 5350 Technology Drive, Erie, PA 16510

technology for ECLSS. An assessment was completed on different areas of growth for ECLSS. This paper presents one of those ideas; using predatory bacteria within the water recovery system.

This project focusses on using predatory bacteria to prey on resilient bacteria within the water recovery system (WRS). The bacteria would be used as a secondary measure of protecting the system in parallel with the pre-treatment of urine in the urinary processing assemble (UPA) and the addition of iodine or silver to the water in the water processing assembly (WPA). In addition to preventing the build-up of biofilms in the current system, if the predatory bacteria is successful, it may be a possible primary source of biocide, limiting the need for brine in the UPA.

The structure of this report is as follows: in Section II the current technologies, challenges, and scientific areas of growth are included. In Section III the requirements and specification for a test stand are described. Section IV presents a discussion on the benefits of this project. Section V concludes the paper with an overview of the current status and the next steps.

II. Background

A. Current ISS Technology

1. Water Recovery System

The WRS provides potable water for oxygen recovery, drinking, hygiene, urinal flush water, and various payloads. Waste water is provided through crew urine, humidity condensate, and Sabatier product water. The water must be processed to become potable. There are two main components to the WRS: the Urine Processor Assembly (UPA), shown in Figure 1, and the Water Processor Assembly (WPA), shown in Figure 2.

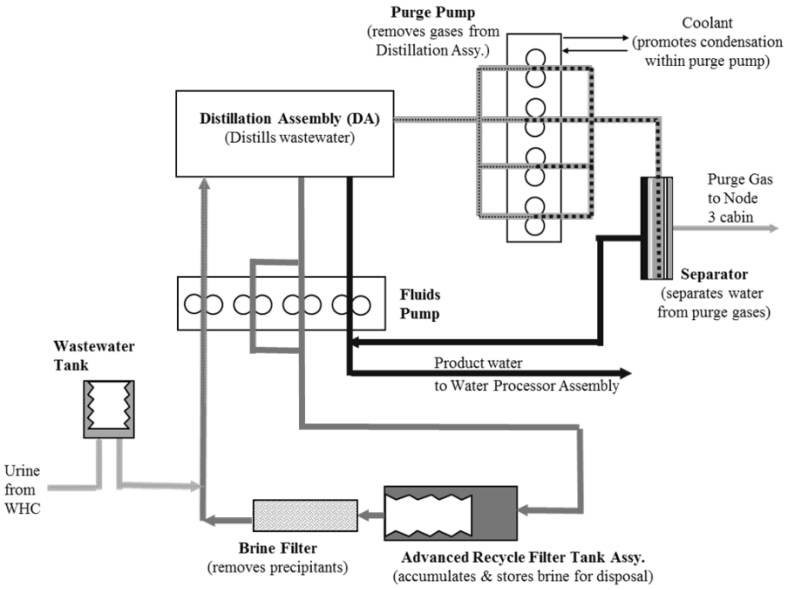

Figure 1: Simplified Diagram of the UPA. The darkest lines display the product water, which carry the highest risk of biofilm. Image used with permission from author [2]

The UPA extracts waste water from urine. Prior to entering the UPA, shown in Figure 1, a mixture of urine and flush water is pretreated with an inorganic acid to prevent microbial growth (pH = 1) before entering the distillation assembly. As long as there is no human error and the pH brine stays below 1.4, there is no risk of microbial growth. However, due to the toxic level of the brine, astronauts are not able to perform any repairs to the UPA that carries a risk of exposure to the brine; all repairs require completely isolated orbital replacement units (ORUs). Untreated water carries a risk of microbial growth. This can occur in the Purge Pump and the Distillation Assembly of the UPA, as well as the Water Processor Feed tanks in the WPA.

In the WPA, displayed in Figure 2, distillate from the UPA and water from the dehumidifier is processed to reduce the Total Organic Content [1] in order to produce potable water. The waste water is stored in bellows: storage tanks that allow for expansion or compression based on a pressure input. The spring-like form of the bellows results in many nooks where biofilm can form. An example of one of the bellows is displayed in Figure 3.

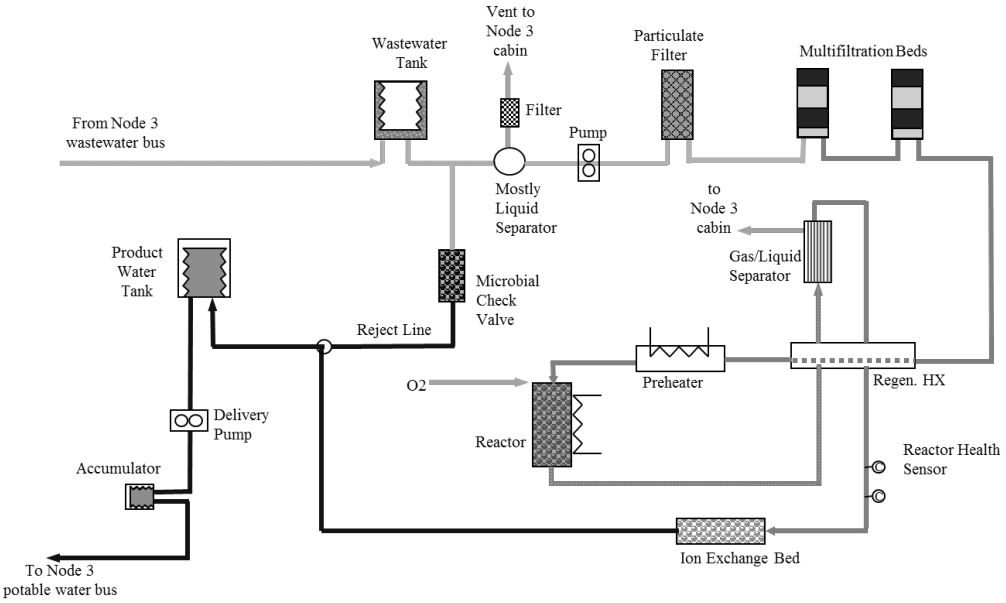

Figure 2: Simplified Diagram of WPA. Image used with permission from author [2]

2. Long Duration Missions

In order to facilitate manned missions to Mars, there will be a cislunar mission in a Lagrangian point between the earth and moon's gravity. This will allow a proving ground for the Mars mission, while still being close enough to earth in the event of an emergency. Both the cislunar and Mars missions will include at least one year of occupancy, followed by a year of a dormant space shuttle without any crew. When astronauts return after dormancy, the life support systems must be ready to be used again. Microbial control of the WRS is identified as one of the challenges that must be addressed before these missions can take place [2].

For long duration missions the WRS must be easily maintained and repaired by the crew, as resupply missions are not an option. Communication between the Astronauts and Earth may take up to 20 minutes, so the repair process must be clear and straight forward. Currently on the ISS there are Orbital Replacement Units (ORUs) with key quick disconnects (QDs) such that astronauts can only put the replacement part together in one method. While QDs are useful devices, they can take up a lot of space within a fluid system. Replacement ORUs also take up extra space. Any additional parts brought into the system should consider these challenges.

During dormancy there is a risk of biomass formation in the lines as a result of microbial activity. Extreme biomass growth can be prevented by running the system periodically. However this has been deemed as too risky as a hardware failure occurring without a crew could result in an unusable system. Currently the design plan is to treat the water in the system with a biocide [3]. Current research at MSFC is being done on using silver as the primary biocide within the WRS. Potential future areas include the use of UV light as a biocide.

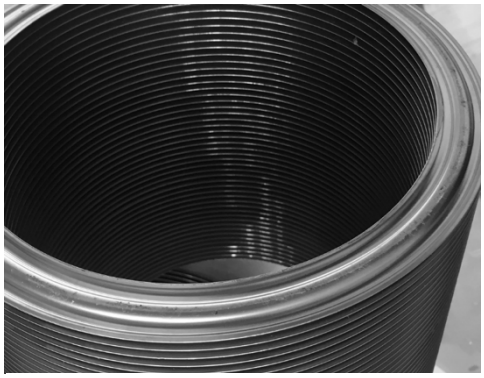

Figure 3. Bellows are used to store water within the WRS. Microbial growth in the crevices carries the risk of erosion.

3. Biofilm Hazards and Complications

Biofilm is the name for a community of microbial growth that sticks together, and can consist of multiple species of bacteria and fungi [4]. Bacteria species are categorized as either Gram-positive or Gram-negative, based on their cell wall properties. Gram-negative bacteria tend to be more resistant to traditional antibiotic treatments than Gram-positive. In the biofilm, the fungi or bacteria create a protective coating that allows them to be up to 1000 times more resistant to antifungals or antibiotics than they are as solitary species. Preventative measures against biofilm includes the use of chemical agent in the environment, bactericidal coating on surfaces [5], predatory species [6], and anti-adhesion coating [3].

Microbial activity and biofilm can occur anywhere in the WRS that has untreated water. The biofilm can cause wear and tear on a system, and added resistance in pipe flow due to build ups in valves and at filters. There is also a risk of crevice erosion due to microbial activity in bellows of the WRS's storage tanks. Figure 4 shows biofilm on a valve and filter.

Figure 4. Biofilm on a Quick Disconnect (QD) valve and a filter from the Distillate Filter.

The presence of biofilm is a risk that increases with the dormant nature of the cislunar missions. After the WRS is used, the system must be completely turned off to decrease the risk of the system breaking in the absence of astronauts who can problem solve and maintain. Without the system running, biofilms can build up and can cause blockages which may damage the system. Due to the protective nature of biofilm, the larger the biomass the harder it is to effectively treat.

In 2013 a study was conducted with biofilm built up on a distillate filter from the UPA on the ISS. There were 8 bacteria species found, and 4 fungal species. Of the 8 bacteria species, only one was Gram-positive, the others were all Gram-negative. The Gram-negative species had the greatest colony forming units (CFUs) across all the samples.

B. Predatory Bacteria

Predatory bacteria are seen as a potential tool to prevent biofilm build up on medical implants and as an antibiotic within the human body. Shatkez et al [7] studied the effect of predatory bacteria on the diversity of gut bacteria within mice and found that the overall benefits were positive over the course of a week. The two species considered for this study prey exclusively on Gram-negative bacteria, even those clustered in biofilms. Studies have shown that in a controlled setting they can decrease biofilm colonies [8].

Bdellovibrio bacteriovorus are predatory bacteria that enter prey bacteria to reproduce, which leads to lysis (break-up) of the host as shown in Figure 4. In nature, *B. bacteriovorus* is found in freshwater, seawater, sewage, and animal intestines, but only in the presence of prey [9]. (*B. bacteriovorus* are found in higher levels in healthy human digestive systems compared with that of people with Celiacs or Crohn's disease [10].

Micavibrio aeruginosavorus is another predatory bacteria alternative. Instead of entering prey bacteria, this bacterium will attach to the surface and suck out the nutrients. They tend to prey on a narrower range of species compared with the *B. bacteriovorus,* but they may outperform *B. bacteriovorus* at decreasing the biofilm of those species [11].

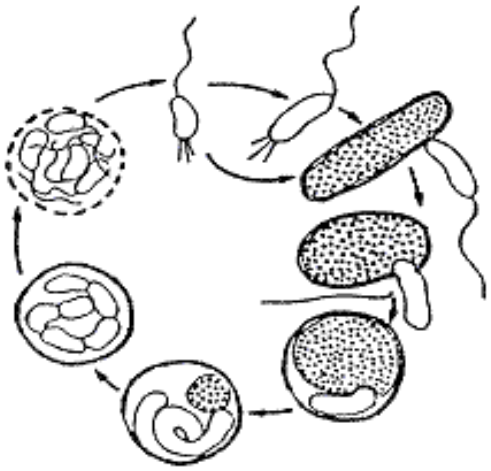

Figure 5. The lifecycle of B. bacteriovorus. The whole process takes several hours. Image used with permission from author *[13]*

III. Planned Methodology

Before predatory bacteria can be pursued as a feasible option for the UPA, several major questions must be answered: Does the addition of predatory bacteria decrease the biofilm of the bacteria found within the UPA? In the event of excess predatory bacteria, will it compromise the system by itself? If predatory bacteria can decrease biofilm, can it do so to a level to prevent wear and tear on the system?

This methodology is planned under the assumption that predatory bacteria can decrease the biofilm found within the UPA. The biological study on this challenge, which considers the first question, is currently being looked into, and will need to be further developed before an engineering study should be conducted.

C.Test Stand Requirements

To test the use of predatory bacteria within the UPA, a set up will be designed to mimic the dormant and running stage of the UPA. This device will have a constant flow rate while running, and pressure sensors to measure the pressure drop caused by bacteria in the system. The fluid in the system will be ersatz waste water provided by MSFC.

Three primary scenarios will be tested. The first (prey-only) will be an intentional creation of biofilm within the testing environment to a level where a pressure drop can be detected. The second (predatory-prey) will be run in parallel with the first. After two healthy biofilm colonies are created to a level where a significant pressure drop can be detected, predatory bacteria will be introduced into one of the environments in an attempt to mitigate the effect of the film. A third scenario will be predatory-only to make sure the predatory bacteria on their own do not cause damages to the system.

4. Fluid Environments in the UPA

Anywhere in the UPA untreated water has the potential for bacteria growth. Some key areas are in the interface of the DA where waste water is condensed before flowing through the fluids pump. Due to the toxic brine within the DA, it cannot be accessed by astronauts during use. However, as the DA is at the interface between the pretreated urine and the untreated water, there is risk of the two liquids mixing. In the event that pretreated urine leaks into the treated water, the higher pH level results in potential for bacterial growth. Figure 6 shows biomass that grew after such an incident occurred. Filters and valves within the system are also key areas where biofilm has formed in the past. Untreated water stored in the waste water tank bellows carries the risk for biofilm in the crevices.

In order to replicate the fluid environments the test stand will share similar ranges of temperatures and pressures. Approximate environment standards have been provided and are listed in Table 1. The ersatz fluid provided should replicated the untreated distillate waste water.

Table 1: Fluid system requirements in the UPA

	Minimum	Maximum
Flow rate	30 ml/min	300 ml/min
Temperature	80℉	90℉
Pressure	40 mmHg	760 mmHg

5. Bacteria input points

Due to the need to keep the UPA as contained as possible, QDs are used in-between ORUs to prevent any leakage of fluid. The connection between ORUs are the limited areas where predatory bacteria could be put into the system. This may cause several challenges, as though predatory bacteria population have top speeds of 160 µm/s in liquid environments, it would need to be proven how far they would travel from an input location [12]. The ability for the predatory bacteria to move throughout the system should be proven to be efficient when placed through a set input port.

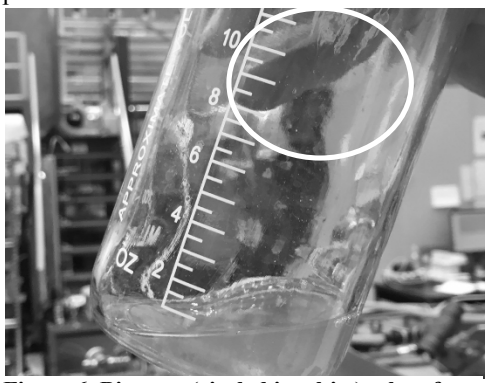

Figure 6. Biomass (circled in white) taken from the UPA on the ISS

6. Bellows Storage

As the bellows are a site with potential for biofilm buildup, the test stand should also contain at least a section of the bellows geometry. Growing bacteria within a full bellow tank may be difficult to assess growth levels. Either a section of the bellow wall, or a modified tank that can be opened, would need to be used within the testing.

D. Future Steps and Challenges

As this is an interdisciplinary study, it will require multiple experts to grow the biofilm, breed the predatory bacteria, and assess the effectiveness of the predatory bacteria. In order to handle this process several steps would be needed.

7. Study on ISS Biofilm

As early studies with predatory bacteria and certain Gram-negative prey show promising results on the reduction of biofilm, the next step is to repeat these early studies with bacteria from the ISS. At the predatory bacteria kill off the prey Gram-negative bacteria present in biofilm, it is important to know if that delays the total biofilm growth, or

if the Gram-positive and fungal species end up taking over the niche, and there is no reduction in overall growth. Some of the bacteria found within the ISS are classified as Biosafety Level (BSL) 2. This causes challenges in terms the procedures required for handling and disposing of the specimen. Creation of a test stand must consider the challenges of working with BSL 2 specimens.

8. Large scale prey studies

For preliminary studies, it is suggested that a BSL 1 species, such as *E.Coli* or *Pseudomonas aeruginosa,* should be selected as the prey bacteria to mimic the growth of biofilm within the ISS. By using a substitute prey, effects of biofilm within the system can be studied prior to replicating the current biofilm. The cleaning procedure of the test stand can be proven before working with BSL 2 species.

IV. Discussion

E. Alignment and Potential Applications:

This technology follows TA 6.1.2: Water Recovery and Management, specifically Brine Processing (6.1.2.3) and Potable Water Microbial Control (6.1.2.4). One long term goal within Water Recovery (TA 6.1.2) is the ability to replace the highly toxic brine to a fluid that is less dangerous to the astronauts. If this technology proves to be valid and useful, it may be possible to replace the brine with a less toxic material on combination with the predatory bacteria. This would allow astronauts to be able to make repairs to the UPA during spaceflight, a feature which is not possible in the current system.

Outside of NASA, the field of predatory bacteria is promising in the endeavor of fighting antibiotic resistant bacteria. The Center for Disease Control states that at least 2 million people become infected with antibiotic resistant bacteria each year, and over 23 thousand people annually die as a result of those infections. The lessons learned from this study may prove useful in the effort of preventing biofilm within medical devices.

Creating a test stand to mimic bacterial growth within the UPA is not limited to the study of predatory bacteria. Regardless of the solution, an appropriate biocide must be selected. The design and build of a test stand can be used to compare and contrast various solutions including predatory bacteria, UV light, silver, and other biocide methods.

V. Conclusions

The groundwork for a new project has been identified. Any biocide used within the WRS must be tested on earth and in micro gravity before it can be used in a long duration mission such as the cislunar or Mars missions. This paper argues the merits in using Predatory Bacteria as a method of biofilm mitigation within the WRS.

At this point biologists are looking into the use of predatory bacteria on ISS biofilm within a lab setting. If the preliminary data shows that predatory bacteria can mitigate the multi species biofilm from the ISS, a scaled up test stand should be built. Prior to using the existing bacteria, scaled up testing methods should be restricted to alternative prey due to the BSL of the ISS bacteria.

Once the use of predatory bacteria has been proven to a sufficient degree, a dormancy simulation environment should be created at MSFC combining the features above. To demonstrate the use of predatory bacteria in a dormant environment, a device that can store and release freeze dried bacteria over time must be designed. This experiment could take into account all of the potential areas for growth, as well as test out other biocide experiments.

Acknowledgements

This research was conducted through the NASA Marshall Space Flight Center Faculty Fellowship program. I'd like to thank Dr. Morgan B. Abney for the opportunity to work with ECLSS and her support this summer. I'd also like to thank members of the first JAMFest: Mr. David Reynolds, Ms. Brittany Brown, Mr. Colton Caviglia, Dr. Tim Geisy, Ms. Cara Johnson, Mr. David Long, and Ms. Mononita Nur.

References

[1] J. E. Straub II, D. K. Plumlee and W. T. Wallace, "Chemical Characterization and Identification of Organosilicon Contaminants in ISS Potable Water," in *46th International Conference on Environmental Systems*, Vienna, Austria, 2016.

[2] W. F. Scneider, R. L. Gatens, M. S. Anderson, J. L. Broyan, A. V. MaCatangay, J. Perry and N. Toomarian, "NASA Environmental Controll and Life Support Technology Development and Maturation for Exploation: 2015-2016 Overview," in *46th International Conference on Environmental Systems*, Vienna, Austria, 2016.

[3] D. L. Carter, D. Tabb and M. Anderson, "Water Recovery System Architecture and Operational Concepts to Accommodate Dormancy," in *47th International Conference on Environmantal Systems*, Charleston, SC, 2017.

[4] M. Chen, Q. Yu and H. Sun, "Novel Strategies for the Preventation and Treatment of Biofilm Related Infections," *International Journal of Molecular Sciences,* vol. 14, pp. 18488-18501, 2013.

[5] L. R. Martinez and A. Casadevall, "Specific Antibody Can Prevent Fungal Biofilm Formation and This Effect Correlates with Protective Efficacy," *American Society for Microbiology,* vol. 73, no. 10, pp. 6350-6362, 2005.

[6] A. Chavez-Dozal, C. Gorman, M. Erken, P. D. Steinberg, D. McDougald and M. K. Nishiguchi, "Predation Response of Vibrio fischeri Biofilms to Bacterivorus Protists," *Applied and Environmental Microbiology,* vol. 79, no. 2, 2013.

[7] K. Shatzkes, C. Tang, E. Singleton, S. Shukla, M. Zuena, S. Gupta, S. Dharani, J. Rinaggio, N. D. Connell and D. E. Kadouri, "Effect of predatory bacteria on the gut bacterial microbiota in rats," *Nature,* 2017.

[8] D. Kadouri and G. A. O'Toole, "Susceptibility of Biofilms to Bdellovibrio bacteriovorus Attack," *American Society for Microbiology,* vol. 71, no. 7, pp. 4044-4051, 2005.

[9] Socket, R. Elizabeth and C. Lambert, "Bdellovibrio as therapeutic agents: a predatory renaissance?," *Nature Reviews: Microbiology,* vol. 2, pp. 669-675, 2004.

[10] V. Iebba, F. Santangelo, V. Totino, M. Nicoletti, A. Gagliardi and R. V. De Blaise, "Higher Prevalence and Abundance of Bdellovibrio bacteriovorus in the Human Gut of Healthy Subjects," *PLOS One,* 2013.

[11] D. Kadouri, N. C. Venzon and G. A. O'Toole, "Vulnerability of Pathogenic Biofilms to Micavibrio aeruginosavorus," *Applied and Environmental Microbiology,* vol. 73, no. 2, pp. 605-614, 2007.

[12] C. Lambert, A. K. Fenton, L. Hobley and R. E. Sockett, "Predatory Bdellovibria Bacteria Use Gliding Motility to Scout for Prey on Surfaces," *Journal of Bacteriology,* vol. 193, no. 12, pp. 3139-3141, 2011.

[13] N. Markelova, "File:Bdello-cycle.png," 17 August 2008. [Online]. Available: https://commons.wikimedia.org/wiki/File:Bdello-cycle.png. [Accessed 8 8 2017].

Interactive Concept of Operations Narrative Simulators

Andre R. Denham[1]
The University of Alabama, Tuscaloosa, AL, 35487

This paper reports on an exploratory design and development project. Specifically this paper discusses the design and development of Interactive Concept of Operations Narrative Simulators (ICONS) as a means of enhancing the functionality of traditional Concept of Operations documents by leveraging the affordances provided by applications commonly used within the Interactive Fiction literary genre. Recommendations for an ICONS design and development methodology, along a detailed description of a practical proof-of-concept ICONS created using this approach are discussed. The report concludes with a discussion of how ICONS can be extended to the K-12 mathematics education domain and conclude with a discussion of how ICONS can be used to assist those involved with strategic planning at Marshall Space Flight Center.

I. Introduction

Concept of Operations (ConOps) documents play a vital role in the design and development of the systems NASA uses to accomplish its mission. A ConOps document provides stakeholders with a detailed description of a proposed system by explicating its attributes from an operational point of view. This quantitative and qualitative breakdown of a system's characteristics provides the reader with insight into the system's purpose and intended use. The process of creating a ConOps is important as it provides an opportunity for stakeholders to identify and specify requirements, determine design functions, and pinpoint potential user interface issues well in advance of the development of the system. The exercise of creating a ConOps also provides an opportunity to create system definition documentation and conduct a formative assessment to identify additional stakeholders who may have been overlooked initially, but through subsequent analyses deemed vital to the design, development, and implementation of the system.

While there are a variety of formats for a ConOps, NASA documentation requirements specify that a minimum, a ConOps should include the following[1]:

1) Operational goals from the viewpoint of the all stakeholders.
2) Overview of the System of interest, including supporting systems.
3) Intended use of the system during all life-cycle phases of the program/project, including but not limited to:
    a. Manufacturing and assembly
    b. Integration and test.
    c. Transportation and storage.
    d. Ground operations/launch integration.
    e. Launch Operations – launch, deployment, on-orbit checkout.
    f. Maintenance and disposal.
4) Operational timelines
5) Command and data architecture.
6) End-to-end communication strategy.
7) Integrated logistic support (resupply, maintenance, assembly).
8) Operational facilities.
9) Contingency and off-nominal operations.

[1] Assistant Professor of Instructional Technology, Department of Educational Leadership, Policy and Technology

ConOps are usually developed through a series of brainstorming sessions. These brainstorming session are held in a traditional manner, where a facilitator leads out in the sharing of ideas out loud and a scribe is assigned to capture all that is discussed. This approach to ConOps development lends itself to being dominated by vocal individuals and the pace of discussions can make it challenging for the assigned scribe to capture all of the concepts and ideas put forth in the session. Furthermore, those who were not present during the ConOps development phase will have to envision the system being described in the document, which may lead to misinterpretations of the system and the glossing over of vital information. Increasing the interactivity of ConOps may serve as a means of amplifying the functionality of these important strategic documents.

The overarching goal of the summer faculty fellowship being reported on in this paper was to develop a means of reimaging ConOps by creating a new form of these documents called Interactive Concept of Operations Narrative Simulator (ICONS). The purpose of ICONS is to widening the interactivity of ConOps beyond static text and images as a means of encouraging active reading. This would be accomplished by leveraging the affordances of Inform 7, a design system used for the development of interactive fiction via natural language coding, Twine, an open-source application for the development and delivery of interactive nonlinear stories, existing NASA and web-based resources, and design guidelines gleaned from a variety of fields. This report will discuss the catalyst for this project, the design and development of a proof-of-concept narrative simulation based on existing International Space Station procedures, a proof-of-concept application of ICONS for mathematics word problems, propose a workflow process for developing ICONS, and provide recommendations for future work which will also include a discussion of the broader impacts of ICONS inside and outside of NASA.

II. Background

The genesis of ICONS stemmed from one of the project collaborator's experience in the Space 2100 project. During the ConOps development process for the "Massless Exploration Space 2100 Sprint", the collaborator felt ConOps were being developed inefficiently. Development was spurred by brainstorming sessions in which one individual served as the facilitator, and one to two other persons served as scribes. The remaining attendees were tasked with presenting ideas to the large group for vetting and subsequent inclusion within the ConOps. This resulted in brainstorming sessions where a few individuals dominated the conversation and the scribe(s) struggled with the task of capturing all of the concepts discussed during each session.

The collaborator also realized that technological advances provided an opportunity to enhance ConOps. While the current text based format of ConOps have proven to be effective, going beyond static text and images could potentially enhance their functionality and readability. What was needed was the identification of technology or technologies that would allow for the leveraging of existing digital and web-based resources. In the attempt to pinpoint the tool(s) necessary to create the next generation of ConOps, it became apparent there was a greater need to focus on increasing the interactivity of the scenarios presented within ConOps as a means of encouraging active reading.

Schilit, Golovchinsky, and Price[2] define active reading as not simply the act of look at words on paper, but a combining of critical thinking, reading, and learning which are all crucial elements of education and knowledge work. Victor[3] defines an active reader as someone who:

> ask questions, considers alternatives, questions assumptions, and even questions the trustworthiness of the author. An active reader tries to generalize specific examples, and devise specific examples for generalities. An active reader doesn't passively sponge up information, but uses the author's argument as a springboard for critical thought and deep understanding.

Typical ConOps do not explicitly or implicitly support active reading. ConOps simply presents information and places the responsibility on the reader to decide whether they will passively or actively interact with the text. Within the field of literacy, the technological approach commonly used to increase the likelihood of active reading tend to center on providing readers with digital documents and encouraging them to use the annotation tools (highlighters, under liner, note taking, comment features, stylus, etc.) embedded within the application used to display the text[2]. While this approach has proven successful, it still places the tools for active reading extrinsic to the digital document and places the onus on the reader to choose whether to use them or not. What is needed is a technology that can be intrinsically integrated within a ConOps that implicitly requires the reader to actively interact with the text. The literary genre of interactive fiction and the recent technological advances within this community provides a potential means for intrinsically supporting active reading of ConOps.

A. Interactive Fiction

Interactive fiction (IF), also known as text adventures or text games, is a dialog system contained within a text-based computer simulation[4]. IF eschews the point-and-click and/or controller user interfaces commonly found in

most digital games and instead requires the user to employ text based, conversational commands to control the main character(s) and interact with the simulated environment. Similar to choose-your-own adventure books, the narratives within a piece of IF are non-linear and frequently contain puzzles, quests, and games for the player to navigate in order to advance the story line. The reader/player is afforded the opportunity to make decisions throughout the gameplay that will determine the outcome of the story. Modern IF differs from choose-your-own adventure books in that they can go beyond text, and also include multimedia and external web resources.

Modern IF development tools democratized the process of creating IF. These IF development tools allow for the design of interactive stories through the creation of integrated design environments that allowed authors to create "worlds" where players can use simple text commands such as "open door" to interact with the environment and control the narrative. Along with the tools needed to release either an executable application, or more commonly, provide an option to publish directly to HTML, IF so authors can share their works online. This has led to a surge in the size and productivity of the online IF community.

B. Project Goals

The availability of free, robust IF design and development applications, along with the crowd sourced resources readily available online, provides a compelling tool for supporting active reading of ConOps. For instances, creating ICONS within ConOps where readers are required to control the steps take within a simulation will require them to focus their attention, and avoid the temptation to gloss over what might be vital information.

This project sought to conduct exploratory design and development of the ICONS concept by creating the following end products:

1) A proof-of-concept narrative simulation based on existing International Space Station procedures
2) A proof-of-concept application of ICONS for word problems
3) A workflow process for developing ICONS

III. Proof-of-Concept ICONS

This portion of the report will focus on the design and development of a proof-of-concept narrative simulation based on an existing International Space Station (ISS) laboratory procedure. This discussion of the proof-of-concept ICONS will begin with an overview of Inform 7 and Twine, the IF development tools used throughout this project, and their role within the ICONS design and development process. Following that will be detailed presentation of a proof-of-concept ICONS based on a heart cell experiment which took place on the ISS. This section will conclude with additional examples of application of ICONS within the domain of K-12 mathematics education.

A. Inform 7

Inform is an integrated development environment for interactive fiction, created by Graham Nelson in 1993. The release of Inform served as a catalyst for a substantial increase in the number of people creating IF, by allowing authors to easily create story files, which are also known as Z-Code, from the source code[5]. The resulting story files can then be executed within any Z-Code interpreter, which are programs that are designed to run the Z-Code virtual machine. There are a large variety of IF platforms, so the major breakthrough for Inform was providing a means for a Z-code file to be executable on any IF platform without the need for adjustments to the source code for each platform. Inform can also handle the interpretation of source code for the Glulx virtual machine created by Andrew Plotkin to address limitation issues commonly found in older Z-virtual machines[5].

Inform 7 is the latest version of this IF design and development tool and is a free application available for use on Mac OS, Windows, and Linux. Inform 7 uses an object-oriented, procedural programming language that is adept at handling inferences between object types and their properties based on their use. For example, the statement "Sarah has a purse" creates a character named Sarah because Inform understands that only people are capable of carrying things. This statement also creates a thing called a purse, and assigns the purse as having the property of being portable, as objects that can be carried can be transported by characters. Inform 7 allows authors to manage the relationships between objects, along with the ability for authors to create their own relationships, such as jealousy or anger. This programming language is used to create story files, which are interpreted by the Inform compiler. Inform 7 also contains the Inform Library, which is used to parse the commands input by players through the text-based interface and handle the subsequent updating of the game environment. The source code for Inform 7 is distinctly readable, which lessens the slope of the learning curve for those who are new to the application. Below is an example of Inform 7 source code taken from the Inform 7 Recipe Book[6]:

"The Power of the Keys"
Afterlife is a room. "Fluffy white clouds gather round you here in the afterlife." The Pearly Gates are a door in Afterlife. "The Pearly Gates - large, white, wrought-iron and splendidly monumental - stand above you." Heaven is a room. The Gates are above the Afterlife and below Heaven.

St Peter is a man in the Afterlife. "St Peter, cheery if absent-minded, studies his celestial clipboard."

Before going through the Pearly Gates:
    say "St Peter coughs disarmingly. 'If you'd read your Bible,' he says, 'you might recall Revelation 21:21 saying that the twelve gates were twelve pearls, each gate being made from a single pearl. I really don't know why people keep imagining it like the entrance to some sort of public park - oh, well. In you go.'";
    end the story.

Test me with "enter gates".

An example of the Inform 7 integrated development environment can be found in the figure below.

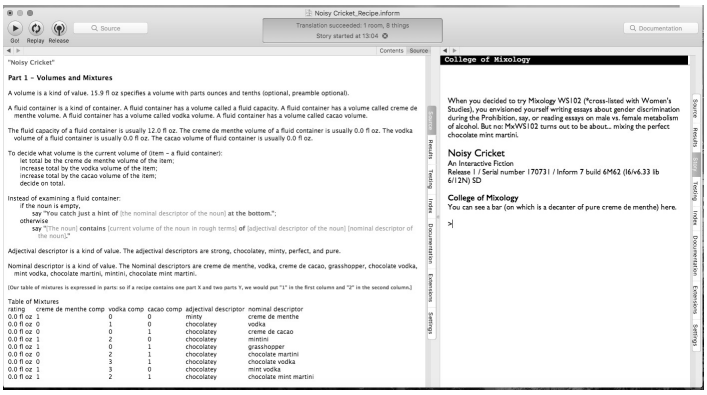

Figure 1. Inform 7 Integrated Development Environment.

B. Twine

Twine is an open-source web-based application for developing IF. Twine can also be downloaded for Mac OS, Windows, and Linux as a stand-along application, and is primarily used to develop hypertext IF and games. Twine differs from Inform 7 in that the development environment is visual rather than text-based. This negates the need for authors to learn a programming language. If you do have programming experience, Twine does allow for the extension of its capabilities through the inclusion of variables, conditional logic, images, CSS, and JavaScript[7].

Twine supports IF where the narrative is created through branching. For example one might start a Twine story by creating a passage of text that says, “You’ve parked your car and walked into the mall. You need to buy a dress for your cousin’s wedding in a few weeks and don’t know where to start”. At that point you would need to provide the reader with options on what to do next. Within the passage you would then also include the following text at the bottom of the passage:

[[Go into the formal wear section of Belk]]
[[Find a salesperson in Belk to help you find a dress]]
[[Check bank account to see how much money you have to spend on the dress]]

The brackets tell Twine to create three new passages for the story, with each branch being connected to the original passages (see Figure 2).

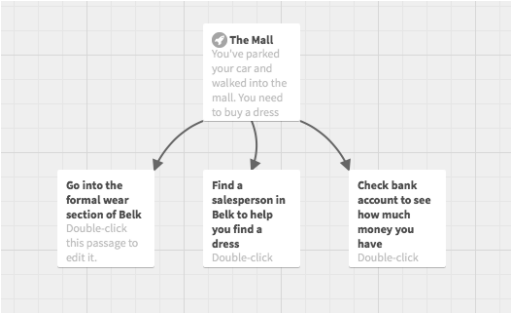

Figure 2. Twine Interactive Fiction Development Environment.

From there you can continue branching the story out by adding additional parts of the narrative to each of the three new passages, while making sure to provide the reader/player with choices within each passage. Twine publishes the story to an HTML file, which allows for the sharing of IF and a simple hypertext interface for the reader/player to control the unfolding of the narrative (see Figure 3). Twine differs from Inform 7 in that many of the additional layers of interactivity that can be added to a Twine story through the use of JavaScript, CSS, images, variables, and conditional logic are already native to Inform 7. In other words, Twine requires the utilization of additional applications to create elements of interactivity that are already included within Inform 7.

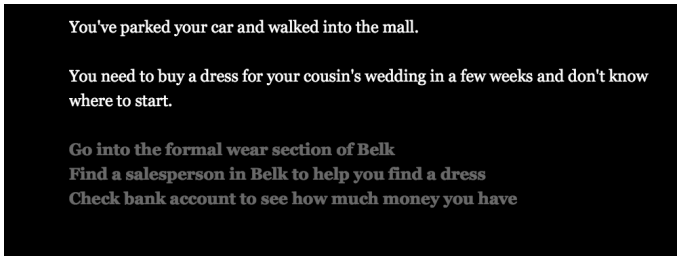

Figure 3. Example Twine Story.

C. Development Process

A major goal for this project was to propose a process for developing ICONS. This process needed to be replicable and provide guidance to those who may be interested in developing ICONS. Using the IF development tools Twine and Inform 7, the following development process was created:

1. Rapid prototype the ICONS using Twine
2. Develop the ICONS within Inform 7
3. Evaluate and Implement the ICONS

1. Rapid Prototype the ICONS

During the first stage of ICONS design and development, the goal is to begin the process of transforming a traditional ConOps scenario into an ICONS. It is recommended that Twine be used to accomplish this as it facilitates rapid prototyping of scenarios, due to its ease of use. During the designing of an ICONS within Twine, the developer should focus not only on creating a simulation of a system, operation, and/or procedure, but the crafting of additional narratives. For example, these additional narratives could highlight steps in a procedure when an error can occur, or to show the interconnectedness of various parts of a system.

To help the development of additional narratives, it is recommended that ICONS developers make use of one of the common patterns in choice-based games based on the size of the scenario. For large-scale ICONS development, developers should make use of standard design patterns such as, but not limited to, Time Cave, Gauntlet, Branch and Bottleneck, Quest, and Loop and Grow[8]. The Time Cave design pattern is considered the oldest of the choice-based design patterns and contains many branches. The choices that players make throughout the game all carry equal weight and once a player begins going down a branch they will not be able to merge with another branch.

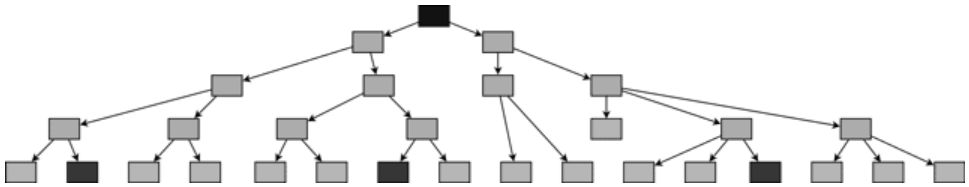

Figure 4. Time Cave Design Pattern.

While the Time Cave design pattern is broad, the Gauntlet design pattern is long. Gauntlets have a central linear thread, with the branches either containing, dead ends, opportunities to go back a step, or the ability to rejoin the central thread. This design pattern makes it quickly evident to players that they are on a prescribed path and the world they're interacting with is tightly constrained. That being said, the Gauntlet design pattern makes sure that readers/players must interact with all of the important content within a story. The same cannot be said for the Time Cave design pattern.

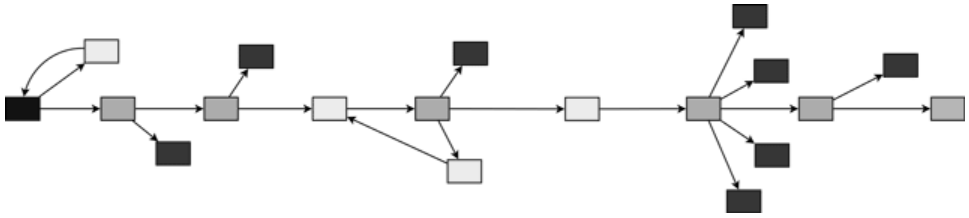

Figure 5. Gauntlet Design Pattern.

Within the branch and bottleneck design pattern, the story will frequently branch, but all branches will at some point rejoin. This rejoining of branches will take place around an element or event that makes sense for all versions of the narrative (which requires constant state-tracking). Branch and bottleneck is well suited for ICONS where the passage of time is important to the scenario.

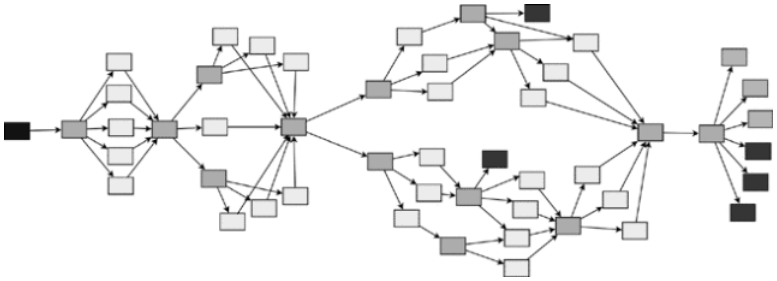

Figure 6. Branch and Bottleneck Design Pattern.

IF created using the quest design pattern contains branches that are unconnected but can rejoin at a few winning nodes. Quest design patterns are best suited for ICONS in which the goal is to support the exploration of a particular setting or where geography is of importance.

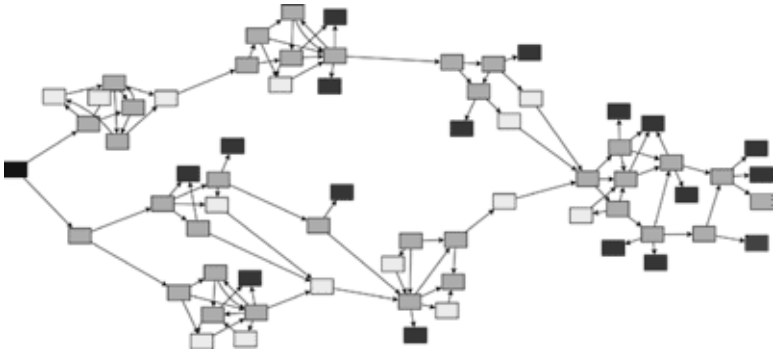

Figure 7. Quest Design Pattern.

Finally the Loop and Grow design pattern loops a central thread/narrative, but uses state-tracking to alter the options presented to the reader/player each turn around the loop. This design pattern is best suited for ICONS where there is a need to warrant the repetition of portions of a narrative. Loop and Grow is typically used within another design pattern when the reader/player is required to perform a routine task, travel through time, and/or complete a set of tasks to some level of abstraction[8].

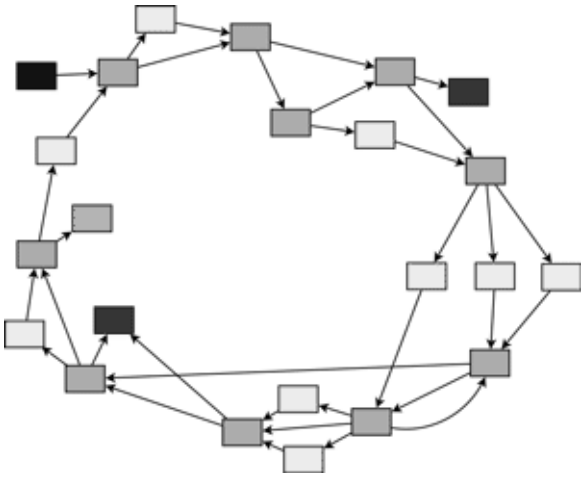

Figure 8. Loop and Grow Design Pattern.

For small-scale ICONS development, developers should make use of standard design patterns such as, but not limited to, Confirmation-required, Track Switching, Sorting Hat, and Endgame Time Cave[9]. The Confirmation-required design pattern allows readers/players to engage in increasingly risky behavior by making them opt in before each risky decision. Track switching is a variation of Confirmation-required where the player is allowed to reverse course after a series of decisions have been made. Sorting hat design patterns are usually applied within the first chapter of IF. A decision that a player makes at the beginning of the story places them one of several linear paths. Finally, the Endgame Time Cave design pattern is the opposite of the Sorting Hat and is used to conclude a game. Examples of each design pattern can be found below in their respective order.

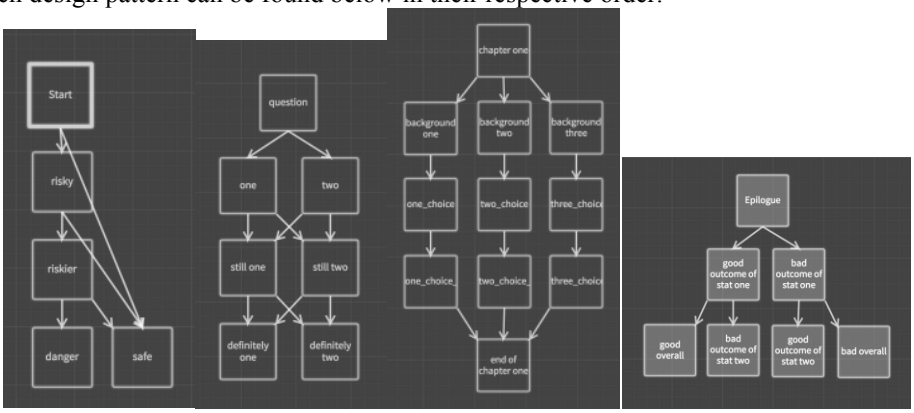

Figure 8. Small Scale Design Patterns.

2. Develop the ICONS within Inform 7

Once ICONS have been designed using Twine and one of the prescribed design patterns, development of the ICONS should commence in Inform 7. As stated earlier, Inform 7 provides access to a host of native features with the most important being the text parser. In addition, Twine allows for the inclusion of extensions. Extensions are source text shared by other IF authors which help to expedite the development process. An extension is supported by the original author, and typically contains documentation and examples of its intended use. Extensions are available that allow for the controlling of time, management of non-player characters, use of mathematical equations, manipulation of typography and layout, inclusion of multimedia, and the integration of physics to name a few.

Of all the extensions available to authors, the ability to include multimedia was the one that was most important to this project. It is recommended that the Vorple extension[10] developed by Juhana Leinonen, be leveraged as a

means of adding depth to ICONS. Vorple allows authors to go beyond the Z-virtual machine to allow the Inform source code to communicate with the web browser where the story is being executed. Through the use of a virtual file system, Vorple allows for the execution of JavaScript, the use of hyperlinks, the inclusion of images and sounds, modification of the notification and scoring system, and control of the command prompt. This allows for the inclusion of existing NASA web-based resources within ICONS, as well as the inclusion of other resources such as, but not limited to, embeddable videos and web pages.

Using the Twine design document as a guide, the development of the ICONS should be straightforward. It is also recommended that someone with a literary background be included in the development team to assist with the fleshing out of the various narratives/storylines. This will to make it more likely that the ICONS being developed is not only technically correct, but that it is also an engaging piece of IF.

3. Evaluate and Implement the ICONS

Once ICONS have been developed, it is imperative that it be evaluated. The first evaluations should focus on ascertaining if the ICONS is engaging and immersive, and to identify any bugs or glitches in the story/text game. This evaluation should be conducted by a small group (5-7) of stakeholders and people who are familiar with project. It is recommended that focus groups and/or talk-a-louds where the reader/player goes through the ICONS with a member of the development team present and provides on the spot evaluation of the story. ICONS developers should remain in this phase and make iterative refinements to the source code until the majority of issues have been addressed. Once the first phase of evaluation is completed, the ICONS should be released to the entire group of stakeholders. This evaluation phase should focus on making sure that the ICONS is technically correct and properly meets a pre-established criteria for simulating a scenario, system, procedure, or mission. Once again, iterative refinements informed by the feedback received from the larger body of stakeholders should be taking place during this phase of evaluation. Once stakeholders have signed off on the ICONS as being engaging, immersive, technically sound, and in fidelity to the intended system, scenario, and/or mission it represents, the development team is now free to release the ICONS for open use. It is recommended that at this point the development team seek feedback from those outside the stakeholder community in order to acquire additional insights into the effectiveness of the ICONS and to improve their skills in designing and developing future ICONS.

Heart Experiment International Space Station ICONS

In order to validate the aforementioned design process, a proof-of-concept ICONS was developed. This ICONS was developed using the procedures from an experiment that was performed on the ISS. The focus of this study, entitled Effects of Microgravity of Stem Cell-Derived Heart Cells (Heart Cells), was to supplement our "understanding of microgravity on heart function, the improvement of heart disease modeling capabilities, and the development of appropriate methods for cell therapy for people with heart disease on Earth"[11]. It was beyond the scope of this project to develop an ICONS for this entire study, so only one phase of the study, Heart Cells Multiwell BioCell Insert into Microscope, was used to create an ICONS.

Twine was used to design this ICONS using a combination of the Confirmation-Choice, Track Switching, and Gauntlet design patterns. At various points throughout the narrative readers/players were provided with the ability to make choices that would end the story or continue moving them along. For example, once the BioCell has been removed from its habitat, it must be allowed to cool for twenty minutes before proceeding. If the player does not wait for the allotted time frame before proceeding, the game will end and provide text identifying the mistake and how that decision negatively impacted the experiment. Figure 10 provides a portion of the ICONS designed using Twine.

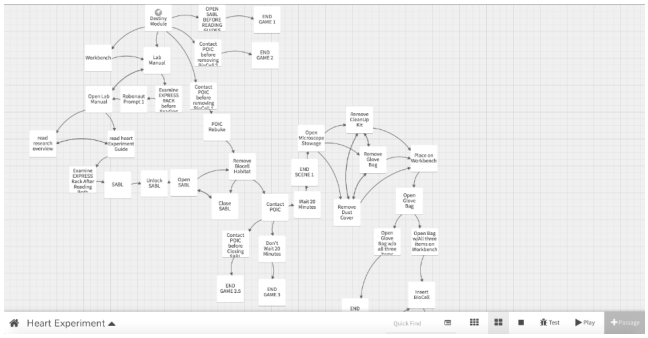

Figure 10. Twine Heart Cell Design.

Using the ICONS designed in Twine as a guide, the ICONS was fully developed within Inform 7. The suite of Vorple extensions were included within the ICONS to enhance the overall presentation and as an attempt to increase the fidelity of the procedure being simulated to the actually experiment taking place on the ISS. Images of various steps of the procedure were included along with images of the ISS, and a scoring system that added or subtracted points based on the decisions that the reader/players makes.

Figure 11. Heart Cell ICONS Proof-of-Concept using Inform 7.

D. K-12 Application of ICONS

Due to a series of reorganizations and subsequent schedule demands placed upon the teams that provided the Heart Cell experiment procedures, evaluation of the proof-of-concept ICONS was left to the discretion of the development team. This serendipitous turn of events enabled the project team to focus their attention on exploring, designing, and developing potential K-12 application of ICONS within the domain of mathematics. In order to properly scope the work, it was decided to focus on word problems. This idea of leveraging ICONS to assist in the creation of interactive narrative word problems for mathematics education is supported by empirical research. Gunbas[12] conducted a study found that found students who were asked to solve mathematics word problems which were embedded within the narrative of a computer-based story, significantly outperformed students who were asked to solve the same problems within a paper-based story or in the text based word problem format typically found in mathematics textbooks and assessments.

Using the design process described earlier, several small-scale text games were created to demonstrate the applicability of ICONS to the design and development of narrative based mathematics word problems. For example, an interactive word problem was created in which a reader/player entered a room in which they found a safe. Within the safe was a key that was needed to open another door within the game. In order to find the six-digit combination to the safe, the player had to find the area and circumference of three circles (rounded to the nearest whole number) that were located within the room. Another scenario had the reader/player in possession of two dice and a notebook. The reader/player was provided with instructions to roll the dice and record the sum of the resulting dice roll in their notebook. This information would then later be used to ascertain the probability of getting a particular sum on a roll of two die. The finally scenario had players sitting at a table with a deck of cards on their left hand side and a discard container on their right. The reader/player could only have four cards in their hand at a particular time. The goal of the game was to collect four of a kind, with the reader/player being allowed to discard of any card in their hand, but not be allowed to pick that card up again. The collecting and discarding of cards continued until the player had exhausted all the cards in the deck or until they had four of a kind in their possession. The challenge was that the cards were not typical playing cards, but had various representations of ratios (fraction, decimal, percent) on them.

IV. Potential Follow-On Activities

The ICONS project developed as a result of this MSFC Summer 2017 Faculty Fellowship is not intended to be a one off. Instead the time spent working on ICONS is intended to serve as the foundation for the transformation of the manner in which ConOps are designed and developed. While writing this report, the author participated in a scenario based planning meeting conducted within the MSFC Office of Strategy. Scenario planning, defined as “a

disciplined method for imagining possible futures that companies have applied to a great range of issues"[13], is a tool used by those within the strategic planning community to help avoid the two most common errors committed when conducting strategic planning – overconfidence and tunnel vision.

When creating scenarios for strategic planning, it is recommended that each scenario contain the following building blocks[13]:

1. Drivers of change: enable identification of trends and uncertainties
2. Rules of interaction: Define the relationships among trends and uncertainties and enable the development of multiple scenarios.

In addition to the building blocks of scenarios necessary for strategic planning, it is also recommended that a framework be used to develop scenarios where two uncertainties are used as vertical and horizontal axes. The resulting four quadrants of uncertainty can then be used for narrative development[14]. Using these building blocks and scenario framework, it is not difficult to imagine the tools and processes used to design and develop the proof-of-concept ICONS being used in the development of scenario for strategic planning. Twine and Inform 7 could be used to create an ICONS that represents each of the four quadrants. To further illustrate this, let us use the two biggest uncertainties facing NASA or any enterprise of this size: supply and demand. By placing the supply and demand in terms of NASA's budget and compelling missions on two axes, one could create these four quadrants:

1. Bold budget and compelling mission
2. Shy budget and compelling mission
3. Bold budget and languid mission
4. Shy budge and languid mission:

In the first quadrant, the scenario could focus on the developing and deploying of space and planetary infrastructure without partners. A scenario representative of the second quadrant could be where space infrastructure delivery services are offered in order to encourage partnership development. The third quadrant could have a strategy where delivery services, propulsion systems, and operations infrastructure are offered. The fourth quadrant could have a scenario where the focus is entirely on fostering industry and governmental partnerships, and the offering of technologies.

Using Twine to design a scenario will require strategic developers to avoid overconfidence and tunnel vision by forcing time to be spent thinking about trends and uncertainties that may arise within a given scenario. Twine could be used to create branching decision trees for each scenario, with the scenario framework being at the top level, space markets at the mid-level, and vignettes related to categories of products and services at the lower level. This branching tree would then be used to guide the development of specific scenarios within Inform 7 to describe a market as a room within the world, services as scenes, and products as objects.

Twine could also be used in to capture the results of strategy development sessions. For example, a strategy development session could be conducted where participants are divided into four groups and assigned one of four quadrants created from two axes of uncertainty. Each group would be tasked with using Twine (after a brief tutorial) to collectively create as many scenarios related to their assigned quadrant as possible within the allotted timeframe. The scenarios created during this strategic planning session could then be used to guide the development of an ICONS using Inform 7.

The work from the ICONS project can also be used to inform further research into the impact of interactive computer-based mathematics word problems. The scenarios developed during the summer could be further developed and used in empirical investigations into the viability of this approach to designing word problems. It might be that IF presents a novel means of designing and developing the next generation of formative and summative assessment for students by leveraging the theoretical benefits of anchored instruction.

The ICONS development process could also be used to create scenarios that connect the mathematics students learn in school to their practical application within common NASA systems. For instance, the Environmental Control and Life Support Systems (ECLSS) needed for space exploration have to be designed to support those manning the controls of space vehicles. These systems are responsible for maintaining oxygen levels and atmospheric pressure. Additionally, ECLSS is responsible for purifying the water astronauts need to survive, and manage the waste they generate. Finally, in the unfortunate event of a fire, ECLSS is responsible for providing fire detection and suppression. Using the ISS as a context for an ICONS and a failure in the ECLSS system as the compelling problem, one could craft a narrative where students are asked to solve problems that require them to apply their knowledge of algebra, physics, chemistry, and other STEM subjects.

Future projects could benefit from ICONS by simulating the usage of the system within the context of an ecosystem or market. Center Director Todd May outlined a strategy that includes enabling new markets through space exploration beyond Low Earth Orbit and focusing on Design, Development, Test, and Evaluation. Strategic scenario analysis could identify systems and vignettes to be implemented as ICONS. Through these ICONS,

strategic analyst could simulate operations of future space infrastructure that enables future markets beyond Low Earth Orbit. Success in this endeavor will allow for the creation of the markets needed to support exploration of our galaxy and beyond. This will require going beyond traditional methodology for strategic planning to design and development processes that will facilitate the development of the next generation of ConOps. The work reported on in this paper provides a potential avenue for accomplishing this through the use of ICONS.

Acknowledgments

Andre R. Denham thanks Christopher Randall, Daniel O'Neil, the MSFC Office of Strategic Analysis and Communication, the MSFC Office of the Chief Technologist, the MSFC Office of Human Exploration and Development, and the Education Office of MSFC for the opportunity to participate in the 2017 MSFC Summer Faculty Fellowship Program.

References

[1]"Data Requirements Description: STD/SE-CONOPS" *Marshall Integrated Document Library* [online repository], URL: https://masterlist.msfc.nasa.gov/drm/drd_docs/SE-CONOPS.pdf [cited 1 August 2017].

[2]Schilit, B. N., Golovchinsky, G., and Price, M. N., "Beyond paper: supporting active reading with free form digital ink annotations," *SIGCHI conference on Human factors in computing systems*, 1998, pp. 249-256.

[3]Victor, B., "Explorable Explanations" *Worry Dream* [Blog posting], URL: http://worrydream.com/#!/ExplorableExplanations [cited 1 August 2017].

[4]Niesz, A. J., & Holland, N. N., "Interactive fiction," *Critical Inquiry*, Vol. 11, No. 1, 1984, pp. 110, 129.

[5]"Inform 7" [website], URL: https://en.wikipedia.org/wiki/Inform [cited 1 August 2017].

[6]"Preface", *Inform 7 Recipe Book,* [website], URL: http://inform7.com/learn/man/RB_1_1.html [cited 1 August 2017].

[7]"Twine", [website], URL: http://twinery.org [cited 1 August 2017].

[8]Ashwell, S. K., "Standard Patterns in Choice Based Games" *These Heterogeneous Tasks* [Blog posting], URL: https://heterogenoustasks.wordpress.com/2015/01/26/standard-patterns-in-choice-based-games/ [cited 1 August 2017].

[9]Short, E., "Small Scale Structures in CYOA" *Emily Short's Interactive Storytelling* [Blog posting], URL: https://emshort.blog/2016/11/05/small-scale-structures-in-cyoa/ [cited 1 August 2017].

[10]"Inform 7 Interactive Fiction with Vorple", [website], URL: http://vorple-if.com/doc/ [cited 1 August 2017].

[11]"Effects of Microgravity on Stem Cell-Derived Heart Cells (Heart Cells) – 07.12.17", [website], URL: https://www.nasa.gov/mission_pages/station/research/experiments/1914.html [cited 1 August 2017].

[12]Gunbas, N., "Students' mathematics word problem-solving achievement in a computer-based story", *Journal of Computer Assisted Learning*, Vol. 31, No. 1, 2015, pp. 78, 95.

[13]Schoemaker, P. J., "Scenario planning: a tool for strategic thinking", *Sloan Management Review*, Vol. 36, No. 2, 1995, pp. 25, 40.

[14]Garvin, D. A., & Levesque, L. "A note on scenario planning," HBS Case Collection, Harvard University, Cambridge, Massachusetts, 2005 (unpublished).

Opportunities for Improving the Delivery and Utility of the Advanced Concepts Office's Products

David C. Gross, PhD[1]
The University of Arizona, Tucson, AZ, 85721, USA

Mark N. Rogers,.[2] and Rachel J. Mccauley[3]
NASA Marshall Space Flight Center, Huntsville, AL, Zip 35812, USA

The Advanced Concepts Office supports the development and maturation of alternate and innovative concepts for subsystems, spacecraft systems, payloads, and transportation systems. The organization performs complete and integrated systems analyses and independent assessments of potential concepts. It also performs technology assessments and subsystem trades for current projects and lead or support the creation of new projects and their initiatives. Advanced Concepts generally does this work in response to requests for support from customer organizations. Therefore, it experiences an especially focused version of the challenge facing all organizations working to drive innovation: to communicate (and in a sense sell) its innovations to a customer which is intelligent and motivated but who does not (yet) share the understanding developed by the innovator. This study examines the state of communication between ACO and its customers, and makes specific recommendations toward improving that communication that fall into three major classes: increase ACO-customer interaction, broaden basis of communication, and increase ACO credibility.

Tech excellence funding for core but most funding for projects. Has ability to refuse tech concurrence

Nomenclature

ACO	=	Advanced Concepts Organization, i.e. ED04 at Marshall Space Flight Center
ED	=	Engineering Directorate at Marshall Space Flight Center
MSFC	=	Marshall Space Flight Center
NASA	=	National Aeronautics and Space Administration
SLS	=	Space Launch System

I. Introduction

The Advanced Concept Office (ACO) analyzes mission and spacecraft concepts for NASA and as such is a key driver for innovation. Previous ACO studies have examined the technical expertise, tools, and techniques that ACO brings to be bear on its product and have made various recommendations that the organization is pursuing appropriately. This study differs in that the focus is not and ACO and its related technologies but on the interaction between ACO and its customer community. As is the case for many organizations working within a larger enterprise, as ACO is within NASA, the customer feedback mechanisms present in a typical consumer market are not present. In a typical consumer market, sellers receive feedback by observing the customer's decisions about with whom, where, how, and why to do business, and those decisions are unrestrained. In contrast, ACO's customer's decisions are effected by organizational structure, expected and/or established practice and many other considerations. Therefore ACO must seek out customer feedback and interpret it to understand how to improve the benefit their customers receive. As ACO experiences very large pressures from a number of other sources such as the ever-present march of technology, pressures on discretionary expenditures in the federal budget such as NASA, and the demands of

[1] Assistant Professor, Room 129, Engineering Building, University of Arizona, davidcgross@email.arizona.edu
[2] Manager, Advanced Concepts, ED04, and Marshall Space Flight Center
[3] Deputy Manager, Advanced Concepts, ED04, and Marshall Space Flight Center

customers competing for ACO's attention, it would be easy to assume all is well and neglect this. Instead, ACO management proactively leveraged the MSFC's faculty fellowship program to initiative this study with the following objective.

> *Evaluate current engineering product deliverable process for all ACO customers (such as Space Launch System Systems Engineering and Integration, SLS Spacecraft and Payload Integration/Evolution Office, Science & Technology, Engineering Directorate, and other NASA offices). Research optimized changes or improvements and develop a report with recommendations and comparison of industry process.*

The present report is the result of this study.

II. Methodology

ACO is an organization seeking innovation, and seeking to help their customers innovate. Terrill (Ref. 1) shows that such organization face clear impediments to innovation such as:

1) Engineering Culture
2) Risk Identification and Mitigation
3) Compartmentalization
4) Predicting the Future from Extrapolating the Past

Engineering culture is oriented toward "finding the fault", in fact; engineering works best in organizations that manage to set aside fault finding as personal attacks, but instead work in open and trusting collaborate to lay all such bear for correction. This is a difficult proposition, requiring a great deal of faith in one's teammates. One approach for developing this culture is to create openness *within* the team but to restrict it sharply *outside* of the team. While this may create a safe environment within the team, it necessarily reduces communication and interaction with "others' including customers. ACO engineering culture us more open than many because it is independent from spacecraft or mission initiatives – it does not have a need to "defend" any concept. On the other hand, the pressure to decrease the cost and schedule required for its products while simultaneously increasing accuracy and detail naturally causes teams and individuals to go "head down" (i.e., reduce openness) in order to get the job done.

Risk identification and mitigation typically focuses on negative impacts; indeed many risk assessment procedures assess risk simply as a product of magnitude of negative impact (severity) and likelihood of occurrence. Even risk procedures that include opportunity or possible advantage rarely result in the expression of such. Ironically, to identify an opportunity is to increase risk (we could be wrong, we could end up with more work but no more budget, etc.). The pressures on ACO regarding cost, schedule, and quality lead to a natural foreclosing of consideration of opportunity as a way to get the job done.

Compartmentalization or stove piping, is prevalent in industry including aerospace. Immediate needs tend to drive advocacy of particular innovations as opposed to potential generalized benefits. ACO's diverse technological workforce and capability enable it to avoid this impediment but its focus on being responsive to the immediate customer request, compelled by the aforementioned pressures, work against its advocacy of more general innovation. ACO adopted its diverse character to fulfill its charter to analyze mission and/or space *operational* concepts. While broad, this creates an organizational separation of ACO from equally important considerations of producability/manufacturability such as facility capabilities/planned enhancements, production costs, production schedules, etc.

Despite the common disclaimer "past performance is no predictor of future gain", extrapolation from past performance is precisely what most organizations do and is an obvious and significant impediment to any innovation. How does one propose adopting of an unprecedented concept, as it will be evaluated by the experience developed in precedent concepts? In addition to potentially frustrating efforts by ACO to propose innovation outside of the organization, this is potentially a hidden limitation within ACO: often analyses tools include poorly expressed and understood assumptions and ground rules which limit assessment of an innovation's full potential benefit (or cost).

Chutivongse and Gerdsri. (Ref. 2) propose steps to becoming an innovative organization, which relies on developing and executing an organizational strategy addressing the following:

1) Organizational structure
2) Organizational climate
3) Knowledge management
4) Human resource management
5) Leadership style
6) Strategic alliances

Since the time allocated for the present study did not permit the development of a complete strategy, the study focused on developing a baseline understanding of ACO along these the dimensions, to serve as a foundation for creating such a strategy. The present study adopted the following tools to gather raw data about ACO products and delivery:

1) Structured survey of ACO staff
2) Structured interviews of selected ACO staff
3) Structure survey of ACO customers
4) Structured interviews of selected ACO customers
5) Structured survey of similar organizations for benchmarking best practices

A. Survey Design

The survey design in this study conformed to the general approach and guidelines discussed in Saris and Gallhofer (Ref. 3).

The purpose of the surveys was to explore here-to-fore unexpressed ideas for improving the delivery and utility of the ACO's products in the survey target audience. None of the surveys had sufficient sample size for statistical significance; therefore, the results are not reliable indicators of a consensus of the community nor are they sound directives for management action in themselves. Instead, the study combines observations drawn from the results with engineering judgement to recommend next steps ACO may take to further understand the current state of its product delivery process and improve it.

The surveys consisted of twenty (20) prompts designed for respondents to complete in less than one half hour of labor time in order to maximize the number of complete responses. The survey design was to present a quantitative prompt followed by a qualitative prompt. The quantitative prompts provided both a numerical result for analysis and "seeded" the responder's mind for the subsequent qualitative question. Each prompt required a response to complete the survey. This report shows *generalized* prompts, meaning they use fully elaborated names and terms. The prompts actually in the surveys were edited for reading comfort into versions specific to the survey audience, e.g., in the survey of ACO staff, "ACO" was replaced with "our" or "we". Both surveys used equivalent prompts aimed at soliciting different perspectives of each audience except where the discussion of results noted otherwise.

The quantitative prompts typically required responses on a five (5) point Likert scale such as [NEVER | RARELY | SOMETIMES | USUALLY| ALWAYS].[4] The quantitative prompts as presented to respondents mixed the order of the responses, i.e., sometimes the highest value answer appeared first and sometimes last, in order to improve quality of responses (avoiding ill-considered responses of "always check the same box"). The surveys also employed quantitative prompts for ranking.

The discussion of each quantitative prompt in this report begins by referencing a figure showing a box-and-whisker plot summarizing the responses from the ACO Staff and the ACO Customers whose title is the generalized prompt being considered. Figure 1 shows the interpretation of the box-and-whisker plot.[5] The generalized prompts show the highest value Likert scale value available for this question in brackets with a question mark as [always?], whereas the actual survey prompts showed all possible responses and required the respondent to select one. The discussion and figure convert all quantitative results such that high numerical scores are the preferred response (except one prompt as noted in the discussion). The quantitative prompts discussion proceeds to draw observations from:

1) the quantitative results from the prompt under consideration and
2) information developed prior to the prompt in this report.

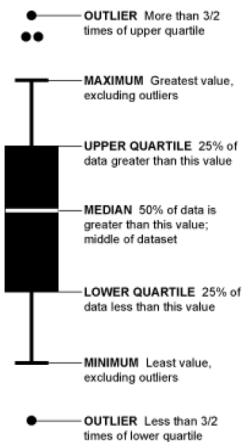

Figure 1. Standard Box-and-Whisker Plot

In contrast to the quantitative prompts, the survey design formed qualitative prompts as fill-in-the-blank expression. The discussion of each qualitative prompt in this report begins by referencing a table whose title is the generalized prompt under consideration and whose contents are the most significant responses received. The quantitative prompt discussion proceeds to draw observations from:

1) the responses to the quantitative prompt under consideration and
2) notes from the related interviews (discussed below).

A. Interviews

The purpose of the interviews was to develop and mature the ideas emerging from the surveys with "thought leaders" in the ACO staff and customer base. The study interviewed such thought leaders, or "high information potential" individuals because they are

1) identifiable in several different kinds of organizations;
2) distinctive information transceivers (transmitter and receiver);
3) both a producer and a catalyst in his/her own organization; and
4) extenders and an amplifiers of information search.[6]

The ACO manager and deputy selected the individuals for interviews. The interview procedure was to present the extend survey responses to and engage the interviewee in a free flowing discussion. The interviewer made no attempt to restrict topics of discussion but did point out selected survey results to stimulate discussion. As in the survey, the interviews promised anonymity to interviewees to encourage open and complete responses.

III. Results

A. ACO Staff and Customer Surveys

Figure 2 summarizes the responses to **Prompt 1** "ACO's products are [always?] what the customer **wants**." Unsurprisingly, the results indicate that both the staff and customers feel ACO products are usually what the customer needed. Note however that the customer is somewhat less sanguine about this issue than the staff. This preliminary indication is repeated in subsequent questions.

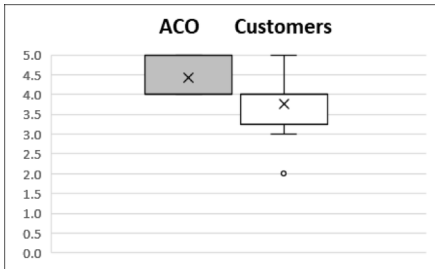

Figure 2. Results from Prompt 1 ***"ACO's products are [always?] what the customer wants."***

The most significant responses to **Prompt 2** "Customers **value** ACO's products because _____."

1) From the ACO Staff were:
   a. they are timely and informative
   b. [they are] rigorous technical work, presented in a concise and cogent format.
   c. we take their concept and take the first step towards making it a reality
2) from the ACO Customers were:
   a. They allow us to answer the what-if questions....
   b. They provide critical "first look" data to make informed decisions
   c. They provide technical excellence in the timeframe my project needs their products
   d. Timely, appropriate level of detail & cost effective

Figure 3 summarizes the responses to **Prompt 3** "ACO's products are [always?] what the customers **need**." Similar to the prompts about wants and value both the ACO Staff and Customer communities indicate similar contentment while the Customers' score is somewhat lower than the Staff's.

The most significant responses to **Prompt 4** "Customers **use** ACO's products to _____."

1) From the ACO Staff were:
   a. propose new missions and technology development
   b. communicate and work w/ other NASA centers
   c. support proposals, program plans or management reviews
   d. determine the feasibility of specific systems, investigate the sensitivities of design trades, and perform long-term strategic and alignment analyses
2) From the ACO Customers were:
   a. support discussions with decision makers regarding strategic decisions
   b. make technical decisions that affect strategic capabilities
   c. market, make informed decisions, scope and prioritize activities.

Figure 3. Results from Prompt 3 ***"ACO's products are [always?] what the customers need."***

Figure 4 summarizes the responses to **Prompt 5** "The customers are [extremely satisfied?] with ACO's products." Similar to the previous quantitative prompts both the ACO Staff and Customer communities indicate similar satisfaction while the Customers' score is somewhat lower than the Staff's.

The most significant responses to **Prompt 6** "ACO could improve the **value** of its product for the customer by _____."

1) From the ACO Staff were:
    a. showing how the results align with NASA and MSFC objectives
    b. anticipating the customers' needs
    c. better assessing the uncertainty of our analysis, and including cost
    d. increasing turnaround times in order to provide more technical depth
    e. improving rapid response (quick turn-around) capability
    f. improving graphics and animation capabilities
    g. constantly being cognizant of what the customer will need in the future and develop the analytical capability to provide that information
    h. learning more about what to do after a concept study to turn a concept into reality.
2) From the ACO Customers were:
    a. "Telling the Story" better
    b. better working integration with larger engineering
    c. explaining the key driving functions or requirements of a system versus point designs
    d. initiating studies and inserting their technical knowledge

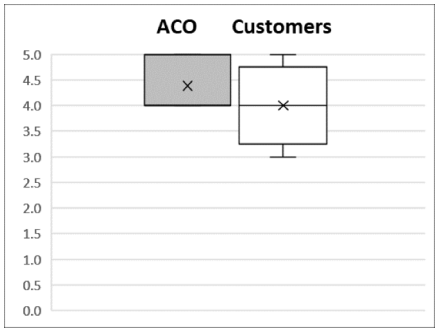

Figure 4. Results from Prompt 5 "*The customers are [extremely satisfied?] with ACO's products.*"

Figure 5 summarizes the responses to **Prompt 7** "The customers find ACO's products [very easy?] to **understand**." The responses to this prompt how there is some concern within the ACO Staff regarding understandability of their product, which tends to support the need for the present study. The responses from the ACO Customers reflects similar concerns.

Prompt 8 differed from the other qualitative prompts in that instead of asking both the staff and the customers the same question, it asked inverse questions.

Prompt 8 for the staff was: "The most likely product or aspect of our product that the **customer** might misunderstand/misinterpret/misapply and why is _____." and the most significant staff responses were:

1) extrapolating the results to new applications without understanding the ranges/conditions of validity
2) interpreting a conceptual design as a final solution and not accounting for the quick turnaround aspect of the product.
3) trade study options, sensitivity study results, technology roadmaps
4) the background and validation of our toolset
5) relationships between point design vehicle performance, because assumptions not normally presented may skew results beyond that which is immediately apparent
6) Results are very dependent on ground rules and assumptions. Customers are likely to compare our products to other products where these have changed.
7) the chart package. It's difficult to encapsulate everything done in a study in a single set of charts.

Figure 51 Results from Prompt 7: *"The customers find ACO's products [very easy?] to understand."*

Prompt 8 **for the ACO Customer was "**The most likely aspect of the Customer's need/problem/issue that **ACO** might misunderstand/misinterpret/misapply and why is _____." And the most significant customer responses were:

1) that most of their products flow into requirements of a system, not a point design
2) there are a wide range of products / fidelity possible from ACO, and constant communication between the customer's concerns and priority may not be a "standard" product.
3) the science of the mission, which may help refine the product ACO provides

Figure 6 summarizes the responses to **Prompt 9** "ACO is [very familiar?] with **how** the Customers use their products.**"** For the first time, the responses show substantially less contentment within the CO Staff than within the Customers. One interpretation of this is that the Customers are interacting with ACO senior staff, who presumably

are more familiar with how the Customer uses their product but the ACO staff includes junior members who are less familiar. In any case, this leads to the observation there is room for improving the ACO's familiarity with the Customer's use of ACO products.

The most significant responses to **Prompt 10** "ACO could do better if they **knew** _____ about Customers needs/problems/issues."

1) From the ACO Staff were:
    a. more about the customer's and the concept's background
    b. the intended usage
    c. customer objectives, program (political) constraints
    d. more about their long range goals and organizational capabilities
2) From the ACO Customers were:
    a. the programmatic nature of our decisions
    b. [that we] include ACO in my publications & presentations

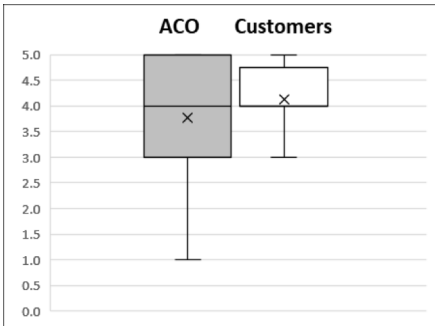

Figure 6. Results from Prompt 9 ***"ACO is [very familiar?] with how the Customers use their products."***

Prompt 10 also exposed the extent to which the "customer of the ACO customer" or derived customer matters. Figure 7 summarizes the responses to **Prompt 11** "ACO's product value is [much greater?] than products from **other NASA** organizations with similar roles.**"** While ACO's role is not precisely duplicated by any other organization in NASA, and while ACO does not seek to expand its charter to encompass work currently chartered to other organizations, there are some doing similar kinds of work, i.e., concept analysis. The results here indicate that ACO's Customers may see less value in the current form of ACO products than those of similar organizations and this leads to a recommendation to benchmark ACO processes against other similar organizations.

The most significant responses to **Prompt 12** "**NASA organizations** with **similar roles** to ACO include _____." were:

1) MSFC
    a. EV40
    b. EV70
    c. EV74
    d. ST24
2) Ames Research Center Mission Design Center
3) Glenn Research Center Collaborative Modeling for Parametric Assessment of Space Systems (COMPASS)
4) Goddard Space Flight Center Mission Design Lab/Integrated Design Lab
5) Jet Propulsion Lab Team-X
6) Johnson Space Center
    a. Future Capabilities Team
    b. Mars Study Capabilities
7) Langley Research Center Advanced Concepts Lab

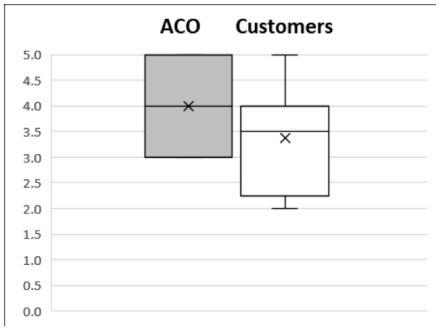

Figure 7: Results from Prompt 11 ***"ACO's product value is [much greater?] than products from other NASA organizations with similar roles."***

Figure 8 summarizes the responses to **Prompt 13:** "ACO's product value is [much greater?] than products from other organizations **outside of NASA** with similar roles." The results here are similar to those for Prompt 11 (regarding organizations within NASA): The results here indicate that ACO's Customers may see less value in the current form of ACO products than those of similar organizations and this leads to a recommendation to benchmark ACO processes against other similar organizations.

The most significant responses to **Prompt 14 "**Organizations **outside of NASA** with similar roles to Advanced Concepts include _____." were:

1) European Space Agency Concurrent Design Facility
2) Johns Hopkins Applied Physics Laboratory
3) Lockheed Skunkworks
4) SpaceX
5) United Launch Alliance Advanced Programs

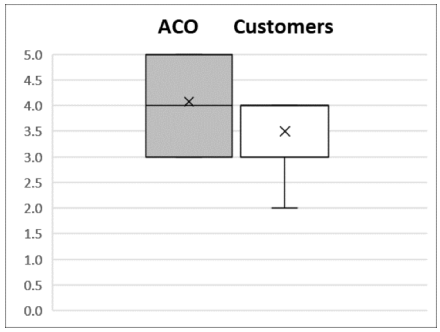

Figure 8. Results from Prompt 13: ***"ACO's product value is [much greater?] than products from other organizations outside of NASA with similar roles."***

6) Virgin Galactic
7) US Army Yuma Proving Grounds
8) Kaiser Permanente Strategic Planning
9) Orbital-ATK
   a. Ballistics
   b. Propulsion
10) Aerojet-Rocketdyne Advanced Concepts

Figure 9 summarizes the responses to **Prompt 15** "ACO's **independent strategic judgement** is [extremely important?] to NASA." The results show an equal perception of the importance of ACO's independent strategic judgement to NASA between the staff and customers, although the level is lower than desired.

As was the case for Prompt 8, **Prompt 16** was different for the staff and customers. Prompt 16 for the staff was "ACO could increase **ACO's** importance to NASA Senior Leadership by _____." and the most significant staff responses were:

1) helping them better understand what we do and why it is important
2) including cost estimation in our analysis
3) more technical depth on the civil servant side
4) Aligning with Center priorities, improving rapid response capability
5) providing more and higher fidelity analyses in the same timeframe
6) Continuing to exceed their expectations and provide valuable design products for their use
7) providing more direct input to NASA Headquarters organizations utilizing improved graphics capabilities
8) being in front of them more often

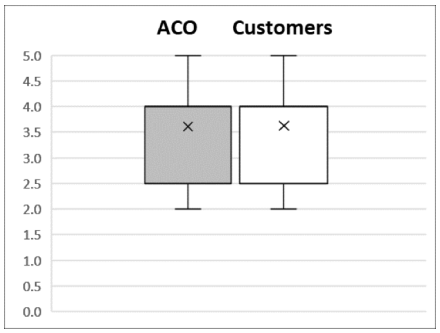

Figure 9. Results from Prompt 15 ***"ACO's independent strategic judgement is [extremely important?] to NASA."***

Prompt 16 for the customers was "ACO could increase the **Customer's** organization's importance to NASA by _____." and the most significant responses were:

1) providing the "so what" factor to its products
2) identifying systems/concepts with high return on investment towards NASA's overall agency objectives

Figure 10 summarizes the responses to **Prompt 17 "Rank according to value to the Customers of each aspect of ACO's work."** The survey did not ask ACO staff to rank the value of their own experience and expertise. The results suggest both the staff and customer place a high value on assessment of concept and trade study of alternatives, which of course are typically the originating reason for a customer to request ACO's support. The results indicate Customers place a great emphasis on the integrated nature of ACO's assessments, which may be a result of individual staff members not directly creating such integration. The results indicate a lower value for the independence of assessment, which one hopes is more of an indicator that they take such independence for granted rather than a true assignment of value.

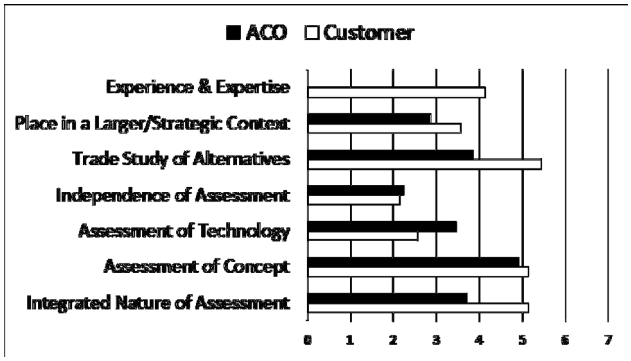

Figure 10. Results from Prompt 17 ***"Rank according to value to the Customers of each aspect of ACO's work."***

Figure 11 summarizes the responses to **Prompt 18 "Rank according to opportunity for improvement each aspect of ACO's work."** The survey did not ask ACO staff to rank the opportunity for improving their own experience and expertise. These results show the Customers believe the best opportunities for improvement is to place ACO's assessments in a larger context and to improve the integrated nature of the assessment. The follow up interviews indicate that "integrated" here may be beyond ACO's current charter, which focuses on assessment operational concepts to integration with detailed design, manufacturing, etc.

Figure 12 summarizes the responses to **Prompt 19 "ACO's balance between being responsive to the Customer's immediate request vs. placing in the larger context of Marshall's strategic vectors is [about even?]."** This is the single quantitative prompt mentioned earlier that has not been converted such that the highest value is the preferred outcome. The preferred outcome here is "3", or "about even" per ACO's organizational goals. The full Likert scale used in this prompt was:

1) Very skewed toward immediate request
2) Somewhat skewed toward immediate request
3) About even
4) Somewhat skewed toward larger context
5) Very skewed toward larger context

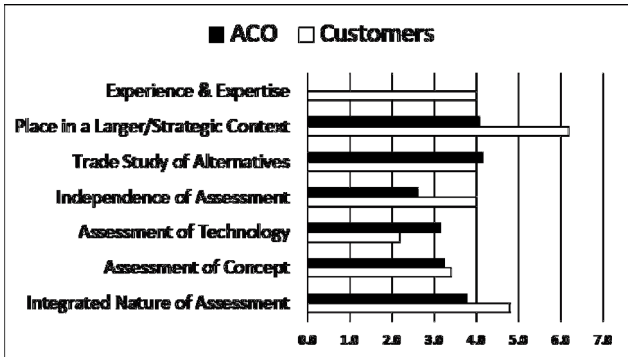

Figure 11. Results from Prompt 18 ***"Rank according to opportunity for improvement each aspect of ACO's***

Figure 12 therefore indicates the ACO staff believes the current products are somewhat skewed toward the immediate customer request whereas the customer perceives more balance.

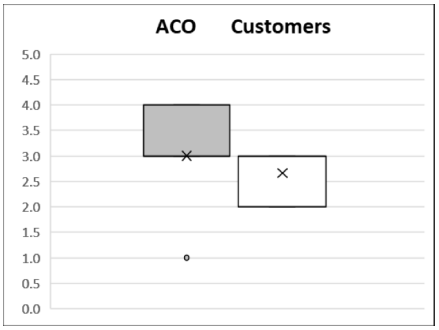

Figure 12. Results from Prompt 19 ***"ACO's balance between being responsive to the Customer's immediate request vs. placing in the larger context of Marshall's strategic vectors is [about***

The most significant responses to **Prompt 20** "Advanced Concepts should improve the **applicability/relevance** of its products by _____."

1) From the ACO Staff were:
    a. better documentation of trades; making products easier to understand; more thorough notes to accompany chart sets
    b. more comprehensive publishing of study results.
    c. increasing the amount of data and making the product interactive
    d. Focusing on the larger context of the product as well
    e. Improving graphic and documentation capabilities, and improving historical databases
    f. enhancing the visualization of results and providing the customer a simplified means to explore complex results with many interdepencies
    g. automate chart design so that content can be made uniform
    h. Present more work at higher levels of management at the center and agency
2) From the ACO Customers were:
    a. integration with full scale development engineering
    b. providing the bigger picture insight into Center goals and objectives
    c. focusing on external needs/gaps of the agencies mission directorates with guidance rather than ED driven priorities.

B. Benchmarking

Benchmarking involves "comparing actual or planned practices, such as processes and operations, to those of comparable organizations to identify best practices, generate ideas for improvement" and it provides "a basis for measuring performance".[7] Since ACO's charter is to conduct analysis of mission and spacecraft concepts that arise within the context of a federal agency (NASA) and such concepts may eventually lead to federal acquisitions, there are other organizations conducting similar kinds of concept analysis. The ACO Staff and Customer surveys suggested several such organizations. Furthermore, there are a number of organizations conducting such work which face the core challenge posed for investigation by this study, namely to communicate (and in a sense sell) its innovations to a customer which is intelligent and motivated but who does not (yet) share the understanding developed via the work of seeking innovation.

Therefore, the study included a design and deployment of a survey for organizations against which ACO might benchmark its practices. Just as in the ACO Staff and Customer surveys the purpose of the survey was to gather baseline information to enable a complete benchmarking at a later date. Regretfully, the time allocated for this study did not permit extensive responses to this third survey so the present report does not discuss its findings in detail.

However, the very preliminary responses received to date do suggest the value of ACO pursing a full benchmarking and some opportunities for improving product delivery.

For example, responses to the Benchmarking survey prompt "We are currently **improving** the value of our product by _____ (describe quality improvement initiative if any)." included:

1) Strategically aligning with the goals of our organization and continually working towards more of a process-improvement mindset.
2) Performing Fish Bone and Why Analysis as well as other methodologies in an effort to improve product performance, reliability, and survivability.

Further, responses to the Benchmarking survey prompt "Our product typically **includes** (check all that apply)" shows active inclusion of product elements beyond ACO's current product baseline such as interactive immerse visualization and integration of operational, engineering, manufacturing, and cost assessments.

C. Recommendations

The study makes the following recommendations based on the results of the literature review regarding product delivery by innovative organization, surveys of the ACO Staff, Customer, & Benchmarking Organizations, and personal interviews. The preceding discussion in this report has summarizes those results; space limitations do not permit full presentation of all results, nor does space permit full elaboration of each recommendation.

The study recommends that:

1) ACO should proactively work to increase ACO-customer interaction by:
    a. Addressing formally in each study sensitivities to customer inputs of objectives, ground rules, assumptions, and concepts
    b. Deploying a standard procedure for describing customer context (objectives, assumptions, ground rules, limitations, criteria by which solution will be judged …)
    c. Interacting with study customers outside the context of a specific study such as attending each other's staff or brainstorming meetings
    d. Building relationships with derived customers, i.e., customers of ACO's customers
        i. Partnering with direct customers to meet/understand/serve derived customers
        ii. Soliciting feedback from derived customers
    e. Recognizing MSFC and NASA leadership as customers as well as the immediate study requesters
        i. Enhancing senior leadership technical knowledge and credibility by delivering short (two-page) technical notes summarizing most important affirmations and pitfalls for their use at conferences and other community meetings
        ii. Communicating use of and feedback regarding NASA and Marshall strategic vectors
    f. Recognizing detailed design (post milestone A) is a customer as well as the immediate study requesters
    g. Continuing to recognize that transfer of people is essential to the transfer of ideas
        i. Continuing to "borrow" experts from other technical organizations
        ii. Loaning out experts to other organizations
        iii. Developing high information potential individuals
        iv. Developing relationships with suitable technical people elsewhere in the engineering directorate and other sites.
2) ACO should broaden its products by:
    a. Addressing "so what" question by evaluating each study in light of contribution to or detriment from NASA and Marshall strategic vectors
    b. Improving alignment of study products with required products for Mission Concept Review
    c. Addressing customer's desire for increased awareness of trade space by "delivering an equation rather than a solution" via application of multidisciplinary design, analysis, and optimization approaches to additional analysis topics beyond current use in trajectory
    d. Developing low cost, rapid turnaround techniques for immersive interactive visualization and deliver such as appropriate to study
    e. Creating portfolio of ideal projects within the context of Marshall strategic vectors as background to specific customer-driven studies
    f. Seeking to understand/integrate of additional assessments relevant to study such as cost, Manufacturing, facilitation
3) ACO should increase its credibility by:
    a. Delivering more than immediate study results, i.e., specifically address larger context

b. Developing scorecard for each study addressing "where we got it right | where we got it wrong"
c. Conducting longitudinal study of outcomes for delivered studies specifically documenting outcomes such as which have flown, as credibility is directly related to flights
d. Publishing pedigree of each tool
e. Executing specific verification and validation procedures on each study
f. Providing resources for and encouraging staff to publish NASA technical notes on tools, techniques, and results
g. Pursuing formal benchmarking with organizations identified herein and more
h. Developing and executing a plan for improving as an innovative organization

IV. Conclusion

This study examined the state of communication between ACO and its customers, and made specific recommendations toward improving that communication that fall into three major classes: increase ACO-customer interaction, broaden basis of communication, and increase ACO credibility. The study confirmed that ACO has and continues to provide timely and accurate technical assessment of mission and spacecraft concepts to a wide range of customers. Not within the scope of this study but noteworthy is that ACO is pursuing a number of internal initiatives to improve the quality of its assessments and reduce the time such assessments require which are essential in fulfilling its role. Adopting the recommendations herein regarding improving ACO's delivery and communication of products should additionally enhance the value ACO contributes to MSFC and NASA as a whole. The study's time and resources limitations prohibited work that should be completed to fully mature the recommendations; specifically ACO should pursue a complete benchmarking with a range of similar organizations. Finally, implementing any of the recommendation would require resources of funding and personnel which ACO management would need to secure.

Acknowledgments

The Authors thank the NASA team members participating in surveys and interviews for this report, although they are not named per the promise of anonymity. The author additionally thanks Dr. Frank Six, Dr. Gerald Karr, and Ms. Rachel Damiani for their work in coordinating the 2017 NASA Marshall Space Flight Center Faculty Fellowship Program, which funded this study. The professionalism and collegiality of all of these individuals has been exemplary. Finally,

References

[1] R. J. Terrile, "Pathways and challenges to innovation in aerospace," in *IEEE Aerospace and Electronic Systems Magazine*, vol. 26, no. 12, pp. 4-9, Dec. 2011.

[2] Chutivongse, N., and N. Gerdsri. "Proposed steps to analyze organizational characteristics and develop a roadmap for being an innovative organization." Management of Engineering and Technology (PICMET), 2015 Portland International Conference on. IEEE, 2015.

[3] Saris, W. E. and Gallhofer, I. N. (2007) *Wiley Series in Survey Methodology, in Design, Evaluation, and Analysis of Questionnaires for Survey Research*, John Wiley & Sons, Inc., Hoboken, NJ, USA.

[4] Allen, Elaine and Seaman, Christopher (2007). "Likert Scales and Data Analyses". *Quality Progress*. pp. 64–65.

[5] Massart, D.L., Smeyers-Verbeke, X. Caprona, and Karin Schlesier. "Visual presentation of data by means of box plots. *LC GC Europe solutions for separation scientist*, 18(4):215, April 2005.

[6] W. E. Holland, "Characteristics of individuals with high information potential in government research and development organizations," in *IEEE Transactions on Engineering Management*, vol. EM-19, no. 2, pp. 38-44, May 1972.

[7] Guide, P. M. B. O. K. "A guide to the project management body of knowledge." Project Management Institute. Vol. 3. 2004.

A Parametric Trade Study on the Use of Variable Conductance Heat Pipes for the Peregrine Lunar Lander Mission

Daniel K. Harris[1]
Auburn University, Auburn, AL, 36801

Nomenclature & Abbreviations

^oC	=	temperature in degrees Celsius
K	=	temperature in Kelvin
kg	=	kilogram
m	=	meter
CCHP	=	Constant Conductance Heat Pipe
MLI	=	Multi-Layer Insulation Blanket
VCHP	=	Variable Conductance Heat Pipe

Abstract

The following report summarizes the work and findings through a NASA Faculty Fellowship conducted at Marshall Space Flight Center under the supervision of Shawn Breeding of the Thermal and Mechanical Analysis Branch (ES22). The modeling work was performed on the proposed Peregrine Lunar Lander and involved analyzing the benefits of adding variable conductance heat pipes to the lander's panel structures. It is shown that these devices show favorable benefits to the overall thermal performance while the lander is in direct sunlight. These devices also add the possibility of mission survival during lunar night environments, which is not feasible using heaters alone. Model results and further modeling recommendations are offered.

I. Introduction

Several for-profit commercial lunar missions are in the planning stages. One of these endeavors is the Peregrine Lander being developed by Astrobotic in Pittsburgh Penn. (www.astrobotic.com/peregrine). The Peregrine Lander is a commercial space vehicle designed to land on the moon within 100 meters of an intended target landing site. The lander is approximately 1.5 meters high and about 2.5 meters in diameter. The focus of this study was to investigate the impact on the lander's avionics system by the use of variable conductance heat pipes (VCHP) as a thermal control mechanism for operations after the lander is on the moon surface up to and including sunset. The heat pipe studies were completed using Thermal Desktop® software available through C&R Technologies. The trade studies included embedding VCHPs into the avionics panels and modeling their impact on performance as a function of lander orientation to the lunar surface in addition to lunar night survival analyses. The current mission planning for the Peregrine Lander does not include any night survival. The Lander mission is currently considered compete after lunar sunset. It was found that addition of VCHPs into the lander's avionics panels will help mitigate lander surface orientation variations of up to ±90° from the intended nominal landing orientation. In addition, it was also shown that the VCHPs can achieve lunar night survivability for avionics components, such as the batteries, if appropriate MLI blanketing is used in tandem with the VCHPs. The results achieved through this trade study give a reasonable expectation of improved performance and survivability using these passive thermal management devices. Further design details into the heat pipes themselves along with a weight trade-off study is recommended.

Note: This report was generated using color figures and graphs. Some details and overall clarity may be lost when printed in black & white. Original color versions of this paper are available in PDF format through contacting the author of this report. Requests can be sent directly to harridk@auburn.edu.

[1] Associate Professor, Mechanical Engineering, Auburn University

II. Background

The baseline lunar lander thermal model was modified to incorporate the use of CCHPs and VCHPs in an effort to learn the impact these devices could have on the lunar lander panels as the lunar day progresses. Additionally, although the current mission does not include nighttime survival, the use of VCHPs for lunar nigh survival of the battery was also investigated. The following three paragraphs give brief descriptions of the lunar environment, Peregrine lander design, and variable conductance heat pipes.

A. Lunar Environments

The environmental backdrop of these trade studies is for a lander that has just finished six orbits around the moon and has landed 55 hours after sunrise at a location 45 degrees north in latitude. For purposes of initial conditions it is assumed that the lander is in a cold orbit condition at the initiation of the lunar day analyses. The current mission plans call for end of mission at sunset, or about 310 hours after landing. The lunar day lasts approximately 710 hours, or 29.58 days, with day and night being about evenly split at 355 hours each. The lunar regolith experiences large temperature excursions between day and night conditions, which can cause challenges to maintain temperatures during these two extremes. As seen in ref. 1 chapter 5.7 and Figure 5-23, the daytime lunar regolith can reach 400 K (127^{o}C), whereas night temperatures can be a slow as 110 K (-163^{o}C).

B. Peregrine Lander Design

The Peregrine Lander is a 1.8 meter high and 2.5 meter diameter space vehicle that can accommodate payloads of up to 265 kg. The lander features four aluminum decks for payload as well as avionics and electronics mounting. Payloads can attach to the topside or underside of the deck panel. Panel A is reserved for spacecraft avionics and power. Panels B, C, and D are dedicated for lease for commercial partners. Figure 1 below shows a top view of the four avionics panels as is taken from Astrobotic's website.

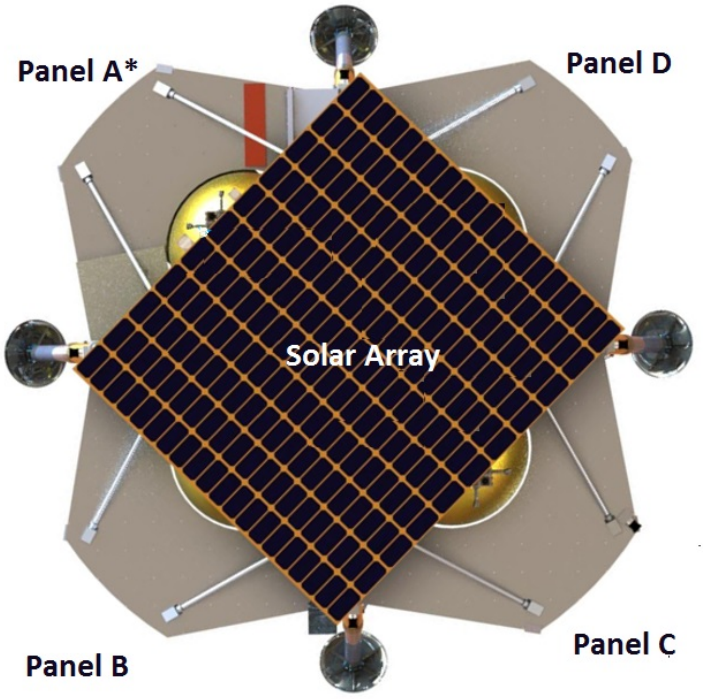

Figure 1. Top View of Peregrine Lander Solar Array Panel and All Four Avionics Panels.

Only Panel A and its associated battery temperatures were of primary concern during the studies described herein. Two arrangements were looked at where one arrangement had six VCHPS connecting all four panels (Quad Panel Design) and another arrangement where two VCHPs was connecting only Panels A, B, and D (3-Panel Design). It was determined that bridging Panel A to Panel C was of no useful benefit and the pipe distance was too long for heat pipe operations and, therefore, the 3-Panel Design was preferable. Hence, Panels B & D were used for study where thermal connections from Panel A to Panels B & D was accomplished through the use of VCHPs. It was of primary interest to determine if thermally bridging Panel A to Panels B & D would help (a) mitigate battery maximum extreme temperatures during lunar day operations; (b) extend the useful life of the batteries through the lunar night via the use of heaters in tandem with the VCHPs. The mitigation of lunar day maximum battery temperatures were studied for landing orientations of the nominal planned lunar surface orientation including an uncertainty of ±90°.

C. Variable Conductance Heat Pipes

Heat pipes are passive thermal management devices that move heat very effectively by not incurring large temperature gradients. The basis of their operation is through the use of a pure substance working fluid (e.g. water, ammonia, ethanol, sodium, etc.) as a liquid-vapor 2-phase transport liquid entrapped in a hermetically sealed pipe. The temperature difference between the evaporator and the condenser end is minimized by moving the heat almost isothermally through vaporization and condensation processes. For terrestrial or lunar applications a wick material is needed to move condensate from the condenser end to the evaporator end. These and many more details of heat pipe operating principles, design, and fabrication are beyond the scope of this report. For a more detail description of heat pipes and their operating principles see ref. 2-4.

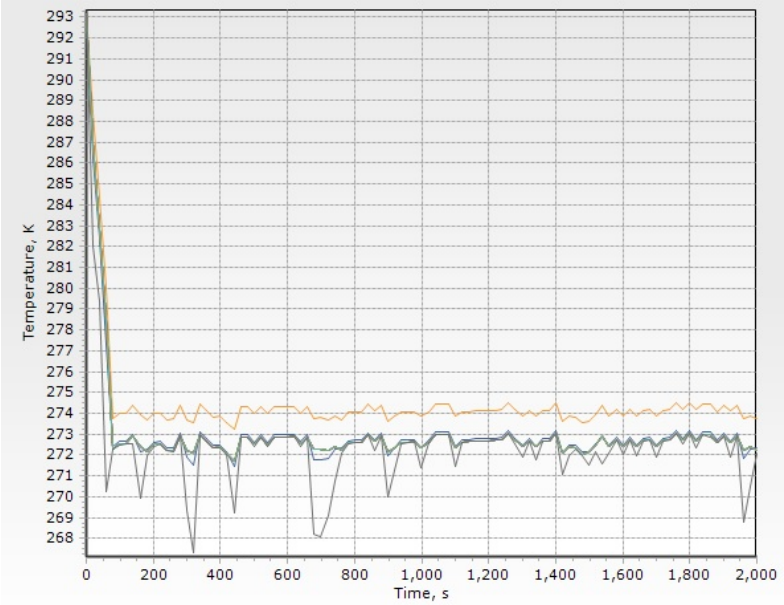

Figure 2. Thermal Desktop® VCHP Model Results.

There are several types and variations of heat pipes available. The simplest and most common is the constant-conductance heat pipe, CCHP. As the title suggests, these heat pipes have a very high thermal conductance that is invariant with the heat load being transported through the heat pipe. These are simple devices to build and are very reliable. However, these devices continue to operate regardless of the evaporator temperature, as long as the freezing point of the contained liquid is not reached. Therefore, for lunar applications, these pipes would not be suitable during lunar night environments where the regolith temperatures can reach as low as 110 K since this temperature would be well below any survival temperature for electronics. So, even though CCHPs help achieve adequate cooling and thermal management during hot environments, they are undesirable when the environment temperature drops to very low values. Fortunately, there is a class of heat pipes that operate as normal CCHPs during warm environments, but that also stop operating as the environmental temperature drops below a set

temperature. These heat pipes are known as variable conductance heat pipes VCHP and these passive devices are appropriate for lunar day/night thermal controls. These heat pipes are also described in detail in ref. 2 & 4.

III. Modeling and Results of VCHPs for Peregrine Lander

The lander model was amended to include 2 VCHPs that each attached Panel A to Panels B & D, respectively. The lunar transient day analysis started 55 hours after lunar sunrise and continued through sunset 310 hours later. For all analyses the nominal (planned) lander orientation on the lunar surface is for Panel A to be pointing approximately due north. The lander orientation for all three 90°rotations at sunrise right after landing is shown in Figure 3.

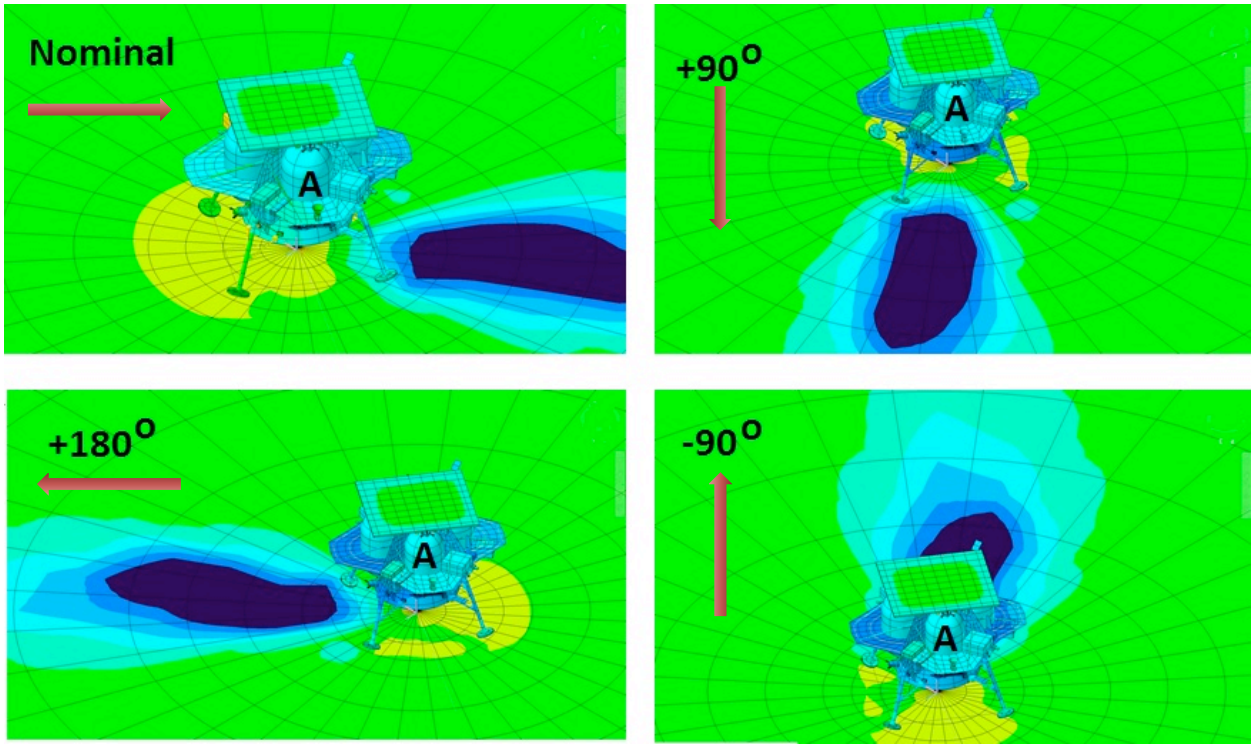

Figure 3. Lander Surface Orientations Showing Location of Panel A. (Solar Vector Shown)

The results of all thirteen simulations are summarized in Table 1 in addition to the 15 temperature plots in the appendix. Table 1 contains a baseline model whereby no heat pipes were included in the model. This baseline arrangement represents the current lander configurations for all four orientations shown in Figure 3. The last row in Table 1 is for the lunar night analyses during which orientation is not considered since there is no solar load vector or shadows. Also, while the lunar day analyses for the Quad Panel Design are shown for CCHP operation, the lunar night results are for VCHP operation in the 3-Panel Design. This is done to show comparisons between the operations of VCHPs versus CCHPs during the lunar day. However, there is no reason to model and compare CCHP operations during lunar night since these heat pipes do not stop operating regardless of temperatures and loading.

Table 1. Summary of Results from Analyses Using Thermal Desktop®

Surface Day	No Heat Pipe Panels	Quad Panel CCHPs	3-Panel VCHPs
Nominal	36°C	42°C	38°C
+90°	52°C	37°C	55°C

+180^{o}	67^{o}C	41^{o}C	Not Studied
+270^{o}	64^{o}C	49^{o}C	64^{o}C
Surface Night - VCHP	Not Studied	80^{o}C / 13^{o}C (Max / Min)	30^{o}C / 3^{o}C (Max / Min)

A. Heat Pipe Influences and Effects

As can be seen in Table 1, for lunar day operation the nominal orientation is the most favorable orientation for the Panel A thermal environments. This is an expected results since Panel A is facing northwest in the nominal orientation. Next, in Table 1, the Quad Panel Design is listed for operation with CCHPs. As can also be seen, CCHPs present unfavorable temperatures since the heat pipes are free to transport heat from a warmer panel to the avionics panel (Panel A) even when this is not desirable. These results are included to show the importance of the variable operation features of VCHPs in that they can be designed to turn on or off at set designed temperatures. This operation is all achieved passively. Finally, for lunar day operation the 3-Panel Design shows no favorable or unfavorable impact on the avionics panel (Panel A) and maximum battery temperatures.

B. Landing Orientation Sensitivity

The results summarized in Table 1 also show the influence lander surface orientation has on the temperatures in Panel A. In addition to the differences in the solar vector angles among the different lander orientations, there are also shadowing effects from the lander structure itself that is very different for various lander orientations. This explains why the +90 and -90 degree orientations results are not interchangeable or mirror opposites. The differences in the solar angle vector as the lunar day progresses is also due to the latitude of 45°N. The overall conclusion on the influence of lander surface orientation is that the nominal orientation is the coolest orientation for Panel A (lander avionics panel) for the nominal design and holds for the 3-Panel VCHP design. It also appears that a -90° rotation presents a warmer environment for Panel A than a +90° rotation.

C. Lunar Night Survivability

The last row of Table 1 and Figure A.4 shows some modeling results comparing battery temperature survivability for CCHPs and VCHPs. Also Figure A.4C shows the impact battery heaters have on survivability when paired with VCHPs. The results here show that VCHPs may help the batteries and other electronics survive the lunar night with an appropriate blanketing arrangement coupled with heater operation. However, further study is needed before this can be conclusively stated.

IV. Future Recommendations

The inclusion of VCHPs onto the Peregrine Lunar Lander avionics panels has been shown to offer some promise through modeling studies conducted herein. The inclusion of panel VCHPs the bridge between the Panels A, B, and D offer some mitigation in daylight maximum temperatures experienced on the main avionics panel (Panel A). Furthermore, the inclusion of these devices may also mitigate the impact of lander surface orientation on Panel A temperatures for angles up to ±90 degrees form the nominal surface orientation. Additionally, VCHPs offer some opportunities for lunar night survival that may extend the useful life of the lander after landing beyond the current end-of-life terminator at sunset.

These studies have offered an opportunity for further investigations and more detailed design studies. The following follow-up list of analyses and studies are suggested as next-steps and are by no means to be considered exhaustive and conclusive.

- Parametric trade study on the sizing, number and geometrical arrangement of VCHPs and the impact on lander day operations and night survivability. This trade should include a more realistic modeling methodology for the pipe attachment to the panels', pipe sizing and orientation, as well as more realistic logic for the condenser logic as opposed to the bang-bang logic used within this work.
- Lander inclination impacts on VCHP operations due to heat pipe design parameters such as length, structure orientation, diameter, working fluid, container material, evaporator or condenser elevations, etc. VCHP diode operations were not considered in this effort. This characteristic of VCHPs should be added in future analyses.

- VCHP designs impacts on blanketing and heater designs and requirements.
- The use of CCHPs embedded into the avionics panels and combined with VCHPs in order to enhance thermal bridging amongst and within the four avionics panels.
- A repeat of this study using loop heat pipes with thermal switch valves as a competing technology option.
- Finally, a weight and volume trade comparison between VCHPs and any other competing heat pipe technology considered in place of VCHPs.

Appendix

The following four figures show the battery temperature results as generated by the embedded plotter used by Thermal Desktop® for the baseline studies, the Quad Design studies using CCHPs, the 3-Panel Design studies using VCHP as well as a figure showing the lunar nighttime results. These results are all summarize in Table 1 in the main text.

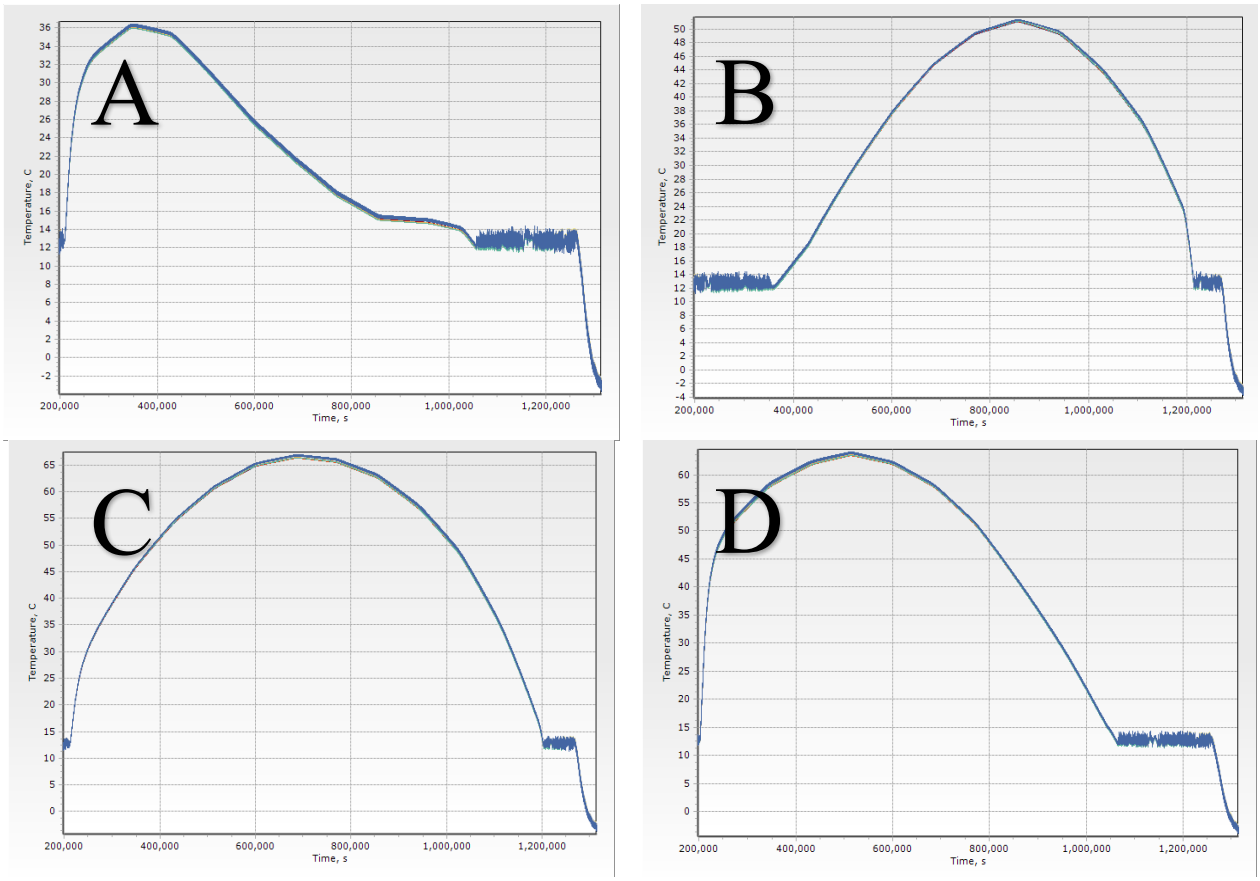

Figure A.1 Battery Temperatures (K) During Lunar Day Operation versus Time (seconds) for Baseline Design (No Heat Pipes).

LEGEND
A: Nominal Orientation
B: +90^{o}
C: 180^{o}
D: -90^{o}

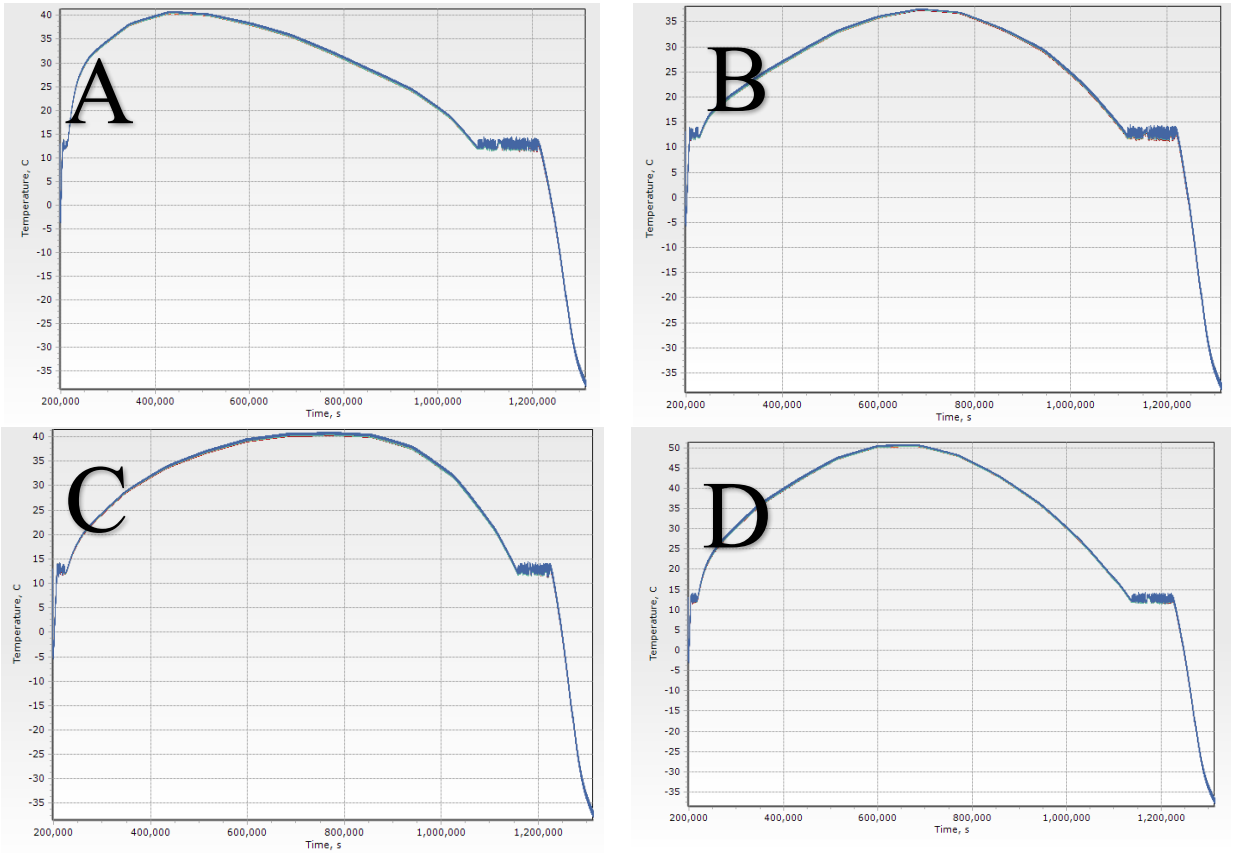

Figure A.2 Battery Temperatures (K) During Lunar Day Operation versus Time (seconds) for Quad Panel Design Using CCHPs.

LEGEND
A: Nominal Orientation
B: +90^{o}
C: 180^{o}
D: -90^{o}

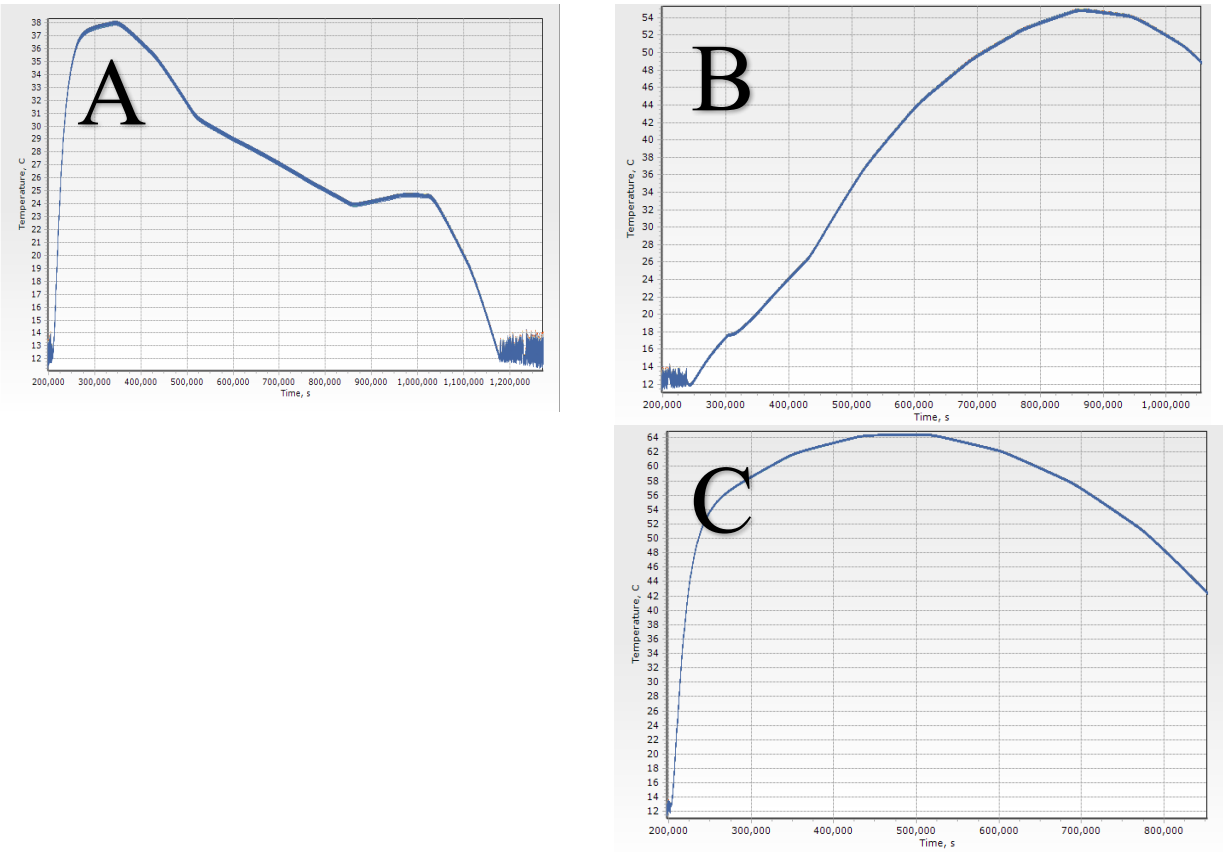

Figure A.3 Battery Temperatures (K) During Lunar Day Operation versus Time (seconds) for 3-Panel Design Using VCHPs.

LEGEND
A: Nominal Orientation
B: +90^{o}
C: -90^{o}

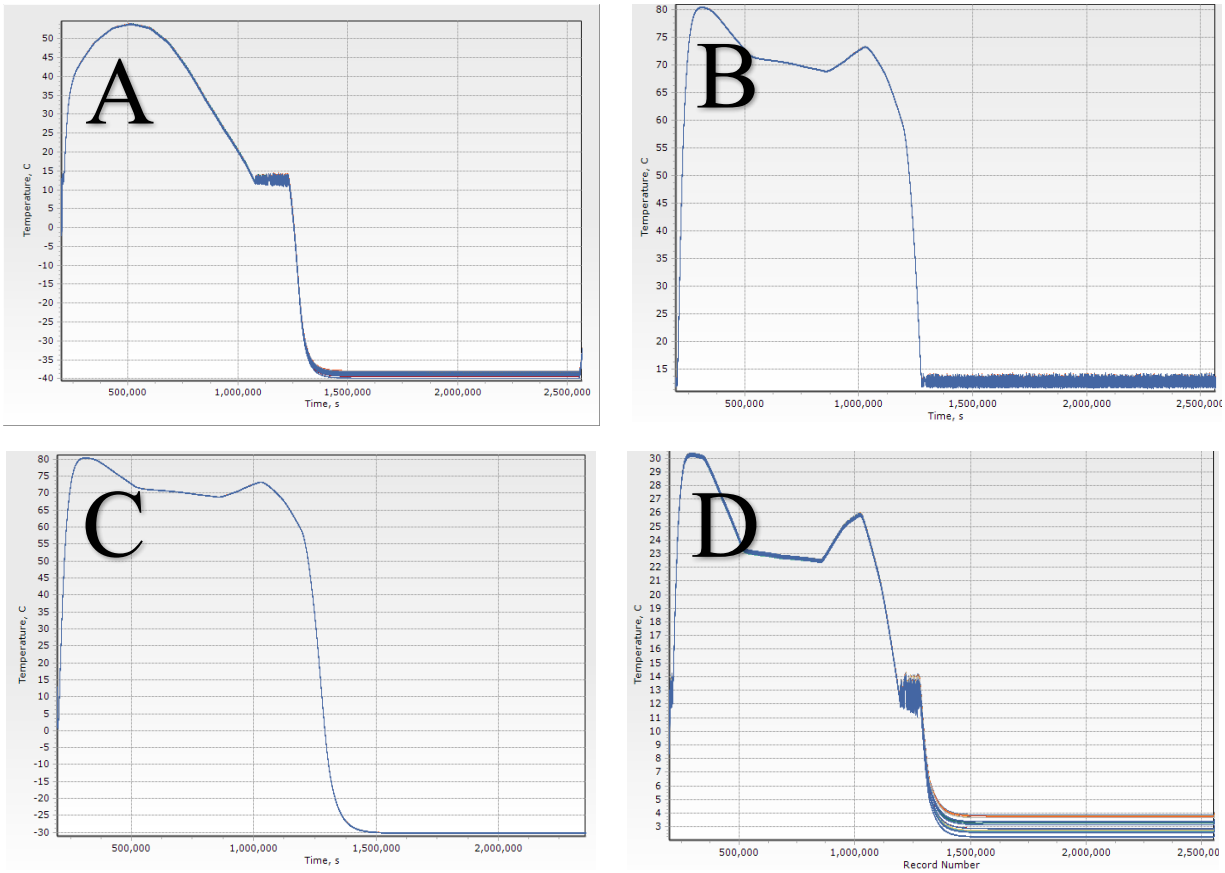

Figure A.4 Battery Temperatures (K) For Full Lunar Day And Night Operation versus Time (seconds) for Various Designs With and Without Battery Heater Operation.

LEGEND
A: Quad Panel Design CCHPs
B: Quad Panel Design VCHPs
C: Quad Panel Design VCHPs with No Battery Heater Operation
D: 3-Panel Design with VCHPs

Acknowledgments

I would like to thank NASA for the opportunity and funding for this 10 week summer fellowship. Additionally I also would like to thank Shawn Breeding and Dr. Jeff Fisher for their technical and logistical support during my stay at NASA Marshall. Finally, I would like to thank Shawn Breeding and Stephanie Mauro of NASA, as well as Kevin Higdon of Jacobs for their support and help in teaching me the Thermal Desktop® software and modeling tool.

References

[1]Eckart, Peter, *The Lunar Base Handbook*, 2nd ed., McGraw-Hill., Boston MA, 2006, Chaps. 5, 7, 11.

[2]Dunn, P. D., and Reay, D. A., *Heat Pipes*, 4th ed., Pergamon, Elsevier Sciences Inc., New York, 1994, Chaps. 2, 6.

[3]Peterson, G. P., *An Introduction to Heat Pipes – Modeling, Testing and Applications*, Wiley Interscience, New York, 1994, Chaps. 2,3,4,6.

[4]Faghri, A., *Heat Pipe Science and Technology*, Taylor & Francis, Washington DC, 1995, pp. 493-502.

[5]A. K. Mozumder, A. F. Akon, M. S. H. Chowdhury, and S. C. Banik, "Performance of Heat Pipe for Different Working Fluids and Fill Ratios," Journal of Mechanical Engineering, 41(2), Dec. 2010, Trans. Of Mech. Eng. Div., Bangladesh.

Improving global monitoring of agricultural drought

Douglas B. McRoberts[1]
Texas A&M University, College Station, TX, 77845

and
Christopher R. Hain[2]
NASA Short-term Prediction Research and Transition Center, Huntsville, AL, 35805

In this study, methods are explored to better quantify agricultural drought at a global scale, with a focus on the summertime, which is the primary growing season for the majority of the world's agricultural production regions. The cornerstone of our efforts is the Evaporative Stress Index (ESI), which is a remotely sensed indicator of anomalous surface moisture fluxes, a quantity commonly referred to as evapotranspiration (ET). Negative anomalies in ET typically indicates the onset of drought and can precede other indicators by weeks. We compare the performance of the ESI to other commonly-used drought indicators through a method called triple colocation (TC) analysis, which can be used to compute the correlation of each indicator to an unknown truth. Additionally, we perform lag-correlation analysis to quantify the ability of the ESI to predict future vegetative anomalies. The results of our analyses show that in most of the world's most productive agricultural regions, the ESI was both highly correlated to the TC-derived "true" ET anomaly and was significantly correlated to future vegetative health anomalies.

Nomenclature

α	=	intercept
β	=	slope
E	=	expected value
ε	=	random error
G	=	soil heat flux
H	=	sensible heat
j	=	Julian day
λ	=	latent heat of evaporation
μ	=	climatological mean
Q	=	covariance
r	=	Pearson's correlation coefficient
RN	=	net radiation
σ	=	climatological standard deviation
σ_ε	=	error variance
t	=	time in days
τ	=	unknown truth in triple colocation
θ	=	TC drought index variable
X	=	drought index value
x	=	east-west location
y	=	north-south location
Z	=	standardized anomaly

[1] Research Assistant Professor, Department of Geography, 3147 TAMU.
[2] Research Scientist, NASA SPoRT, 320 Sparkman Dr. NW.

I. Introduction

Drought is a complex phenomenon that has far-reaching ramifications across a number of sectors, and is typically monitored using an ensemble of diagnostic tools that provide insight into different components of the hydrological budget[1]. Accurate and timely drought information is particularly important for stakeholders in agriculture, who can take action to mitigate crop and livestock losses if given enough lead time. Summertime drought can be difficult to properly monitor because high temperatures and atmospheric demand often lead to rapidly evolving events called "flash droughts" that can have catastrophic consequences because they typically occur during the agricultural growing season and with very little lead time. Early identification of summertime agricultural droughts is best accomplished through real-time detection of reduced soil moisture fluxes at the surface, which typically precedes moisture depravation in the root-zone layer and the wilting of crops and vegetation (Fig. 1). In this paper, we explore methods for providing better early warning capabilities for the rapid onset of agricultural drought during the Northern Hemisphere summertime (June through August; JJA).

In recent years, global drought monitoring efforts have improved through incorporation of satellite remote sensing products that provide critical information about water and energy balances. Despite the availability of numerous remotely-sensed sources of information (e.g., vegetative health, evapotranspiration (ET), soil moisture, surface temperature, irrigation, etc.), most drought indices and land surface models (LSMs) use a water-balance approach that is dependent upon reliable precipitation data. However, the fidelity of this data is dependent upon the existence of reliable and densely populated gauge networks, even in satellites, which use gauges for calibration. Simply put, these networks are not routinely available in most regions of the world.

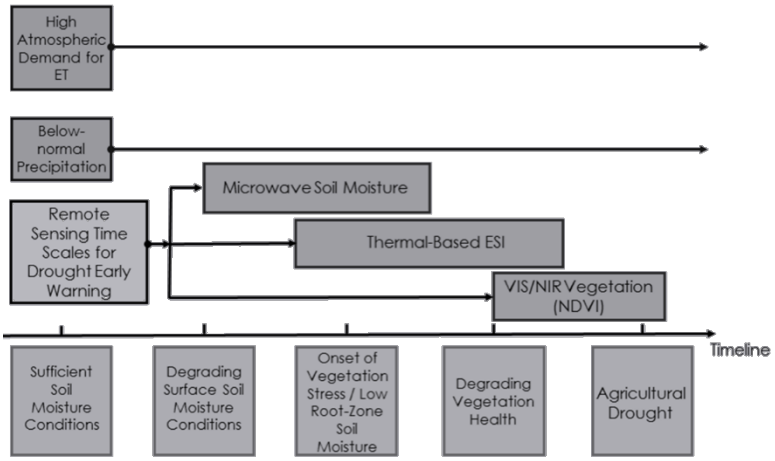

Figure 1. Typical evolution of an agricultural drought.

An alternative to precipitation-based drought monitoring is to estimate ET (the combined soil evaporation and plant transpiration) using a thermal energy balance approach. Anderson et al.[2-3] demonstrated that satellite thermal infrared (IR, i.e., clear sky) and microwave (MW, i.e., cloudy sky) retrievals of land surface temperatures (LSTs) and shortwave (VIS/IR) retrievals of vegetation cover are closely linked to observed ET. Anderson et al.[4] introduced the Atmosphere-Land Exchange Inverse (ALEXI) two-source (soil and canopy) surface energy balance model (Fig. 2), based largely on the work of Norman et al.[5]. The ALEXI model use the rate of increase in morning LST over 4 hours (from 1.5 hours to 5.5 hours after sunrise) to derive the surface sensible (H) and latent (λE) heat fluxes. The ALEXI total energy balance for soil is:

$$RN_S - G = H + \lambda E_S \tag{1}$$

In Eq. (1), RN_C is the net downward radiation at the surface, G is the soil heat flux, λ is the latent heat of evaporation and E_S is evaporation. For a vegetative canopy, the energy balance is (changing subscripts in RN_C and E_c):

$$RN_C = H + \lambda E_C \tag{2}$$

Given the ALEXI energy balance model, which combines the soil and canopy energy balances, Anderson et al.[6] introduced the Evaporative Stress Index (ESI), which is the ratio of model-derived ET to potential ET (PET) based off of the morning change in LST. To estimate LST, ALEXI uses a simple slab model of mixed-layer growth (Fig. 2), based on the McNaughton and Spriggs[7] model. PET is the amount of ET occurring when moisture is sufficient and is computed using knowledge of temperatures, land surfaces, winds, and radiation[8]. Moisture-depleted soils will have a decreased latent heat flux, increased sensible heat flux, and an observed increase in the morning LST change. As the ESI decreases, the surface water supply (ET) decreases and the atmospheric demand for water (PET) increases.

In this study, we compare the ability of the ESI to accurately capture anomalies in soil moisture fluxes to other widely-used global drought indices. Given the lack of a sufficient reference set in most regions, we use the Stoffelen[9] method of triple colocation (TC) analysis, which computes error statistics without the need for a reference data set.

The TC analysis gives a sense of how accurate the ALEXI energy balance model estimates real-time ET anomalies, but doesn't necessarily indicate ESI's value in forecasting rapid drought onset. Given that moisture depravation precedes vegetation degradation (Fig. 1), we explore the ability of ESI to provide early drought warning relative to other drought indices. A correlation analysis was performed between each drought indicator and time-lagged, remotely-sensed vegetative health indicators, namely the Normalized Difference Vegetation Index (NDVI) and the Leaf Area Index (LAI).

This paper serves as an overview of methods that can be used to develop and improve a global drought early warning system using the ESI as a cornerstone of these efforts. However, this is not meant to be an exhaustive investigation into optimizing the ESI integration into a global drought monitoring system, as those details have not been fully explored, with plans to do some in the near future.

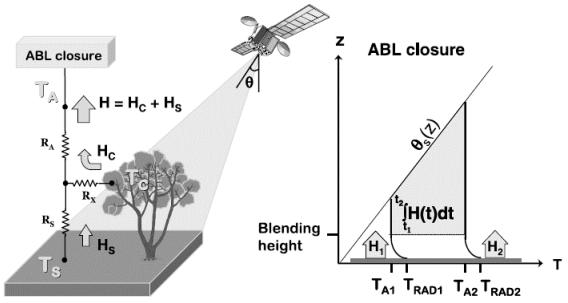

Figure 2. Schematic of the ALEXI model (left) and model of mixed-layer used to estimate LST (right).

II. Data

In this study, we compare the ability of the ESI to accurately capture anomalies in soil moisture fluxes to four other widely-used global drought indices. Of particular interest is its performance in the JJA period, which is the growing season in most of the Northern Hemisphere. The drought indices will be composited to 4-week and 12-week time scales for analysis.

Traditional intercomparison studies validate accuracy by comparison to ground-based observations, but ET and soil moisture observations are limited in most regions[10] and validation of ESI has been done where data is readily available (e.g., Anderson et al.[3]). Given the lack of a sufficient reference set, we use the Stoffelen[9] method of triple colocation (TC) analysis, which computes error statistics without the need for a reference data set. In this study, we'll perform the TC analysis on 12-week composited data.

The TC analysis gives a sense of how accurate the ALEXI energy balance model estimates soil moisture anomalies, but doesn't necessarily indicate ESI's value in detecting rapid drought onset. Given that moisture depravation precedes vegetation degradation (Fig. 1), we explore the ability of ESI to provide early drought warning relative to other drought indices. A correlation analysis was performed between each drought indicator and time-lagged, remotely-sensed vegetative health indicators, namely the Normalized Difference Vegetation Index (NDVI) and the Leaf Area Index (LAI), using the 4-week composited data.

A. Data overview

All the drought and vegetation data used in the TC and lag-correlation analyses originate from remotely-sensed sources and, when necessary, were regridded from their native resolutions to a 0.25˚×0.25˚ grid spanning the entire globe between 60˚S and 60˚N. Daily values for each index were averaged over 28-day and 84-week sliding windows,

with a 7-day time step in between each computation (i.e., 13 4-week and 12-week averages in the JJA period each year). A time-averaged index value $\langle X \rangle_t$ of length t days, ending at Julian day j is computed as:

$$\langle X(j,x,y) \rangle_t = \frac{1}{t} \sum_{n=j-t+1}^{j} X(n,x,y) \tag{3}$$

Each time-averaged X is transformed to a standardized anomaly (Z) using the climatological mean (μ) and standard deviation (σ) to provide a consistent metric for comparison between indices:

$$Z = \frac{\langle X \rangle_t - \mu_t}{\sigma_t} \tag{4}$$

B. Drought indices

1. ALEXI Evaporative Stress Index (ESI)

The ESI is a measure of surface moisture flux computed as the ratio of a measured or estimated ET to a reference ET value (i.e., PET). In this study, we use the Anderson et al. (1997) ALEXI-derived ET and the Penman-Monteith (FAO56) equation for PET. The thermal IR LST retrievals are at 0.05˚ resolution from the Moderate Resolution Imaging Spectroradiometer (MODIS) instruments on NASA's Terra and Aqua satellites[11-12]. The MW LST sensors are taken from the NOAA Operational Soil Moisture Product System (SMOPS), which is mapped onto a 0.25˚ global grid.

2. European Space Agency (ESA) soil moisture

The ESA produces a soil moisture product is a composite from 10 different active and passive sensors mapped onto a 0.25˚ global grid[13]. The ESA product represents perhaps the most complete global record of soil moisture in the first few cm of the soil layer based on satellite observations, with the dataset extending back to 1979.

3. Noah LSM soil moisture

In general, LSMs provide short-term forecasts of a large number of hydrologic variables, include ET and soil moisture, with estimates dependent on the model physics and the accuracy and resolution of the meteorological inputs "forcing" the model[1,11]. We compare the ESI to the Noah LSM, which uses Global Land Data Assimilation (GLDAS) forcing and both water and energy balance principles in a four-layer soil structure and is available on a global 0.25˚ grid[14].

4. Vegetative health Index (VHI)

The VHI is a weighted composite of normalized vegetation conditions (NDVI; explained in next section) and normalized brightness temperatures[1] (BTs). Instead of the normalization done in Eq. (4), both the NDVI and BT are normalized by the climatological minimum and maximum with values between zero and one:

$$VHI = a\left[\frac{NDVI - NDVI_{\min}}{NDVI_{\max} - NDVI_{\min}}\right] + (1-a)\left[\frac{BT_{\max} - BT}{BT_{\max} - BT_{\min}}\right] \tag{5}$$

The VHI uses the same thermal and vegetative components used to compute the ESI, so it will be used as a direct comparison to the ESI in this study. Global NDVI and BT data are retrieved from the Advanced Very High Resolution Radiometer (AVHRR) at 0.14˚ resolution.

5. *Standardized Precipitation Index (SPI)*

The SPI is a precipitation-only index that determines the probability of a given aggregated precipitation total occurring given a well-defined historical probability distribution[15]. By convention, the SPI is a normalized anomaly computed in Eq. (4). In this study, SPI was computed using the Climate Data Record (CDR) of Precipitation Estimation from Remotely Sensed Information using Artificial Neural Networks (PERSIANN-CDR)[16]. PERSIANN-CDR merges gridded satellite data with the Global Precipitation Climatology Project into a time series dating back to the early 1980s, available on a global 0.25˚ grid between 60˚S and 60˚N.

C. Vegetative health indices

1. NDVI

The NDVI measures vegetative health as the relative difference between reflected near IR (NIR) and visible (VIS) light. Healthy vegetation absorbs more VIS light and reflects more near IR light than stressed vegetation. NDVI is computed as the difference between the reflected NIR and VIS light divided by the total reflection. NDVI-CDR is available with complete global coverage at 0.05˚, dating to 1981 and constructed using AVHRR reflectance. The source of the NDVI data is the Global Inventory Modeling and Mapping Studies (GIMMS) Satellite Drift Corrected and NOAA-16 Incorporated Normalized Difference Vegetation Index[17].

2. LAI

LAI measures the percentage of ground area covered by green leaf area, and ranges from zero to one. 4-day LAI data are available at 1 km resolution from the MODIS Terra+Aqua[18] and smoothed using a digital filter[19]. A disadvantage of the LAI (and NDVI) is that its effectiveness is limited to regions with a sufficient canopy.

III. Methods

A. Triple colocation (TC) analysis

1. Background

Traditional intercomparison studies validate accuracy by comparison to ground-based observations, but ET and soil moisture observations are limited in most regions[10] and validation of ESI has been done where data is readily available[3,19]. Scipal et al.[20] introduced TC analysis for soil moisture. Konigs et al.[21] state the basic assumptions in TC are that errors three independent estimates ($\langle X_1 \rangle, \langle X_2 \rangle, \langle X_3 \rangle$) are uncorrelated with each other and with the truth $\langle X_T \rangle$. TC analyses typically use data from different sources (e.g., satellite, model, ground-based), but in this study, we extend the independence to different observation parameters (e.g., ET, precipitation, soil moisture, vegetation) from satellite-based datasets. In this section, we detail the computation of a TC correlation coefficient for each drought index that can be interpreted as its effectiveness in representing the true surface ET state.

2. Formulation of TC correlation with an unknown truth

A basic assumption of TC analysis is that each dataset has a linear relationship with the truth[18], which allows us to compute a correlation coefficient between each estimate dataset and the truth. The estimates are expressed as a set of ordinary least squares (OLS) equations with intercept (α), slope (β), and a random error term (ε):

$$\begin{aligned} X_1 &= \alpha_1 + \beta_1 \langle X_T \rangle + \varepsilon_1 = \alpha_1 + \theta_1 + \varepsilon_1 \\ X_2 &= \alpha_2 + \beta_2 \langle X_T \rangle + \varepsilon_2 = \alpha_2 + \theta_2 + \varepsilon_2 \\ X_3 &= \alpha_3 + \beta_3 \langle X_T \rangle + \varepsilon_3 = \alpha_3 + \theta_3 + \varepsilon_3 \end{aligned} \tag{6}$$

In Eq. (6), the quantity $\theta_i = \beta_i \langle X_T \rangle$ is introduced to create a set of solvable equations. McColl et al.[22] approached the TC solution by construction a covariance matrix (Q), using the assumption that that additive bias (α) disappears when using anomalies. Therefore, each $Q_{i,j}$ value is expressed as:

$$Q_{i,j} = \left\langle (\theta_i + \varepsilon_i)(\theta_j + \varepsilon_j) \right\rangle \tag{7}$$

In the anomaly space, $\langle \varepsilon_i \varepsilon_j \rangle$ is zero when $i \neq j$ and is equal to $\sigma^2_{\varepsilon_i}$ when $i = j$, so we can express Eq. (7) as:

$$Q_{i,j} = \theta_i \theta_j + \langle \varepsilon_i \varepsilon_j \rangle = \begin{cases} \theta_i \theta_j & \text{if } i \neq j \\ \sigma_i^2 & \text{if } i = j \end{cases} \tag{8}$$

In OLS regression, the relation between linear slope and correlation (ρ) is expressed as:

$$\rho_{i,T} = \beta_i \frac{\sigma_T}{\sigma_i} \tag{9}$$

In Eq. (9), $\rho_{i,T}$ is the correlation between drought index i and the truth. Assuming the expected value of the truth for an anomaly (i.e., climatology) is zero, we can equate the expected value of the squared truth $E\left(\langle X_T \rangle^2\right)$ to the variance (σ_T^2). The correlation in Eq. (9) can now be expressed as:

$$\rho_{i,T} = \frac{\theta_i}{\sqrt{Q_{ii}}} \tag{10}$$

Using the set of equations in Eq. (6), we can express a given θ_i as:

$$\theta_i = \sqrt{\frac{Q_{ij}Q_{ik}}{Q_{jk}}} \tag{11}$$

Combining the correlation $\rho_{i,T}$ in Eq. (10) with the formula for θ_i in Eq. (11), we can express $\rho_{i,T}$ as:

$$\rho_{i,T} = \sqrt{\frac{Q_{ij}Q_{ik}}{Q_{ii}Q_{jk}}} \tag{12}$$

3. Application of TC to our study

In this study, we use Eq. (12) to compute the correlation of each index i with the truth, given two other drought indices j and k. Overall, we are comparing the correlation of five different indices to the TC analysis truth, so instead of computing a single correlation $\rho_{i,T}$ to assess the strength of an index, we compute a composite correlation $|\rho_{i,T}|$ that is the average of all the individually computed correlation coefficients:

$$\left|\rho_{i,T}\right| = \frac{1}{12}\sum_{j=1}^{5}\sum_{k=1}^{5}\rho_{i,T}\left(j \neq i, k \neq j\right) \tag{13}$$

In Eq. (13), i is the drought index of interest and j and k are indices used for a particular TC correlation computation.

B. Lag correlation analysis with vegetative health

The second method for quantifying the effectiveness of ESI as a global drought indicator is a straightforward lag correlation analysis. Instead of the TC correlation in Eq. (12), we use the more common Pearson's correlation coefficient between drought indicator i and vegetative health indicator v:

$$\rho_{i,v} = \frac{\sum_{t=1}^{n}\langle X_i \rangle_{t-2} \times X_v(t)}{\sum_{t=1}^{n}\langle X_i \rangle_{t-2}\sum_{t=1}^{n}X_v(t)} \tag{14}$$

The time scale for t is weeks, thus we are comparing vegetative health indicator v to a composite drought indicator i with a timestamp 2 weeks earlier. An important difference in the comparison is that, unlike the drought indices, NDVI and LAI are not composites but rather single-day indicators; thus the difference in notation in Eq. (14). The timestamp for a given drought index composite $\langle X_i \rangle_{t-2}$ is at the end of the 4-week period, so we can infer that the strongest signal in the composite occurs in the middle of the period (i.e., 4 weeks prior to the vegetative health indicator v it is being compared to). The goal of this lag-correlation analysis is to compare the state of vegetation to the antecedent state of drought indicators, taken 4 weeks earlier.

IV. Results

A. TC analysis of drought indices

4. Intracomparison

Given the TC analysis methods described in Section 3a, the overall performance of the five drought indices (ESI, ESA soil moisture, Noah LSM soil moisture, SPI, VHI) was computed independently at each 0.25˚×0.25˚ grid cell. Figure 3 displays the spatial pattern of the single index with the highest correlation metric, computed using (13). The 12-week index averages ending in the JJA were computed using (3) and normalized using (4).

The general takeaway from the analysis (Fig. 3) is that there are more coherent patterns of the best performing indices in the mid-latitudes of both the Northern and Southern Hemispheres than in the tropics, where noise dominates over any real signals. According to the TC analysis, the ESI outperformed the other four indicators in the central North America, eastern Europe, and northwestern Asia. The ESA soil moisture product TC correlations are highest across southern South America, southern Africa, central Asia, and Australia. The Noah LSM soil moisture was had the highest TC metrics in much of eastern North America, eastern South America, and western Europe. The mid-latitude regions where the ESI, ESA soil moisture, and Noah LSM soil moisture had spatial coherency as the dominant indicator are important because these regions make up most of our global agricultural yield. In the future, the TC analysis results can be used to objectively blend the different drought indicators into a single map, removing the subjectivity currently used in many composite drought maps.

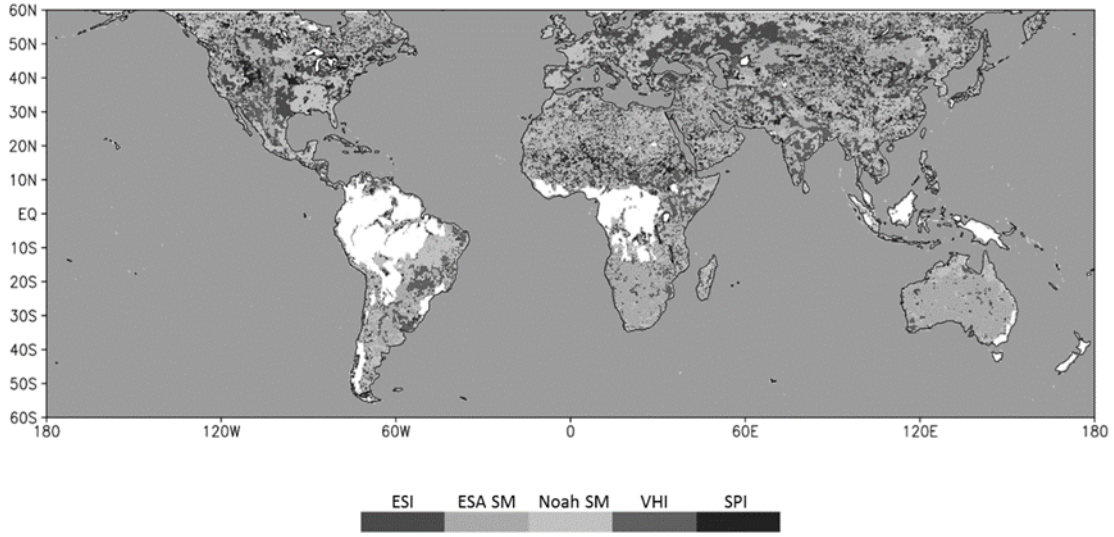

Figure 3. Drought index best correlated with the "truth" using TC analysis for the period JJA using data from 2001-2016. White areas indicate regions where data were insufficient to compute reliable correlations.

In general, the SPI and VHI were outperformed in the TC analysis by the other three drought indices, with no clear indication of being the preferred drought indicator in any region. In many grid cells, there were several drought indices with correlation values at or near one for the JJA period (e.g., most of Europe), though only a single "best" index is shown on Fig. 3. To avoid an artificial preference for the ESI in Fig. 3, ties in the TC correlation analysis were broken by displaying the index furthest to the right on the scale (e.g., if all five indices are tied, VHI is displayed).

2. Individual TC correlations

In addition to comparing the relative performance of each drought index, we examined the spatial patterns of the TC analysis for each drought index individually. The TC analysis vets the ESI as a reliable mid-latitude drought indicator in Northern Hemispheric regions that are not at high elevations (Fig. 4), with more limited effectiveness in similar Southern Hemisphere latitudes, likely due to the fact the analysis takes place during the cool season. The ESA soil moisture product was very effective in the mid latitudes of the Southern Hemisphere, but in the Northern Hemisphere was more limited than the ESI, with the exception of western Asia. The performance of both the ESI and ESA soil moisture products was noisy in the Tropics.

Out of all the drought indices examined, the Noah LSM had the highest diversity of regions where the TC analysis indicated good performance, making it the most flexible drought index we analyzed. This is not surprising given the diversity of sensors and datasets used in the model forcing, which unlike the other products, does provide some drought assessment skill in the tropics. An examination of the mid-latitudes shows that, in general, the Noah LSM has high TC correlations in regions where the ESA soil moisture product does not, and lower correlations in regions with ESA correlations close to one. A credit to the ESI is that in most lower-elevation regions in the Northern Hemisphere mid-latitudes, it rates well in area where either the ESI soil moisture or Noah LSM correlations are near one.

The regions with high VHI correlations in the Northern Hemisphere and Tropics is similar to the ESA soil moisture product, with lower correlations in the Southern Hemisphere. Overall, the SPI does not compare favorably to the other drought indicators, which is intuitive given that it accounts only for precipitation (a component of drought forcing) rather than the more direct measurements of drought severity provided by the other indicators.

It is worth noting that the lower correlations of ESI in the Southern Hemisphere relative to the Northern Hemisphere were expected given that JJA is the cool season and ET is not as active given that vegetation is at a minimum during these months. The performance of ESI in the Northern Hemisphere agricultural regions during JJA (the primary growing season) is superior to the other indices (see Fig. 4 for map of agricultural production).

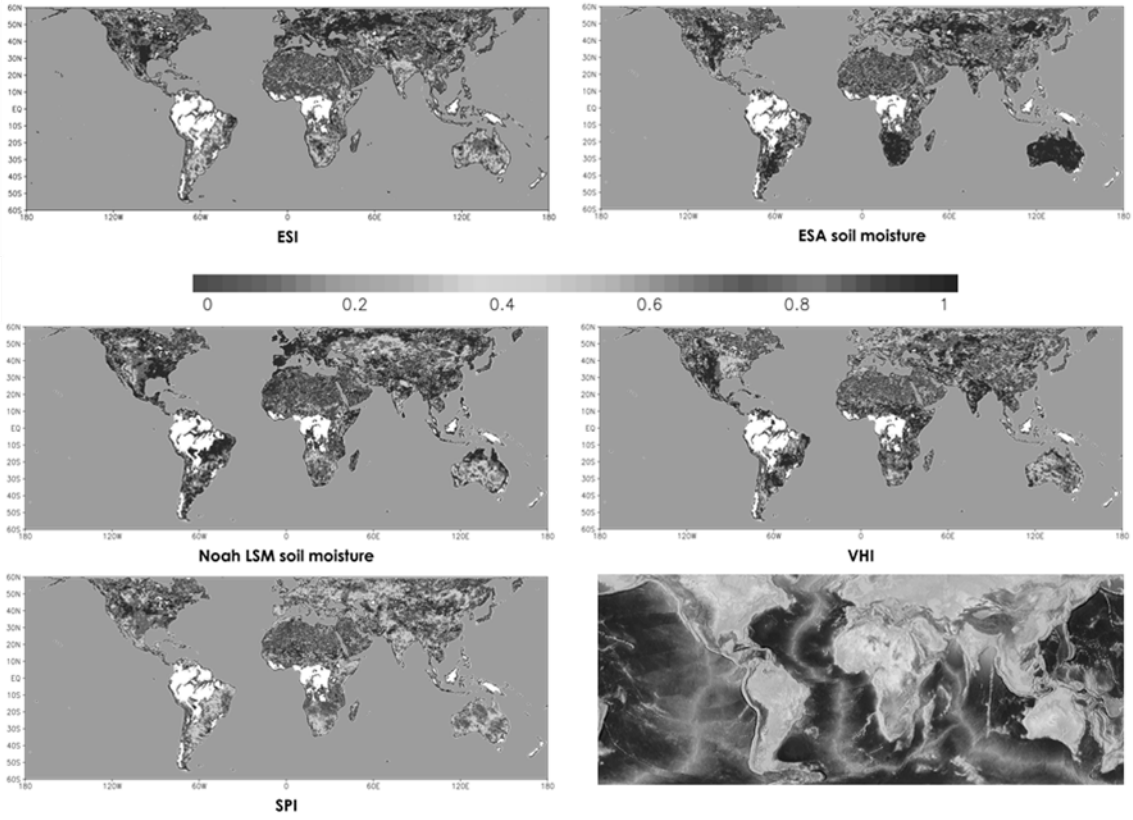

Figure 4. The TC correlation coefficients, found using 12-week averages of each drought index during JJA periods from 2001-2016 (all but lower right). Also included is a basic world topographical map (bottom right), taken from a free media repository atlas of the world.

B. 4-week lag correlation analysis with vegetative health

Given the focus of this paper, the results in this section are limited to the lag correlation analyses done between the ESI and vegetation during the JJA period (Fig. 5). Although it is not statistically appropriate to compare the magnitudes of the TC and lag-correlation results, both analyses indicate the highest correlations were found in the mid-latitudes of the Northern Hemisphere. This is true for both the NDVI and the LAI, with a much greater spatial variance of ESI performance using the LAI as a vegetative health indicator. Additionally, overall correlation values in the Southern Hemisphere mid-latitudes (Brazil, southern Africa, and Australia) compared more favorably with similar Northern Hemispheric latitudes than in the TC analysis.

Overall, the ESI was better correlated to lagged NDVI than lagged LAI. In the tropics, the ESI provides a bit of predictive power, with correlations generally between 0.3 and 0.5. Conversely, the majority of ESI correlations with LAI were close to zero in the Tropics, which contains mostly desert in arid areas (i.e., LAI ~ 0) and rain forests in wet regions (LAI ~ 1) with an invariant leaf cover. The biggest takeaway from this ESI lag-correlation analysis is that it appears the ESI provides an advanced forecast of vegetation health in the mid-latitudes, which contains much of the global agricultural output (Fig. 5).

The biggest overall takeaway from this ESI lag-correlation analysis is that it appears the ESI provides an advanced forecast of vegetation health in the mid-latitudes, which contains much of the global agricultural output (Fig. 5). This is supported by both the NDVI and LAI assessments. The correlation values should be taken with a grain of salt as summertime conditions, relative to normal, tend to be autocorrelated on monthly and seasonal time scales. However, the lag-correlation analysis provides an increased confidence, in combination with the TC correlation analysis, that the ESI can be used effectively in an early drought warning system for most global agricultural regions.

Four weeks was chosen as a representative lag for the effects of negative anomalies in ground moisture fluxes (indicated by ESI) to influence the vegetative health in agricultural regions. If the focus of this study was the effects of moisture deficits in forested regions, a longer lag would be more appropriate. Future work will include a more comprehensive examination of different lag times to evaluate the ESI's capability to forecast drought onset on multiple temporal scales. Additionally, we will explore the blending of ESI with other drought indicators.

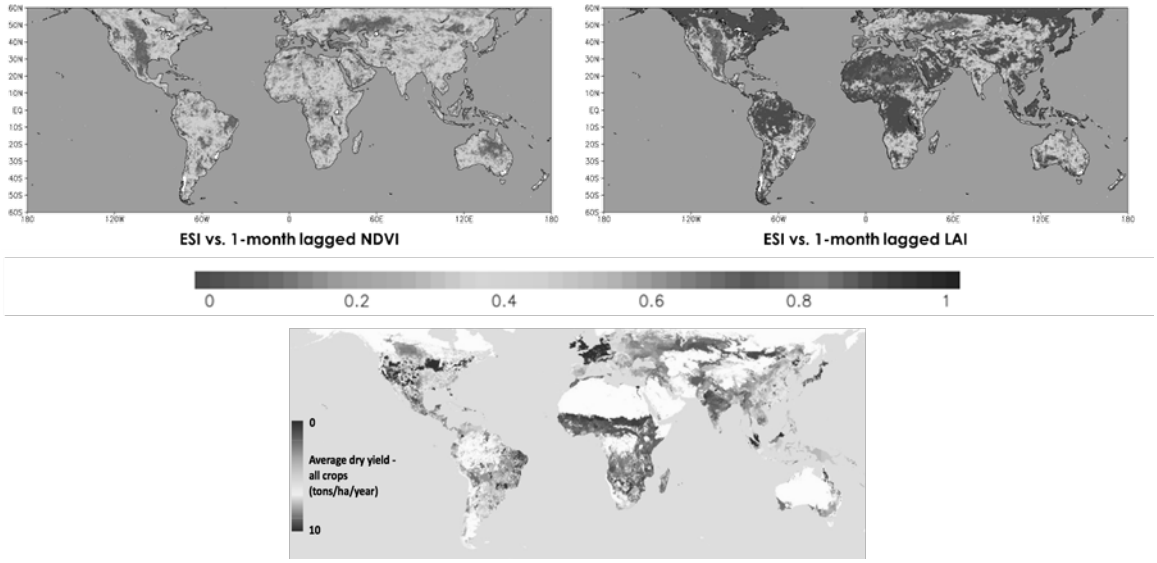

Figure 5. The overall JJA correlation between ESI and NDVI (top left) and ESI and LAI (top right), using data from 2001-2016. Included is an assessment of the cropland distribution and average annual yield (bottom), taken from West et al. (2010).

V. Discussion

In this paper, we explored methods for comparing the effectiveness of ESI as a global drought indicator, and more importantly as a potential early indicator for summertime agricultural drought. TC analysis is a common method used to quantify performance of soil moisture and moisture flux indices, which lack reliable global observations. TC analysis allows for computation of correlations to an unknown truth to objectively quantify the capability for ESI to monitor global summertime ET in comparison to four other commonly used global drought products (ESA soil moisture, Noah LSM soil moisture, VHI, and SPI). The key takeaway is that the ESI is a reliable drought indicator during the summertime months in most regions of the world with significant agricultural production. Lag-correlation analysis comparing ESI to future vegetative health indicated that correlations were highest in these same agricultural regions. Because of these findings, work is in progress to make ESI a cornerstone of a summertime drought early warning system. As previously mentioned, the summertime (JJA) is critical for crop yields because it contains the majority of the growing season for most of the world's agriculture.

The results of this paper have led to important research questions the authors will seek to answer in the near future. The first is to create an optimal and objectively-constructed set of global drought monitoring products that blends the

drought indices from this study (and potentially additional products). The TC analysis correlations can be used as a foundation for the blending with the relative weight of each product varying by region, season, and time scale (i.e., short-term vs. long-term). Testing can be used to determine whether a single indicator is sufficient or it is appropriate to used several products, and this includes validation against *in situ* observations.

Our future work aims at providing an objective, global drought assessment product, with seasonal variations in the blending of products weighted by indices providing the most information for a given time of year and time scale. For instance, ESI will be weighted heavily during the Northern Hemisphere's growing season. Our current work and planned future work has potentially significant ramifications for global drought monitoring efforts in that the current approach of subjectively blending different drought indicators may be replaced by a statistically-valid, objective blending of global drought products. The same blending approach can be applied to the lag-correlations to objectively determine an ideal blending of products to provide drought early warning. Of particular importance will be examining lag-correlations at different time scale for historical cases of rapid drought onset. These analogs could be used to make probabilistic forecasts for an upcoming growing season. Expansion of the analysis to look at December-January (DJF) lag-correlations will provide a better sense of the ESI's drought warning capabilities in the Southern Hemisphere. Future

Acknowledgments

McRoberts would like to acknowledge the guidance, support, and efforts of the team at the NASA-SPoRT, and in particular my mentor for this project and co-author Dr. Christopher Hain, project advisor Dr. Gary Jedlovec, and Bradley Zavodsky. I would also like to acknowledge the support of the NASA Marshall Space Flight Center Faculty Fellowship Program and in particular Dr. Gerald Karr, Dr. Frank Six, Rachael Damiani, and Mona Miller.

References

[1]Anderson, M. C., Hain, C., Otkin, J., Zhan, X., Mo, K., Svoboda, M., Wardlow, B., and Pimstein, A., "An Intercomparison of Drought Indicators Based on Thermal Remote Sensing and NLDAS-2 Simulations with U.S. Drought Monitor Classifications," *Journal of Hydrometeorology*, Vol. 14, No. 4, 2013, pp. 1035-1056.

[2]Anderson, M. C., Norman, J. M., Mecikalski, J. R., Otkin, J. A., and Kustas, W. P., "A climatological study of evapotranspiration and moisture stress across the continental U.S. based on thermal remote sensing: 1. Model formulation.," *Journal of Geophysical Research*, Vol. 112, 2007, pp. D10117.

[3]Anderson, M. C., Norman, J. M., Mecikalski, J. R., Otkin, J. A., and Kustas, W. P., "A climatological study of evapotranspiration and moisture stress across the continental U.S. based on thermal remote sensing: 2. Surface moisture climatology.," *Journal of Geophysical Research*, Vol. 112, 2007, pp. D11112.

[4]Anderson, M. C., Norman, J. M., Diak, G. R., Kustas, W. P., and Mecikalski, J. R., "A two-source time-integrated model for estimating surface fluxes using thermal infrared remote sensing," *Remote Sensing of Environment*, Vol. 60, 1997, pp. 195-216.

[5]Norman, J. M., Kustas, W. P., and Humes, K. S., "A two-source approach for estimating soil and vegetation energy fluxes from observations of directional radiometric surface temperature," *Agricultural and Forest Meteorology*, Vol. 77, 1995, pp. 263-295.

[6]Anderson, M. C., Hain, C. R., Wardlow, B., Mecikalski, J. R., and Kustas, W. P., "Evaluation of a drought index based on thermal remote sensing of evapotranspiration over the continental United States," *Journal of Climate*, Vol. 24, 2011, pp. 2025-2044.

[7]McNaughton, K. G., and Spriggs, T. W., "A mixed-layer model for regional evaporation," *Boundary-Layer Meteorology*, Vol. 34, No. 3, 1986, pp. 243-262.

[8]Monteith, J. L., "Evaporation and environment," *The State and Movement of Water in Living Organisms, Symposium for the Federation of American Societies for Experimental Biology*, Vol. 19, 1965, pp. 205-234.

[9]Stoffelen, A., "Toward the true near-surface wind speed: Error modeling and calibration using triple collocation," *Journal of Geophysical Research*, Vol. 103, 1998, pp. 7755-7766.

[10]Han, E., Crow, W. T., Holmes, T., and Bolten, J., "Benchmarking a Soil Moisture Data Assimilation System for Agricultural Drought Monitoring," *Journal of Hydrometeorology*, Vol. 15, 2014, pp. 1117-1134.

[11]Wan, Z., Wan, S. H., and Hulley, G., "MOD11C1 MODIS/Terra Land Surface Temperature/Emissivity Daily L3 Global 0.05Deg CMG V006. NASA EOSDIS Land Processes DAAC," *Land Surface Temperature Database* [online database], URL: http://doi.org/10.5067/MODIS/MOD11C1.006 [cited 1 September 2017].

[12]Wan, Z., Wan, S. H., and Hulley, G., "MOD11C1 MODIS/Aqua Land Surface Temperature/Emissivity Daily L3 Global 0.05Deg CMG V006. NASA EOSDIS Land Processes DAAC," *Land Surface Temperature Database* [online database], URL: http://doi.org/10.5067/MODIS/MYD11C1.006 [cited 1 September 2017].

[13]Enenkel, M., Reimer, C., Dorigo, W., Wagner, W., Pfeil, I., Parinussa, R. and De Jeu, R., "Combining satellite observations to develop a global soil moisture product for near-real-time applications," *Hydrology and Earth System Sciences*, Vol. 20, No. 10, 2016, 4191-4208.

[14]Ek, M. B., Mitchell, K. E., Lin, Y., Rogers, E., Grunmann, P., Koren, V., Gayand, G., and Tarpley, J. D., "Implementation

of Noah land surface model advances in the national centers for environmental prediction operational mesoscale eta model," *Journal of Geophysical Research*, Vol. 108, pp. 8851.

[15]McKee, T. B., Doesken, N. J., and Kleist, J., "The relationship of drought frequency and duration to time scales.," *Preprints, Eighth Conf. on Applied Climatology*, American Meteorological Society, Anaheim, CA, 1993, pp. 179-184.

[16]Ashouri, H., Hsu, K. L., Sorooshian, S., Braithwaite, D. K., Knapp, K. R., Cecil, L. D., Nelson, B. R. and Prat, O. P., "PERSIANN-CDR: Daily precipitation climate data record from multisatellite observations for hydrological and climate studies," *Bulletin of the American Meteorological Society*, Vol. 96, No. 1, 2015, pp.69-83.

[17]Tucker, C. J., Pinzon, J. E., Brown, M. E., Slayback, D., Pak E. W., Mahoney, R., Vermote, E., and El Saleous, N., "An Extended AVHRR 8-km NDVI Data Set Compatible with MODIS and SPOT Vegetation NDVI Data," *International Journal of Remote Sensing*, Vol 26, No. 20, 2005, pp. 4485-4498.

[18]Ranga, M., Knyazikhin, Y., Park, T., "MOD15A3H MODIS/Combined Terra+Aqua Leaf Area Index/FPAR Daily L4 Global 500m SIN Grid," *NASA LP DAAC* [online database], URL: http://doi.org/10.5067/MODIS/MOD15A3H.006 [cited 1 September 2017].

[19]Anderson, M. C., Zolin, C. A., Hain, C. R., Semmens, K., Yilmaz, M. T. and Gao, F., "Comparison of satellite-derived LAI and precipitation anomalies over Brazil with a thermal infrared-based Evaporative Stress Index for 2003–2013," *Journal of Hydrology*, Vol. 526, 2016, pp. 287-302.

[20]Scipal, K., Holmes, T., De Jeu, R., Naeimi, V. and Wagner, W., 2008, "A possible solution for the problem of estimating the error structure of global soil moisture data sets," *Geophysical Research Letters*, Vol. 35, No. 24, 2008, pp. L24403.

[21]Konings, A. G., McColl, K. A., Alemohammad, S. H. and Entekhabi, D., 2015, "Calculating Absolute Error Variances from Triple Collocation," Technical Paper, Massachusetts Inst. Of Technology., Boston, MA, 2015.

[22]McColl, K. A., Vogelzang, J., Konings, A. G., Entekhabi, D., Piles, M. and Stoffelen, A., "Extended triple collocation: Estimating errors and correlation coefficients with respect to an unknown target," *Geophysical Research Letters*, Vol. 41, No. 17, pp. 6229-6236.

Simulation of Neutrino Detection and Background Rejection for a Heavy Liquid Scintillator in a Space Environment

Robert McTaggart[1]
South Dakota State University, Brookings, SD, 57007

Abstract: The GEANT4 simulation package is used to study a liquid scintillator detector to be placed within 10 solar radii of the Sun. Signal strength is enhanced by taking advantage of the inverse square law, reducing signal attenuation via a smaller detector, replacing hydrogen with deuterium in the liquid scintillator, and doping the detector with gallium. The preliminary design includes a heat shield made of carbon foam, a tungsten shield to block solar particles, a tungsten detector shell, and a veto made of scintillating fiber. An initial design is tested by simulating primary background sources (gamma rays and Galactic Cosmic Ray protons), as well as several neutrino processes.

Nomenclature

ν_e	=	electron neutrino
$\bar{\nu}_e$	=	antielectron neutrino
e^-	=	electron
e^+	=	positron
γ	=	gamma ray
d	=	deuterium or deuteron or ^2H
GCR	=	Galactic Cosmic Ray
DGRB	=	Diffuse Gamma Ray Background
AU	=	Astronomical Unit
MeV	=	One Million electron-Volts
GeV	=	One Billion electron-Volts
TeV	=	One Trillion electron-Volts
eV	=	One electron-Volt = 1.602 E-19 Joules

I. Introduction

The neutrino is a subatomic particle that is produced by nuclear processes such as radioactive decay, nuclear fission, supernovae, solar particle events, and the fusion that powers the Sun. The Sun is largely transparent to the neutrino because the neutrino interacts so weakly with everything else. Whereas photons can bounce around within the Sun for thousands of years, the almost massless and completely chargeless neutrino escapes at the speed of light. Thus neutrinos offer a unique opportunity to image the internal dynamics of the Sun.

When experiments like those performed deep underground by Davis and Bahcall at the Homestake Mine in South Dakota started to look for solar neutrinos[1], the number of electron neutrinos they detected at 1 AU was roughly one-third the number that should have been found from the Sun.

Fortunately, a solution existed in the theory of *neutrino oscillation*[2]. Due to its tiny but non-zero mass, the electron neutrino can transform (or oscillate) into either a muon neutrino or a tau neutrino. If the other two do not interact with the detector, then it is easy to see neutrinos go missing if only electron neutrinos interact.

Today, terrestrial neutrino searches[3,4,5] have improved by removing naturally-occurring radioactive impurities from materials, improving detector technologies, going underground to reduce the cosmic ray background, building

[1] Associate Professor of Physics, Department of Physics, South Dakota State University

much larger detectors, and operating longer. So why should one consider space-based neutrino detection near the Sun?

A space-based detector would apply the inverse-square law to increase the flux of neutrinos[6]. At 7 solar radii the flux increases by a factor of 1,000. At 3 solar radii the flux increases by a factor of 10,000. Smaller detectors then become more feasible if not desirable, as they can reduce losses due to light attenuation seen in very large Earth-based detectors.

Moreover, a space-based detector is not confined to the plane of the ecliptic. Polar orbits inside of 10 solar radii from the Sun benefit neutrino science because (a.) neutrinos pass through less matter at the poles compared with the equator, (b.) orbits will not be completely circular so distances will vary, and (c.) the neutrino flux is incoherent. Thus polar orbits may have great potential for neutrino oscillation physics and investigation of the solar dynamo[7,8].

II. Solar Neutrino Detector Design

Solar neutrinos[9] have energies between 0 and 18 MeV, and the detector design intends to maximize neutrino signals in this energy range while reducing the background noise.

For some perspective of what 18 MeV means, 1 MeV is one million electron-Volts, and one electron-Volt (eV) is the energy that an electron acquires after passing through a one Volt battery. Chemical processes are on the order of a few electron-Volts, and typical high energy processes surpass 1 GeV (1000 MeV). In fact, Galactic Cosmic Ray (GCR) protons on the order of a few TeV (1000 GeV) may hit the detector once per day.

Solar neutrino production occurs copiously via the proton-proton (pp) fusion[10] process up to 0.423 MeV, with contributions from Nitrogen-13, Oxygen-15, and Fluorine-17 extending to almost 2 MeV. Beryllium-7 capture and proton-electron-proton (pep) fusion provide discrete neutrino lines around 1 MeV. At higher energies solar neutrinos only come from either Boron-8 or helium-proton (hep) fusion. Between 15.5 MeV and 19 MeV, only the hep channel contributes. Each process also occurs in a unique radial distribution within the Sun[9].

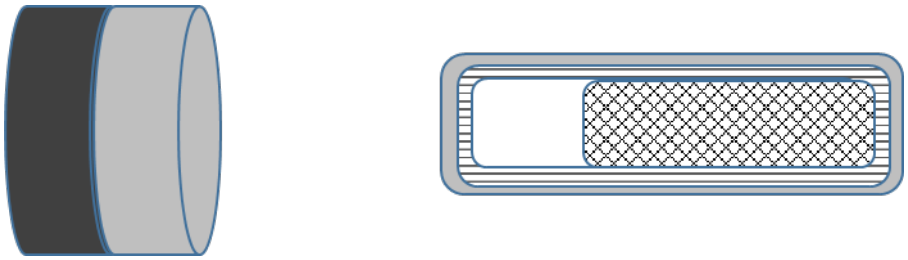

Figure 1. Conceptual Drawing of the NuSolar Detector.
The liquid scintillator occupies the interior of the object on the right.

At the heart of the neutrino detector is a cylinder of liquid scintillator, 44 cm in length, a radius of 15 cm, and a mass of 25 kg. Initially this was modeled as a mineral oil (CH_2) for its optical properties, but later it was changed to CD_2 where D is deuterium. We refer to CD_2 in this report as *heavy liquid scintillator*, since heavy water is D_2O.

Deuterium makes the liquid scintillator both a particle physics target and a detector, opening additional neutrino physics channels while keeping the favorable optical properties of the mineral oil. Studying neutrinos with deuterium is not new, as SNOLAB performed neutrino searches with heavy water[11], but using deuterium in liquid scintillator is relatively new. Simulations assume that the hydrogen is 98% Deuterium, 1% Protonium, and 1% Tritium. We note that a few neutrino reactions are also possible with antineutrinos.

Doping the scintillator with gallium is done to achieve sensitivity below 2 MeV, ultimately pairing a delayed second pulse to go with the electron. Simulations used 1% natural gallium by weight as a dopant in the heavy scintillator, but the simulation forces the use of Gallium-69 for the kinematics of a neutrino collision with gallium.

The m1 state of Germanium-69 emits a 87 keV gamma ray with a half-life of 5 microseconds. The end result is an electron pulse followed by a gamma ray for background rejection. As a result, the detector would have access to some of the neutrinos produced by the pp channel. Other solar neutrino experiments like GALLEX[12] have used Gallium-71, which yields Germanium-71 with the emission of a 198 keV gamma ray 20 milliseconds later. An alternative would be Indium-115 considered by the LENS[13] Collaboration. This has a lower threshold and an excited state in Sn-115 that emits a pair of gamma rays at 116 and 497 keV after 3.2 microseconds. Ultimately timing issues, optical clarity of the scintillator, and the ability to detect specific gamma rays at each energy for each dopant and its concentration will be defined in a future study, which will require both timing and optical photons to be integrated into the Geant4 simulation program.

Surrounding the liquid scintillator is a 1.5 centimeter polystyrene shell representing a scintillating fiber veto detector made of polystyrene. Individual fibers are not modeled in the simulation. A shell made of tungsten with a thickness of 0.5 cm surrounds both the veto and the liquid scintillator detectors. The liquid scintillator volume is placed slightly off-center to accommodate future data acquisition and power inside the veto. In front of the detector we place a tungsten disk with a thickness of 10 cm and a radius of 40 cm to block solar electrons and protons. There is 30 cm of empty space between this shield and the detector.

Tungsten has been selected in part due to its high melting point and its ability to shield radiation[14, 15, 16] without the toxicity of lead. While developing new shielding materials with tungsten or other high-Z materials would have other applications, for now the disk is pure tungsten and the 10 cm thickness awaits further optimization. To improve heat rejection, about 12 cm of a carbon foam is placed in front of the tungsten disk, inspired by the Solar Probe Plus mission[17]. The temperatures behind the shield should stay around 21 degrees °C without the carbon foam, which will maintain the chemical stability of the liquid scintillator.

It is clear that particles can scatter from anything in the infrastructure and generate unwanted background events, so the efficacy of the veto detector in rejecting said background events is very important. In other words, how many events leave energy in the liquid scintillator detector while leaving no signal in the fiber veto detector, thus generating false positives. Later the veto detector can be improved by using either more fiber, different detectors, or enhanced shower generation. Optical photons were not modeled in the present simulations.

The timing of events will be important in discriminating background events from real neutrino events. Namely that events that produce signals in the veto detector before or after passage through the scintillator should be rejected, and events that occur in the scintillator first are more likely to be candidates for a neutrino event.

III. The Galactic Cosmic Ray Background

Cosmic rays outside the solar system obey a power law spectrum, and their propagation in the galaxy can be described using a "Leaky-Box" model incorporating diffusion and the magnetohydrodynamics of plasmas[18]. But the solar magnetic field helps to reduce the flux of lower energy particles, which modulates the aforementioned power law[19]. An analysis was performed by Nasser Barghouty and a summer student Shivam Hingorani to describe the Galactic Cosmic Ray Background which is modulated by the solar wind at a location inside 10 solar radii starting with data collected at 1 AU by PAMELA[20]. Basically the solar magnetic field produces a pressure that the incoming background particles must fight through. They used data collected by PAMELA in 2006 at a solar minimum, assuming that any other condition will reduce cosmic rays even further via turbulence.

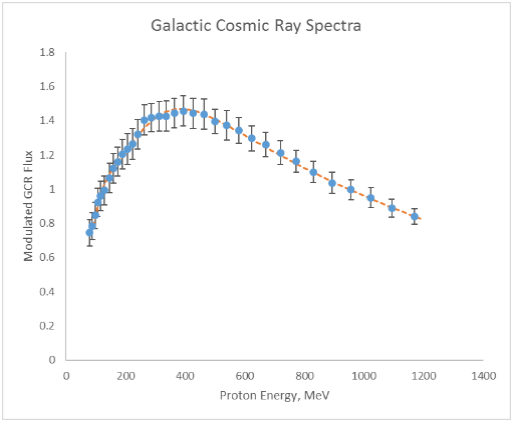

Figure 2. Modulated Galactic Cosmic Ray Spectra and fit below 1200 MeV.

The modified cosmic ray flux was then fit by a phenomenological model of a power law (α = -2.7) times a 5th-order polynomial with energy-dependent parameters between 80 MeV and 40 GeV, and then extrapolated out to 4 TeV. The resulting histogram was used to weight an energy spectrum for starting primary protons for the Geant4 Monte Carlo. The protons were started on the surface of a one-meter radius sphere surrounding the detector as the isotropic soource. In Figure 2 one can see the fit between 0 and 1200 MeV.

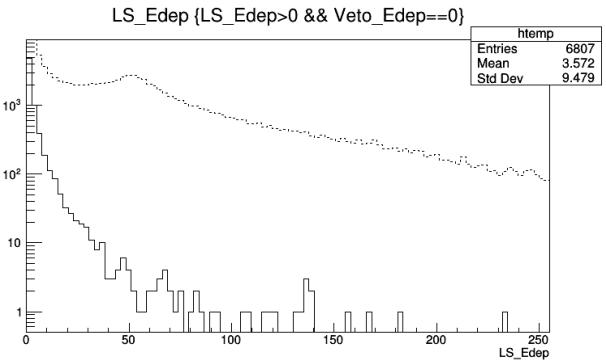

Figure 3. Energy deposition in the liquid scintillator detector (above) and without any energy in the veto detector (below) for GCR protons.

The efficacy of the scintillating fiber veto detector was analyzed first by generating two million proton events in the Monte Carlo. Some of these events left a non-zero energy deposit in the liquid scintillator detector. A small fraction of these produced signals in the liquid scintillator without depositing any energy in said veto detector. That fraction is the failure rate (i.e. 100% minus this fraction is the success rate)...for the veto detector only.

Those events in the bottom graph of Figure 3 would be missed by the veto detector, and thus have the potential to contribute unwanted background events in the energies of the solar neutrino spectrum. We find that the overall failure rate of this initial design for GCR protons is 5% (or the success rate is 95%). Some of these low energy events would not become background candidates given future energy cuts in both the veto detector and the liquid scintillator detector.

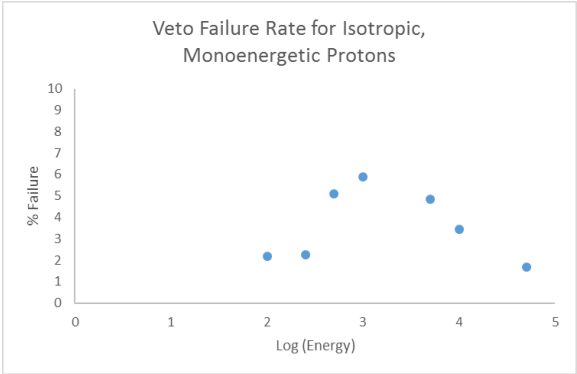

Figure 4. Veto failure rate for monoenergetic protons with an isotropic angular distribution.

Next, the failure rate was examined for discrete energies, as shown in Figure 4. The failure rate was above average between 50 MeV and 5 GeV, which is important for future shielding and veto detector design.

The other benefit of such collecting this data at different energies is that one may determine a rate for these unwanted events. One may calculate this rate in events per second based upon the phenomenological function in Eq. (1.).

The 100,000 is the number of events in the simulation, and recall that a spherical surface of radius 1 meter provided the isotropic protons. Note that not all of the protons go into the volume, which is why there is no "4π". The number of background events is just the number one finds in a graph like Figure 3 at each proton energy. In Table 1 we summarize the anticipated rates for events that escape rejection.

Please note that all events, whether they deposit an energy in the range that solar neutrinos would or not, are counted if they pass this particular set of data cuts. Additional cuts on energy or event topology (like requiring double pulsing) would reduce the rates.

$$(1.)\ \left(\frac{\#}{\text{MeV - m}^2\text{ - s - sr}}\right)*(\text{Energy[MeV]})*\left(\frac{\pi*1\text{m}*1\text{m}}{100{,}000}\right)*(\#\text{ of bkg events})$$

Galactic Cosmic Ray Protons		
Energy (MeV)	Number of Events per Second	Number of Events per Day
100	9.58E-02	8,280
250	1.07E+00	92,148
500	5.76E+00	497,387
1,000	1.12E+01	964,751
5,000	5.93E+00	512,288
10,000	2.11E+00	181,933
50,000	9.05E-01	78,234

Table 1. Expected GCR Background Rates in the Liquid Scintillator

IV. The Diffuse Galactic Gamma Ray Background

Recently, the Fermi Large Area Telescope (*Fermi* LAT) analyzed the diffuse gamma ray background (DGRB)[21]. Between 1 MeV and 279 GeV it follows a power law of -2.31 before dropping off. We repeat what was done for GCR protons for an isotropic diffuse gamma ray background[22] with this new power law, and then with several monoenergetic gamma rays.

There were not a lot of very high energy gamma rays in the overall distribution for 2 million gamma rays, and perhaps 10 million or more would bring those out. But part of this is simply geometry, and part is due to many more events being generated near 1 MeV that simply do not make it to the liquid scintillator. In Figure 5, the spectrum for events in the liquid scintillator detector that fail to leave energy in the veto detector is shown below the spectrum for those events that leave any non-zero energy in the detector.

22,643 of the 37,030 events leaving anything in the liquid scintillator made it through, for an apparent failure rate of 61.1%. Notably, much of this energy is in the solar neutrino energy range.

When monoenergetic beams of gamma rays were sent into the detector (as in Figure 6) for 100,000 events, it becomes clear that much of the inefficiency occurs for 10 MeV gammas and below, and after 100 MeV the failure rate flattens out. It may be that a different veto detector with metal layers could help with shower development in the veto for lower energy gammas to help identify background events.

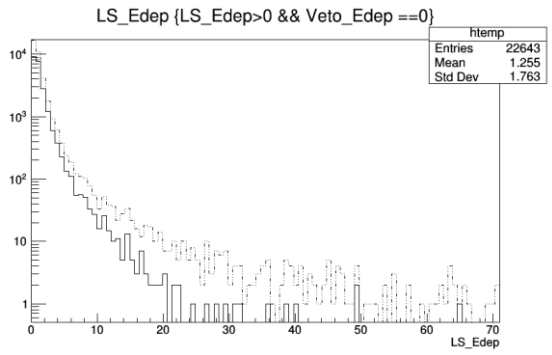

Figure 5. Energy deposited in the liquid scintillator by the Diffuse Gamma Ray Background (above) and without deposition in the veto (below).

As with the GCRs, we apply a formula to determine the background rate from the DGRB. However, since we take the gamma ray intensity from Ref. 21 that uses a E^2dN/dE curve, we divide by the energy in Eq. 2. This leads to a summation of the background rates at the energies listed in Table 2 below.

$$(2.)\ \left\{\left(\frac{\#\ *\ \mathrm{MeV}}{\mathrm{cm}^2\text{ - s - sr}}\right)/\left(\mathrm{Energy}[\mathrm{MeV}]\right)\right\} * \left(\frac{\pi * 100\mathrm{cm} * 100\mathrm{cm}}{100{,}000}\right) * \left(\#\ \mathrm{of\ bkg\ events}\right)$$

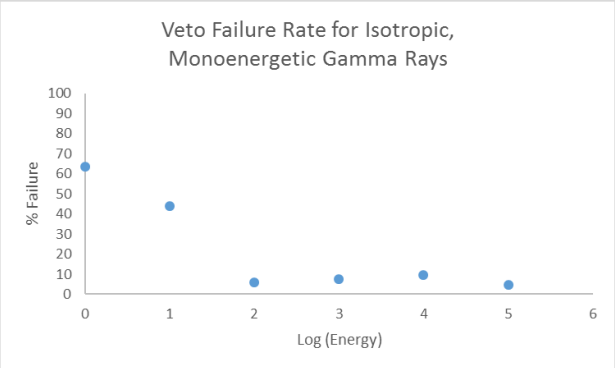

Figure 6. Veto Failure Rates for isotropic gamma rays up to 100 GeV.

Diffuse Gamma-Ray Background		
Energy (MeV)	Number of Events per Second	Number of Events per Day
1	1.29E+00	111,831
10	6.01E-02	5,195
100	1.30E-03	112
1,000	8.44E-05	7.3
10,000	5.44E-06	0.47
100,000	1.78E-07	0.015

Table 2: Anticipated background event rates for gamma rays (left) and cosmic ray protons (right) that leave energy in the liquid scintillator but by-pass the veto.

V. Solar Protons, Electrons, Neutrons

Simulations were performed with protons (4-200 MeV), electrons (10 – 100 MeV), and neutrons (10 MeV – 1000 GeV) hitting normal to the carbon foam in a beam configuration. Nominally these would simulate the impact of any solar particle event. The good news is that neither protons nor electrons from solar proton events appear to leave an energy deposit.

Most of the neutrons are stopped as well. 100,000 neutrons obeying a power law with $\alpha = -3$ to mimic a solar particle event were sent in a beam to the front of the assembly. 3,338 of these left some energy in the liquid scintillator detector in Figure 7. 1,237 of these did not leave anything in the veto, for a failure rate of 37%. But another way to look at it is that shielding and the veto kept 100 * (100,000 – 1,237) / 100,000 = 98.7% of the events that hit the carbon foam from reaching the liquid scintillator undetected by the veto.

The good news is that outside of solar particle events, few if any solar neutrons are anticipated. To be clear, there will still be neutrons from background events and sometimes from neutrino channels.

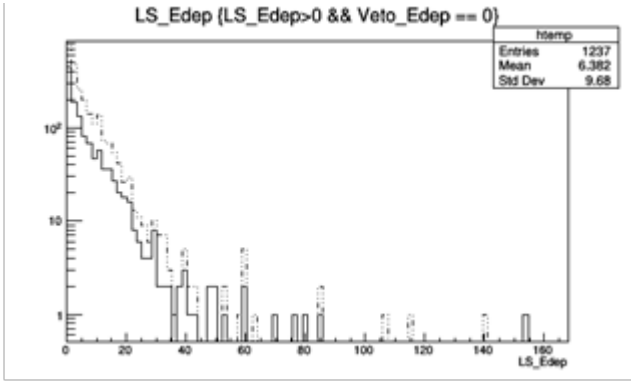

Figure 7. Energy deposition of solar neutrons from a solar particle event in the liquid scintillator detector (top) and those events that were not detected by the veto detector (bottom).

While the detector is not currently being optimized for solar neutrons, their study would also benefit from a closer proximity to the Sun. In fact, the slower the solar neutron, the closer to the sun one has to be to observe it before it decays (about 15 minutes in its rest frame). Such neutrons may provide insight into solar flare

development[23, 24] since they are not affected by solar magnetic fields, and would complement other gamma-ray data coming from neutron capture.

VI. Simulation of Neutrino Events

Currently Geant4[25] does not include any libraries for neutrino cross sections or process any neutrino events. However, it will produce them and pass them along in straight lines, and one can build filters to count the number of neutrinos that hit a given volume. As a result, only the by-products of neutrino collisions with the detector are modeled within the PrimaryGenerationAction subroutine, including all relevant kinematics to perform boosts back to the rest frame of the detector. Further analysis is required to make the connection to event rates.

In the macro that controls the physics of the simulation, we develop a volume source that occupies the same dimensions as the liquid scintillator detector. The first particle gun selects a random location in that volume and fires a neutrino in the z-direction. This neutrino is not physical: It is just being used to deliver the energy and a random location for the other particle guns that are utilized in the program, and the neutrino produced will not interact with anything.

Next, the kinematics for collisions like those in Eqs. (3.) and (4.) below are determined. The program assumes that the total 3-momentum must always lie along the positive z-axis. Currently each neutrino process requires a separate run of the NuSolar program.

$$(3.)\ \nu_e + d \rightarrow {}^2He + e^- \ ;\ {}^2He \rightarrow p + p$$

$$(4.)\ \nu_e + {}^{69}Ga \rightarrow {}^{69}Ge^{m1} + e^- \ ;\ {}^{69}Ge^{m1} \rightarrow {}^{69}Ge + \gamma$$

Processes described by Eq. (4.) and others that also generate a delayed gamma ray are of interest because they generate a double-pulse to help eliminate backgrounds through a topological cut.

The simulations for the 3-body processes that make up neutrino channels in the heavy liquid scintillator detector currently do not assume any weighting in phase space (i.e. all distributions are "flat"). So while the final energies may be appropriate, the number of particles at each energy may change once that is incorporated.

If the process goes through an intermediary resonance, it is generated with the other particle (i.e. an electron, positron, neutrino, or antineutrino) back-to-back in the total center of mass frame. The decay products of the resonance are generated back-to-back in the center of mass frame of said resonance. Then all final state particles are boosted back to the lab frame (where the detector is at rest), and the Geant4 particle gun is fired for each one individually with the corresponding energy, particle type, momentum direction, and charge if necessary.

In the case where there is no intermediary resonance, the energy for the electron/positron/neutrino/antineutrino is found by randomly choosing an energy between the minimum and maximum allowed energies, and then the program shares the remaining momentum and energy with the other two particles as if there were a resonance.

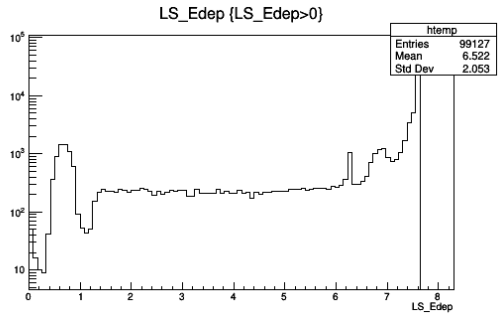

Figure 8. Energy deposition in the liquid scintillator detector for 100,000 9-MeV neutrinos that interact at random locations within the liquid scintillator detector for Eq. (3.). An intermediary Helium-2 is produced.

In Figures 8 and 9 we provide a representative energy deposition in the liquid scintillator detector for Eqs. (3.) and (4.) respectively. For brevity, only the spectra for 9 MeV neutrinos are shown. We note that the topology of the two processes are slightly different, and that the abscissa uses Log units to bring out some of the detail. Eventually one may be able to model a profile of a neutrino energy deposition for each process in addition to looking at timing information

There are a couple of neutrino processes that are not distinguishable from antineutrino processes. In Eq. (5.) the neutrino/antineutrino simply breaks up the deuterium, and in Eq. (6.) the neutrino/antineutrino places the Carbon-12 into an excited state that decays back into the Carbon-12 ground state with the emission of a 15 MeV gamma ray.

$$(5.)\ \nu_e + d \rightarrow p + n + \nu_e$$
$$(6.)\ \nu_e + {}^{12}C \rightarrow {}^{12}C^{*} + \nu_e'$$

One sees in Figure 10 that there is energy above 9 MeV in the liquid scintillator. We believe this is the result of spallation with the Carbon-12 in the scintillator or the veto, which has energy states at 4.4 MeV and 7.3 MeV above the ground state that can release one or more alpha particles. Proton filters in the program have accumulated new proton tracks where none existed before (just deuterium and carbon in the detector).

Because the reaction in Eq. (6.) only begins at just above 15 MeV and the solar neutrino spectrum ends at 18 MeV, it will have a limited role in solar neutrino detection. However, it may play a greater part in antineutrino detection for astrophysical searchers or for solar particle events. In Figure 11 we show an initial energy deposition plot at 16 MeV, close to the threshold. Likely what is happening is that either the slow-moving electron is completely absorbed (left), or the gamma-ray is completely absorbed (right) or partial energies are deposited.

The production of Nitrogen-12 in Eq. (7.) and its subsequent decay can be useful for the generation of a double-pulse for the highest energy solar neutrinos, but it has a half-life of 20 milliseconds and a threshold of 17.34 MeV[26, 27, 28]. Plus the inclusion of the beta decay in the program for Nitrogen-12 must wait for the next round of analysis. In essence that becomes a four-particle final state instead of a three-particle final state, and the energy distribution of that particular beta decay will definitely impact the results. Solar particle events also generate regular neutrinos with high energies, so this channel may become more important in those cases.

$$(7.)\ \nu_e + {}^{12}C \rightarrow {}^{12}N + e^{-}$$

For all of the neutrino processes, we see some events with extra protons, but no events with extra neutrons in the scintillator (above and beyond the number in the final state). More work is required, because the initial one or two neutrons may escape, and an extra one or two that are detectable could indeed be produced via spallation.

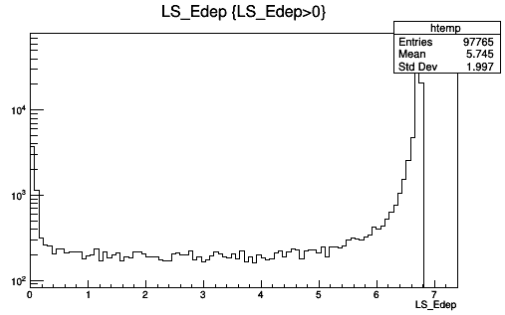

Figure 9. Energy deposition in the liquid scintillator detector for 100,000 9-MeV neutrinos that interact at random locations within the liquid scintillator detector for Eq. (2.). An intermediary m1 state of Gallium-69 is produced.

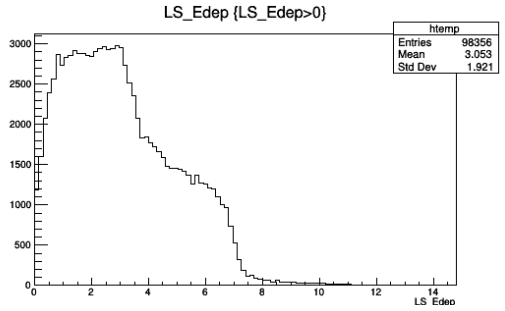

Figure 10. Energy deposition in the liquid scintillator detector for 100,000 random neutrino (or antineutrino) interactions within the liquid scintillator detector for Eq. (5.), the breakup of deuterium.

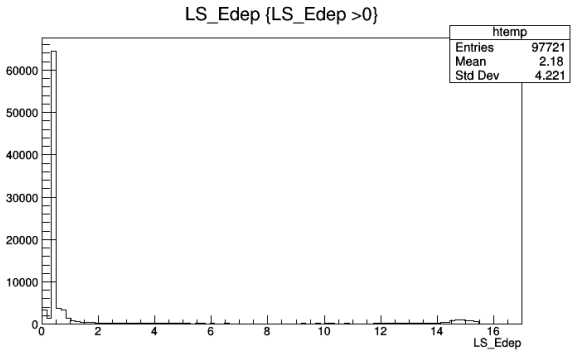

Figure 11. Energy deposition in the liquid scintillator detector for the Carbon-12 reaction in Eq. (4.) for 100,000 random neutrino interactions in the volume of the liquid scintillator and an energy of 16 MeV.

VII. Simulation of Antineutrino Events

Solar fusion does not generate antineutrinos, but the decays of pions from solar flare events do. While they are a potential background for solar neutrino studies, their detection would be of interest for the formation and progression of solar particle events. In addition, a prototype detector will likely need to be tested in a high flux of neutrinos, and one can only do that today with antineutrinos from research reactors or accelerators.

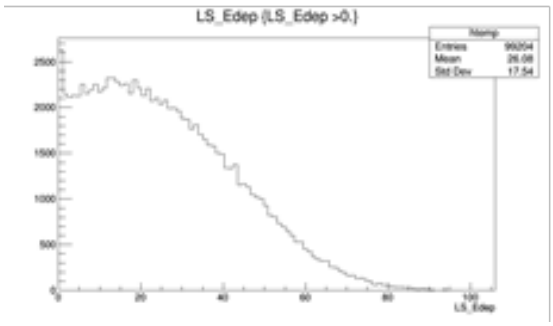

Figure 12. Energy deposition for 100 MeV antineutrinos obeying Eq. (6.), generated randomly throughout the liquid scintillator detector.

The use of deuterium facilitates two antineutrino channels for deuterium, but one of them (the break-up of deuterium) is shared with regular neutrinos in Eq. (5.). Thus Eq. (8.) is the unique antineutrino signal from deuterium. We note that if one were to use regular hydrogen instead of deuterium, then inverse beta decay with a threshold of 1.8 MeV would generate a single neutron and one positron back-to-back in the center-of-mass frame, as well as a gamma ray from a neutron capture that generates deuterium and a 2.22 MeV gamma ray about 250 μs later. It turns out that the threshold for Eq. (8.) is closer to 4 MeV due to the heavier masses involved.

$$(8.)\ \bar{\nu}_e + d \rightarrow n + n + e^+$$

Future studies need to evaluate the mixing of a dopant for neutron detection such as Gadolinium that has a high neutron capture cross-section to evaluate double-pulses. In figure 12 above we include the energy deposited in the liquid scintillator at 100 MeV (for solar flares), and 5 MeV (for testing with reactor antineutrinos) in Figure 13 without a neutron dopant.

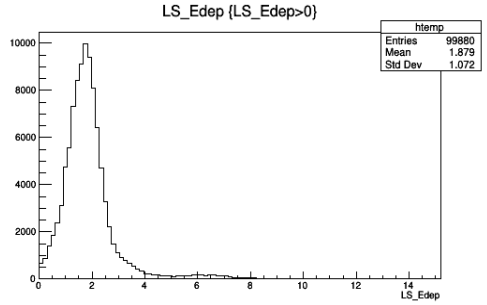

Figure 13. Energy deposition for 5MeV antineutrinos obeying Eq. (6.) for testing of a prototype near a reactor.

As with regular neutrinos, there exists an antineutrino channel in Eq. (9.) that generates Boron-12 and a subsequent beta decay which has not been evaluated by the NuSolar program. It has a slightly lower threshold of 14.39 MeV, but would also become more important for solar flare studies.

$$(9.)\ \bar{\nu}_e + {}^{12}C \rightarrow {}^{12}B + e^+$$

In Figure 14 the result of colliding 100 MeV antineutrinos with Carbon-12 is displayed. It is interesting to compare this plot with Figure 12, as that is also the result of events with 100 MeV antineutrinos, but a different channel.

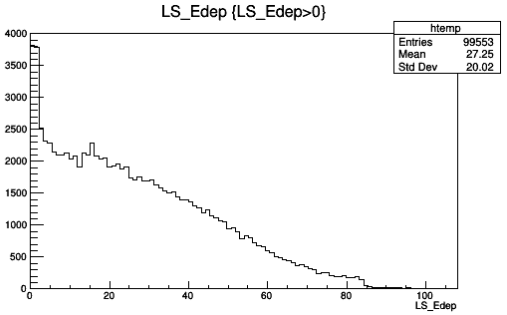

Figure 14. Energy deposition for 100 MeV antineutrinos that obey Eq. (6.), i.e. the inelastic scattering off of Carbon-12.

VI. Conclusions

The groundwork has been laid for future progress in the development of a space-based neutrino detector.

First, a phenomenological function (see the Appendix) was derived to describe the GCR proton spectrum based upon PAMELA data for a modulated proton spectrum using Excel. Second, a computer executable called NuSolar was built using the Geant4 simulation toolkit. The program not only compiled successfully, it generated plots in Root for use in analysis of several different backgrounds and filling ntuples with many different variables. Moreover, the response of several different neutrino topologies were evaluated, albeit without the necessary phase

space weighting for the energy distributions that can be included later. This program can be changed to suit the needs of future simulation work.

One of the surprising outcomes of the study was the apparent lack of any extra neutron production by solar neutrino processes given that spallation was occurring with the Carbon-12. At this point we cannot say whether the neutrons that generate tracks are the initial ones, or due to spallation. It would be interesting if extra neutrons could be used to help filter some background from neutrino events. Further study will be needed with neutron dopants like gadolinium, which may benefit the efficiency of processes like Eqs. (5.) and (8.).

In terms of future work, the main component necessary to improve the program is a full integration of timing for different events, particularly if double-pulses are to be evaluated. Optical photons were studied in the Summer 2016 Faculty Fellowship[29] that evaluated an antineutrino detector based upon a cube of polyvinyltoluene doped with gadolinium and an anti-coincidence counter made of interlocking polystyrene panels. While optical photons are ultimately necessary to evaluate the detector response, the focus at this stage of development was simply energy deposition. In particular the trade-offs between more neutrino dopants like gallium vs. reduced light collection will depend on optical photons being in the program.

Other background analyses must wait for a more complete design, including naturally-occurring radioactivity in the materials selected and long-term radioactivity from activation products generated by cosmic rays or photoactivation by gamma-rays, or scattering and spallation from more physical infrastructure. This will lead to enhanced anti-coincidence architecture and perhaps different material selections stemming from the present study.

Appendix

For completeness, the function used to fit the PAMELA data for the GCR background is provided below. No data was fit beyond 40 GeV. The histogram that weighted the cosmic ray proton energies used this function until 4 TeV. In essence there was a lot of trial and error performed to fit the lower end of the spectrum successfully in Figure 2.

$$(10.)\; f(E) = E^{-2.7}\left(\sum_{n=0}^{5} a_n E^n e^{-\left(\frac{E}{b_n}\right)^{c_i}}\right)$$

n	a_n	b_n	c_n
0	-2268.4	3997.688	2.143394
1	34377.39	420705.9	0.621516
2	477.2909	583.399254	0.48393
3	-336.085072	12.62152606	0.491935263
4	11.68520684	5.976552396	0.530340166
5	0.00119948	29.87605958	0.688578763

Table 3. Coefficients used in fitting the modulated GCR spectrum for protons.

Acknowledgments

I would like to thank everyone who contributed to the Summer 2017 NASA MSFC Faculty Fellowship program, including Frank Six, Gerald Karr, Rachael Damiani, Mona Miller, and others. I would like to thank all of the staff at UAH Housing who made me feel at home in Huntsville. Finally I would like to thank the members of the team who supported and encouraged me all summer and provided sound guidance: Mark Christl, John Watts, Nickolas Solomey, Nasser Barghouty, Mohammed Sabra, Peter Bertone, and the summer student Shivam Hingorani.

References

[1]R. Davis. "A review of the homestake solar neutrino experiment." *Progress in Particle and Nuclear Physics,* Vol. 32, 1994, pp. 13-32.

[2]Y. Suzuki. "Solar Neutrinos". Accessed at http://www.slac.stanford.edu/econf/C990809/docs/suzuki.pdf. Accessed on July 30, 2017.

[3] K. Abe et al (Super-Kamiokande Collaboration). "Solar neutrino measurements in Super-Kamiokande-IV." *Phys Rev D* 94, 052010. 20 September 2016.

[4] R. Acciarri et al. "Long-Baseline Neutrino Facility (LBNF) and Deep Underground Neutrino Experiment (DUNE) Conceptual Design Report, Volume 4 The DUNE Detectors at LBNF." Submitted 12 Jan 2016. Accessed at https://arxiv.org/abs/1601.02984 on July 30, 2017.

[5] O. Smirnov et al. "Solar neutrino with Borexino: results and perspectives." Accessed at https://arxiv.org/pdf/1410.0779.pdf on July 30, 2017.

[6] N. Solomey. "Studying the Sun's Nuclear Furnace with a Neutrino Detector Spacecraft in Close Solar Orbit." AAS/Solar Physics Division Meeting. Volume 47. May, 2016.

[7] P.A. Sturrock, L. Bertello, E. Fischbach, D. Javorsek II, J.H. Jenkins, A. Kosovichev, A.G. Parkhomov, "An analysis of apparent r-mode oscillations in solar activity, the solar diameter, the solar neutrino flux, and nuclear decay rates, with implications concerning the Sun's internal structure and rotation, and neutrino processes," *Astroparticle Physics,* Vol. 42, February 2013, pp. 62-69.

[8] S. Turck-Chieze and S. Couvidat. "Solar neutrinos, helioseismology and the solar internal dynamics." *Rep. Prog. Phys.* **74** 086901 , 20 July 2011. https://doi.org/10.1088/0034-4885/74/8/086901 .

[9] M. Wurm. "Solar Neutrino Spectroscopy." April 24, 2017. Accessed at https://arxiv.org/pdf/1704.06331.pdf on August 1, 2017.

[10] Borexino Collaboration. "Neutrinos from the primary proton–proton fusion process in the Sun." Nature 512, 383-386. 28 August 2014. https://dx.doi.org/10.1038/nature13702.

[11] D. Waller for the SNO Collaboration. "Results from the Sudbury Neutrino Observatory." SLAC Summer Institute on Particle Physics (SSI04), Aug. 2-13, 2004. Accessed at https://www.slac.stanford.edu/econf/C040802/papers/WET001.PDF on July 30, 2017.

[12] D. Vignaud. "The GALLEX solar neutrino experiment." *Nuclear Physics B – Proceedings Supplements*. Vol. 60, No. 3, January 1998, pp. 20-29.

[13] S. Derek Rountree for the LENS Collaboration. "Mini-LENS: Operation of a Prototype Low-Energy Solar Neutrino Spectrometer Underground." APS Meeting, February 13, 2010. Accessed at http://www1.phys.vt.edu/~kimballton/lens/public/presentations/files/rountreeapsapr10.pdf on July 30, 2017.

[14] S. Chen, M. Bourham, A. Rabiei. "Attenuation efficiency of X-ray and comparison to gamma ray and neutrons in composite metal foams." *Radiation Physics and Chemistry.* Volume 117, December 2015, pp. 12-22. https://doi.org/10.1016/j.radphyschem.2015.07.003 .

[15] B. Klamm. "Passive Space Radiation Shielding: Mass and Volume Optimization of Tungsten-Doped PolyPhenolic and Polyethylene Resins." 29th Annual AIAA/USU Conference on Small Satellites. Accessed at http://digitalcommons.usu.edu/cgi/viewcontent.cgi?article=3188&context=smallsat on July 30, 2017.

[16] G. P. Lahti and P. F. Herrmann. "Comparison of Tungsten and Depleted Uranium in Minimum-Weight, Layered Shields for a Space Power Reactor. NASA Technical Memorandum X-1874, September 1969. Accessed at https://ntrs.nasa.gov/archive/nasa/casi.ntrs.nasa.gov/19690026439.pdf on July 30, 2017.

[17] "New Heat Shield to Protect Mission to the Sun." March 2, 2017. Accessed at https://science.nasa.gov/technology/technology-stories/heat-shield-protect-mission-to-sun on July 30, 2017.

[18] A.F. Barghouty. "A Review of the Ginzburg-Syrovatskii's Galactic Cosmic-Ray Propagation Model and Its Leaky-Box Limit." NASA/TP—2012–217464, July 2012. Accessed at https://ntrs.nasa.gov/archive/nasa/casi.ntrs.nasa.gov/20120013305.pdf on July 30, 2017.

[19] H.D. May. "Turn-up in the differential GCR energy spectrum below 100 MeV." Accessed at http://vixra.org/pdf/1111.0054v2.pdf on July 30, 2017.

[20] O. Adriani et al. "Measurements of Cosmic-Ray Hydrogen and Helium Isotopes with the PAMELA Experiment." *The Astrophysical Journal*. Vol. 818, No. 1, 2016, pp. 62.

[21] M. Fornasa and M.A. Sanchez-Conde. "The nature of the Diffuse Gamma-Ray Background." *Physics Reports.* Vol. 598. 8 October 2015, pp 1-58. https://doi.org/10.1016/j.physrep.2015.09.002

[22] Y. Inoue. "Cosmic Gamma-ray Background Radiation." 5th Fermi Symposium: Nagoya, Japan. 20-24 October, 2014. Accessed at https://arxiv.org/pdf/1412.3886.pdf on July 30, 2017.

[23] J.F. Valdes-Galicia et al. "Solar neutron events as a tool to study particle acceleration at the Sun." *Advances in Space Research*. Vol. 43, No. 4, 16 February 2009, pp. 565-572.

[24] R.J. Murphy, B. Kozlovsky, and G.H.Share. "The production of low-energy neutrons in solar flares and the importance of their detection in the inner heliosphere." *The Astrophysical Journal Supplement Series.* 202:3 (32 pp), September 2012.

[25] J. Allison et al. "Recent Developments in GEANT4." *J NIMA*. Vol. 835, 1 Nov 2016, pp. 186-225.

[26] H. Ming-Yang et al. "Detection of supernova neutrinos at spallation neutron sources." Accessed at https://arxiv.org/pdf/1511.00806.pdf on July 30, 2017.

[27] C. Athanassopoulos et al. LSND Collaboration. "Measurements of the reactions 12C(ve, e−)12Ng.s. and 12C(ve, e−)12N*." 23 May 1997. Accessed at https://arxiv.org/pdf/nucl-ex/9705001.pdf on July 31, 2017.

[28] L.B. Auerbach et al. LSND Collaboration. "Measurements of Charged Current Reactions of ν_e on 12C." 2 October 2001. Accessed at https://arxiv.org/pdf/hep-ex/0105068.pdf on July 31, 2017.

[29] R. McTaggart. "Modeling the Detection of Solar Neutrinos via Inverse Beta Decay in a Space Environment." NASA/TM-2017-218234. Marshall Space Flight Center Faculty Fellowship Program. N.F. Six, Program Director, G. Karr, Compiler. March, 2017, pp. 124. Accessed at https://ntrs.nasa.gov/archive/nasa/casi.ntrs.nasa.gov/20170005169.pdf on July 31, 2017.

Materials Degradation in the Jovian Radiation Environment

Gennady Miloshevsky[1]
Purdue University, West Lafayette, Indiana, 47907

Jarvis A. Caffrey[2], Jonathan E. Jones[3], and Thomas F. Zoladz[4]
NASA Marshall Space Flight Center, Huntsville, Alabama, 35812

The radiation environment of Jupiter represents a significant hazard for Europa Lander deorbit stage components, and presents a significant potential mission risk. The radiolytic degradation of ammonium perchlorate (AP) oxidizer in solid propellants may affect its properties and performance. The Monte Carlo code MONSOL was used for modeling of laboratory experiments on the electron irradiation of propellant samples. An approach for flattening dose profiles along the depth of irradiated samples is proposed. Depth-dose distributions produced by Jovian electrons in multi-layer slabs of materials are calculated. It is found that the absorbed dose in a particular slab is significantly affected by backscattered electrons and photons from neighboring slabs. The dose and radiolytic decomposition of AP crystals are investigated and radiation-induced chemical yields and weight percent of radical products are reported.

I. Introduction

NASA's proposed Europa Lander mission is planned to launch in the late 2020s and would perform repeated gravitational maneuvers spanning multiple years before finally igniting a braking stage solid rocket motor to initiate entry, descent, and landing. Europa is embedded within the harsh radiation environment of the Jovian magnetosphere.[1] It is believed that much of the ionized plasma trapped in the Jovian belts is supplied by volcanic eruptions on Jupiter's moon Io. The radiation environment in the vicinity of Europa includes energetic electrons, protons, and heavier ions such as S^+, C^+, O^+. However, the bulk radiation damage to the spacecraft would be dominated by high fluxes of deeply penetrating electrons with the energy in excess of 100 MeV.[2] Europa Lander gravitational maneuvers will mostly occur in lower intensity regions around Jupiter at or beyond the orbit of Ganymede, and will experience the highest intensity of radiation in the final hours as it approaches Europa. A separate mission, Europa Clipper, will lay the foundation for Europa Lander and will be launched several years prior, accumulating an even greater total ionizing dose but with no requirement to engage a braking motor.

A typical solid propellant fuel used in rocket motors contains an oxidizer such as ammonium perchlorate (AP) (60-80%), a hydroxy terminated polybutadiene (HTPB) binder (10-15%), and aluminum powder (15-20%). Ammonium perchlorate (NH_4ClO_4) is an ionic crystal in which atoms are held together by ionic bonds. In the past decades, a large number of experimental and theoretical studies have been devoted to the investigation of thermal decomposition of AP crystals. The primary products of AP decomposition detected in many experiments are ammonia and perchloric acid. Therefore, it was proposed that the first step in AP decomposition is proton transfer.[3] The entire process involves several stages: 1) pair of NH_4^+ and ClO_4^- ions in AP lattice (see Fig. 1); 2) proton transfer from the cation NH_4^+ to the anion ClO_4^- in AP molecule; and 3) decomposition into ammonia NH_3 and perchloric acid $HClO_4$. The molecules of NH_3 and $HClO_4$ then react with the gas phase in AP crystal forming the products such as Cl_2, O_2, N_2, NO, N_2O, H_2O, etc. Concerning the mechanism of AP

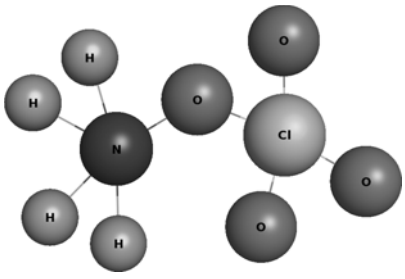

Figure 1. Ammonium perchlorate molecule NH_4ClO_4.

[1] Associate Professor, School of Nuclear Engineering, 400 Central Drive, Purdue University.
[2] Nuclear and Radiological Engineer, Propulsion Research (ER24), NASA MSFC.
[3] Technical Assistant, Solid Propulsion Devision (ER50), NASA MSFC.
[4] Branch Chief, Solid Separation and Maneuvering Systems Branch (ER52), NASA MSFC.

decomposition, it was established that the decomposition of single crystal orthorhombic AP at low temperatures (<513 K) is initiated by dislocation defects and occurs at mosaic crystal boundaries.[4] The decomposition further proceeds in a 3D manner consuming the boundary regions. AP crystals decompose only about 20 to 30% leaving a residue chemically identical with the original AP salt. The rate of thermal decomposition of AP was described by the Avrami-Erofeyev kinetic equation. The results of this earlier work are in contradiction with the recent study investigating the thermal decomposition of large single crystals of deuterated and non-deuterated AP at low-temperature.[5] It is found that at low temperature (250 °C) the decomposition proceeds inside the AP crystal with the desorption and transport of gaseous species from the bulk to the crystal's faces. The thermal decomposition stops when transformation of AP is about 30% with formation of the same porous products at lower (250 °C) and higher (350 °C) temperature. This limited decomposition of AP is in agreement with earlier predictions.[4] The slower decomposition of deuterated samples with 'snow' on the surface of AP crystals was observed.

The thermal decomposition of single crystal orthorhombic AP pre-irradiated by γ-rays was later investigated.[6] It was observed that the preliminary exposure of AP crystals to ionizing radiation shortens the time for thermal decomposition. The reaction rate constant of decomposition was found to be enhanced, accelerating the propagation of decomposition kinetics in the AP crystal. The change in the decomposition rate constant was attributed to the increase in the number of decomposition nuclei (presumably associated with dislocations) produced by the γ-radiation. The pure effect of γ-ray and X-ray irradiation on the decomposition of large AP crystals (5 x 3 x 3 cm) at room temperature in air and in the dark was experimentally studied.[7] The unirradiated AP crystals were water clear and free of inclusions and surface defects. Optical, transmission, and scanning electron microscopy were used to examine the irradiated AP crystals. At γ-ray doses between 10^3 and 10^5 rad, the AP crystals remained water clear and no radiation-induced defects were detected. At 1 Mrad irradiation, slightly opaque (milky) AP crystals were found with small, very flat pits on the *m* face similar to the pits formed during the early stages of thermal decomposition. At 5 Mrad γ-dose, the AP crystals became nearly opaque and milky white with circular pits and many tiny pits resolved by transmission microscopy on the *m* face. The γ-ray dose in 10 Mrad resulted in completely opaque AP crystals resembling white plastic. The formation of holes, channels, large bubbles, and cavities on some parts of the surface of AP was observed. The appreciable effect of X-rays on AP degradation was only observed at doses above 16 Mrad. The radiation-induced decomposition of AP was *found to be similar* in many respects to the thermal or chemically-induced decomposition. In both cases, there was an induction period during which the AP samples must receive the specific amount of heat or radiation dose before decomposition starts. The initial thermal, chemical or radiation effects caused the appearance of small pits that were aligned in some areas, but randomly distributed in other areas of the AP crystal. The characteristics of pits formed by thermal, chemical, or radiation treatment were quite similar on the first stage. They were roughly of the same size with density ~2 - 40 x 10^6 cm^{-2}, and aligned pits lie in the same crystal directions no matter how produced. On the second, or intermediate, decomposition stage, there was an extensive decomposition in all three treatment cases over the entire external crystal surface. At the last stage of decomposition, the separated blocks of undissolved crystals and "sponge-like" or coral structures containing rectangular voids were formed. However, there are the *specific effects induced by radiation* that were not observed during thermal and chemical treatment of AP. The high X-ray doses produced highly strained AP crystal with development of pronounced curvature, their fracture into blocks, and separation of blocks from the original crystal. The γ-ray induced decomposition occurred throughout the irradiated volume of the crystal, whereas the thermal and chemical decomposition started on the surface and penetrated inward. The sites of decomposition were localized inside the AP crystal where dislocations, slip planes, boundaries intersect. Therefore, the radiation-induced decomposition could not be simply related to the absorbed dose, since it occurred only at dislocation-related sites, voids, cracks that are not randomly distributed in the AP crystal. Some mechanisms must exist for the transport of produced species from the location of each ionization event to decomposition sites.

The chemical reactions and compositional changes in AP induced by radiations can produce dramatically different microstructure and can have a profound influence on its properties. To date, very little research in radiation chemistry has been carried out in the field of the radiolysis of AP salts. The radiation-induced decomposition of AP into the various chemical fragments and their radiation-chemical yields (so called *G* values) were reported in the earlier experimental study.[8] *G* values represent the number of molecules of the product formed per 100 eV of absorbed ionizing energy. The study was performed over the dose range up to 120 Mrad using the source of ^{60}Co γ-rays. The radiolysis products of AP are found to be different than those for alkali metal perchlorates. The major products of AP radiolysis are chloride, chlorine, chlorate and hypochlorite. Their radiolytic yields in μmol/g are reported for different radiation doses. Chloride (Cl^-), chlorine (Cl_2), and chlorate (ClO_3^-) have the largest *G* values. Chlorate was detected as the major product in the later study of γ-ray induced radiolysis of AP using IR spectro-photometry.[9] However, the other radiolytic products were not identified. The very recent study of the radiolytic decomposition of AP was conducted using various spectroscopy and spectrometry methods.[10] AP was exposed to

electrons at low temperature of 5.5 K. This very important work is a first experimental study of AP irradiated under cryogenic temperatures when primary chemical species created by radiation are immobile. Three different classes of molecules were detected: 1) nitrogen-based molecules NH_3, NH_2OH, N_2, and NO_2; 2) chlorine containing species ClO, ClO_2, and Cl_2O_3; and 3) oxygen molecules O_2. The first step of AP decomposition was confirmed to be deprotonation of NH_4^+. Ammonia (NH_3) may oxidize forming hydroxylamine (NH_2OH) or decay yielding molecular nitrogen (N_2). Perchlorate ions (ClO_4^-) can lose an oxygen yielding ClO_3^- and O. Molecular oxygen (O_2) is then formed via recombination of atomic oxygen (O). Chlorate (ClO_3^-) may further decompose into chlorite (ClO_2^-) and chlorine dioxide (ClO_2). However, *G* values for these species are not reported. These limited data are yet insufficient for the development of predictive models of radiation-induced degradation of AP at various temperatures.

The understanding of radiolytic decomposition mechanisms of AP are of great importance. It was established about 50 years ago in earlier experimental studies that the exposure of propellant to high energy radiation changes its composition and physical properties. However, the mechanism of the radiolytic decomposition of AP is not yet well understood. Therefore, the radiation effects on solid propellants during extended exposure to the Jovian radiation environment must be evaluated. The primary goal of this research is to develop theoretical models and computer codes as experimentally validated predictive tools for evaluations of AP degradation in the Jovian radiation environment. The main phases of this work should involve the evaluation of 1) deposited ionizing dose and atom displacement damage in the irradiated AP samples and multi-layer structures; 2) radiation-induced decomposition of AP due to breakage of chemical bonds with the creation of various fragments (radicals) of NH_3^+, ClO_4^-, HCl, H_2, O_2, H_2O, HNO, OH, ClO, Cl_2, N_2, NH_2, NO_2, etc.; and 3) long-time evolution of AP microstructure involving diffusion and chemical reactions between radicals, nucleation and growth of dislocations, defect clusters, precipitates, voids, and gas bubbles. The remainder of this report is organized as follows: In Section II, a description is provided of the MONSOL computer code used in this work for calculating the depth-dose profiles in materials. The modeling of laboratory irradiation experiments involving the mono-energetic electron beams is presented in Section III. Section IV contains a discussion of the results on the dose distribution in multi-layer materials due to an environmental source of electrons. The depth-dose distribution in a single AP crystal, radiolytic yield and weight percent of chemical radicals are reported in Section V. A summary is given in Section VI.

II. MONSOL Computer Code

The radiation dose deposited by high-energy particles in materials can be evaluated using the Monte Carlo (MC) transport approach. The MC method makes it possible to simulate random trajectories of electrons and photons as analogues to real particles using the theoretical cross sections of interaction processes. A three-dimensional MC model was developed and implemented in the MONSOL code[11] including all possible interactions of electrons and photons with materials. MONSOL was developed by the first author of this report, used in a number of practical applications, and has been well refined over the past years. The MONSOL code treats the coupled electron-photon transport.[12] The MC techniques implemented in MONSOL incorporate a mixed scattering model for the simulation of charged particle transport. Close collisions, with scattering angle and/or energy loss greater than predefined cutoff values are simulated in detail, by using analytical differential cross sections for the different interaction mechanisms and exact sampling methods. Distant collisions, with scattering angle or energy loss less than the corresponding cutoffs, are described by means of a multiple scattering theory. The interactions of photons with the medium are categorized primarily as the photoelectric effect, Compton scattering, and electron-positron pair production. The simulation of photon transport is straightforward since the mean number of interaction events in each history is fairly small. The MONSOL code is capable of carrying out numerical experiments on the effects of high-energy radiation (electrons, positrons, photons, ions and neutrons) on 3D configurations of solid-state composites. It was used recently in a project sponsored by National Nuclear Security Administration for investigating the correlation between different parameters (energy, angle, multiplicity, arrival time, etc.) of γ-ray and neutron radiation emitted from special nuclear materials.[13, 14] The details of the MONSOL code, benchmarks against results obtained from other MC codes, flowchart of the MC algorithm for tracing photons are described in these papers.

The recent validations of MONSOL results against the experimental data (calorimetric measurements performed at Sandia Laboratories)[15] on the energy deposition by MeV electrons into different materials are illustrated in Fig. 2. The specific goal was to validate the MONSOL code for materials such as C, Al, and hydrogen-rich compounds that are relevant to the present research. Fig. 2a and Fig. 2b show the energy deposition profiles in Al by electrons with 1.033 MeV for two incident angles of 0° and 60° to the surface normal, respectively. As the incident angle increases, the peak of absorbed energy is shifted toward the surface. The absorbed energy per unit mass of material is proportional to the absorbed dose. The maximum dose increases from ~3.2 MeV·cm^2/g for 0° to ~5 MeV·cm^2/g for 60°. This approach enables the major fraction of the absorbed dose to be localized near the surface of an irradiated

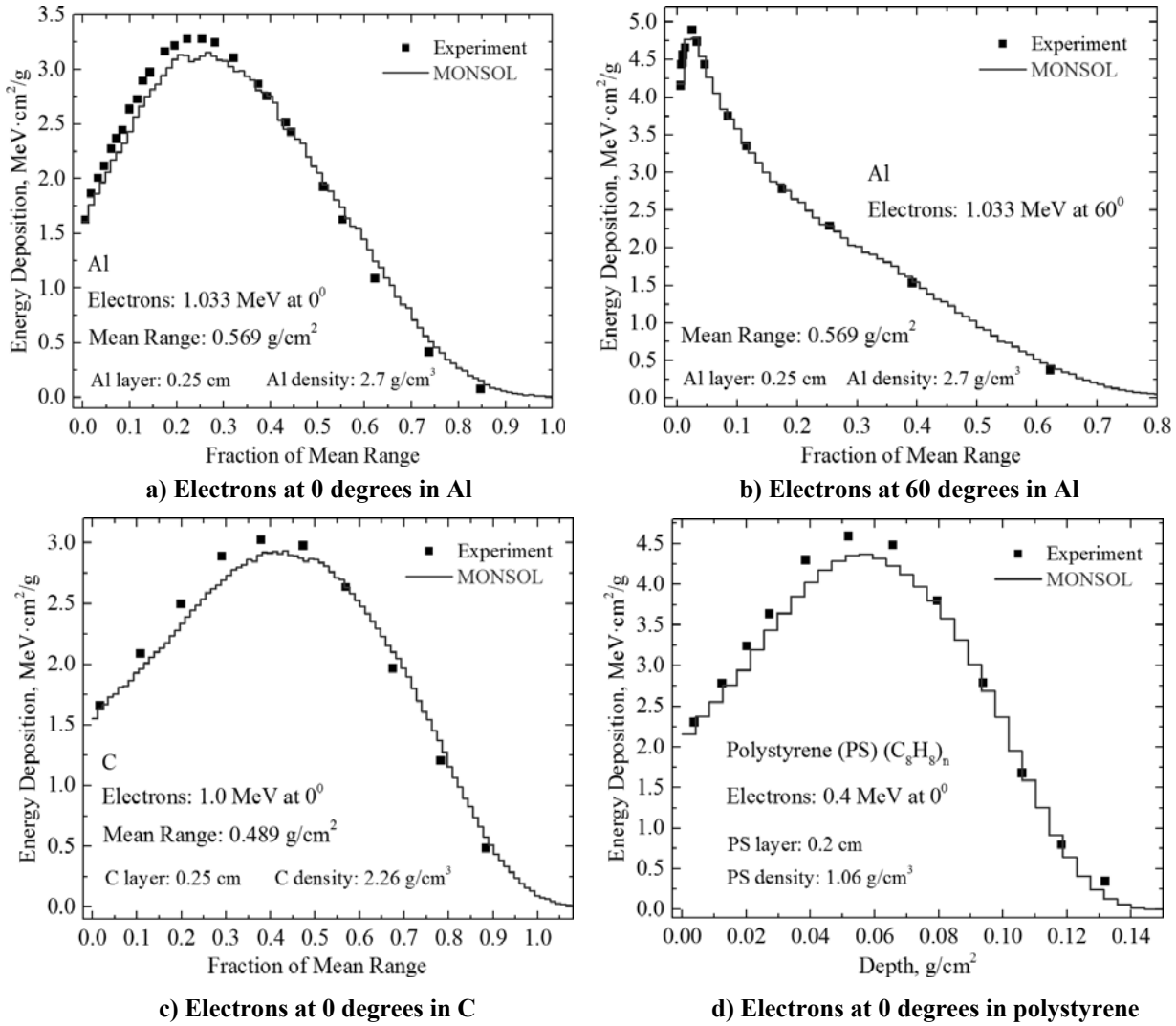

Figure 2. Profiles of energy deposition by monoenergetic electrons in different materials.

sample. The shapes of the theoretical histograms and the experimental curves are found in very good agreement, especially for 60°. The calculated location of the dose maximum and penetration depth of electrons agree closely with experimental measurements. The computational data are slightly lower in the vicinity of the peak for the 0° incidence angle. These differences can be attributed to experimental uncertainties or statistical errors in the MC technique. In Fig. 2c, the calculated dose distribution at normal incidence of electrons with 1 MeV for carbon is compared to the calorimetric measurements. The calculated and experimental peak positions of depth-dose distribution show very good agreement, although there appears to be a slight forward displacement of the calculated profile. It should be noted that the depth-dose distribution is affected by the material's density. The maximum absorbed dose is slightly higher and the dose peak occurs nearer to the surface for Al compared to that for C. In hydrogen-rich materials, there are more electrons per unit mass compared to high-*Z* elements. Therefore, the absorbed dose is higher (Fig. 2d) even for lower incident energy of electrons (0.4 MeV), since the energy deposition per unit length is proportional to the electron density. For polystyrene, the differences between the calculated and measured profile[16] of deposited energy are small (Fig. 2d). The peak position is nearly the same. The calculated value of absorbed dose at the peak of depth-dose distribution curve is slightly lower.

III. Modeling of Laboratory Irradiation Experiments

MONSOL modeling was performed for analysis of a HTPB hybrid propellant irradiation experiment using a mono-energetic electron beam at Marshall Space Flight Center. The irradiation experiment was performed as a pathfinder test plan in framework of the Europa DOS-Lander project. The experiment called for an available stock

of HTPB hybrid propellant samples to be exposed to approximately 6 Mrad of electron radiation. This level exceeds the expected dose to propellant anticipated in the Jovian environment by a factor of 5, as determined by separate analysis. The samples for testing were fabricated into slabs and dog-bones with thickness of one-fourth and one-half inch. The preference is to use samples of 1/2" thickness (1.27 cm) in order to conform with the JANNAF Class C dog-bone standard. The samples were arranged on a plate within a 14" diameter circle and irradiated by mono-energetic 2 MeV electrons with electron fluence of 2.1×10^{14} e^-/cm^2 and irradiation time of 520 minutes. The pre- and post-irradiated samples were then characterized to determine the effects of electron radiation on material properties such as modulus, hardness, electrical and thermal conductivity.

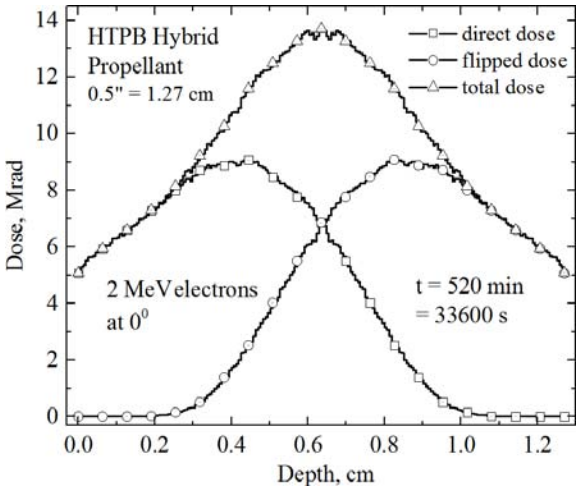

Figure 3. Depth-dose profiles in HTPB hybrid propellant irradiated by 2 MeV electrons.

There are two problems that should be solved in these irradiation experiments. First, the penetration depth of 2 MeV electrons in this material is about 1.1 cm, which is less than the thickness of 1/2" samples (Fig. 3, direct dose curve). This means that the backside of samples remains unirradiated. A way for resolving this issue is to flip the sample and perform an irradiation of the opposite side (Fig. 3, flipped dose curve). However, it is seen that the total accumulated dose (curve with open triangles) is much higher in the middle of the sample compared to that near the sample's faces. Second, it is highly desirable to produce a uniform (flat) dose distribution along the depth of sample. This is crucial for performing the post-irradiation tests of properties of samples. A standard approach to flatten the dose profile is to use successive electron beam irradiations with different energy and fluence. However, this requires multi-level and multi-time irradiations of both sides of samples, thus increasing time and cost of experiments. Furthermore, such a technique is only effective for a sample plate of all identical materials with identical thickness.

An alternative approach for flattening the total dose profile along the depth of an irradiated sample is proposed. The basic idea is to use a metallic plate placed in the front of the sample. Some dose in the rising portion of the depth-dose curve is then absorbed in a plate. The thickness of plate affects the shape of the remaining depth-dose profile in the sample. The more radiation dose that is absorbed in the plate, the higher is the dose near the surface of

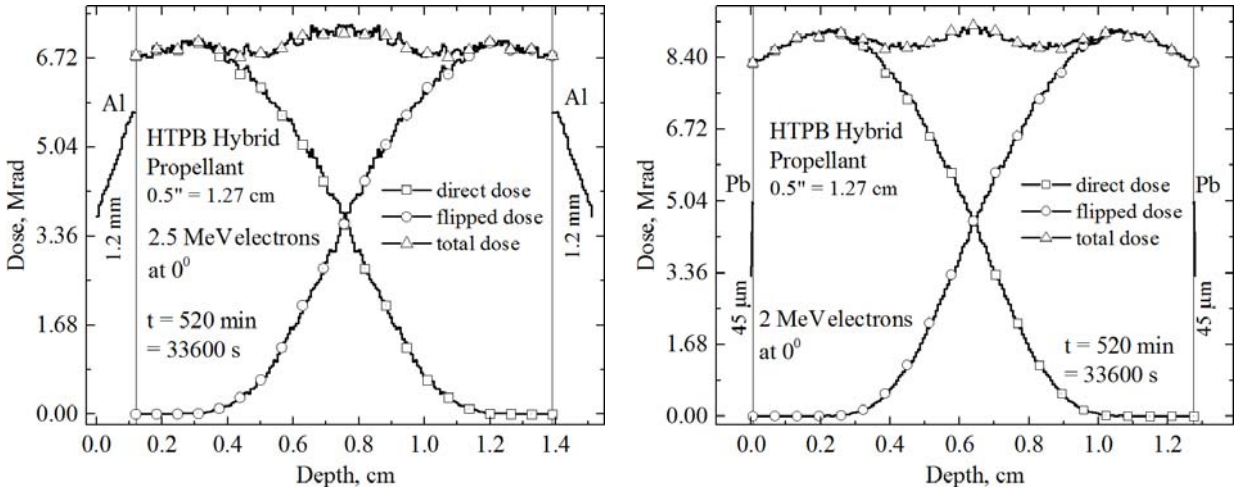

a) Dose flattening with Al plate **b) Dose flattening with Pb plate**

Figure 4. Dose-depth profiles in sample of HTPB hybrid propellant irradiated from front and back sides.

sample, up to a certain thickness. At a particular thickness of metallic plate, it is possible to achieve roughly a constant dose in the near-surface region of sample. This approach effectively eliminates the rising portion of the depth-dose curve and homogenizes the dose within a certain region near the surface of a sample. Among other benefits, this method also rules out the need to execute multiple irradiations of samples with different energies. For a thick sample, only two irradiations (one side and then the opposite side) are required. The flattened total depth-dose

profiles (curves with open triangles) in HTPB Hybrid Propellant with thickness 0.5" are illustrated in Fig. 4a and Fig. 4b for Al and Pb screens, respectively. It is seen that a sheet of Al with thickness ~1.2 mm is needed to achieve a constant dose near the both faces of the sample. A much thinner film of Pb (~45 μm) can produce the same effect. However, the total absorbed dose in the propellant sample is increased ~25% when a high-*Z* metal is used. It should be noted that the absorbed dose distribution in a sample is affected by the incident energy of electron beam, thickness, and mass density of a sample. For example, the dose profile cannot be flattened by electrons with maximum energy of 2.5 MeV in a propellant of the same thickness as in Fig. 4 but higher mass density, since the electron range is shorter and the region in the center of sample might not be covered. There is a maximum thickness of material that can be treated using any of the aforementioned techniques, mainly driven by the maximum kinetic electron energy achieved by the accelerator. However, for samples within the viable range of thicknesses, the proposed approach should work well for homogenizing dose profiles in materials.

IV. Modeling of Depth-Dose Distribution in Materials due to Space Environment Electrons

A. Energy Spectrum of Jovian Electrons in Europa's Orbit

Materials used in spacecrafts are affected by energetic particles across a broad range of energy and particle species. The prediction of the radiation environment in the Jovian magnetosphere is based on the best available model to date such as the Galileo Interim Radiation Electron model v.2 (GIRE2).[17] This model relies on the data collected from the Galileo spacecraft which performed 35 orbits around Jupiter while measuring the radiation environment. The GIRE2 model is a useful tool for evaluating the electron environment for the future Europa Lander mission. Both the GIRE2 and the previous GIRE data map the particle energy spectra for electrons between tens of keV to more than one hundred of MeV, and also distribute said spectra across a spatial grid. Trajectory analysis through this grid then permits the approximation of the anticipated incident radiation environment on a given spacecraft. For the purpose of testing the implementation of a typical Jovian electron energy spectrum, some empirical models from available literature are used that describe the particle flux at Europa's orbit.[18] The modeled differential intensity of electrons (e^- per cm^2 s sr MeV) shown in Fig. 5, derived from these models, shows the degree of variation in both energy and intensity across many orders of magnitude. The electron flux (curve with open circles) is derived by the integration of differential intensity over the energy and solid angle. The energy flux (curve with open triangles) is obtained by averaging the energy of electrons using the differential intensity function. The legends at curves in Fig. 5 indicate the relevant units for a vertical axis on the left. The electron flux curve is used in the MC simulations to sample the energy of electrons impacting materials.

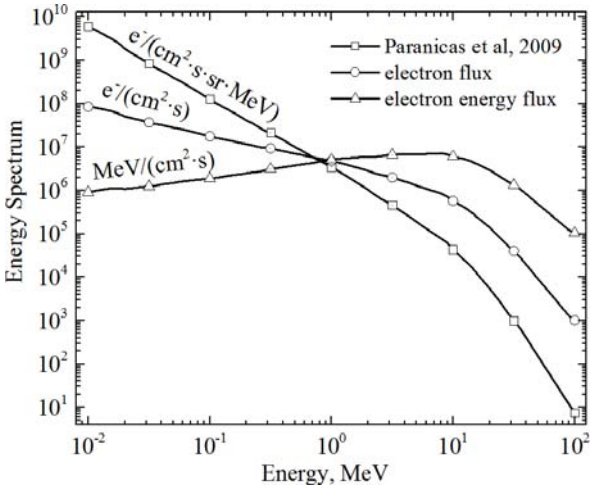

Figure 5. Energy spectrum of electrons determined near Europa's orbit.

B. Validation of MONSOL for Case of Environmental Spectrum of Electrons

Before describing the depth-dose profiles in multi-layer materials due to the effects of Jovian electrons, a benchmark is provided for MONSOL against the depth dose curves in Al for an experiment in literature that attempted to replicate the radiation environment at the standard geosynchronous orbit (GEO).[19] From that report, the total environment dose (curve with solid squares) and experiment dose (curve with solid circles) due to three beams of mono-energetic electrons of different energy and fluence are shown in Fig. 6. The largest drop in the depth-dose profile occurs in the near-surface layers (note log scale for dose and depth). It is seen that the depth-dose profile due to environment radiation can be approximated by using separate radiation sources of several beams of mono-energetic electrons and proper choice of fluences. The MONSOL code was set up to perform runs for each of three electron beams with energies and fluences indicated in Fig. 6. Two types of electron irradiation were modeled. First, a sample of Al was irradiated by each of three beams independently (sequential irradiation) (Fig. 6a). The three separate depth-dose profiles are illustrated. The agreement with portions of the total depth-dose profile (curve with solid squares) and the dose due to three beams (curve with solid circles) is quite good in almost all detail except for the case of 2 MeV electrons. The MONSOL modeled penetration depth of electrons is slightly greater. Second, a

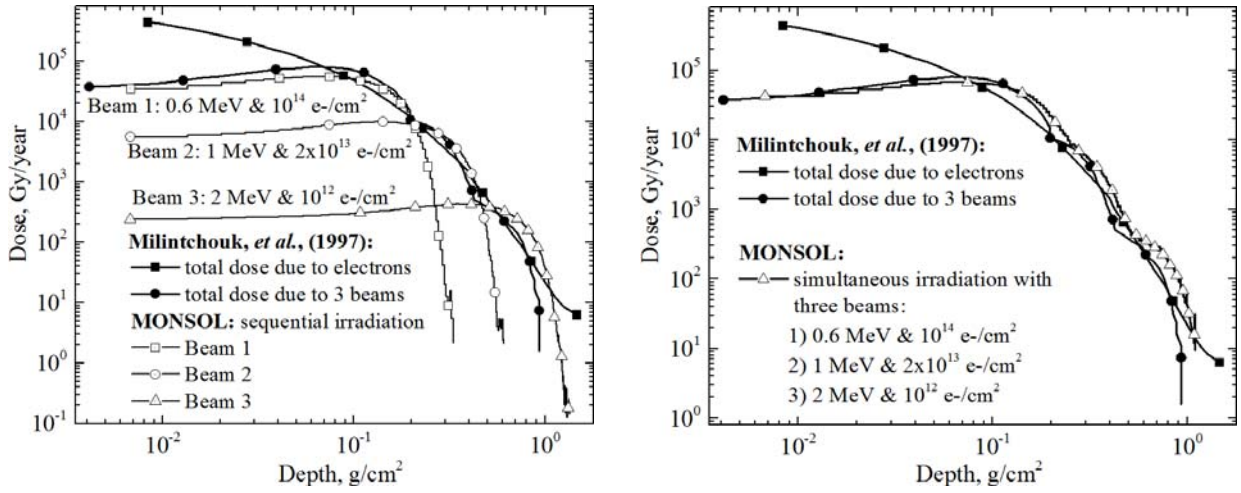

a) Sequential irradiation **b) Simultaneous irradiation**

Figure 6. Depth-dose profiles in Al for radiation environment at GEO orbit and for three beams of electrons of different energy and fluence.

sample of Al was irradiated simultaneously (coupled irradiation) by three electron beams in a single MONSOL run. The depth-dose profile is shown in Fig. 6b (curve with open triangles). Since the dose deposited in a material by different mono-monoenergetic electron beams is additive, the sum of doses from three independent irradiations (Fig. 6a) should be equal to the total dose deposited by three simultaneous beams (Fig. 6b). The good agreement provides the confidence that the depth-dose profiles due to Jovian electrons would be predicted accurately.

C. Depth-Dose Distribution in Shielded Propellant at Europa's Orbit

In this subsection, we discuss the dose rate at Europa's orbit due to Jovian electrons absorbed in the multi-layer system composed of casing, insulator, liner, and propellant. The schematic is illustrated in Fig. 7. This system is irradiated by electrons in a wide range of energies from 10 keV to over 100 MeV. The electron energy spectrum

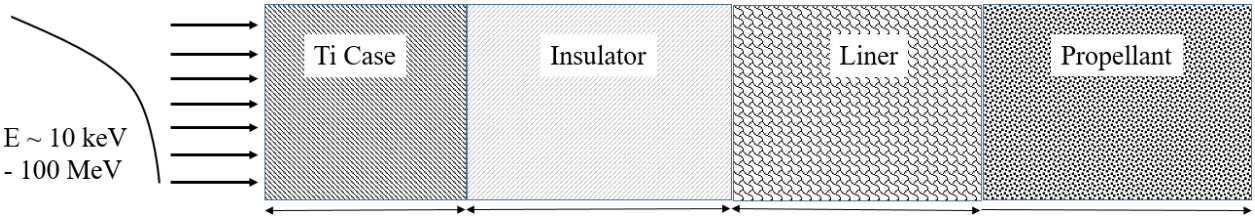

Figure 7. Schematic of multi-layer material slabs composed of Ti case, insulator, liner and propellant and irradiated by electrons with a wide spectrum of energies.

determined at the orbit of Europa[18] (Fig. 5) is used as a placeholder in our modeling of dose rate. This energy spectrum is representative of the approximate spectral shape, but does not accurately reflect the total fluence experienced by the spacecraft as it traverses the Jovian system. True incident fluences expected for the spacecraft must be calculated using the GIRE2 model that integrates the exposure using a spacecraft trajectory.[20] Since this method assumes a constant flux based upon the environment at Europa's orbit, it is possible to roughly anchor this analysis against a separate estimate of true incident dose rate and then assume a scaling factor in the form of an exposure time. The exposure time determined in this method does not represent actual exposure time of the spacecraft, as in reality it will pass through elliptical orbits with highly variable intensity. Still, it served its purpose in providing a convenient placeholder for incident fluence while developing the method for depth-dose analysis.

The normalized dose accumulated in slabs of different materials (Fig. 7) during one month of exposure to electrons at Europa's orbit is shown in Fig. 8. The slab of Ti receives the largest radiation dose in the near-surface region. This near surface dose would be even further enhanced due to a contribution of protons that are not considered in our modeling. Protons and heavy ions have a very short penetration depth on the order of tens of microns. The dose drops sharply along the depth of Ti case. The absorbed dose further decreases about two orders of

magnitude in a propellant layer. It is important to note that this assessment is based upon a representative energy spectrum of the radiation environment at Europa's orbit.

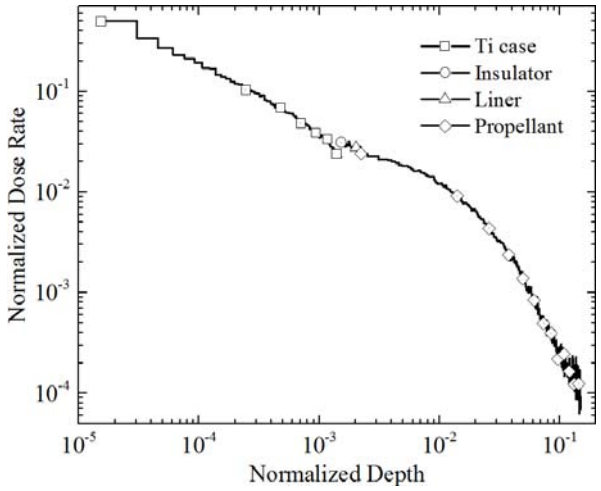

Figure 8. Depth-dose profile in the shielded propellant due to exposure to Jovian electrons at Europa's orbit during one month.

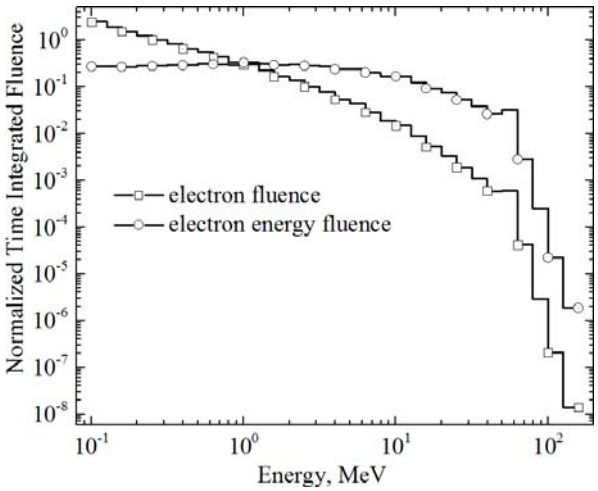

Figure 9. Total electron and energy fluence accumulated prior to Europa landing.

D. Depth-Dose Distribution in Propellant during Europa Lander Mission

The normalized time-integrated electron and energy flux giving the total electron and energy fluence through the entire Europa Lander mission are shown in Fig. 9. These data are derived from the GIRE2 model for a candidate spacecraft trajectory. This spectrum covering the energy range from 100 keV up to more than 150 MeV is used for evaluating the cumulative dose in an isolated Ti sheet and the multi-layer solid rocket motor system (Fig. 7).

The electron irradiation of a single layer of Ti was modeled. The depth-dose profile is shown in Fig. 10a. The depth-dose distribution in the four-layer system composed of Ti, insulator, liner, and propellant slabs and irradiated

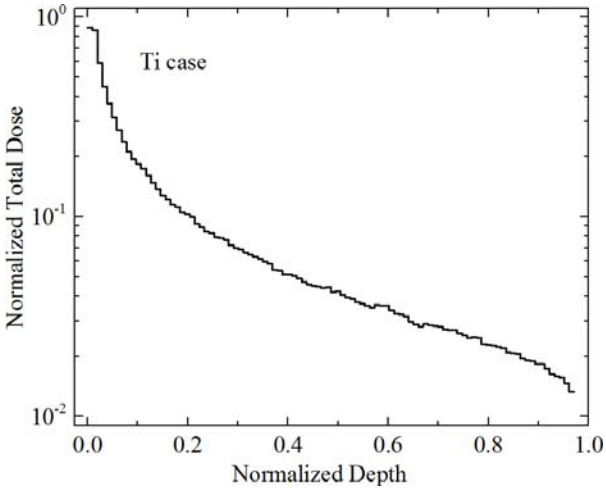

a) Single slab of Ti

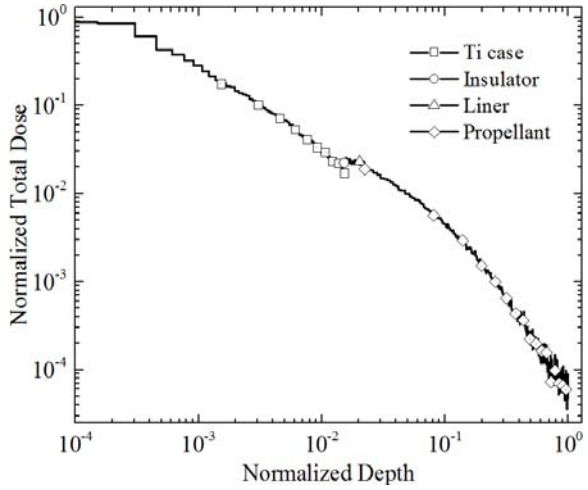

b) Slab of Ti followed by other slabs

Figure 10. Effect of truncation of multi-layer system on depth-dose profiles.

by Jovian electrons is shown in Fig. 10b. It is found that the value of dose behind Ti slab which is in direct contact with the rest of the multi-layer system (Fig. 10b) is about ~43% higher than the dose behind a single slab of Ti (Fig. 10a). The overdose is due to the contribution of neighboring slabs located behind a Ti sheet (Fig. 10b). We conclude that the depth-dose profile in a slab is affected when it is followed or preceded by other slabs of different materials. The effect is mainly due to the energy deposition by backscattered electrons and photons from neighboring layers of materials with very different properties.[21] Depth-dose distributions in multi-layer configurations depend strongly on

the atomic composition of particular materials as well as on their mass density. The build-up of energy deposition by radiation backscatter would be higher from the denser propellant. The percentage of the absorbed dose in the insulating and liner materials would be also considerably increased by the contribution from backscattering. It is noteworthy that accurate estimation of depth-dose distributions should be performed considering the irradiation of a multi-layer system, not just a single slab of material.

V. Radiolysis of AP by Energetic Electrons

A. Depth-Dose Distribution in AP Crystals Irradiated by 2 MeV Electrons

The depth-dose distributions in AP samples irradiated by energetic electrons serve as input data for radiolytic models of AP decomposition into radicals and chemical products. The depth-dose distributions produced by 2 MeV electrons in AP crystal were calculated using MONSOL, MCNP6, and EGSnrc computer codes and compared in Fig. 11. The dose is normalized per unit of fluence. The penetration depth of 2 MeV electrons in AP crystal is about ~0.6 cm. A good agreement is seen for the location of the peak energy deposition at ~0.18 cm predicted by MCNP6 and MONSOL. However, the height of dose peak yielded by MONSOL is reduced about ~8%, and as a consequence the rising portion of the depth-dose curve is shifted slightly deeper. The tails of depth-dose distributions obtained from both codes are in very good agreement. The height of peak dose predicted by EGSnrc is nearly the same as that yielded by MCNP6. The dose in the rising portion of the curve agrees well with that predicted by MONSOL. However, both the position of the dose peak and the falling portion of the energy deposition curve are shifted deeper compared to the other two curves. This benchmark ensures that the depth-dose distribution produced by electrons in AP material is correctly calculated.

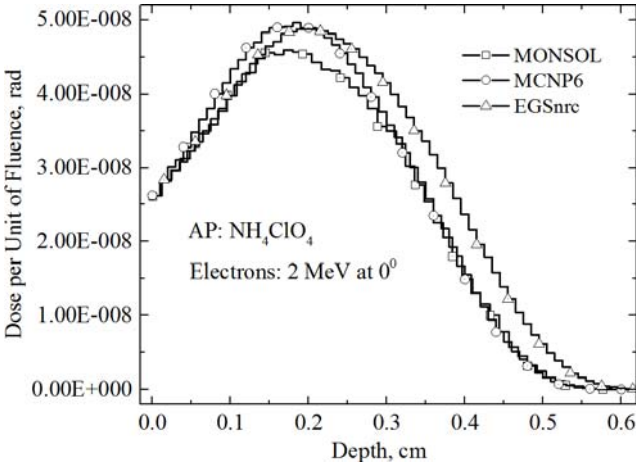

Figure 11. Depth-dose profiles for 2 MeV electrons in AP crystal at normal incidence calculated using three different codes.

B. Chemical Yields and Weight Percent of AP Products

Radiation yields of products are usually reported in terms of experimentally determined *G* values. Originally *G* value of product was defined as a number of product molecules produced per *100 eV* of absorbed energy. In the SI system the unit of *G* value is *mol/J*. The conversion factor between these two units is *1 mol/J = 9.648x10^6 molecules/100 eV*. The reported chemical products of the radiolysis of AP and approximate initial *G* values (*molecules/100 eV*) are as follows: Cl^- - 2.5; ClO_3^- - 1.3; $C1_2$ - 1.2; ClO^- - 0.45; $NO_3^- + NO_2^- < 0.05$; $ClO_2 < 0.02$; and $ClO_2^- < 0.02$.[8] These data were derived from the measurement of radiolytic yields of AP irradiated by a ^{60}Co source of γ-rays with absorbed doses higher than 8 Mrad.[22] The validity of these *G* values is less clear for lower doses of interest in our research. The initial yields of radiolysis products of AP were later summarized in a review paper.[23] The other data on *G* values were obtained in the experiments performed in the Soviet Union using 200 keV X-rays and 4.7 MeV protons. There is good agreement between the *G* values from different experiments. For example, the reported *G* values of Cl^- with highest yield are 2.1±0.1 (200 keV X-rays), 2.7 (4.7 MeV protons), and 2.5 (^{60}Co γ-rays). This provides some confidence in the accuracy of the reported *G* values. Unfortunately, the publications describing those original experiments and their dose levels are not available.[23]

The evaluation of radiolytic yield and weight percent of products in AP was performed for the Jovian electron environment with the time-integrated fluence (Fig. 9) accumulated during entire Europa Lander mission. The multi-layer system illustrated in Fig. 7 was used, but with propellant substituted with pure AP material. The calculated depth-dose profile in AP (not shown) was very similar to that shown in Fig. 10b for propellant. The chemical yield and weight percent of products in AP are shown in Fig. 12. The highest yield of Cl^- is ~4.8 μmol/g on the surface (Fig. 12a). The yield of Cl^-, ClO_3^-, $C1_2$ and ClO^- is prevailing in the near-surface region with its further decrease along the depth. Fluctuations in the curves at the large depth arise from limited MC statistics. The yield of $NO_3^- + NO_2^-$, ClO_2 and ClO_2^- is insignificant, since their *G* values are small. The yield of ClO_2 (shown) and ClO_2^- (not shown) is the same because they share equal *G* values. The weight percent curves of products as a function of the depth shown in Fig. 12b resemble those of the chemical yield. Nevertheless, there is one distinction. In contrast to

the chemical yield, the weight percent of ClO_3^- on the surface is highest, ~0.021. This is because the molar mass of ClO_3^- is greater than the molar masses of Cl^- and $C1_2$. Overall, it can be concluded that the content of products in AP expected during spacecraft approach to Europa is very low.

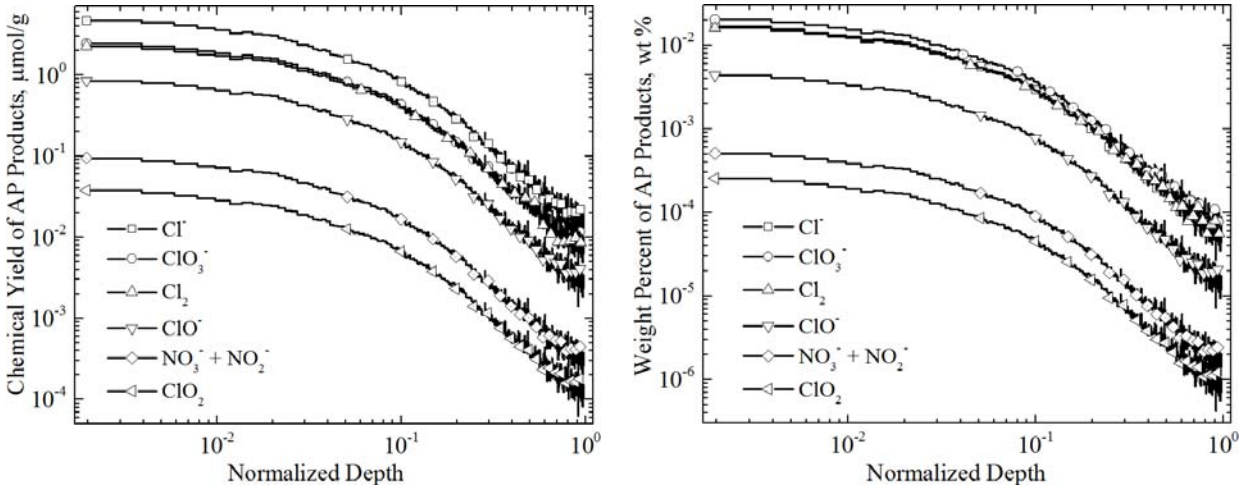

a) Chemical yield **b) Weight percent**

Figure 12. Chemical yield and weight percent of radiolytic products in AP irradiated by Jovian electrons during Europa Lander mission.

C. Future Developments

Further experimental and computational research is needed on the development of models for realistic predictions of radiation-induced decomposition of AP crystals. First, there is a lack of parameters needed in computational models such as 1) threshold energies for displacement of AP atoms from their lattice sites; 2) values of energy required to break bonds for N, Cl, O, and H atoms in AP; 3) rate constants describing chemical reactions between radiation-produced reactive radicals; 4) diffusion coefficients describing diffusion of chemically inert species in AP; and 5) rate constants for reaction of chemically stable species with dislocations, voids, bubbles, grain boundaries, and precipitates developed in AP crystals. Both experimental measurements and classical or quantum Molecular Dynamics simulations can be used as a source of these parametric data. Second, the algorithms and models have to be developed and implemented for 1) production of chemical radicals: this model describing the chemical yield of AP products is already implemented (Subsection B), but it has to be extended to include other possible species to be identified in future research; 2) prediction of chemical reactions between reactive radicals with formation of chemically inert products; 3) prediction of diffusion of produced chemically stable species in AP; 4) prediction of nucleation and growth of dislocations, voids, bubbles, etc.; and 5) prediction of reactions of stable species with dislocations, grain boundaries, voids, and bubbles. The depth-dose distributions in AP crystals calculated using MONSOL and described in this report can be used as a source term in many of these models.

VI. Conclusion

The depth-dose distributions produced by the impact of mono-energetic as well as space environment electrons on single-layer and multi-layer materials are studied using the MONSOL code. An approach using a forefront metallic plate for homogenizing the dose profile along the sample's depth in laboratory irradiation experiments is proposed. It is found that the dose absorbed in a particular slab of material sandwiched between other slabs is considerably increased due to the energy deposition by backscattered electrons and photons from neighboring slabs. It is recommended that dose evaluations to be performed considering the irradiation of a full multi-layer system rather than isolated slabs of material. It is found that the weight percent of chemical products accumulated in AP during Europa Lander mission is low. Future research should incorporate the calculated depth-dose profiles in the models describing chemical reactions between AP products and their diffusion, thus predicting degradation of AP.

Acknowledgments

G. Miloshevsky thanks the NASA MSFC Summer Faculty Fellow Program managers and staff for supporting this research that allowed him the opportunity to closely collaborate with MSFC engineers and scientists.

References

[1]Kivelson, M. G., Khurana, K. K., and Volwerk, M. "Europa's interaction with the Jovian magnetosphere." Univ. of Ariz. Press, Tucson, Ariz., 2009, pp. 545-570.

[2]Paranicas, C., Mauk, B. H., Khurana, K., Jun, I., Garrett, H., Krupp, N., and Roussos, E., "Europa's near-surface radiation environment," *Geophysical Research Letters*, Vol. 34, No. 15, 2007, p. L15103.

[3]Boldyrev, V. V., "Thermal decomposition of ammonium perchlorate," *Thermochimica Acta*, Vol. 443, No. 1, 2006, pp. 1-36.

[4]Galwey, A. K., and Jacobs, P. W. M., "The thermal decomposition of ammonium perchlorate at low temperatures," *Proceedings of the Royal Society of London, Series A*, Vol. 455, No. 1279, 1960, p. A254.

[5]Majda, D., Korobov, A., Filek, U., Sulikowski, B., Midgley, P., Vowles, D., and Klinowski, J., "Low-temperature thermal decomposition of large single crystals of ammonium perchlorate," *Chemical Physics Letters*, Vol. 454, No. 4, 2008, pp. 233-236.

[6]Herley, P. J., and Levy, P. W., "Thermal Decomposition of Irradiated Orthorhombic Ammonium Perchlorate," *Nature*, Vol. 211, No. 5055, 1966, pp. 1287-1288.

[7]Herley, P. J., and Levy, P. W. "Microscopic observations of X-ray and gamma-ray induced decomposition of ammonium perchlorate crystals," *Washington Proc. of the Natl. Symp. on Nat. and Manmade Radiation in Space*. NASA, 1972, pp. 584-594.

[8]Odian, G., Acker, T., and Pletzke, T., "γ-Radiolysis of Ammonium Perchlorate," *The Journal of Physical Chemistry*, Vol. 69, No. 7, 1965, pp. 2477-2479.

[9]Dedgaonkar, V. G., and Sarwade, D. B., "Studies on gamma radiolysis of microcrystalline ammonium perchlorate," *Journal of Radioanalytical and Nuclear Chemistry*, Vol. 199, No. 3, 1995, pp. 191-196.

[10]Gobi, S., Bergantini, A., Turner, A. M., and Kaiser, R. I., "Electron Radiolysis of Ammonium Perchlorate: A Reflectron Time-of-Flight Mass Spectrometric Study," *The Journal of Physical Chemistry A*, Vol. 121, No. 20, 2017, pp. 3879-3890.

[11]Miloshevsky, G. V. "The MONSOL code: Technical description." Luikov Institute of Heat and Mass Transfer, Minsk, Belarus, 2000.

[12]Leroy, C., and Rancoita, P. G. *Principles of Radiation Interaction in Matter and Detection*: World Scientific, Singapore, 2004.

[13]Miloshevsky, G., and Hassanein, A., "Energy–angle correlation of neutrons and gamma-rays emitted from an HEU source," *Nuclear Instruments and Methods in Physics Research Section A: Accelerators, Spectrometers, Detectors and Associated Equipment*, Vol. 749, 2014, pp. 47-56.

[14]Miloshevsky, G., and Hassanein, A., "Multiplicity correlation between neutrons and gamma-rays emitted from SNM and non-SNM sources," *Nuclear Instruments and Methods in Physics Research Section B: Beam Interactions with Materials and Atoms*, Vol. 342, 2015, pp. 277-285.

[15]Lockwood, J. G., Ruggles, E. L., Miller, H. G., and Halbleib, A. J. "Calorimetric measurement of electron energy deposition in extended media - Theory vs experiment." Sandia National Laboratories report SAND79-0414, Albuquerque, New Mexico, 1987.

[16]McLaughlin, W. L., and Hussmann, E. K. "The measurement of electron and gamma-ray dose distributions in various media," *Proc. of Symp. on Utilization of Large Radiation Sources and Accelerators in Industrial Processing*. IAEA STI/PUB/236, International Atomic Energy Agency, Vienna Munich, 1969.

[17]Garrett, H. B., Kokorowski, M., Jun, I., and Evans, R. W. "Galileo Interim Radiation Electron Model Update - 2012." JPL Publication 12-9, Jet Propulsion Laboratory, California Institute of Technology, Pasadena, CA, 2012.

[18]Paranicas, C., Cooper, J. F., Garrett, H. B., Johnson, R. E., and Sturner, S. J., "Europa's radiation environment and its effects on the surface," *in Europa, The University of Arizona space science series, edited by R. T. Pappalardo, W. B. McKinnon, K. K. Khurana, and R. Dotson (University of Arizona Press, Tucson)* 2009, pp. 529-544.

[19]Milintchouk, A., Van Eesbeek, M., Holmes-Siedle, A., and Levadou, F. "Degradation of materials under the action of soft X-ray radiation from solar flares," *Proc. 7th Int. Symposium on Materials in Space Environment*. Toulouse, France, 1997, pp. 87-96.

[20]de Soria-Santacruz Pich, M., Garrett, H. B., Evans, R. W., Jun, I., Kim, W., and Paranicas, C. "The GIRE2 model and its application to the Europa mission," *2016 IEEE Aerospace Conference*. 2016, pp. 1-7.

[21]Tabata, T., and Ito, R., "An Algorithm for Electron Depth-Dose Distributions in Multilayer Slab Absorbers," *Japanese Journal of Applied Physics*, Vol. 20, No. 1, 1981, p. 249.

[22]Odian, G., Acker, L., Pletzke, T., Henley, E., and McAlevy III, R. F. "Radiation Induced Solid Propellant Decomposition." Tech. Documentary Report on Contract AF 49 (638)-1125, Radiation Applications Inc., 1964.

[23]Zakharov, Y. A., and Nevostruev, V. A., "Radiolysis of Solid Inorganic Salts with Oxygen-containing Anions," *Russian Chemical Reviews*, Vol. 37, No. 1, 1968, p. 61.

Towards the Development of Low Power Arcjet for Use with Green Propellant

Trevor M. Moeller[1]
University of Tennessee Space Institute, Tullahoma, TN, 37388, USA

Conventional arcjet propellants are hydrazine and ammonia. Both are toxic and environmentally unfriendly, requiring the use of complicated handling logistics and increased cost. If successfully demonstrated in arcjets, the use of green propellants would alleviate these issues. This paper details improvements made to the design of a low-power arcjet to be used in testing. Diagnostic tools to be used to assess thruster performance were also developed. These include emission spectroscopy for the detection of thruster insulator erotion and a two-cord heterodyne laser interferometer for measure electron number densities and estimate the exit velocity of the propellant.

Nomenclature

c	=	speed of light in vacuum
$D12$	=	distance between lens 1 and lens 2
$D23$	=	distance between lens 2 and lens 3
ϵ_o	=	permittivity of free space
$f1$	=	focal length of lens 1
$f2$	=	focal length of lens 2
$f3$	=	focal length of lens 3
$I1$	=	image of lens 1
$I2$	=	image of lens 2
$I3$	=	image of lens 3
λ	=	wavelength
l	=	length along laser beam
$L1$	=	lens 1
$L2$	=	lens 2
$L3$	=	lens 3
$M1$	=	magnification of lens 1
$M2$	=	magnification of lens 2
$M3$	=	magnification of lens 3
M_e	=	electron mass
M_{total}	=	magnification of lens system
n'	=	index of refraction
$O1$	=	object of lens 1
$O2$	=	object of lens 2
$O3$	=	object of lens 3
φ	=	phase shift
q	=	charge on electron
$S1$	=	distance between lens 1 and its object
$S2$	=	distance between lens 2 and its object
$S3$	=	distance between lens 3 and its object
$S1'$	=	distance between lens 1 and its image
$S2'$	=	distance between lens 2 and its image
$S3'$	=	distance between lens 3 and its image

[1] Associate Professor, Department of Mechanical, Aerospace and Biomedical Engineering, MS 24, AIAA Associate Fellow.

I. Introduction

ARCJETS are electric propulsion devices that generate thrust through the thermal expansion of the propellant, just like a chemical rocket. However, the thermal energy in the propellant of the former is not limited by the combustion of an oxidizer and fuel; Ohmic heating provides much higher propellant temperatures, resulting in higher specific impulse leading to a reduced propellant requirement for the same mission. For this reason arcjets have found wide use for station keeping on satellites. Arcjets on satellites traditionally use hydrazine (N_2H_4) as a propellant, as it is a monopropellant that releases heat when decomposed with a catalyst, and it has a relatively low mixture molecular weight (5.333 g/mole). Unfortunately, hydrazine is hazardous to people and the environment. Green propellants have low toxicity and offer high-performance and high-efficiency compared to conventional chemical propellants[1]. Successful demonstration and adoption of a green alternative for arcjet propellant would greatly reduce propellant handling procedures and logistics[2].

II. Thruster Hardware

Arcjets are comprised of an anode and a cathode separated by an electrical insulator. The flowpath in the anode forms a Laval nozzle that produces supersonic flow in the diverging nozzle (Figure 1a). Propellant is introduced tangential to the anode wall, upstream of the constrictor (nozzle throat) to form a swirling flow. An arc extends from the tip of the cathode, through the constrictor, to the diverging portion of the anode. The swirling propellant flow stabilizes the arc by promoting a cool boundary layer with low electrical conductivity close the the constrictor wall (Figure 1b). In an ideal arcjet, the anode attachment is a diffuse arc that attaches symmetrically to the expanding nozzle. In reality the arc attaches in one location that rapidly moves circumferentially.

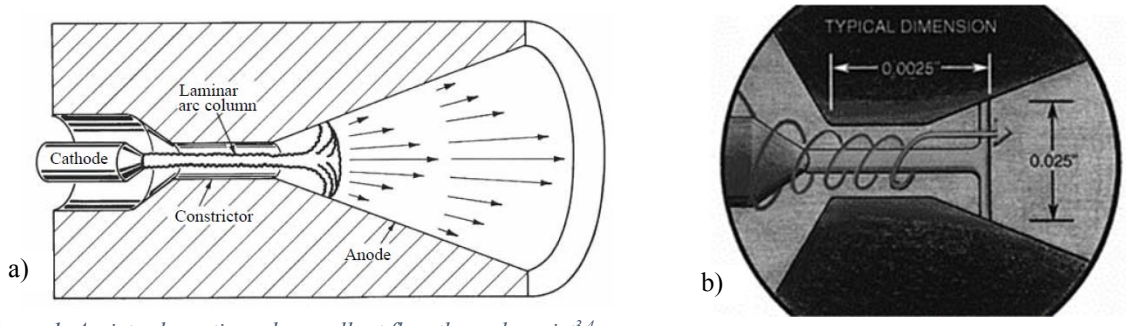

Figure 1. Arcjet schematic and propellant flow through arcjet[3,4]

The arcjet thruster on which the green propellant will be demonstrated is designed to operate at 1 kW. The constrictor is 0.040 inches in diameter and 0.040 inches long (Figure 2). The diverging nozzle is conical with a 22.5 degree half angle. The cathode tip is a 25 degree half-angle cone. Propellant enters the arcjet through a fitting near the breech of the insulator and flows into a manifold that feeds six channels to the nozzle (Figure 3). At the end of each channel, the flow enters a 1/32 inch hole that ends at the wall upstream of the constrictor (see inset in Figure 3). This creates a swirling flow. A photo of the assembled arcjet appears in Figure 4.

Past tests of this arcjet operating with argon propellant resulted in disappointing performance. The argon propellant is not a good propellant for electrothermal devices, and the cathode-anode spacing for the arcjet operating conditions resulted in the electrodes being welded together. It was decided to operate arcjet on hydrogen-nitrogen mixtures that represent dissociated ammonia (NH_3) and dissociated hydrazine (N_2H_4), conventional arcjet propellants, before moving to a green propellant. These tests would provide a baseline for the arcjet performance.

During the period of performance of the present effort, the insulator was redesigned to introduce the propellant tangentially along the anode wall to provide a swirling flow that will reduce arc instabilities in the constrictor (Figure 2. After fabrication the arcjet was assembled. While inserting the cathode into the assembly, it became bound and the insulator cracked. Schedules did not permit fabricating a replacement. Before fabricating a replacement in the future, it is recommended that the insulator design be updated for a loose fit hole for the cathode to allow for easier assembly and cathode thermal expansion during operation. It also is recommended to use a 0.063 inch radius ball end mill to fabricate the manifold that feeds the propellant channels in the insulator. This will reduce stress at the location where the insulator cracked on multiple occassions.

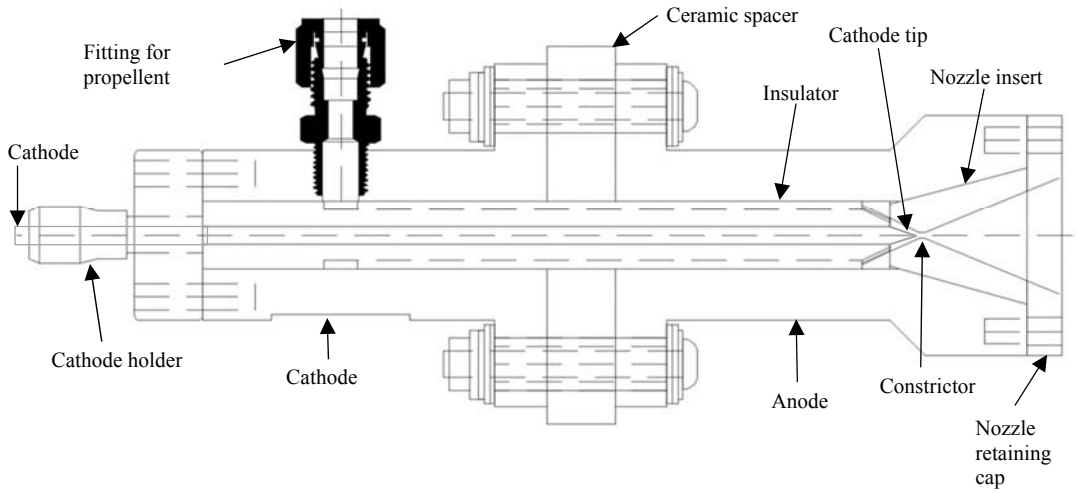

Figure 2. Arcjet assembly

Figure 3. Ceramic insulator with propellant feed channels.

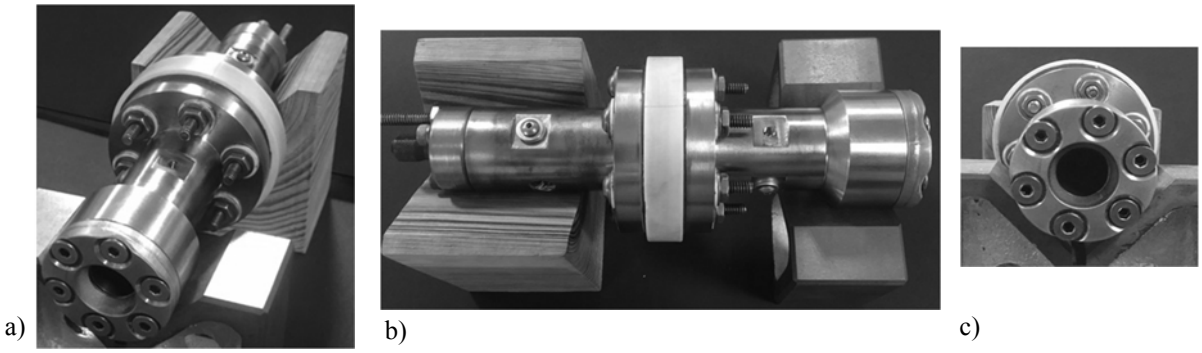

Figure 4. a) Oblique, b) Top, and c) Front view photos of the assembled arcjet.

III. Diagnostics

Emission spectroscopy and heterodyne laser interferometry diagnostic systems were developed. These diagnostics can be used to provide measurements of electron number densities, electron temperature, and species concentrations.

A. Emission Spectroscopy

Atoms and molecules have unique spectra lines associated with transitions between electronic states, and molecules have additional transition structures associated with vibrational and rotational states. When the energy level of the initial state is greater than that of the final state, a photon with energy *hv* is released. Transitions between select states in the atom or molecule result in a spectrum of lines that are unique to that atom or molecule. Hence, the spectral emission of radiation can be used to determine the constituents of a plasma. Measurement of spectral line widths provide information on specie concentrations, and line intensities can be used to determine electron temperatures[5,6].

A schematic of the emission spectroscopy setup as a thruster diagnostic is shown in Figure 5. In the present application, an image of the desired thruster plume area is directed into the the entrance slit of an Acton SP-500i, 0.5 m Czerny-Turner spectrometer. The optics used to produce the image (described below) were selected to almost fill the entrance slit, allowing spatial resolution of spectral emission. The instrument used to collect the spectral image depends on the wavelength of interest. A Princeton Instruments PI-MAX Camera is available for data acquisition in the visible part of the spectrum. It has an intensified, square CCD detector that can provide spatially resolved spectra from the spectrometer. For spectra in the near UV the spectrometer is converted to a monochrometer by fitting it with an exit slit, and a photomultiplier tube sensitive in the UV is used to measure emission intensity as the spectrometer is scanned through the desired spectral range.

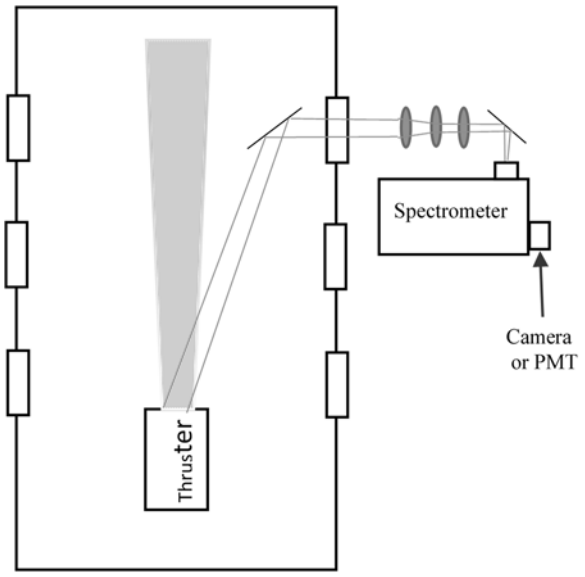

Figure 5. Schematic of setup for emission spectroscopy

A three-lens system, shown schematically in Figure 6, was developed to image the discharges from a pulsed inductive thruster (PIT) and asmall PIT. The small PIT configuration should be suitable for use with the arcjet. Because the object, *O1*, is much larger than the height of the spectrometer entrance slit, expanding (concave) lenses, *L1* and *L2*, are used to produce a virtual image, *I2*, that is focused onto the entrance slit by a converging (convex) lens. Thin lens theory[4] was used to aid the design process.

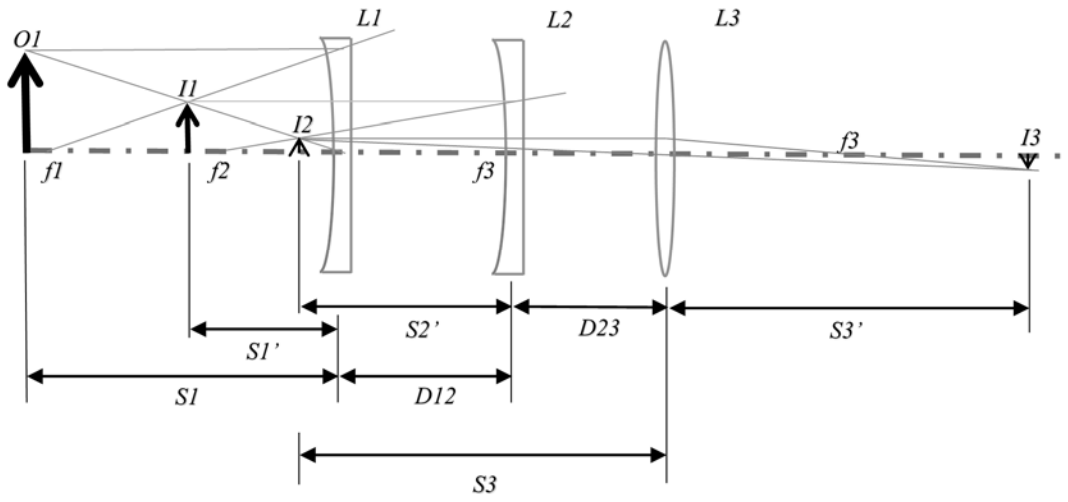

Figure 6. Three-lens imaging system

In a multiple lens arrangement the image of an object from the first lens becomes the object of the second lens, whose image becomes the object of the third lens, and so on. Thin lens equations[7] can be used to determine the image position, when the object postion relative to the lens and the focal length are known. The location of the first image, *S1'*, is given by:

$$S1' = \frac{S1 \cdot f1}{S1 - f1} \tag{1}$$

The location of the object for the second lens, *S2*, relative to *L2* is:

$$S2 = D12 - S1' \tag{2}$$

Note that the focal length for a concave lens is negative, and the distance to the image to a lens is negative with the image is on the left hand side of the lens. Hence the negative sign is used for our case. The image from the first lens, located at *S2*, is the object of the second lens. The location of the image that results from the second lens is given by:

$$S2' = \frac{S2 \cdot f2}{S2 - f2} \tag{3}$$

This image is the object for the third lens. The location of the object with respect to lens 3 is given by:

$$S3 = D23 - S2' \tag{4}$$

Note again that the the negative sign in the preceeding equation results accounts for the negative focal length of the second lens in our case. The final image will be located at *S3'* with respect to the third lens.

$$S3' = \frac{S3 \cdot f3}{S3 - f3} \tag{5}$$

The total distance from the object, *O1*, to the final image is given by

$$D_{total} = S1 + D12 + D23 + S3' \tag{6}$$

To ensure that the image of the object falls within the height of the spectrometer entrance slit, the magnification of the three-lens system must be determined. The total magnification, M_{Total}, of a series of lenses is simply the product of the magnification for the individual lenses. For our case,

$$M_{total} = M_1 \cdot M_2 \cdot M_3 \tag{7}$$

where

$$M_1 = -\frac{s1'}{s1}; \quad M_2 = -\frac{s2'}{s2}; \quad M_3 = -\frac{s3'}{s3} \tag{8}$$

Equations (1) through (8) were entered into a spreadsheet to calculate the total magnification, image height, and position of the image of lens 3 given the object height, the distance between the object and lens 1, distances between the lenses, and the focal lengths of the lenses. Two scenarios are envisioned for imaging a thruster, one for larger thrusters and one for smaller thrusters. The PIT and small PIT are reasonable examples, respectively. For the PIT, the plasma region of interest is approximately 30 cm tall and would be positioned approximately 4 m from the spectrometer. For the small PIT, these values are 9 cm and 2 m. Parametric studies using lenses available from Newport were conducted in an attempt to optimize the optical configuration to achieve a final image height approaching 1.4 cm, the height of the spectrometer entrance slit, and a non-expanding image entering the spectrometer. The latter is accomplished by positioning the object of the convex lens, L3, two focal lengths from lens 3. Because of the spacing constraints and the limited availability of negative focal length (concave) lenses, a configuraton meeting both criteria could not be achieved. This was especially true for imaging the small PIT plume (see Table 1). Note that the negative sign in the image height indicates the image is inverted. Also note that the first two rows of data. Rows 3 and 4 are not ideal, but use lenses that are in-stock, allowing the optical setup concept to be tested earlier. The total distance from the object to the entrance slit is significant enough to require turning mirrors with antireflection coatings for the UV range, and the total distance can be altered significantly while maintaining a reasonable image height.

Table 1. Parameters of optical setup

Object Height (mm)	*f1* (mm)	*f2* (mm)	*f3* (mm)	*S1* (mm)	*D12* (mm)	*D23* (mm)	*S3'* (mm)	*Dtotal* (mm)	*Image Height* (mm)
300	-500	-500	150	4000	300	50	351	4700	-13.46
93.3	-500	-500	150	2000	30	70	299	2399	-9.95
300	-250	-250	100	4000	140	50	208.3	4398	-6.66
90	-200	-250	75	2000	30	25	162	2217	-5.33

Erosion of the boron nitride (BN) electrical insulators typically used in electric propulsion devices makes it is of interest to monitor boron emission lines in the thruster exhaust. Since the preliminary testing of the PIT is done in open air, nitrogen emission lines cannot be used. There are no strong atomic boron lines in the visible part of the spectrum. However, there are strong boron lines at 249.6769 nm and 249.7722 nm [8] in the ultraviolet, thus requiring optics with antireflective coatings for UV wavelengths. Either a UV-sensitive intensified camera or a UV-sensitive photomultiplier tube must be used to detect these lines. An alternate approach would be to use barium (Ba) as a dopant placed on the surface of the BN insulator, since it is an element not likely to be present in the local environment. Also, atomic barium has a strong emission line in the visible at 553.5481 nm [8]. There appear to be no nitrogen or oxygen lines near this wavelength, so the barium line should be discernable, if present. The spectrometer can be spectrally calibrated in this region of the spectrum using a neon/mercury calibration lamp, which has the following lines on either side of the line of interest: NeI 540.05618 nm, HgI 546.0735 nm, NeI 576.4418 nm, and NeI 585.24879 nm [8].

At the end of the period of performance the spectral emission diagnostic was near completion. The spectrometer was calibrated in the visible spectrum using a high-speed camera with intensified detector. Calibration in the UV, where atomic boron lines reside was near completion. For the UV, a high-speed camera with intensified detector was installed, but unfortunately it appeared to malfunction and could not detect lines in either the UV or visible. As an alternate to using the camera for detection, the spectrometer was transformed into a monochrometer through the installation of an exit slit to which a photomultiplier tube (PMT) was mounted. Only vintage PMT equipment was available, and missing components prevented the completion of this diagnostic tool before the end of the period of performance.

To provide the capability to collect spatially-resolved spectral emission across a region of a thruster plume, a three-lens imageing system was designed, as described above. Multiple lens configurations were recommended to allow imaging the desired areas of thruster of different sizes. Lenses were ordered, but many still were on backorder at the completion of the period of performance.

B. Heterodyne Laser Interferometry

Interferometry has long been used as a non-intrusive tool for plasma characterization[9], providing a means of determining line of site electron number density. The refractive index, *n'*, due to electrons in a plasma is related to the electron number density, N_e, [10]

$$n' - 1 = -\frac{\lambda^2 N_e q^2}{8\pi^2 m_e \epsilon_o c^2} \tag{9}$$

The resulting phase shift is given by

$$\varphi = -\frac{2\pi}{\lambda}\int (n' - 1)\, dl \tag{10}$$

Substitution of equation (9) into equation (10) gives

$$\varphi = -\frac{\lambda q^2}{4\pi^2 m_e \epsilon_o c^2}\int N_e\, dl \tag{11}$$

Thus, one can determine the electron number density integrated over a line of site through a plasma by measuring the phase shift. This is accomplished by splitting a laser beam, passing the field beam through a plasma and recombining the beam with the reference beam to produce constructive and destructive interference that results in interference fringes. Laser interferometer techniques are all based on this principle but very in arrangement.

For the work described herein heterodyne laser interferometry with electronic quadrature phase detection was used. The heterodyne laser interferometer was introduced by Weber[11,12]. A schematic of a single cord, heterodyne laser interferometer in a Mach-Zehnder configuration is shown in Figure 5. A 17 mW helium-neon laser with a 632.8 nm beam is split into a reference beam and a field beam with a pellicle beam splitter (BS in Figure 7). The field beam is modulated by an acousto-optic modulator (AOM), which adds a sinuosoidal phase modulated intensity to beam modes greater than one. The first mode (dashed line in Figure 3) is isoloated and used for the field beam, which passes through the plasma and is recombined with the reference beam via a beam splitter before illuminating the detector (D). The reference beam (solid line in Figure 7) has an optical path length that can be varied using the translation stage (TS). Laser interferometers are commonly configured so that the reference and field beams have the same length, ensuring the coherence of the beams. However, in Ref. 13 it is shown that it is not necessary to have equal path lengths, but the path length difference must be an even multiple of the laser cavity length.

The single chord heterodyne laser interferometer shown in Figure 7 can be used to measure line of site electron number density using equation (11). The background phase shift, the phase shift of the setup without plasma present, provides the measurement uncertainty. The two chord heterodyne laser interferometer shown in Figure 8 has two field beams that can be used to determine the line of sight electron number density at two distinct locations. They also allow the determination of the directed velocity of the electrons from the known distance between the chords and the time it takes to traverse the distance. For large vacuum chambers, the setup shown in Figure 8 is not practical, as it becomes difficult to direct beam paths around the chamber without obstruction. An alternate setup for large chambers is shown in Figure 9. It provides a simpler optical setup by incorporating two-passes of the field beam through the chamber for each cord. The configuration shown in Figure 8 was set up and demonstrated, and photographs are provided in Figure 10.

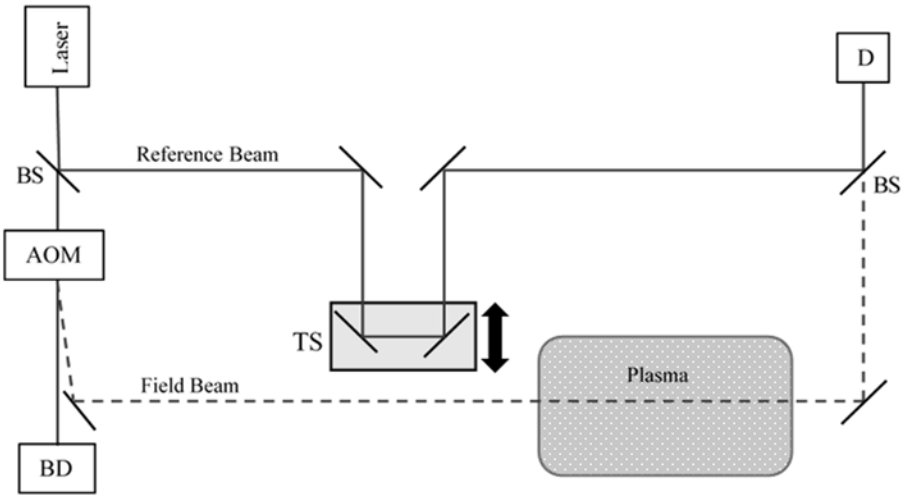

Figure 7. Schematic of heterodyne laser interferometer setup (single cord)

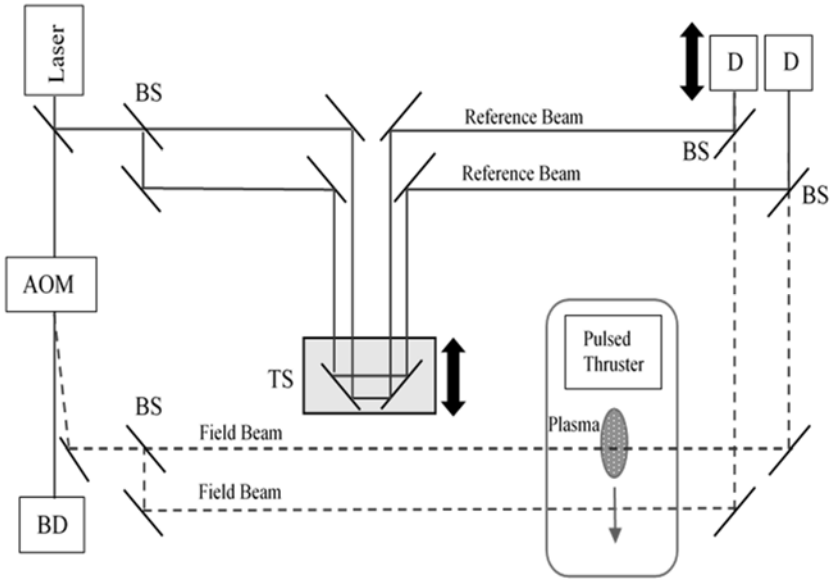

Figure 8. Schematic of heterodyne laser interferometer setup (double cord)

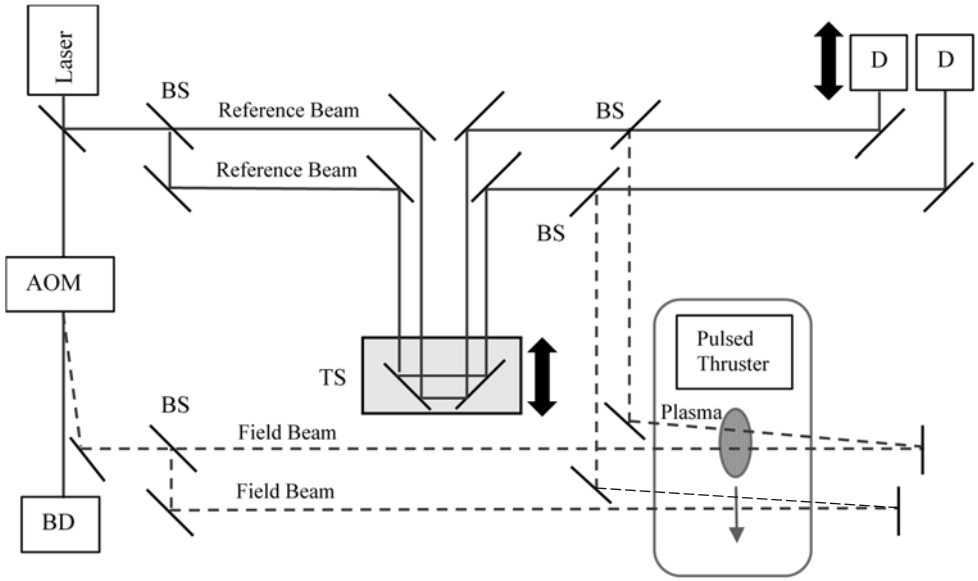

Figure 9. Schematic of alternate heterodyne laser interferometer setup (double cord)

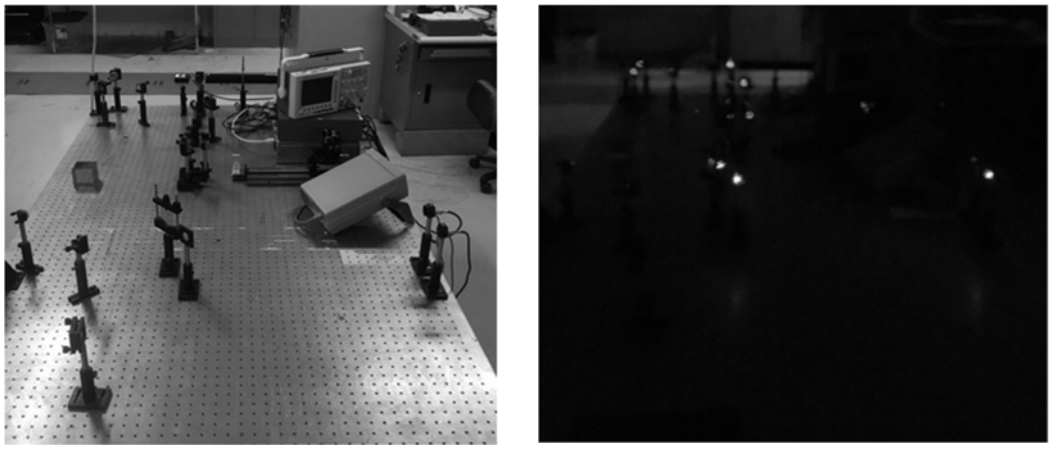

Figure 10. Photographs of heterodyne laser interferometer setup (double cord) in configuration shown in Figure 8

IV. Summary

The purpose of this effort was to work towards the demonstration of an arcjet using green propellant. Tasks included development of two diagnostics tools to be used in performance evaluation—emission spectroscopy and heterodyne laser interfereometery. A two-cord heterodyne laser interferometer with electronic quadrature phase detection was demonstrated, and is ready for implementation. An emission spectroscopy setup is nearly completed and waiting for missing detector components. Imaging systems that will allow spatially resolved spectral images of thruster plumes were designed and components were ordered. Finally, an arcjet thruster was readied for testing with simulated ammonia and hydrazine propellants to establish baseline operation before moving on to a green propellant. The arcjet insulator was updated for swirling flow propellant injection. Improvements to ease assembly and increase insulator robustness were suggested.

Acknowledgments

Trevor M. Moeller thanks Kurt A. Polzin for the opportunity to collaborate with him during this work. Thanks to Adam Martin for his help during the development of the diagnostics described herein. Thanks also to NASA Intern Alicia Ratcliffe for her help throughout the summer, and also to UTSI Graduate Student Theron Price for the assistance

he provided during his stay at MSFC. The University of Tennessee Space Institute funded this NASA MSFC Faculty Fellowship.

References

1. *High Performance Green Propellant for Satellite.* Neff, K., King, P., Anflo, K., and Mollerberg, R. Denver : American Institute of Aeronautics and Astronautics, 2009. AIAA 2009-4878.
2. Jankovsky, Robert S. *HAN-Based Monopropellant Assessment for Spacecraft.* s.l. : NASA, 1996. NASA Technical Memorandum 107287.
3. Jahn, Robert G. *Physics of Electric Propulsion.* s.l. : Dover Publications, 2006.
4. Jahn, Robert G. and Choueiri, Edgar Y. Electric Propulsion. *Encyclopedia of Physical Science and Technology, Third Edition, Volume 5.* s.l. : Academic Press, 2002.
5. Lochte-Holtgreven, W. *Plasma Diagnostics.* New York, NY : Interscience (Wiley), 1968.
6. Griem, Hans R. *Principles of Plasma Spectroscopy (Cambridge Monographs on Plasma Physics).* Cambridge : Cambridge University Press, 2005.
7. Hecht, Eugene and Zajac, Alfred. *Optics.* Reading, Massachussetts : Addison-Wesley Publishing Co., 1974.
8. *Atomic Spectra Database, NIST Standard Reference Database 78.* s.l. : U.S. Department of Commerce , 2016.
9. Holt, E.H. and Haskel, R.E. *Foundations of Plasma Dynamics.* New York : MacMillan, 1965.
10. Smith, L.M., Keefer, D.R., and Wright, N.W. A fiber-optic interferometer for in-situ measurements of plasma number density in pulsed-power applications. *Review of Scientific Instruments.* July 2003, Vol. 74, 7.
11. Weber, B.V. and Hinshelwood, D.D. He–Ne interferometer for density measurements in plasma opening switch experiments. *Review of Scientific Instruments.* 1992, Vol. 63, 5199.
12. Weber, B.V, and Hinshelwood, D.D. Interferometry of flashboard and cable-gun plasma opening switches on Hawk. *IEEE Transactions on Plasma Science.* 1997, Vol. 25, 2.
13. Kumar, Deepak and Bellan, Paul M. Heterodyne interferometer with unequal path lengths. *Review of Scientific Instruments.* 2006, Vol. 77, 083503.

Electric Sail Space Flight Dynamics and Controls

Carlos Montalvo*
University of South Alabama
150 Jaguar Dr, Shelby Hall Rm. 3106
Mobile, AL USA, 36688

1 Introduction

The Electric Sail (E-Sail) is a relatively new concept of advanced in space propulsion. This technology has the potential to provide propellant-less propulsion throughout the solar system. An electric sail deploys multiple long (20 km) tethers that are positively charged. The solar wind interacts with the tethers to provide propulsion. Based on the E-Sails characteristic acceleration, the E-Sail can reach the Heliopause region in 10 years. A solar sails characteristic acceleration puts a solar sail in the Heliopause region in 20 years which can be compared to chemical rockets which is 24 years. The only spacecraft to reach the Heliopause region is the Voyager 1 and 2 spacecraft which reached the Heliopause region in 36 years. The increase in performance from a solar sail to an E-Sail lies in the growing sheath width of the electric sail which grows with distance from the sun. As such, an E-sail will continue to accelerate to 20 AU as opposed to only 5 AU with a solar sail. Initial studies on E-Sails was completed by Janhunen and Mengali which first created a mathematical model of the thrust produced by the solar wind.[1,2]

Much work has been done in the area of thrust generated by an E-Sail;[3] however, the E-Sail program poses numerous dynamics and controls problems due to its complex design. The Technology Demonstration Mission (TDM) involves two 6U CubeSats connected to a 16 km tether. The satellite initially de-tumbles and then separates both 6U CubeSats. The tether is then deployed. An electron gun is fired to positively charge the tether to interact with the solar wind produced by the sun to create propulsion. This propulsion must be counter-balanced by spinning the entire system. Thus, the entire system must undergo complex deployment and spinning as well as controlling the system by solely using thrust produced by the E-sail.

Previous work has been done in the area of tether deployment. Many designs center around using gravity gradients[4] to deploy the two spacecraft and then use a type of mechanical brake[5] or barberpole[6] to halt the deployment of the tether. The YES2 satellite program utilized the gravity gradient of the Earth to deploy a small payload to re-enter the Earth's atmosphere.[4] The small payload was deployed with a long tether and then subsequently cut so the small payload could re-enter the atmosphere. This project utilized a barberpole to slow the speed of the payload. The work done by Iki et al, involved deploying an electrodynamic tether for removal of large space debris. During deployment a small amount of friction was modeled. Once the tether reaches a critical length, a brake is deployed to increase the force on the secondary payload.[5] A comprehensive review of tether deployment has been put together by Yi et al.[7]

The second problem of in space tether control has been investigated in great detail as well. Chen et al has put together a comprehensive review of tether attitude and motion control.[7] Work on rotational tether has been conducted including the work by Modi et al; however, this project involved the spacecraft rotating along the axis of the tether rather than orthogonal like the E-Sail.[8] Work that directly relates to E-sail control has been performed quite recently by Janhunen,[9].[10] All of this work however has been

*Assistant Professor, Department of Mechanical Engineering, cmontalvo@southalabama.edu, 251-460-7458

performed using analytical solutions with no dynamic models that contain all piece parts put together. The work presented here establishes an E-Sail dynamic model that contains all dynamics associated with E-Sails including a simple propulsion model.

2 E-Sail Simulation Tool

The mathematical model used here begins with the translational dynamics of the satellite which are written using inertial coordinates to simplify the equations of motion. The satellite is assumed to be a rigid body using quaternions to parameterize orientation. Thrusters are placed on board the satellite which imparts forces and torques as well as reaction wheels to control the orientation of the satellite. Each satellite is connected to a tether which is modeled using a viscoelastic tether bead model. The other end of the tether is connected to a confluence point which is modeled with three degrees of freedom and finite mass. Finally, the propulsion model of the tether is modeled as a per unit force that is a function of the voltage bias along the tether. A large voltage bias results in a large per unit force along the tether which can be used to propel the satellite forwards and turn the satellite. The derivation of all of these models has been removed to increase the number of results in this report. However, a larger unabridged version has been written in the event the dynamics are required for future work.

3 Simulation Setup

For the simulations that follow the following parameters are used. In this simulation three reaction wheels and three magnetorquers are used. The reaction wheels are aligned with the principal axis of inertia of the satellite. It is also assumed that all reaction wheels are positioned at the center of mass of the satellite. The number of beads and the length of the tether varies with every simulation below; thus, those parameters will be stated specifically whenever the value changes. Eight thrusters are placed on each corner of the satellite and used to control the satellite. The mass of each satellite is 12 kg, the mass of the tether is 1 kg, the mass of the confluence point is 0.3 kg and the mass of each reaction wheel is 350 g. The total inertia that the reaction wheel can store is 100 mN-s. The inertia of the satellite is $0.13, 0.1, 0.05\ kg-m^2$ along the principal axis of inertia and it's assumed that the cross axis of inertias are zero. The connection point of the tether on the satellite is 0.2 meters along the z-axis of the satellite. The tether has a modulus of 5.8e9 Pa. The thrusters pulse at 25 mN and have an I_{SP} of 40 seconds.

4 Tether Deployment

Tether deployment involves multiple phases. The first phase is detumbling the satellite using thrusters. Once the satellites have a low angular velocity the satellite must separate slightly using thrusters. The satellites must then rotate 90 degrees due to the face that the tether is connected to the top of the satellite. Once the satellites are positioned properly the satellites must deploy thrusters to a desired deployment velocity at which point the tether will begin to reel out. A brake must be actuated to reduce the velocity of the satellite at which point the satellites must again actuate the thrusters to spin the satellite to about 8 revs/day. When the E-sail is creating propulsion, the satellite must spin up otherwise the satellite will collapse on itself from force of the tether. These phases are all described in detail in the sections that follow.

4.1 Initial Separation

Little work was conducted on the initial separation phase. The main issue in this phase stems from hitting the limit on tether length during this phase. Simulations were run where 1 meter of tether was allowed to reel out but the satellites attained too large of an initial separation. Figure 1 shows three separate frames

from the same simulation showing a flapping mode that can be excited when deploying the satellites.

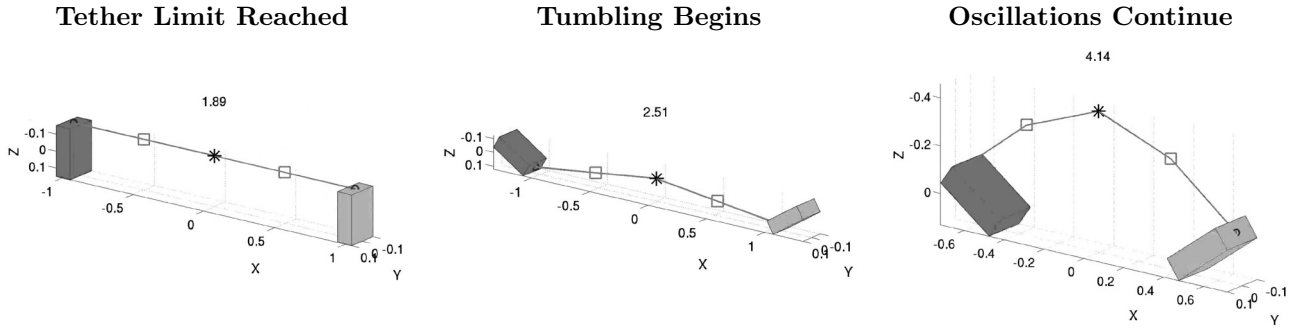

Figure 1: Flapping Mode of Tethered Satellites

In order to mitigate this issue it is possible to actuate thrusters or different sized reaction wheels. The data indicates that anything over a deployment speed of 0.15 m/s can be catastrophic for the system which is why care must be taken during this phase of deployment.

4.2 Final Separation

Once the satellites have separated and oriented themselves at 90 degrees to each other it is time to actuate thrusters and accelerate to a desired deployment velocity. Accelerating to a desired deployment velocity is not an issue, other than the amount of fuel burned. The issue stems from reducing the velocity of the satellites back to zero. Any kinetic energy put into the satellite must be removed using some system. It would be possible to use more propellant and remove the kinetic energy that way but the more cost effective method would be to increase line tension and remove the kinetic energy by transferring it to elastic energy in the tether. There are some complications with this method however. In the simulation below the satellites have been accelerated to 2 m/s and the tether is already 10 meters deployed. The maximum line length is set to 25 meters to simulate the issue in a reasonable amount of time. A friction model has been placed in the tether model using the equation below where u is the velocity of the satellite.

$$T_{MAX} = 0.038u + 0.005 \tag{1}$$

The equation states that the tension in the tether must exceed that T_{MAX} value before any amount of tether can be released. The results of the simulation are shown in Figure 2. The plots show that very little tension is required to deploy the tether. As such the velocity of the satellites is very much unchanged until the tether stop deploying around 0.15 minutes. At this point the velocity becomes negative causing the satellites to collapse towards each other. The tension reaches a maximum of 23 N thus the tether will have to be designed to withstand this amount of tension if this friction model is used. If it's possible to increase the amount of friction in the tether during deployment the satellites lose kinetic energy continuously during deployment rather than all at once. In this scenario the tether friction force is increased to 1 N.

$$T_{MAX} = 0.038u + 1.0 \tag{2}$$

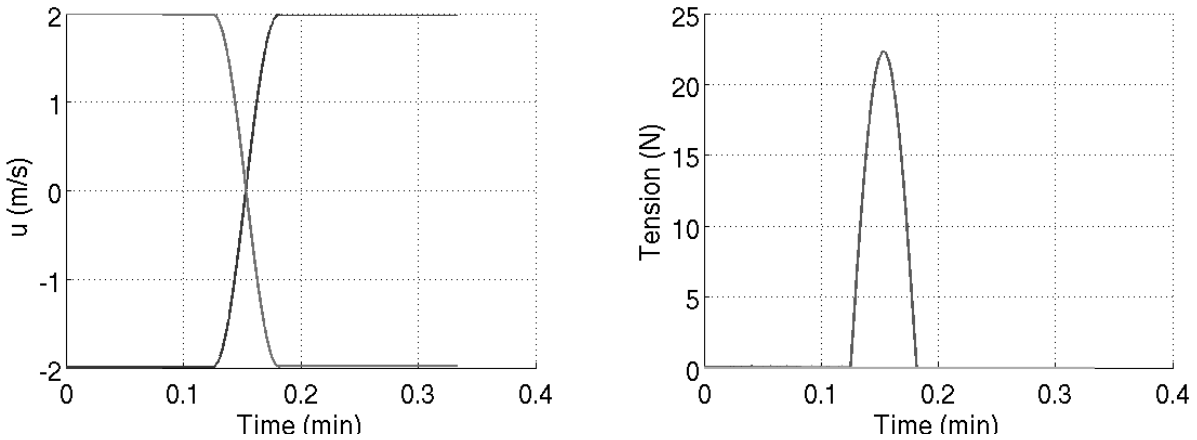

Figure 2: Tether Deployment with Low Friction Model

This results in no tether deployment unless the tension reaches a minimum of 1 N. As such the velocity of the satellites steadily decreases. Once the tether reaches 25 meters the large spike in tension is reduced to 15 N. Thus, with this model it is possible to reduce the spike in tension. The issue of course is that friction cannot simply be changed automatically. It is possible to create a passive brake that is deployed when 75% of the tether has been deployed. Using this model, T_{MAX} becomes

$$T_{MAX} = 0.038u + 0.005 + \lambda(3.0v + 2.3) \tag{3}$$

where λ is either 0 or 1. In this case it is equal to zero when less than 75% of the tether has been deployed and 1 when more than 75% has been deployed.

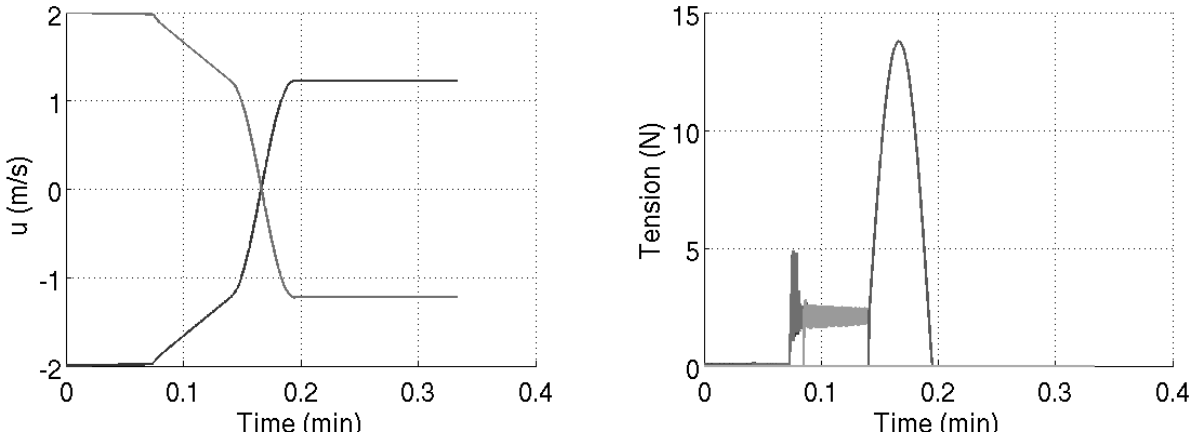

Figure 3: Tether Deployment with Low Friction and Passive Brake

Figures **??** show low line tension up until about 0.08 minutes at which point the brake is engaged and the tension rises to 2.3 N. There are some high frequency oscillations due to the instantaneous onset of the brake. The result though is that the highest line tension is less than 15 N. The performance of this brake could be designed even better if the brake was deployed sooner such that the velocity of the satellites exactly

equaled zero when the tether was fully deployed. To do this, a barberpole mechanism or something similar[6] can be used to actively control the amount of line tension desired. In this case, a simple linear control law is created

$$T_{MAX} = \epsilon(L_T - L_{T0}) \tag{4}$$

where ϵ is some slope designed by the user and L_{T0} is the tether length at which point the active brake is activated. When L_T is less than L_{T0} the tension is simply equal to the friction in the tether which can be given by equation 1. The results of this simulation are shown in Figure 4.

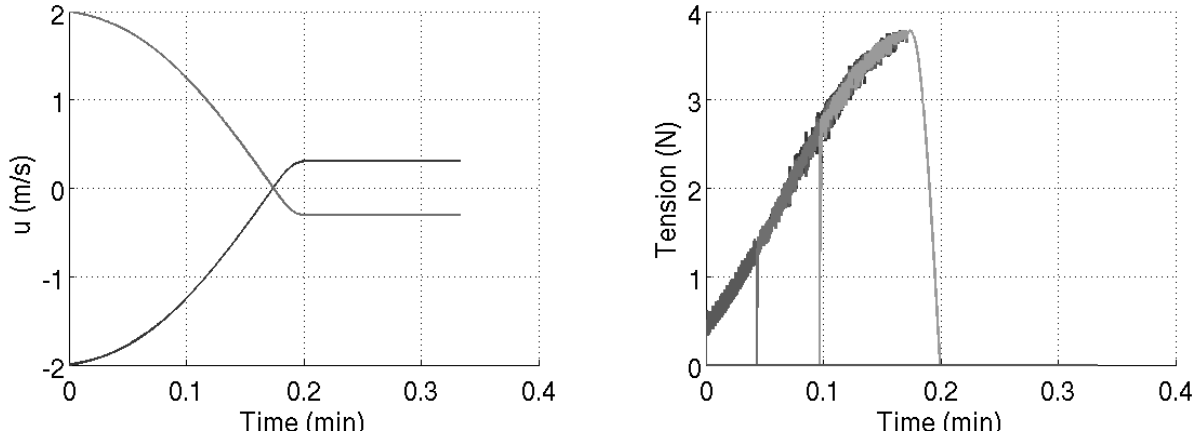

Figure 4: Tether Deployment with Linear Brake Law

The results of this simulation show that the large spike seen in previous simulations is completely removed. This is because the velocity of the satellites becomes negative before the tether is fully deployed. It's easy to see in this case that the slope ϵ can be tuned to perfectly slow the satellites to zero the moment the tether is deployed. The kinetic energy in the satellites must be removed without increasing tension to a large amount. It would seem that a constant controller would work the best. The problems associated with braking at a constant force then reduce to the amount of braking (magnitude) and when to activate the brake (activation time). This really boils down to two variables: deployment velocity and the remaining amount of tether available.

Figure 5 (left) shows the amount of braking force or tension required to slow a satellite to zero as a function of Remaining Tether (m) and Deployment speed (m/s). The Figure indicates the expected result that a low deployment speed and activating the brake early results in low tension while high deployment velocity and activating the brake late will result in high line tension. The initial recommendation then of course is to just deploy as slow as possible and deploy the brake almost immediately. The issue with this of course is that deploying slowly results in a very lengthy maneuver. As shown in Figure 5 (Right) the time to fully deploy the E-sail can approach 16000 seconds which is roughly 4 hours. Furthermore, low deployment velocities will have other issues when it comes to keeping tension on the line. It's possible for the maximum tension to get so low that it will be within the noise of the brake causing the system to exhibit unknown behavior such as snags, snap backs or even entanglement due to slack produced in the line. The plots indicate that a deployment velocity of 5 m/s and activating the brake at 500 meters remaining results in about 1 Newton of tension in the line. The propellant required to reach this deployment velocity is about 176 grams. Thus, trade offs need to be made when determining deployment velocity and mass of propellant required. As a final note, increasing mass on the satellite translates directly to more kinetic energy. A similar study can be conducted to show the effect of mass on the system. The relationship between mass and deployment velocity is non-linear; however, the penalty of adding mass is not as severe if the deployment velocity is kept low.

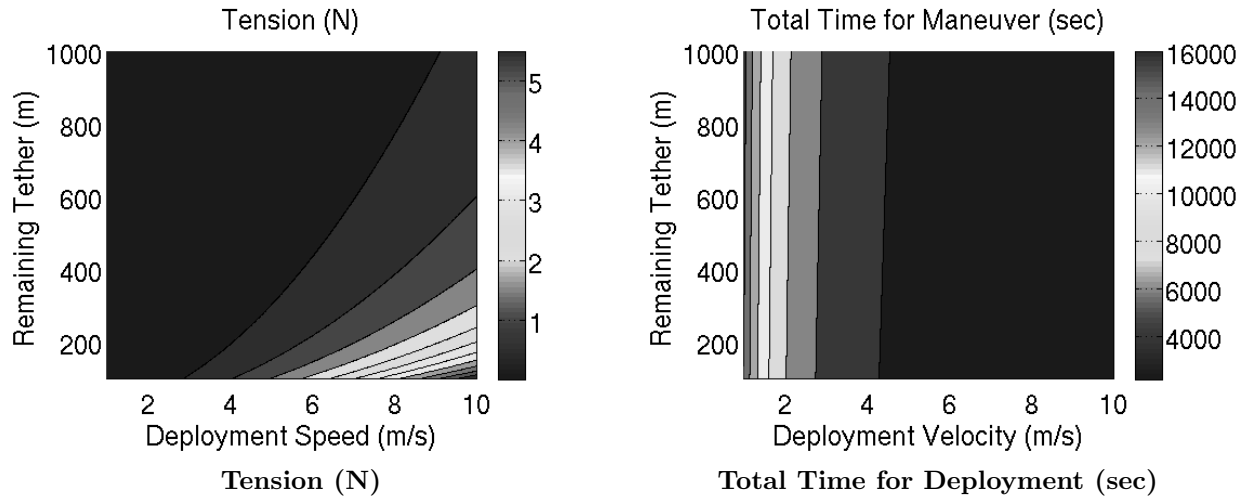

Figure 5: Tension (N) and Deployment Time (sec) vs. Remaining Tether (m) and Deployment Velocity (m/s)

5 E-Sail Controllability

Controllability of the satellite involves three main maneuvers. The first is the initial spin up of the satellites to a nominal 8 revs/day. The second is constant spin rate and constant propulsion to accelerate the E-Sail. The final maneuver is to actuate the tethers with variable voltages to turn the spacecraft.

5.1 Initial Spin Up Maneuver

Spinning up the satellite is not so simple as activating thrusters until a desired spin rate is achieved. As shown in the previous section, the satellites will exhibit a large negative velocity if the braking control law is not designed properly. Regardless of the type of controller used however the satellites will always begin to move towards each other unless the spacecraft is spun up to keep satellites apart due to centrifugal acceleration. The design parameter is then when to begin this spin up maneuver. To show the worst case scenario, 20 meters of tether is deployed and the satellites are spun up to 8 revs/day. The final line length of the tether is set to 50 meters. Thus, the satellites are spun up when less than 50% of the tether is deployed. In addition, the passive brake shown in the previous section is activated when 80% of the tether is deployed. Figure 6 (Left) shows a chart of the tension during spin up. Here, the tether is deployed with relative ease until the brake is deployed around 0.38 minutes. Unfortunately, this brake is not enough to slow down the satellites and a large snap load is created. This large spike in tension does not go away quickly. The damping coefficient of tethers like this is relatively low and thus these tension snaps will take quite a bit of time before these tension snaps are completely removed. The largest problem with this is the orbit of the satellites becomes a square instead of a circular orbit as indicated by Figure 6 (Right).

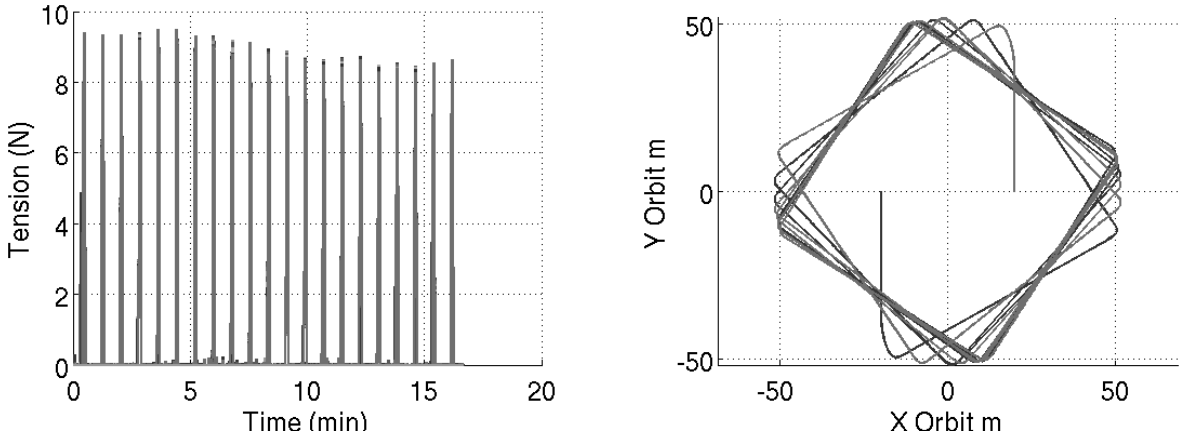

Figure 6: Spin up Maneuver Activated at 40% Deployment

If the spin up maneuver is executed properly the tension spikes can be mitigated as shown in Figure 7. Here, the spin up maneuver is performed when 45 meters of the tether is already deployed which corresponds to 90% deployment. At this deployment percentage the brake activates immediately. The result is only 2.3 N remain in the tether during the spin maneuver. This results in a more circular orbit. Thus, the conclusion once again is to reduce the amount of tension in the tether before operation. It is also worth noting that in order to reach a spin rate of 8 revs/day, the tip velocity of each satellite must be 4.65 m/s when the tether is fully deployed at 16000 meters. In order to reach 4.65 m/s the thrusters must be activated for 40 minutes. During this maneuver 320 grams of propellant is expended. In addition, depending on the connection joint of the satellite to the tether, reaction wheels may need to be activated to keep each satellite pointed toward the tether line of action.

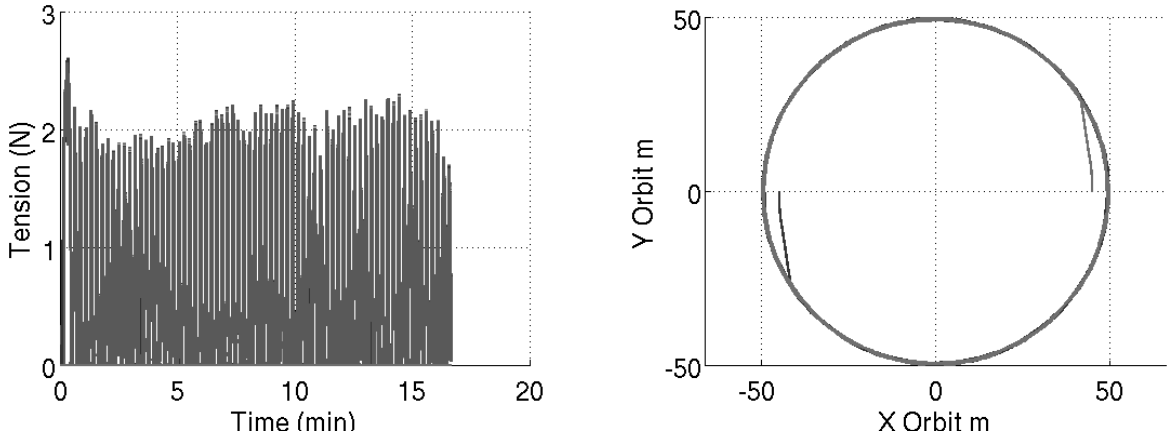

Figure 7: Spin up Maneuver Activated at 90% Deployment

5.2 Linear Acceleration

While the system is spinning, a 6 kV bias is created in each tether. This bias interacts with the solar wind produced by the sun. With a 16 km tether, a 6 kV bias is estimated to produce 1.36 uN/m or 21.8 mN over

the whole tether. The mass of the entire system is estimated to be about 24 kg resulting in 0.91 mm/s^2 of acceleration. If the system does not spin, the system will collapse on itself. If the system is allowed to spin at 8 revs/day, the system exhibits a catenary rather than collapsing in on itself as show in Figure 8. However, this catenary is not steady. An oscillatory mode is found due to competing forces: centrifugal force, tension force, and tether-propulsion force. The flapping amplitude and frequency is clearly a function of these three forces.

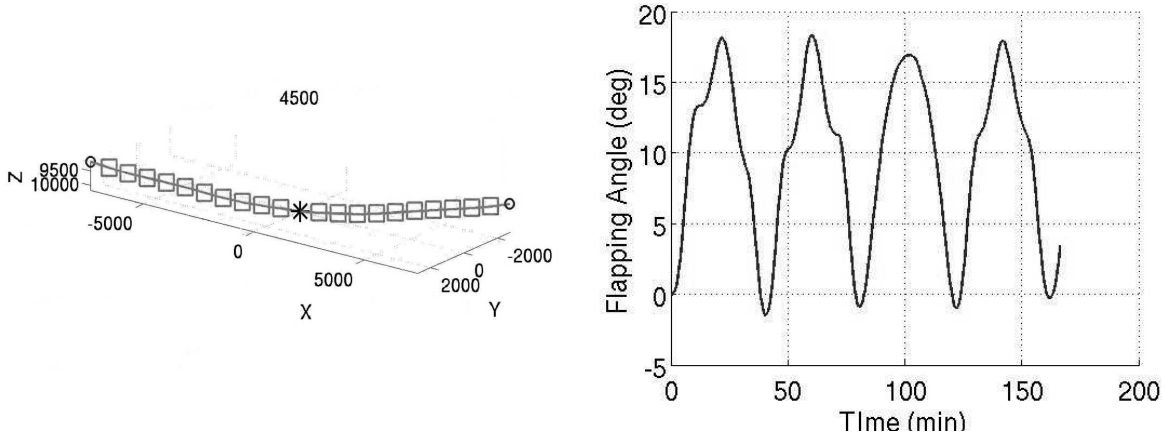

Catenary **Flapping Angle**

Figure 8: E-Sail Propulsion while Spinning

The flapping angle can be seen for this configuration in Figure 8 (Right). Here the flapping amplitude is about 9.14 degrees and the frequency is 0.19 mHz. If the spin rate is allowed to vary, the flapping amplitude and frequency can be reported. As expected the amplitude of this flapping mode declines and the frequency increases. Thus, it may be a better design choice to increase spin rate to try and reduce the amplitude of this oscillation. Even with this flapping mode, the E-sail accelerates to 8 m/s in 150 minutes and will continue increasing in velocity until the solar wind no longer reaches it around 20 AU.

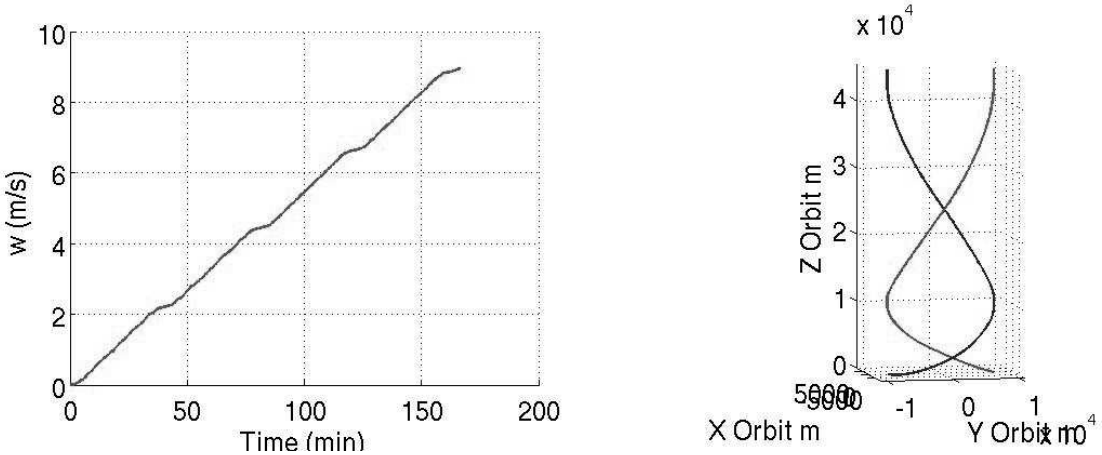

Figure 9: Linear Acceleration of E-Sail

5.3 Turning Capabilities

In order to turn the satellite, the voltage of the satellite is actuated in a sinusoidal fashion. When the tether has an azimuthal angle of zero, one tether is biased to 40 kV and the other is biased to 0 kV. Initial simulation results indicate that the spin rate actually increases as function of time. The result of non-uniform tether bias is a torque on the system to turn the orbital plane of the E-sail. The 40 kV bias is chosen so that a reasonable amount of torque is generated in a short amount of time. Figure 10 shows the results of applying this voltage pattern. The results show that the satellite still accelerates but the satellite also turns towards the negative y-axis and the positive x-axis. The z-coordinate also is not identical for both satellites and is oscillatory indicating that the orbital plane has in fact tilted by a small amount.

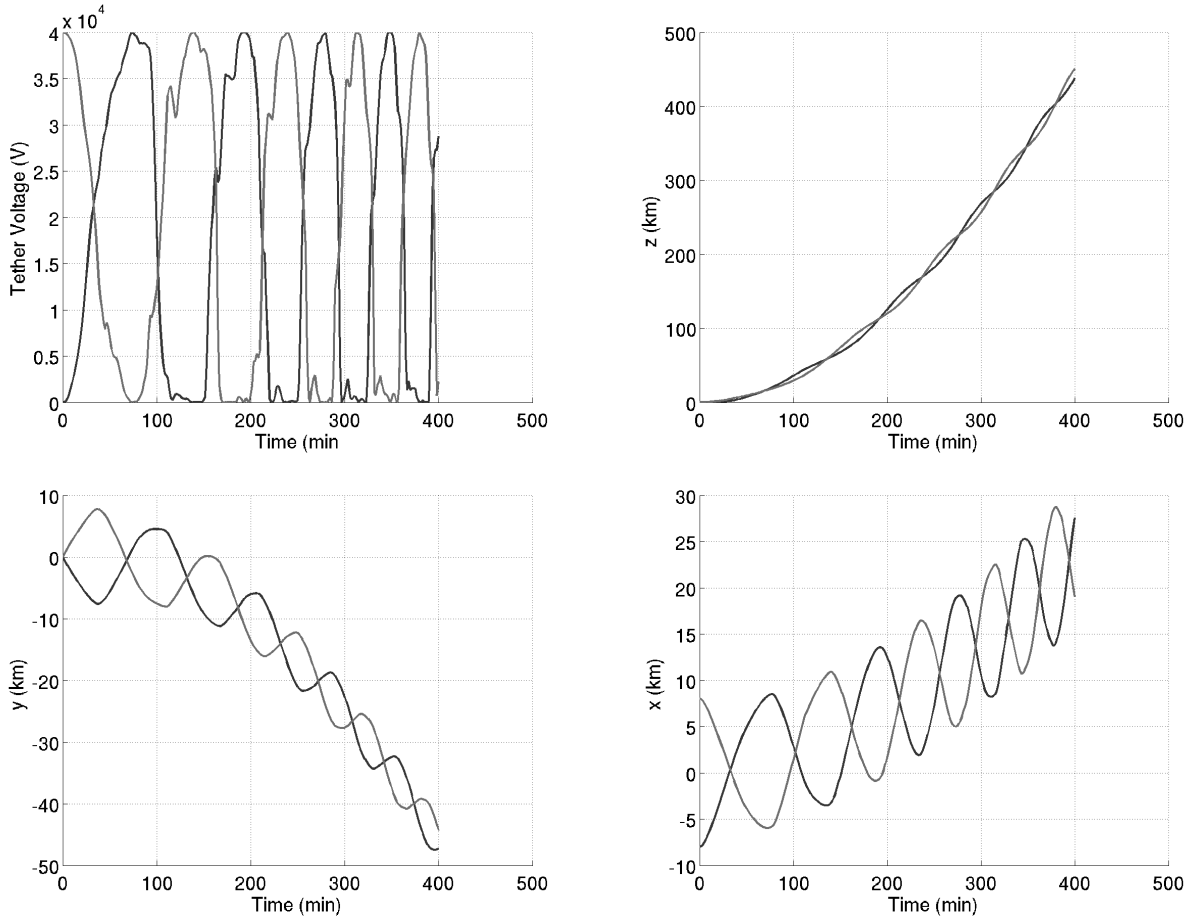

Figure 10: E-Sail Orbital Tilt Maneuever

6 Conclusions

An E-Sail with two 6U satellites and a 16 km tether has been investigated here. A sophisticated simulation tool has been developed that models the satellites, the tether and the propulsion model of the tether interacting with the solar wind. In addition, magnetorquers, reaction wheels and thrusters have been added to the model to simulate complex maneuvers during deployment and spin up. Complex flapping modes were found during deployment and spin up and care must be taken to reduce line tension to reduce the amplitude

of these modes. The mass budget of propellant has been set to 1.25 kilograms. The detumbling maneuver requires 28.9 grams, the deployment process could take 176 grams and the spin up maneuver will take about 320 grams. In total all maneuvers require about 500 grams. A safety factor of 2 produces 1 kg thus the mass budget of 1.25 kg seems reasonable. It is also possible to use reaction wheels to stabilize some of these modes and may even be required when spinning up the spacecraft. The deployment process is quite a complex procedure. The results in this report indicate that the deployment process should follow fixed steps to ensure maximum robustness. These steps include: activating thrusters to separate satellites, deactivate thrusters once desired deployment velocity has been reached, coast, activate brake to slow satellite velocity to zero, activate thrusters to spin and finally, deactivate thrusters once desired spin rate has been achieved. If a TDM is proposed for ISS or SLS in 2021, numerous more trade studies should be conducted to determine optimal deployment and operation of the E-Sail. The results still show promising results and indicate that the E-Sail can be a useful spacecraft for future NEO missions or even deep-space exploration.

References

[1]Pekka Janhunen. The electrical sail–a new propulsion method which may enable fast missions to the outer solar system. *Journal of the British Interplanetary Society*, 61(8):322–325, 2008.

[2]Giovanni Mengali, Alessandro A Quarta, and Pekka Janhunen. Electric sail performance analysis. *Journal of Spacecraft and Rockets*, 45(1):122, 2008.

[3]Pekka Janhunen. Electric sail for spacecraft propulsion. *Journal of Propulsion and Power*, 20(4):763, 2004.

[4]A Hyslop, M Kruijff, and C Menon. Simulating space tether deployment on earth for the yes 2 satellite. In *56 th International Astronautical Congress*, 2005.

[5]Kentaro Iki, Satomi Kawamoto, and Yoshiki Morino. Numerical simulations of an electrodynamic tether deployment from a spool-type reel using thrusters. *Advances in the Astronautical Sciences*, 145:1045–1064, 2012.

[6]Michiel; Vavouliotis Antonios Menon, Carlo; Kruijff. Design and testing of a space mechanism for tether deployment. *Journal of Spacecraft and Rockets*, 44(4):927–939, 07 2007.

[7]Yi Chen, Rui Huang, Xianlin Ren, Liping He, and Ye He. History of the tether concept and tether missions: a review. *ISRN astronomy and astrophysics*, 2013, 2013.

[8]V.J. Modi, S. Pradhan, M. Chu, G. Tyc, and A.K. Misra. Experimental investigation of the dynamics of spinning tethered bodies. *Acta Astronautica*, 39(7):487 – 495, 1996.

[9]Petri Toivanen and Pekka Janhunen. Thrust vectoring of an electric solar wind sail with a realistic sail shape. *Acta Astronautica*, 131:145–151, 2017.

[10]Petri K Toivanen and Pekka Janhunen. Spin plane control and thrust vectoring of electric solar wind sail. *Journal of Propulsion and Power*, 2013.

Modeling Two-phase Flow and Vapor Cycles Using the Generalized Fluid System Simulation Program

Amanda D. Smith*
University of Utah, Salt Lake City, UT 84112
Alok K. Majumdar†
NASA Marshall Space Flight Center, Huntsville, AL, 35812

This work presents three new applications for the general purpose fluid network solver code GFSSP developed at NASA's Marshall Space Flight Center: (1) cooling tower, (2) vapor-compression refrigeration system, and (3) vapor-expansion power generation system. These systems are widely used across engineering disciplines in a variety of energy systems, and these models expand the capabilities and the use of GFSSP to include fluids and features that are not part of its present set of provided examples. GFSSP provides pressure, temperature, and species concentrations at designated locations, or nodes, within a fluid network based on a finite volume formulation of thermodynamics and conservation laws. This paper describes the theoretical basis for the construction of the models, their implementation in the current GFSSP modeling system, and a brief evaluation of the usefulness of the model results, as well as their applicability toward a broader spectrum of analytical problems in both university teaching and engineering research.

Nomenclature

A	Area
C_{min}	Capacity rate of minimum capacity fluid
C_r	Fluid capacity ratio (or capacity rate ratio)
C_s	Slope of enthalpy of saturated air v. temperature
c_p	Specific heat at constant pressure (per unit mass)
$GFSSP$	Generalized Fluid System Simulation Program
h	Enthalpy (per unit mass)
HEX	Heat Exchanger
K_m	Mass transfer coefficient for cooling tower
$\dot{m}$	Mass flow rate
NTU	Number of transfer units
Q, q	Heat transfer, heat transfer per unit mass
$\dot{Q}$	Rate of heat transfer
P	Pressure
T	Temperature (dry bulb unless otherwise noted)
TC	Characteristic cooling tower coefficient
$\dot{V}$	Volumetric flow rate
v	Specific volume
$VTASC$	Visual Thermofluid Analyzer for Systems and Components
w	Work transfer per unit mass
δ	Correction factor for enthalpy of saturated air v. temperature
ϵ	Effectiveness

*Assistant Professor of Mechanical Engineering, University of Utah, 1495 E 100 S, Room 1550, Salt Lake City, UT, 84112
†Aerospace Technologist (AST), NASA Marshall Space Flight Center, Redstone Arsenal, Huntsville, AL, 35812

ω	Humidity ratio

Subscripts

a	Air
act	Actual
ave	Average
in	Inlet conditions
out	Outlet conditions
sat	Saturation conditions
w	Water
wb	Wet bulb

Superscript

$+$	Adjusted capacity rate for water in a cooling tower including both water- and air-side properties

I. Introduction

This project expands the capabilities of NASA's GFSSP software, developed at Marshall Space Flight Center, to include (1) a two-phase flow problem, including psychrometric calculations and two-phase flow, for design and sizing cooling towers, in heating, ventilation, air-conditioning, & refrigeration applications as well as for thermoelectric power plant cooling; (2) a work-consuming vapor cycle, the vapor-compression refrigeration cycle, with applications in air-conditioning and process cooling; and (3) a work-producing vapor cycle, the Rankine cycle, with applications in thermoelectric steam power generation as well as Organic Rankine Cycle systems. These systems are widely used across engineering disciplines in a variety of energy systems,and these models expand the capabilities and the use of GFSSP to include fluids and features that are not part of its present set of provided examples. Section II describes the development of Model (1), Section III describes the development of Models (2) and (3), and Section IV discusses the general applicability of GFSSP toward a broader spectrum of analytical problems, followed by Section V which discusses future plans for university teaching and engineering research inspired by these new models.

I.A. Generalized Fluid System Simulation Program

The Generalized Fluid System Simulation Program (GFSSP) was conceived by the second author in the 1990s and awarded NASA's Software of the Year designation in 2001.[1] It is a fluid-thermal systems network analysis code written in Fortran which may be compiled directly or accessed through the visual thermofluid dynamic analyzer for systems and components (VTASC) graphical user interface. The model outputs provide pressure, temperature and species concentrations for fluids in complex systems, either at steady state or as a time series for transient analysis.[2] It is a finite volume code that represents fluid networks as a connected series of nodes and branches. The work that follows was performed with GFSSP Version 7.

An Educational version of GFSSP is available at no charge to U.S. institutions through an application to Marshall Space Flight Center (MSFC) from a university representative. GFSSP was developed at NASA to analyze aerospace industry problems by members of the Propulsion Systems Department at MSFC, and its core user group consists of NASA employees and contractors. However, its property packages cover a number of fluids commonly used in a variety of engineering systems, and the generalized and flexible nature of the modeling system lend themselves to a number of engineering problems involving complex thermal-fluid networks. This work provides a new set of models built on the GFSSP framework to demonstrate its capabilities in three classical engineering energy systems. The first, a cooling tower performance model, was developed primarily by the first author and will be used for teaching thermodynamics to mechanical engineering students and in sustainability research at the water-energy nexus. The second, a vapor-compression refrigeration system model, and third, Rankine power cycle models were developed primarily by aerospace engineering student C. Ursachi.

II. Two-Phase Flow

II.A. Application: Cooling Tower

Performance modeling of cooling towers is a multiphysics problem involving simultaneous heat and mass transfer, two-phase flow, and psychrometric treatment of atmospheric air. Its applicability extends from small, constant-area cooling towers used for providing chilled water to buildings to large, parabolic cooling towers providing chilled water to the condensers of thermoelectric power plants. Predicting the performance of these devices involves a number of physical process and a great deal of uncertainty.

The earliest mathematical models of cooling towers were developed by Merkel in the 1920s.[3] By assuming that the flow rate of water leaving the tower (due to evaporation or drift) was negligible, and ignoring the computation of the exact state of the air leaving the tower, he was able to avoid the necessity of obtaining detailed detailed data about fill performance and mass transfer coefficients within the tower by treating it as a lumped system with an empirical "Merkel number".[4] Assumptions limiting to the accuracy of the model include: Lewis number of 1 (simplifying the relationship between heat and mass transfer), air exiting the tower is saturated with water (an "ideal" cooling tower in terms of mass transfer), and the aforementioned neglect of water losses (lack of adherence to mass conservation for water).[4]

An important improvement for mechanical engineers surfaced in the 1980s, when the effectiveness-number of transfer units (ϵ-NTU) method, commonly used for heat exchanger (HEX) analysis was adopted for cooling towers.[5–7] The main difficulty in this adaptation was the fact that mass transfer from the water stream to the air stream (that is, *latent* heat transfer from the air stream), since the ϵ-NTU model relies on temperature differences to describe the potential and actual heat transfer from one fluid stream to another. Braun[6] details the impacts of neglecting water losses, usually 1-4% of the total water mass flow rate, and fits his version of the ϵ-NTU model to experimental data, alongside prior models.

The model presented here is based on the ϵ-NTU formulation presented by Jaber and Webb[7] in 1989. The description of the model that follows, and the flowcharts presented in figures and are developed for a single control volume; however, the GFSSP implementation described in can be divided into any desired number of segments. Dividing the model into 2 or more increments will increase accuracy; however, a sensitivity analysis on small-scale cooling towers indicates that dividing the cooling tower into more than 6 segments is unlikely to yield significant returns in accuracy (see Ibid.,[7] Figs. 5–8).

The model of Jaber and Webb[7] has the advantage of conforming precisely to the conventional effectiveness-NTU method of heat exchanger analysis familiar from any basic undergraduate engineering heat transfer course. Because it is traditionally applied where both fluids are in a single phase, the actual and maximum heat transfer possible must be carefully defined. An "air-side effectiveness" was proposed by Braun et al:[6]

$$\frac{Q_{act}}{Q_{max}} = \frac{\texttt{Actual heat transfer from the water stream*}}{\texttt{Heat transfer IF the exiting air were saturated at water inlet temperature}}$$

Jaber and Webb then showed that it was possible to provide a generalized effectiveness which is based on the minimum capacity fluid,[7] as in classical ϵ-NTU HEX analysis:

$$\frac{Q_{act}}{Q_{max}} = \frac{\dot{m}_w c_{p,w}(T_{w,in} - T_{w,out})*}{C_{min}(h_{a,sat@Tw,in} - \delta - h_{a,in})}$$

where δ is a correction factor that helps to account for the non-linearity of enthalpy of saturated air as a function of temperature.[7]

* The numerators of both equations above, representing the heat rejected by the water, are also equal to the heat received by the air stream if the tower is adiabatic (negligible heat transfer through the walls).

II.A.1. Model for Counterflow Sizing Calculation

Given experimental data relating the mass flow rates of air and water, the state of the incoming air, and the temperature of the water entering and exiting the control volume, a mass transfer coefficient K_m that is characteristic of that cooling tower may be obtained.

The steps are illustrated in Figure 1 and are derived from the presentation of Jaber and Webb.[7] Numbers within the flowchart correspond with equations in the referenced document. This was deemed "Counterflow Sizing Calculation" procedure[7] as it determines the NTU value, and thus the 'size' of the tower.

First, the slope of the curve of the enthalpy of saturated air versus temperature is obtained for the range of water temperatures applicable. Next, a water "capacity rate" is calculated which captures the water's potential to release heat to the air. As in any ϵ-NTU analysis, the minimum capacity fluid must be determined to obtain the proper denominator.

The numerator is calculated in a straightforward manner, using a constant specific heat for water over the range of temperatures applicable (an assumption which introduces little to no error).

The correction factor is calculated to improve the accuracy of the denominator (Q_{max}):

$$\delta = \frac{h_{a,sat@Tw,in} + h_{a,sat@Tw,out} - 2h_{a,sat@Tw,ave}}{4}$$

The effectiveness and number of transfer units are calculated as for any HEX ϵ-NTU analysis.

The number of transfer units here, however, has a significant physical meaning in the context of the cooling tower. It represents a mass transfer coefficient (per unit area), multiplied by the tower area, divided by the minimum of the air capacity rate, $\dot{m}_a$, and the water capacity rate, $\dot{m}_w^+ = \frac{\dot{m}_w c_{p,w}}{C_s}$.

The characteristic coefficient of the tower, TC, is provided in relation to the actual mass flow rate of water because the cooling of the water is the ultimate purpose of the device. This tower coefficient may now be used to predict performance for the same tower under other conditions, as described in the following section.

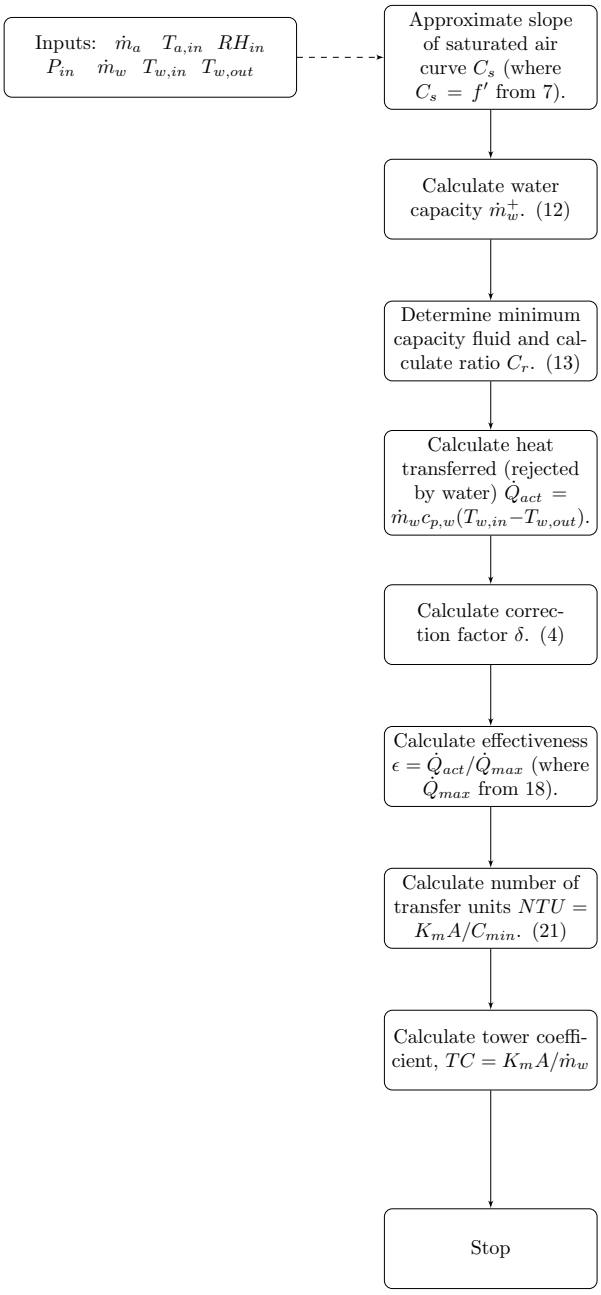

Figure 1. Procedure for calculating tower characteristic coefficient, $K_m A$, given performance data for a specific cooling tower.

II.A.2. Iterative Model for Counterflow Rating Calculation

Given knowledge of the mass transfer coefficient K_m, or the lumped term $K_m A$ that is characteristic of a given cooling tower, a predictive model may be used to model its expected cooling performance.

The steps are illustrated in Figure 2 and are again derived from the presentation of Jaber and Webb.[7] Numbers within the flowchart correspond with equations in the referenced document. This was deemed "Counterflow Rating Calculation" procedure[7] as it determines the exiting water temperature, and thus the 'rating' of the tower given its characteristic coefficient.

Note that a cooling tower 'rating' is commonly used in industry to refer to its performance under a defined set of testing conditions, defined as $\dot{V}_w = 3\frac{gal}{min}$, $T_{w,in} = 95F$, $T_{w,out} = 95F$, and $T_{wb,in} = 78F$ for a "nominal ton" of cooling.[8]

II.A.3. Iterative Model for Counterflow Operational Setting or Fan Selection

An additional model was created for the benefit of practicing engineers who may have the opportunity to select the operational method or fan for an existing forced-draft counterflow cooling tower. Its calculation procedure is an adaptation of both Figure 1 and Figure 2 in which the user provides a desired water outlet temperature, and the necessary air flow rate given the tower's characteristic coefficient.

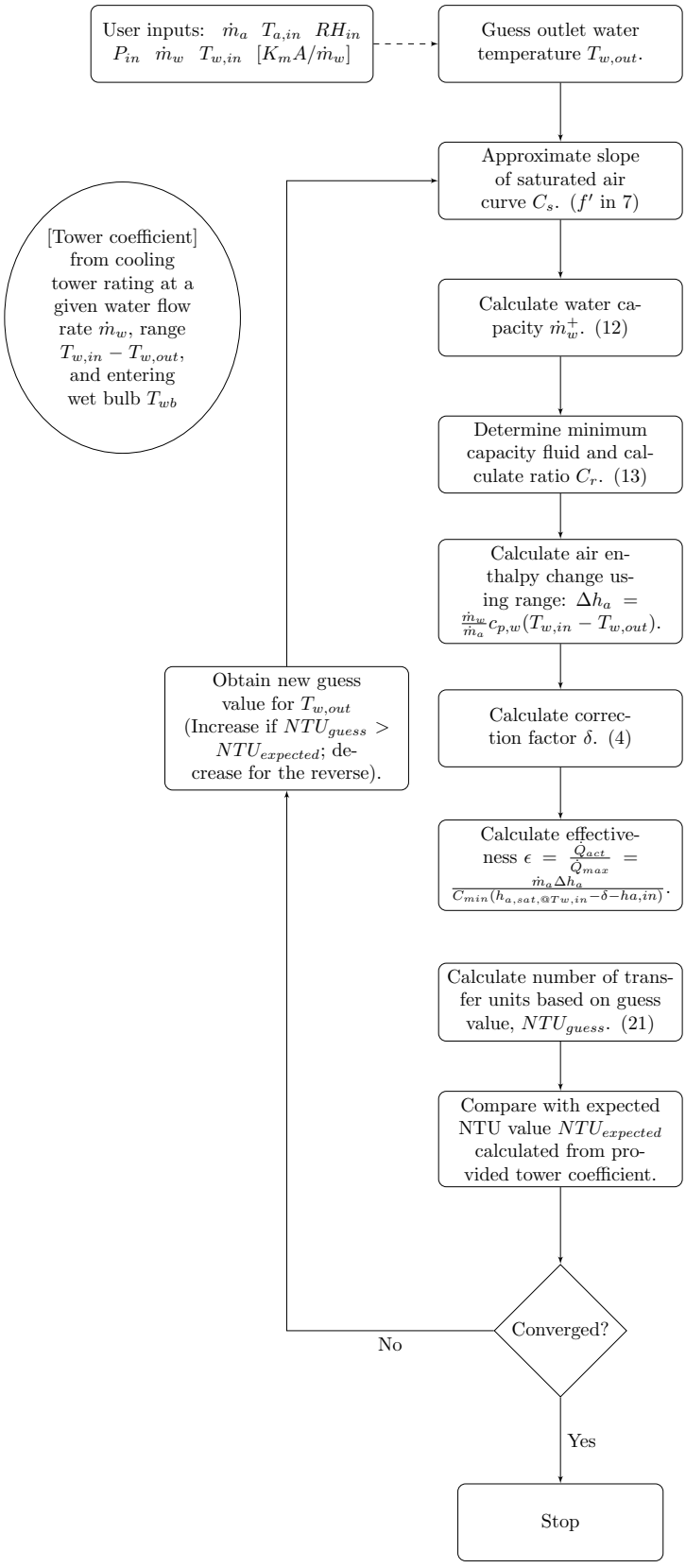

Figure 2. Procedure for calculating tower performance, given K_mA for a specific cooling tower derived from performance data.

II.A.4. Verification and Validation

For the models described in Sections II.A.1, II.A.2, and II.A.3, verification of the Matlab-language versions was performed in comparison with both analytical and theoretical models taken from existing literature.[7,9] Validation was performed using experimental data taken from the PA Hilton laboratory model[10,11] described in Section II.A.5.

II.A.5. Laboratory Model

Schematics for the laboratory demonstration cooling tower are shown in Figure 3. Students use a heater with known output as the basis for their First Law (energy conservation) equations, and enforce mass conservation of water by analyzing the performance of the cooling tower system using a psychrometric chart[12] to look up the expected properties of moist air at a pressure corresponding to an elevation of 1500 m (Salt Lake City, UT has an elevation of about 4200 ft or 1300 m). Further details of the assumptions, procedures, and equations used are provided in the student lab manual. The most current version can be obtained from the first author or downloaded online.[11]

II.A.6. Implementation in GFSSP

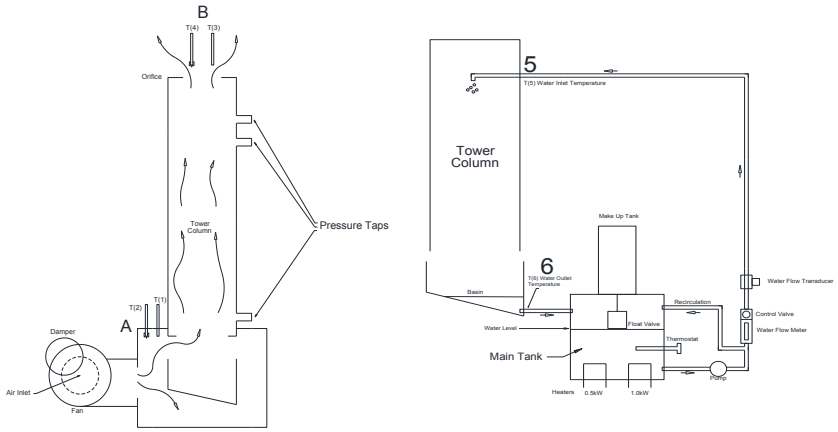

Figure 3. Schematics for Cooling Tower Laboratory Demonstration, University of Utah Department of Mechanical Engineering, courtesy of J. DeSutter. LEFT: Air flow through the cooling tower (bottom to top); RIGHT: Water loop through the cooling tower (top to bottom).

A cooling tower model with 7 nodes and 6 branches has been created as a GFSSP input file. The user provides a guess value for water outlet temperature (which may not be cooler than the entering wet bulb temperature of the air), and providing assumed conditions for the air outlet so that air inlet conditions can be provided to each node through a simple linear interpolation. The tower's characteristic $K_m A$ must be known in advance, or calculated through the procedure shown in Figure 1, available as a Matlab/Octave program.[13] Because the heat losses through the walls of the tower are neglected, $T_{wb,out} = T_{wb,in}$. The numerical solver determines water outlet conditions to a desired level of convergence using the process shown in Figure 2, beginning with the top node (water inlet and air exit), and marching in the direction of the water loop.

GFSSP is already equipped with the capability to enforce conservation laws by fluid species and to calculate and provide species concentrations at the nodes,[2] which for this application corresponds directly to ω. Mass conservation is enforced for air, i.e. O_2 and N_2 molecules (dry air), and for water both in the 'water' loop and in the air loop in the form of water vapor, so that for the entire system $m_{w,in} = m_{w,out}$. At steady state:

$$\dot{m}_{w,evaporated} = \dot{m}_a(\omega_{out} - \omega_{in}) = \dot{m}_{loss}$$

so that water loss is equal to the amount of water that leaves with the air (i.e. the water evaporation rate). This is also the quantity of makeup water that must provided to a real cooling tower in operation.

III. Vapor Cycles

III.A. Application: Vapor Compression Refrigeration Cycle

The development of the vapor compression refrigeration cycle drove the expansion of mechanically driven cooling in the 20th century. It is a classic problem used in teaching thermodynamics and other heating, ventilation, air-conditioning, & refrigeration-related sciences. In its ideal form, it consists of:

- A compressor which takes a refrigerant from its saturated vapor state to a much higher temperature and pressure
- A condenser where the refrigerant rejects heat to its surroundings (the 'warm' medium, which must be below the temperature of the refrigerant entering the condenser for heat transfer to occur)
- An isenthalpic expansion valve which relieves the high pressure of the refrigerant
- An evaporator where the refrigerant absorbs heat from its surroundings (the 'cold' medium, which must be above the local temperature of the refrigerant, although it is colder than the 'warm' medium).

III.A.1. Laboratory Model

A real vapor compression system in operation is more likely to have refrigerant entering the compressor as a slightly superheated fluid already, will have pressure drops in all branches, will likely allow the fluid to cool into a slightly compressed liquid before entering the expansion valve, and the throttling process may not be perfectly isenthalpic.[9] Nevertheless, the simplified mathematical model described in undergraduate thermodynamics texts[9] is an excellent predictor of the performance of a vapor compression refrigeration system. The components of a vapor compression refrigeration demonstration setup at the University of Utah are shown in Figure 4. For the purposes of illustration, the 'warm' medium and 'cold' medium are the same in this case, that is, the atmospheric air in the room.

III.A.2. Mathematical Model

Figure 4. Vapor Compression Laboratory Demonstration, University of Utah Department of Mechanical Engineering

The components above, when modeled as ideal devices (i.e. reversible compressor, condenser, and evaporator; constant enthalpy expansion valve), have the following first law forms after simplifications:

Compressor, isentropic compression:
$w = h_{in} - h_{out} \approx v_{in}(\Delta P)$
Condenser, constant pressure heat rejection:
$q = h_{in-h_{out}}$
Expansion valve, isenthalpic:
$h_{in} \approx h_{out}$
Evaporator, constant pressure heat addition:
$q = h_{in} - h_{out}$
Same simplification as for the condenser above, opposite sign (heat is *added* to the working fluid rather than rejected from it).

Students analyzing the performance of the vapor-compression refrigeration system use property tables[9] to look up the expected properties of the refrigerant, hydrofluorocarbon 134-a (R-134a). Details of the assumptions, procedures, and equations used are provided in the student lab manual which can be obtained from the first author or downloaded online.[11]

III.A.3. Implementation in VTASC

The model for the vapor compression system was built using existing components within the current GFFSP version through the VTASC interface, as shown in Figure 5. The case study illustrated here is based on

an experimental data obtained by students using the equipment shown in Figure 4. The compressor is represented as a mass source in the branch labeled with $\dot{m}$. The condenser (labeled) is represented as a heat exchanger where heat is rejected by the working fluid. The isenthalpic expansion is represented by a Joule Thomson valve (branch 34) which was adjusted to match the characteristics of the needle valve in the experimental setup. The evaporator (labeled) is represented similarly to the condenser where heat is now entering the system as the working fluid changes phase. The cyclic boundary node option[2] is activated at node 12, a node capturing the state of the fluid at the exit of the compressor. Additional branches represent the piping in the bench scale system. Validation was performed using experimental data taken from the laboratory model described in Section III.A.1.

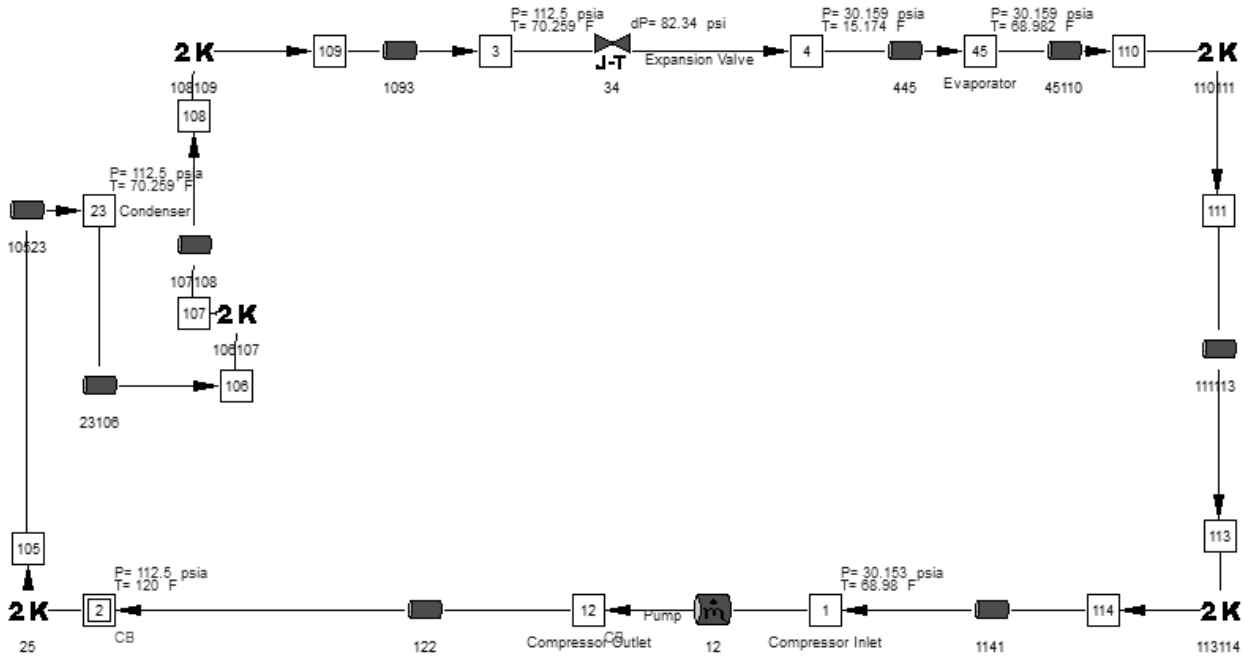

Figure 5. VTASC GFSSP model of a vapor compression refrigeration system, courtesy of C. Ursachi

III.B. Application: Rankine Power Cycle

The Rankine steam cycle is the technical basis for almost all thermoelectric power generation systems, the most common type of electricity generation in land-based power stations. It is a classic problem used in teaching power and energy sciences. In its simplest ideal form, it consists of:

- A pump which takes a working fluid from its saturated liquid state to a much higher pressure compressed liquid state
- A heat exchanger called a boiler with a high-temperature heat source, or 'hot' medium, which takes the working fluid to a superheated vapor state at the same pressure
- A turbine which allows the fluid to expand, releasing pressure and creating shaft work by driving the rotors as it flows through, and
- A heat exchanger called a condenser where the working fluid rejects heat to a 'cold' medium (for a power generation station, river water or chilled water produced by a cooling tower or cooling pond).

A number of modifications are commonly used to increase the work output of the cycle and its overall efficiency, including reheating and regeneration, supercritical steam generation, or low condenser pressures. A real steam cycle in operation is more likely to have water entering the pump as a compressed liquid, will have pressure drops in all branches, and will have additional losses due to heat transfer and fluid friction such as those in a non-isentropic turbine.[9]

This paper describes only an ideal cycle with a single-stage turbine, but a regenerative cycle model (one open feedwater heater) has also been developed in VTASC and more detailed models may be developed in GFSSP using existing components in VTASC and/or customized user subroutines, or obtained by contacting the authors.

III.B.1. Mathematical Model

The components above, when modeled as ideal devices, have the following simplified first law forms:

Pump, isentropic compression: $w = h_{in} - h_{out} \approx v_{in}(\Delta P)$
Boiler, constant pressure heat addition: $q = h_{out} - h_{in}$
Turbine, isentropic expansion: $w = h_{in} - h_{out}$
Same simplification as for the pump above, opposite sign (work is done *by* working fluid rather than on it).
Condenser, constant pressure heat rejection: $q = h_{out} - h_{in}$
Same simplification as for the boiler above, opposite sign (heat is *rejected* from the working fluid rather than added to it).

III.B.2. Implementation in VTASC

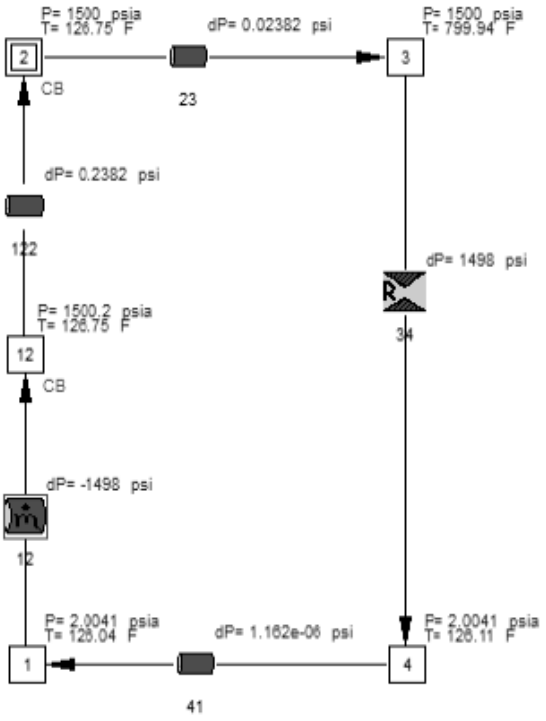

Figure 6. VTASC GFSSP model of a simple Rankine steam cycle, courtesy of C. Ursachi

The model for the Rankine steam cycle power system was built using existing components within the current GFSSP version through the VTASC interface, as shown in Figure 6. The case study illustrated here is based on a theoretical problem presented by Çengel and Boles[9] and was verified with the numbers provided in the associated instructor's manual. The pump is represented as a mass source in the branch labeled with $\dot{m}$. The boiler is represented as a heat exchanger (branch 23) where heat is added to the working fluid. The turbine is represented as a flow restriction 34 such that the enthalpy change of the fluid represents the energy leaving the system in the form of work (or power, at a given instant). The condenser is represented similarly to the boiler (branch 41) where heat is rejected by the working fluid. The cyclic boundary node option[2] is activated at node 12, a node capturing the state of the fluid at the exit of the pump supplying feedwater to the boiler.

IV. Conclusions

This paper described three new applications for the general purpose fluid network software tool, GFSSP: a cooling tower, a vapor-compression refrigeration system, and a Rankine cycle power generation system. These systems demonstrate the flexibility of the GFSSP modeling system and its capabilities in representing some important physical processes, both in NASA applications and in energy systems at the Earth's surface: two-phase flow and phase transformations. These example problems will add to the examples provided with the GFSSP instructional literature and provides pressure,temperature, and species concentrations at designated locations, or nodes, within a fluid network based on a finite volume formulation of thermodynamics and conservation laws. The theoretical basis for the construction of the models, i.e. energy and mass conservation, was described, and the results of the specific models created have demonstrated that it is possible to represent a bench-scale cooling tower and vapor-compression refrigeration system using GFSSP. A number of teaching and research applications are now possible based on these results, and those planned by the authors are described in Section V below.

V. Future Work

The cooling tower model will be used by students in the Fall 2017 Thermodynamics II course at the University of Utah in completing their laboratory assignment corresponding to Section II.A.5, as an aid for predicting the expected performance of the laboratory cooling tower and for analyzing their experimental results. Students will also be able to simulate the performance of the same cooling tower in a sea-level atmosphere (higher ambient pressure) to investigate the effect of altitude on its performance, or in a different climate (higher humidity) to investigate the effect of ambient wet bulb temperature on its effectiveness.

The vapor-compression refrigeration system model will be used by thermodynamics students in completing their laboratory assignment corresponding to Section III.A.1, as an aid for predicting the expected performance of the refrigeration system and for analyzing their experimental results. The compressor is non-isentropic and in fact rejects heat to the atmosphere, so that the working fluid's specific entropy will decrease as it passes through. Students typically have difficulty relating the ideal cycle model to the operation of a real system, and we hypothesize that the use of GFSSP will allow them to think more deeply about the performance of each individual device in the system, thereby improving their understanding of its operation as a whole.

The Rankine power cycle model will be used by thermodynamics students to check their own homework problems. As additional modifications are added, such as multiple feedwater heaters and a reheat stage, GFSSP may be used more extensively in analyzing these complex systems in both undergraduate and graduate thermodynamics courses.

The cooling tower model will be used next as a dynamic (transient) simulation so that its performance in cooling can be studied over time in a variety of realistic conditions, in which the ambient dry bulb and wet bulb are changing. This has implications for: optimal control of cooling systems, changes in cooling tower performance with a changing climate, and water consumption for power generation. Previous work by the author[14] has assumed a rough correlation between water withdrawals and consumption for power generation based on basic knowledge of the cooling system type,[15] but adding a physical representation of the link between power output, ambient conditions, and water losses could greatly reduce the amount of uncertainty inherent in this type of analysis. The dynamic GFSSP model will also be compared against a neural network model that has been developed in Matlab and trained on manufacturer-provided data, to investigate the relative benefits or drawbacks in terms of complexity, computational time, and accuracy between a physics-based model and a machine learning-based model.

The Rankine power cycle model and the cooling tower model, if simulated simultaneously, would provide a valuable model for this large, complex system. The Rankine cycle model may also be adapted to simulate an Organic Rankine Cycle, useful for low-grade waste heat recovery, provided that the working fluid's properties are accessible from, or provided to, GFSSP. Planned developments for the GFSSP modeling system as a whole include a newly designed visual interface and an interface for user subroutines written in languages other than Fortran, which will reduce the learning curve and make it even more friendly toward integration into undergraduate teaching programs and research use in other fields.

Acknowledgments

The authors thank Carmen Ursachi, NASA MSFC Summer Intern for 2016 and 2017, for her excellent work. She created the refrigeration model and power cycle models described here.

The civil servants, contractors, and interns working with the Thermal & Combustion Analysis Branch made this work possible, with particular thanks to Dr. Andre LeClair and ER-43 Branch Chief Alicia Turpin for their support. We also gratefully acknowledge the sponsors and coordinators of the 2017 NASA MSFC Faculty Fellowship program, including but not limited to Dr. Frank Six, Dr. Gerald Karr, and Rachel Damiani.

We appreciate two former teaching assistants for the Thermodynamics II laboratory and PhD candidates at the University of Utah: Zahra Fallahi, who obtained laboratory dimensions for verification and validation of the refrigeration cycle model and provided photographs, and John DeSutter, who produced the schematics and assembled the cooling tower demonstration apparatus. Dr. Smith also wishes to acknowledge the Department of Mechanical Engineering and all of her graduate students and collaborators for their support during her absence from the University of Utah.

References

[1]GFSSP: Generalized Fluid System Simulation Program. https://gfssp.msfc.nasa.gov/. Accessed: 2017-7-27.

[2]A K Majumdar and A C Le Clair. Generalized fluid system simulation program, version 6.0.

[3]Eusiel Rubio-Castro, Medardo Serna-González, José M Ponce-Ortega, and Arturo Jiménez-Gutiérrez. Optimal design of cooling towers. In *Heat and Mass Transfer-Modeling and Simulation*. InTech, 2011.

[4]Johannes C Kloppers and Detlev G Kröger. Cooling tower performance evaluation: Merkel, poppe, and e-NTU methods of analysis. *J. Eng. Gas Turbines Power*, 127(1):1–7, 1 January 2005.

[5]Braun. *Methodologies for the design and control of central cooling plants*. PhD thesis, 1988.

[6]J E Braun, S A Klein, and J W Mitchell. Effectiveness models for cooling towers and cooling coils. *, Refrigerating and Air-Conditioning* , 1989.

[7]H Jaber R.L. Webb. Design of cooling towers by the effectiveness-NTU method. *J. Heat Transfer*, 111(4):837–843, 1989.

[8]ASHRAE. *HVAC Systems and Equipment*. ASHRAE Handbook Online. ASHRAE, 2016.

[9]Yunus Cengel and Michael Boles. *Thermodynamics: An Engineering Approach (Mechanical Engineering)*. McGraw-Hill Education, 8 edition edition, 7 January 2014.

[10]H893 bench top cooling tower — heat transfer teaching equipment - 300. http://www.p-a-hilton.co.uk/products/H893-Bench-Top-Cooling-Tower. Accessed: 2017-8-8.

[11]Amanda D Smith. Student lab manuals for mechanical engineering thermodynamics II at the university of utah. https://github.com/amandadsmith/thermolabs, 28 July 2017. Accessed: 2017-7-28.

[12]Psychrometric charts. http://www.carrier.com/carrieruniversity/en/us/courses-materials/materials/psychrometric-charts/. Accessed: 2017-7-28.

[13]Amanda D Smith. Cooling tower models. https://github.com/SSESLab/coolingtower.

[14]Jaron J Peck and Amanda D Smith. Quantification and regional comparison of water use for power generation: A california ISO case study. *Energy Reports*, 3:22–28, November 2017.

[15]Jordan Macknick, Robin Newmark, Garvin Heath, and K C Hallett. Operational water consumption and withdrawal factors for electricity generating technologies: a review of existing literature. *Environ. Res. Lett.*, 7(4):045802, 1 December 2011.

Design and Technical Study of Neutrino Detector Spacecraft

Nickolas Solomey[1]
Wichita State University, Physics Division, Wichita, KS 67260-0032

A neutrino detector is proposed to be developed for use on a space probe in close orbit of the Sun. The detector will also be protected from radiation by a tungsten shield Sun shade, active veto array and passive cosmic shielding. With the intensity of solar neutrinos substantially greater in a close solar orbit than on the Earth only a small 250 kg detector is needed. It is expected that this detector and space probe studying the core of the Sun, its nuclear furnace and particle physics basic properties will bring new knowledge beyond what is currently possible for Earth bound solar neutrino detectors.

1. Introduction

The Sun provides all of the energy that our planet needs for life and has been doing so for five billion years. Understanding our Sun and its interior is one goal of the NASA Heliophysics program. This is a very difficult task because very little makes it out of the Sun's interior. Never-the-less within the last ten years neutrino detectors on Earth have started to make reliable detection of neutrinos from the fusion reactions in the interior of the Sun and have started to use this information to investigate the Sun's nuclear furnace processes. Using a small detector in close solar orbit is a possible next step to expand this study, one which can provide more information that cannot be obtained by detectors situated on Earth. The Sun is located 150 billion meters from the Earth, even at this distance it is still a major source of neutrinos, as shown in the solar neutrino flux plot in Figure 1 [1]. This plot has many interesting features and includes both a broad spectrum and a few sharp lines.

Changes in solar flux make it advantageous to take a neutrino detector into space since the solar neutrino intensity changes dramatically as the inverse square of the distance from the Sun, by five orders of magnitude when going from the Earth to the Sun or from the Earth to the current position of the Voyager 1 space craft (Table 1). Launch of a neutrino detector into space toward the Sun will: a) aim to significantly reduce the detector size and experimental cost while allowing for improved detector energy resolution and performance, b) attempt to completely eliminate background terrestrial neutrino sources for improved measurement accuracy, and c) conduct unique science experiments near the sun.

NASA's interest in deep space exploration has been a key factor in its unmanned space-craft development and launch. In addition to this, NASA also has done experiments in space where the science benefits from the unique platform of a space-craft can provide unprecedented results. The Hubble Space telescope [2] is really a small and very common instrument, but when it is put into an orbit high above the Earth, it becomes one of the most powerful optical observatories in the world, as it returns impressive science results. Similar to these examples science returns from a small orbiting neutrino detector experiment close to the Sun will be studied; the study falls within the same classification as these experiments and is clearly part of the Heliophysics central mission in Appendix B of the NASA science programs.

1 Prof. of Physics, Department Mathematics, Statistics and Physics, 1845 Fairmount St., Jabara Hall 010, Wichita, KS 67260-0032.

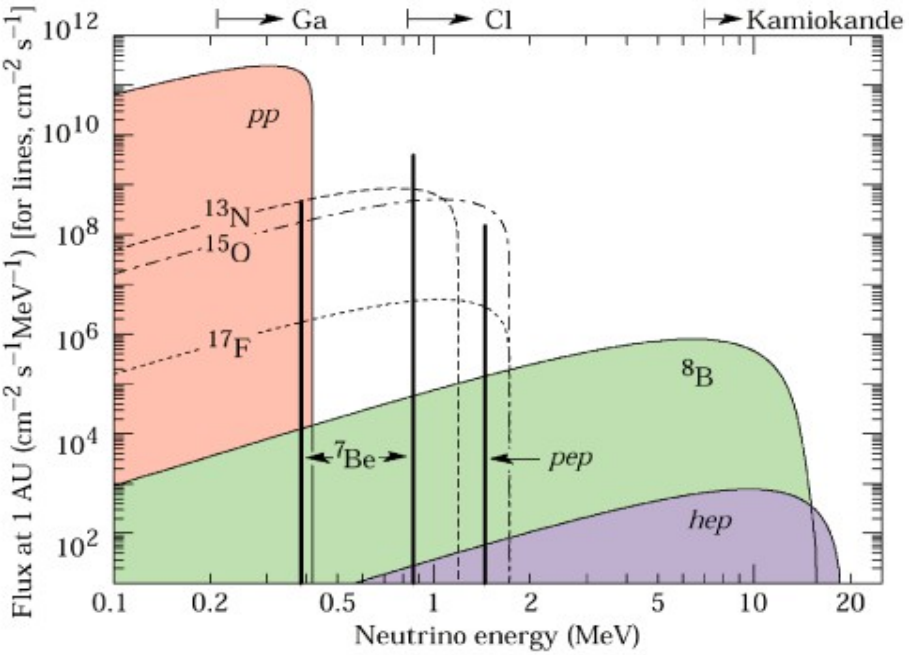

Figure 1: Solar Neutrino Spectrum, with intensity at the mean distance of the Earth, and the neutrino detection regions of a few experiments are shown as bars at the top [1].

II Science Goals

The Science goals fall into three parts, solar physics the study of the nuclear furnace in the interior of the Sun, Particle physics that can be done with the solar neutrinos generated, Nuclear Physics matter effects on neutrino propagation and Dark Matter studies.

Distance from Sun	Solar Neutrino intensity relative to Earth
696342 km	46400
1500000 km (~3 Sun R)	10000
4700000 km (~7 Sun R)	1000
15000000 km	100
474340000 km	10
Mercury	6.7
Venus	1.9
Earth	1

Table 1: Intensity of Solar neutrinos at various distances from the Sun.

See **Figure 2** for current theories on the location radius of nuclear fusion in the Sun's core. It is known that all of the Sun's energy comes from nuclear fusion reactions in the Sun's core, but there remain many unanswered questions in stellar evolution and astrophysics that can be addressed with a close solar orbiting spacecraft equipped with a neutrino detector. These are: a) solar fusion reaction neutrino spectrum, b) size and shape of the nuclear fusion reaction core in 3D, c) nuclear fusion rates, and d) changes of the nuclear fusion reactions over time and regions within the Sun. With a close orbiting satellite, the studies could be expanded due to the larger

event rate. For a satellite out of the ecliptic plane, views of the nuclear fusion core from various solar latitudes could allow for a 3D image of the fusion core.

There are two categories of nuclear physics studies that can be performed with solar neutrinos and a spacecraft detector in near orbit of the Sun. These are studies of the matter effect on neutrino propagation through solar material and rare nuclear isotope fusion. Because the Sun is a rotating ball of gas, the Sun itself has an equatorial bulge much the like the Earth. The amount of matter that neutrinos produced in nuclear fusion processes within the solar core propagate through is different for the equatorial view and polar view. Theoretically, it should be possible to study this effect by placing a satellite in an orbit around the Sun that is not in the ecliptic plane. Also, due to the near solar orbit of the satellite, the detector will be more sensitive to the higher mass fusion processes of heavy isotopes that reside in the solar core than solar neutrino detectors located on the Earth. Both of these studies are specific only to a space-based neutrino detector and cannot be performed by experiments located on the Earth. Particle Physics can use this for the study of neutrino oscillations, and inside the 35 solar Radii limit the neutrinos are de-coherent and this would tell us unique science on particle physics oscillation.

An indirect search for Dark Matter in the core of the Sun can also be a result of such an experiment. Imagine that Dark Matter has accumulated in the gravitational well formed by the large mass of the Sun. This would distort the observed nuclear fusion region, see Fig. 2, displacing the neutrino source from the current calculations without any dark matter and making for a way to not only identify if Dark Matter is in the core of the Sun, but also would allow for a way to measure how much Dark Matter has accumulated in the Sun's core.

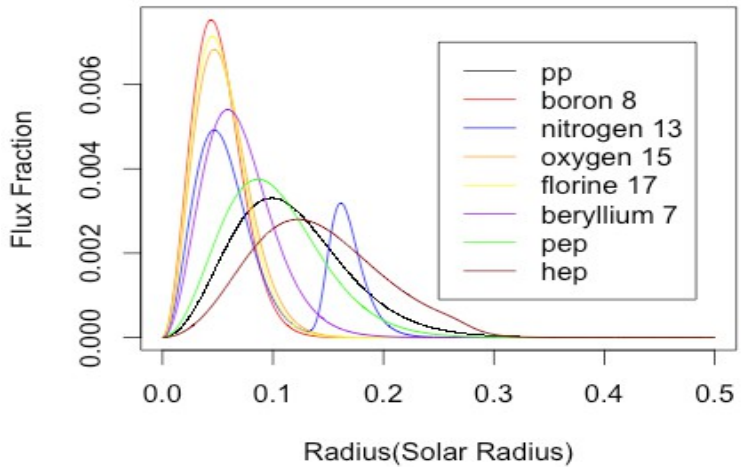

Figure 2**:** Predicted flux and radius of production from the standard solar model, see Ref. [3].

III Technical Development

Development of detector technology suitable for space flight is of major importance since none of the techniques currently used in ground-based solar neutrino detectors have been certified for space flight. Given that the potential science returns as reviewed in Section 2, laboratory-based testing and development of detector technology for these missions are needed. Detector technology for neutrinos detectors are well established and would be classified as a TRL3 (Technical Readiness Level) detector; however, none of this technology is certified for space

flight. This summer aimed to study the science and detector technology using simulations. The technical readiness levels for these will not change, but the end goal of this study will advance the technical readiness level by determining which of the many possible detector should be pursued to get them ready for the space flight technical readiness based upon which detector technology preforms the best in simulation studies, lab tests and accelerator/reactor tests for the best science needs.

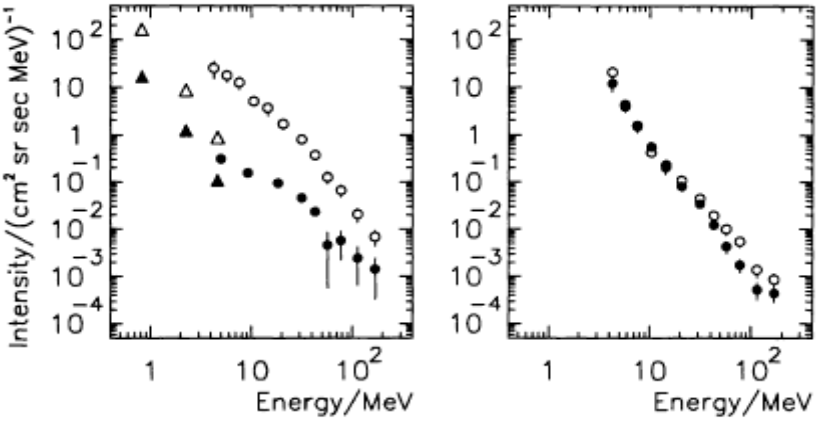

Figure 3: Spectrum of electrons and protons close to the Sun from the Helios Space Probe [4].

Interaction Mode	2nd signature	Timing	Energy	ν energy threshold
$^{12}C + \nu$ into $e^- + {}^{12}N$	^{12}N decays into $^{12}C + e+$	11 ms	e+e- annihilation 2.2 MeV signature	15 MeV
Cl + ν into e- + Ar	Chemical sniffing			0.85 MeV
$^{18}O + \nu$ into e- ^{18}F m1	^{18}F m1 decays into ^{18}F and gamma	162 ns	1121 keV	7 MeV
$^{69}Ga + \nu$ into e- ^{69}Ge m1 or m2	^{69}Ge m1 decays X-ray	5 us	86 keV	0.4 MeV
	^{69}Ge m2 decay gamma	2.8 us	397 keV	0.45 MeV
$^{71}Ga + \nu$ into e- ^{71}Ge m1	^{71}Ge m1 decay gama	20 ms	175 keV	0.4 MeV
D + ν into e- ^{2}He	^{2}He decays to proton proton Topology of event	<1 ns	back to back protons depends on neutrino energy	2.2 MeV

Table 2: Solar Neutrino interaction mode, subsequent decays, timing and energy threshold for reaction.

Our present method of detection is to consider a multiple method, shown in Table 2, one is the neutrino capture on C12 into N12 and a ms secondary decay process. Another method is to replace the H in Liquid Scintillaotr with D using a 100% complete catalytic process and have the Neutrino capture on D into He2 which decays into two signals and another third simultaneous method is to dope with Ga to look for the neutrino capture into Ge m1 or m2 excited state that decays 2 to 5 micro-seconds into the Ge ground state emitting signature X-rays. All three of these methods would cover a broad range of neutrino energies and have a double signal to

separate out the signal from background. Simulations of this detector have been done and show the rates for Galactic Cosmic rays and Solar Electromagnetic radiation very acceptable.

Measurements from the Helios 1 Probe that the charged protons went up to 200 MeV but had an extremely small rate of 10^{-2} (cm^2 sr s MeV)$^{-1}$ and Helios 2 electron spectrum went up to only 20 MeV [4] shown in Figure 3. A simple first detector idea is shown in Figure 4. Cosmic ray rates seen on Earth would be smaller due to the Solar Modulation Theory, this expectations is supported by observations close to the Sun made by Helios 1 and 2 space-crafts. Between the two factors, of the exceptional quiet Sun in Cycle 23/24 and the assumption of a smooth cosmic-ray intensity gradient as a function of distance, it was seen that the expected 'upper limit' of cosmic-ray intensity at a nominal distance of 10 solar radii are well within the error bars of PAMELA's 1-AU data [5]. Galactic gamma ray rates as seen by Egret and Fermi satellite are reasonable low at 10^{-4}/s cm^2 sr [5]. Solar neutrino rates are expected to be ten per hour, and through the double coincident in time will be identified in subsequent data analysis. Keeping the background low by both shielding and active veto will be the two ways to reduce these rates.

The main source of count rate in the detector will be that from solar electromagnetic radiation emission. This is expected to be in the region of 0.5 to 10 MeV and at 10 down to 10^{-1}/s cm^2 sr, again as seen by the Helios space craft and shown in Figure 4. We have been able to do a detailed study of the shielding needed for such a spec craft. The final optimized shielding was determined to be 9 cm of Tungsten and a shield that completely shields a 25 kg detector would need to be 900 kg and less than a meter in diameter. This is very reasonable and the rates from electromagnetic solar radiation would be low. This is shown in figure 5 and is from an internal study conducted in the summer of 2016 by Prof. Solomey and Schmidt.

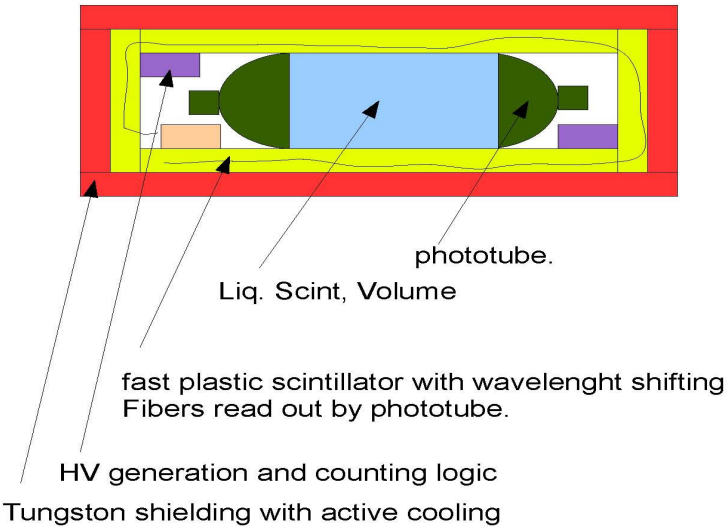

Figure 4: Test detector of a compact neutrino detector that is suitable for space flight.

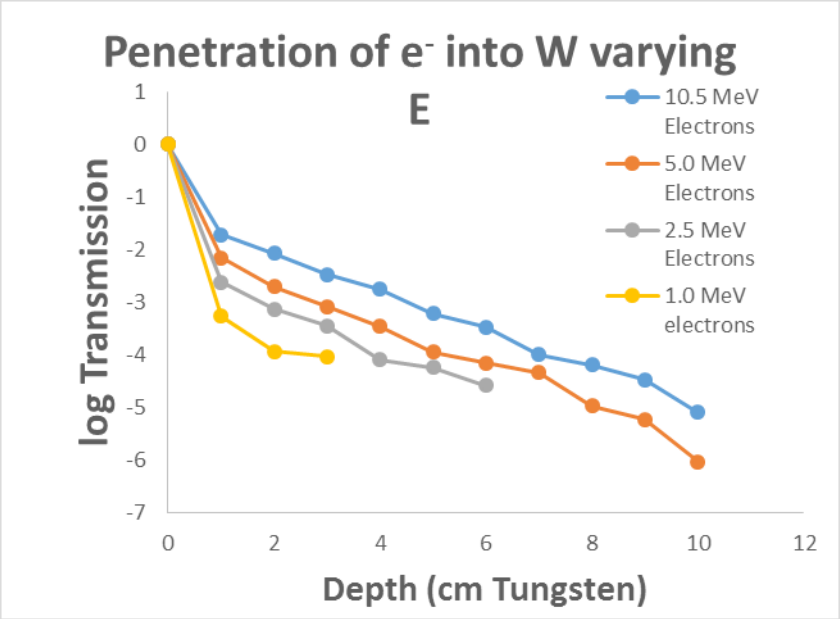

Figure 5: Electromagnetic Radiation penetration through depths of Tungsten for shield studies.

IV Technology Development of Heavy Liquid Scintillator

One of the best methods for solar neutrino detection is the conversion of solar neutrinos on Deuterium. Often used by having a sack of heavy water. However, the process of making "heavy liquid Scintillator" is a known process from the fusion bomb production, where 73 years ago the idea was created where Deuterium gas is infused into any Oil compound and with the help of a catalysts it is possible to have a 100% complete replacement of all the Hydrogen into Deuterium. Although such a detector has never been made for neutrino or particle physics, the process is relatively simple and 100% complete.

Although a large detector might have problems with large amounts of Deuterium because of the 1% contamination of Tritium in the gas, and the old Deuterium bubble chambers had a large radiation dose from that much Tritium, but in a small detector likes what we are planning for a "Neutrino Solar Orbiting Laboratory" this is not a problem since the largest planned active volume of liquid scintillator is 250 to 350 kg. Plus with a small volume like this then the Deuterium gas can be purified making it free of Tritium or at least much better than was possible when liquid Deuterium bubble chambers were used.

The solar neutrino interaction off of Deuterium would produce and electron ionizing track and the production of a He-2 nucleus. This gives the threshold for neutrino sensitivity all the way down to 2.2 MeV solar neutrinos. The He-2 decays with a nanosecond half-life into proton-proton or Deuterium and a positron track (<1%). The space flight detector\ being designed for the "Neutrino Solar Orbiting Laboratory" would have two photo-tubes looking on each side of the cylinder detector volume, see Figure 4. This would be used to our advantage where the timing is very short to measure a double pulse, but the first produced electron track could go into on photo-tube and the recoiling proton-proton emission can go into the photo-tube on the other

end, giving a topology signature instead of a timing signature. If we measure just the prompt light then we would have a signature for the events specific to this interaction and decay process.

V Electronics Signal Processing and Trigger Board Technical Requirements

The base design of the neutrino detector has a volume of liquid scintillator contained by a baggy and viewed by photo-tubes on one or both ends, and these photo-tubes might even become multi-anode segmented devices in future revisions. The baggy is contained by a solid plastic scintillator veto cylinder with end-caps. This veto array could be read out by a single wavelength shifting fiber that wraps around the inside or outside of the cylinder and end caps to a photo-tube, but it could also eventually be a multi-anode photo-tube with multiple segments from an array of sections of the veto. See the sketch of the detector in the Figure 4.

The liquid scintillator will be sensitive to neutrinos though multiple process each having the possibility of a double timed pulse. The basic ones currently considered are using heavy liquid scintillator Deuterium conversion into He-2, which then decays in 5 ns to a signature X-ray, second is a Ga doping where the neutrino iterations converts the Ga to Ge m1 or m2 excited nuclear state that then decays to a 40 keV X-ray or 300 keV gamma in 2.5 micro-seconds or 5 micro-seconds half-life. The third process is capture on C-12 into N-12 that decays with a 10 milli-second half-life with a 2 MeV gamma. Each of these process use a nuclear to capture the solar neutrino and produces an electron with a track segment up to 5 cm in length, a time decay of the second pulse and then a signature second pulse which has a well defined energy level for triggering on. All of this allows for great reduction of background.

The detector must live with a high rate of Galactic Cosmic Rays, High Energy Gamma Ray, and solar EM and protons some of which is shielded by the heat shield and outer container. In the simplest idea of the electronics each channel is stored in a time delay buffer. If a background event goes through after the first neutrino interaction signal is observed and before the second energy signature event then this event may be kept alive because the buffer streams of the photo-tube on the liquid scintillator can identify the background event with the same timing from the veto array observed event of either a GCR entering and exiting the liquid scintillator or a High Energy Photon starting a shower in either the veto array or the liquid scintillator and then the shower exits the liquid scintillator producing a signal in the veto array. For the long lived processes of C-12 where the half-life of the processes is milli-seconds then this is essential to keep the live time high and may even need to reject multi cosmic-ray background events, but it is also helpful for the micro-second decays of the Ga dopant options. For the timing signature see Figure 6. The electronics can also be improved by being sensitive to the 2^{nd} decay which should have a characteristic pulse height of their respective decays.

It is expected that the electronics board would then provide all the signal process of the photo-tube signals of the detector volume and veto array and produce candidate events for neutrino interactions and background event readout converted to digital format and sent to the spacecraft's main computer for data storage and transmission. It is necessary for this board to also monitor live-time and different characteristic rates of backgrounds although the background trigger rate might be to hard to read out all of the events but we need to monitor the number of these different types of background events and to provide some scaled down events for readout and later analysis. The electronics board needs to be able to be programmed by the spacecraft

computer during flight if changes are necessary and in the event that different neutrino processes are used and the ability to set the decay half-life the pulse height of the signature signal events and to be able to handle multiple processes during the testing and flight of the detector.

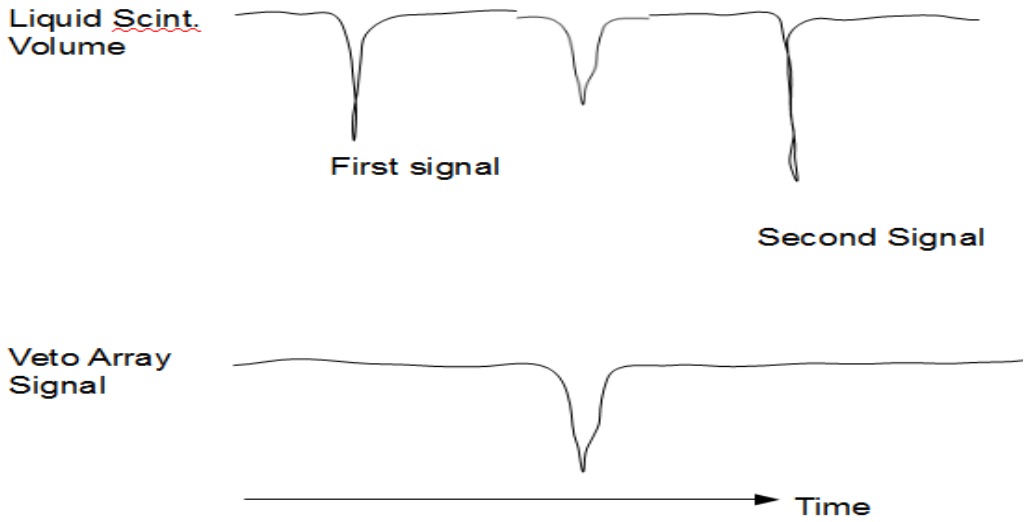

Figure 6: Top trace is the photo-tube pulse height of a neutrino interaction event in the Liquid Scintillator two pulses with a event inserted between the two signals from a background event. The bottom trace is the pulse height from the veto array photo-tube.

VI Rates of Neutrino Signals and Backgrounds from Galactic Cosmic and Gamma Rays

Count rates in the detector will be from Solar Electromagnetic particles that will be blocked and reduced by the EM shield function of the solar shade and Galactic Cosmic and Gamma Rays. These Galactic sources have known rates and the design of the detector outlined in this report has both a passive shield around the whole neutrino detector as well as a active veto array. The passive shield was taken as 0.5 cm of W and the active shield 1.5 cm or polystyrene Scintillator. Fellow NASA summer faculty fellow, Robert McTaggart wrote a detailed Geant-4 Monte-Carlo package for this design and gamma and cosmic rays where simulated. The summary of the rejection and shielding provided for Gamma rays is in Figure 7, and Cosmic Rays Figure 8.

A 1 ton (1000 kg) detector at sever Solar Radii from the Sun would have a neutrino flux 1000x higher, making a 1 kg detector equal to a 1 ton detector on Earth. A small detector has much better light collection and current experiments such as Kamland and Borexino lose about a fourth of the events due to insufficient light collection. If an idealized small detector can be 100% perfect in collecting the light then this 1 kg detector would need to be only 0.25 kg. The Ga isotope needed for neutrino detection is only 50% the concentration in nature, but with a small detector needing only a small amount of doppant, then a single isotope of Ga can be ordered and that yields another factor of two making the 1 ton detector only 0.125 kg. Likewise using D instead of Hydrogen with the idea of a Heavy Liquid Scintillator, yields another factor of 1.5 giving 0.83 kg of mass for a 1 ton detector. In addition to this most solar neutrino experiment use only 1% doping of Ga so as not to make the light collection harder, but with a smaller detector

this number could be increase up to the 19% limit, exactly how much would be the subject of a technical study, not used in this estimate.

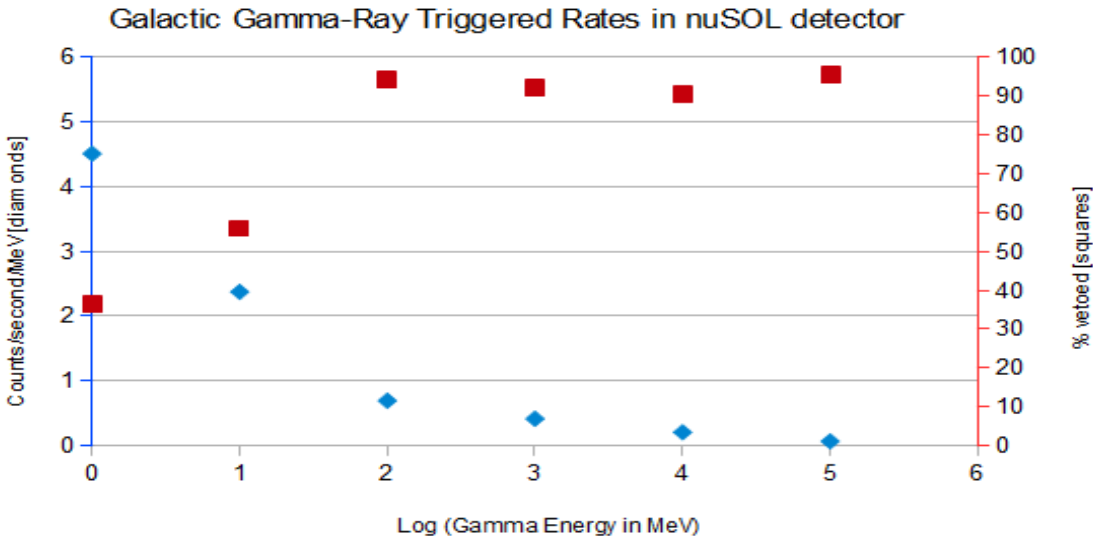

Figure 7: Galactic Gamma-Ray simulated in the detector design, the diamond points associated with the left vertical axis are triggered rates in the neutrino detector volume, and the square points associated with the right vertical access on the rejection rate of the veto design.

The detector could be 83 kg or smaller and our base design of a 250 kg detector would be equal to a 3 kton detector on earth. Table 3 summarizes the expected rates for the Standard Solar Model in the 300 ton Borexino experiment compared to the 250 kg νSOL baseline detector. The number of neutrino events per day would be around 200 neutrino interactions observed per day. The Borexino rates come from the paper in ref. [6].

VII Conclusion

This summer advanced furthered the idea of a neutrino detector close to the Sun for Solar Interior Physics studies, Particle and Nuclear Physics plus the added advantage of a Dark-Matter Search in the Sun. We reached the conclusion that the rates of particles in the detector from the Solar and Galactic backgrounds from Cosmic-ray and Gamma-rays are reasonable. In addition to this these rate studies which were achieved, we also showed how a new technical method of detecting solar neutrinos can be done with "Heavy Liquid Scintillator" where a 100% complete method of changing the hydrogen to Deuterium is possible. We layed out the design specifications for a signal and veto processing board for neutrino event selection, and how it would be used for background rejection and live time monitoring.

References:

[1] M.F. Altmann et al., "Solar Neutrinos", Rep. Prog. Phys. 64 (2001) 97-146.
[2] Spitzer, L. Jr., "Project Rand: Astronomical Advantages of an Extra-Terrestrial Observatory", in NASA SP-2001-4407: Exploring the Unknown, Chapter 3, Document III-1, p. 546.
[3] J. N. Bahcall, A. M. Serenelli, and S. Basu, "New Solar Opacities, Abundances, Helioseismology, and Neutrino Fluxes", ApJ, Volume 621:L85-L88, 2005 March 1.

[4] W. Droge, “Acceleration and Propagation of Solar Energetic Particles” LNP K-L Klein Editor v612, pp 193-212 (2003).
[5] J. Geiseler et al., “Inner heliosphere spatial gradients of GCR protons in the low GeV range”, International Cosmic Ray Conference (Rio de Janeiro 2013).
[6] G. Alimonti et al., Science and Technology of Borexino: a Real Time Detector for low energy Solar Neutrinos, Astroparticle Physics Vol. 16, #3, p205-234 (2002).

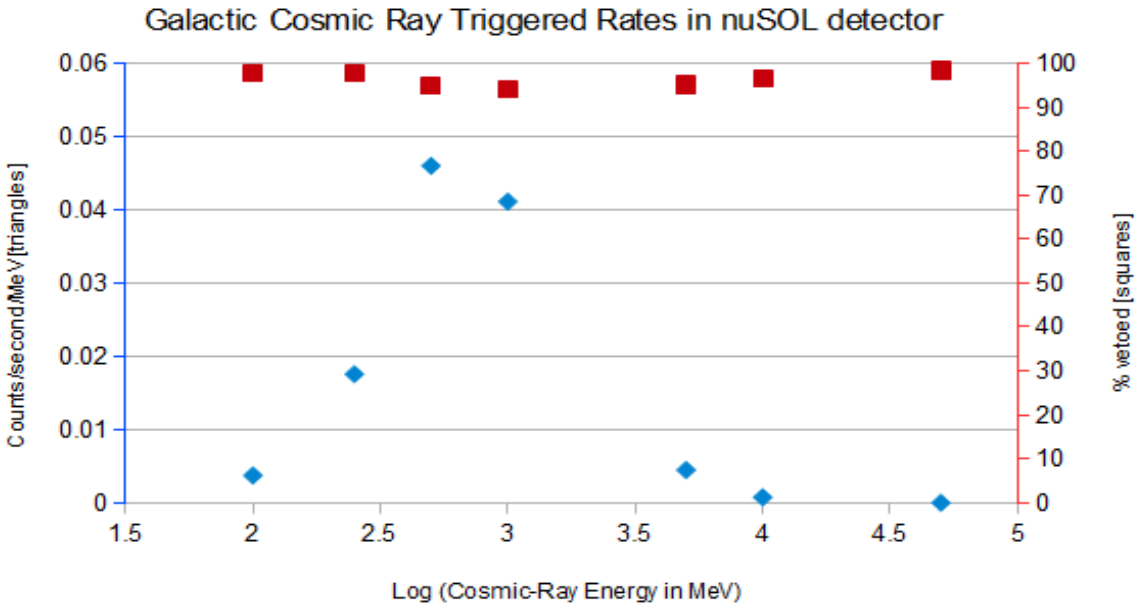

Figure 8: Galactic Cosmic-Ray simulated in the detector design, the diamond points associated with the left vertical axis are triggered rates of un-vetoed events in the neutrino detector volume, and the square points associated with the right vertical access is the rejection rate of the veto design.

Neutrino Energy	300 ton Borexino	250 kg νSOL at 7 $R_\odot$
0.4 – 0.8 MeV	15 ν/day	150 ν/day
0.8 – 1.5 MeV	3.5 ν/day	35 ν/day
>1.5 MeV	0.5 ν/day	5 ν/day

Table 3: Neutrino rates observed in the 300 ton Borexino detector on Earth and a 250 kg νSOL detector at 7 solar Radii, for three intervals of neutrino energy.

Acknowledgment:
Thanks to Robert McTaggart a fellow NASA Summer Faculty Fellow who wrote the Monte-Carlo code used, and NASA Scientists Nasser Barghouty, Mark Christl, M. Sabra and John Watts for their help and useful discussions.

NASA PAST, PRESENT, AND FUTURE MOON LANDING MISSIONS

Dr. Christine Stagnetto-Zweig
Associate Professor -Information Technology Oglala Lakota College, Kyle, SD 57752

Nomenclature

ALHAT = Autonomous Landing and Hazard Avoidance Technology

APL – Nav = Applied Physics Lab -NAV(Navigation)

CDSDS = Consultative Committee for Space Data System

COBALT = CoOperative Blending of Autonomous Landing Technology

EVA = Extravehicular Activity

GN&C= Guidance, Navigation, and Control

GPS = Global Positioning System

GSFC = Goddard Space Flight Center

HEOMD = Human Exploration and Operations Mission Directorate

HDS = Hazard Detection System

JCS = Johnson Space Center

Ka-Band = Transponder for Radio Science

LaRC =Langley Research Center

LRO = Lunar Reconnaissance Orbiter

LCROSS = Lunar Crater Observation and Sensing Satellite

LOI = Lunar Orbit Insertion

LUNAR CATALYST = Lunar Cargo Transportation and Landing by Soft Touchdown

MAPS = Multi-spacecraft Autonomous Position System

M2M = Machine-to-Machine

NACA = National Advisory Committee for Aeronautics

NDL = Navigation Doppler Lidar sensor

NASA= National Aeronautics and Space Administration

NICER = Neutron Star Interior Composition Explorer

RPL = Resource Prospector Lander

RF = Radio Frequency

SPLICE = Safe & Precise Landing Integrated Capabilities Evolution Project

SWaP = Severe Weather Avoidance Program

TRN = Terrain Relative Navigation

X-Band = radio frequencies from 7 to 12.5 GHz (for spacecraft in the deep space frequency bands, X-band refers to a downlink frequency of about 8415 MHz)

Abstract

The Resource Prospector Lander is a NASA project to send an expedition using instruments to locate different elements from the Moon and use a rover designed to excavate elements like oxygen and hydrogen. The objectives are to analyze the soil and determine if humans can live and work on the Moon for extended periods and be able to produce their own air and potable water. The existence of these essential components on the moon is vital to the future manned occupation of the Moon.

NASA has planned the construction of a lander and rover where the small rover is designed to scan the terrain, find, and collect useful materials. The rover is designed to excavate from the Moon hydrogen, oxygen, and water. Furthermore, it is the first step of the project to use the Moon as a possible base for planetary voyages on to Mars.

This research is focused on the optical navigation options for robotic rovers being developed at different centers of NASA and other countries where it is imperative to establish and maintain communication on the ground to the orbital craft.

The optical communication technologies have a higher bandwidth and can send more data to the Earth and the vehicles deployed throughout the solar system.

The MRO (Mars Reconnaissance Orbiter is an example of optical communication because it collects images in high resolution.

I. Introduction

NASA (National Aeronautics and Space Administration) has an impact in the U.S.A and the world. It is responsible for scientific and technological achievements in space (science and applications) and human flights "in response to early Soviet space achievements."

NASA was built on the National Advisory Committee for Aeronautics (NACA), and other government organizations, as the locus of U. S. civil aerospace research and development" [102; para. 1]. In 1958, NASA opened as a business and began to work on human and robotic space flight. Project Mercury was focused on learning if humans can survive in space. The Gemini Project was the second program and the spacecraft where two astronauts successfully docked with an unmanned vehicle at the end of the 1960s. After this program, NASA continued with Project Apollo, in 1969 with Apollo 11. The first Apollo project achieved the first landing of humans on another celestial body. NASA continued with more lunar landing missions through 1972.

Over more than 57 years, NASA has continued with research to help in the construction of aircraft as well as with the exploration of the solar system and beyond. The exploration has included the fundamental paradigm shift from manned missions to robotic exploration such as the Viking and recent rover missions to Mars.

For example, it was NASA, as a group of designers, flight operators, and project managers that made project Apollo a reality. The Apollo era was a remarkable time in U.S. history. In 1969 a group of engineers launched the program to ultimately land men on the Moon, and they captured the imagination of the whole world in doing so. It was iconic when Kennedy, the president of the U.S.A. introduced the new project to the public of landing men on the moon and returning them safely to the Earth. Neil Armstrong, one of the flight officers of Apollo, expressed the importance of the power of technology over Mother Nature demonstrated by being the first humans on the Moon. President Kennedy supported the Apollo program.

On October 1, 1957, the Soviet Union launched the first man into space with the Sputnik 1. The launch was successful. Eisenhower immediately created NASA (National Aeronautics and Space Administration) in response to the Soviet Union experiment. In 1958, NASA opened in the United States and eight thousand employees of the NACA (National Advisory Committee for Aeronautics transferred.

Fries (2001) in her book, explains the NASA Apollo program in details about the Apollo era engineers that made possible the project. In 1950, Siebold worked on different and advanced space vehicle designs to obtain a space business in NASA at the JPL. Siebold was hired by NASA and began to work on Merritt Island in Florida, and supplied his knowledge to the Kennedy Space Center in 1965, but he ultimately opted to work at the JSC (Johnson Space Center), in Houston Texas. Siebold began to work on the first Apollo vehicle. During the Apollo years, Beacham became part of the NASA project; the team consisted of "Robert Strong, Dan O'Neill, Isaac Kuritzky, Ernest Cohen, Isaac Petrovsky, Henry Strassen, Werner Posen, Philip Siebold, Michael Goldbloom, Charles Stern, Henry Beacham, and Bob Jones born between World War I, and the eve of the Great Depression. They were the progeny of an America that would be barely recognizable to the younger men and women who would be working with them at NASA at the height of the Apollo era." (p. 25). The history of each engineer that made possible the Apollo project has unusual and remarkable information because all those engineers worked with passion and were the pioneers of the main project of NASA.

Mohon (2017) describes the Apollo AS-203 that launched from NASA – Kennedy Space Center, in 1956. The mission of the Apollo AS-203 was without crew when the testing of the vehicle began. The second stage, S-IVB stage, obtained the flight information on the orbital conditions in the unit of the Saturn V vehicle.

At present, Marshall is evolving in the Space Launch System and developing the most powerful rocket ever seen before. They are planning to send astronauts to deep space (e.g., Mars). Mohon (2017) explains the Marshall Space Flight Center history with the creation of a powerful rocket and the exploration and scientific missions of the launches to the Moon and Mars. The Lunar Roving Vehicle explored the moon, and they also developed the first space station known a Skylab. Later, Marshall Space Flight Center did more experiments in the Spacelab and built the Hubble Space Telescope and the Chandra X-Ray Observatory. As well, they made small science experiments focused on different disciplines of large space systems and solving problems in the hiring of scientific and engineering experts providing answers about life on Earth and space exploration.

The Apollo-Soyuz test project was done together with the USSR and USA agreement. Both countries cooperated with each other in the exploration of space and developed compatible resources too. Since 1970, the USSR of Science and USA's NASA have shared information for joint missions. Later, in 1971, both countries were working on technical requirements for spacecraft systems and with a high probability of finding compatibility in them. Both countries, USSR and USA, joined efforts in scientific experiments on the design of the spacecraft.

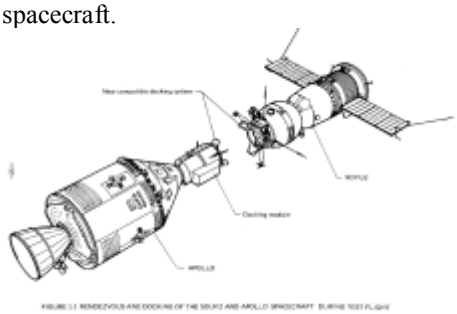

Figure 1: *The first test mission to test the means by accomplishing docking of the Soviet Soyuz-type spacecraft and American Apollo-type spacecraft t and the transfer of cosmonauts and astronauts*

Mission to the Moon

II. Surveyors/Rangers

Surveyor Overview and Common Science Instruments

The first lander program on the Moon was called Surveyor. The vehicle began to use science instruments (e.g., cameras and stress sensors, and progressed imaging and soil analysis experiment) Scientific Instruments used in all missions:

- **"TV camera (all Surveyor spacecraft)**
  The Surveyor TV camera consisted of a vidicon tube camera aligned 16 deg. from the central axis of the spacecraft. The camera was mounted under a mirror that could be moved in azimuth and elevation. Camera operation was remotely operated from Earth. Frame-by-frame coverage of the lunar surface was obtained over 360 degrees in azimuth.
- **Soil mechanics surface sampler (Surveyor 3, 4, 7)**
  The Surveyor soil mechanics surface sampler was designed to dig, scrape, and trench the lunar surface and to transport lunar surface material while being photographed so that the properties of the lunar surface could be determined
- **Alpha-scattering surface analyzer (Surveyor 5, 6, 7)**
  The Surveyor alpha-scattering surface analyzer was designed to measure the abundances of the major elements of the lunar surface. The instrumentation consisted of six alpha radiation sources (curium 242) and two parallel but independent charged particle detector systems. The two detector systems consisted of a two-sensor unit that measured the energy spectra of the alpha particles scattered from the lunar surface, and the other containing four sensors to detect energy spectra of the protons produced via reactions (alpha and solar wind proton) in the surface material.
- **Hardness and bearing strength of lunar surface experiment (Surveyor 6, 7)**
  The objective of this experiment was to determine the hardness and bearing strength of the lunar surface by the use of strain gauges, accelerometers, and rate gyros." [96; para. 100]

The mission of the Surveyor 1

The Surveyor 1 mission was a success because the design and landing technique developed were successful and made this project prosper. It was one of the first robotic spacecraft sent to the Moon and obtained data and achieved successful landings in this interplanetary program. The spacecraft, over 30 days, sent more than 11,000 photographs and data regarding the temperature and surface of the moon [85] The goals of the Surveyor 1 were lunar exploration and scientific investigation of the moon. [91] In 1966, the Surveyor 1 landed on the moon.

Surveyor 2

The mission of the Surveyor 2 was a success despite the fact that one of the rockets failed to ignite, threw it into a gyration, lost control, and crashed into the moon on September 23, 1966, in the SE of the crater

of Copernicus. The Surveyor 2 was designed to land on the Moon and returned to the Earth with photographs of the lunar terrain and obtain data that analyzed the temperatures and lunar surface, for the Apollo missions. The NASA-built 7 Surveyor spacecraft to the Moon.[84] The spacecraft demonstrated that launch, communication, and control from the Earth to the Moon could be done, including the objectives of sending images and data from the lunar surface. [60]

Surveyor 3

The Surveyor 3 objectives, according to Williams (2017), were a series of 7 robotic lunar soft landings supporting the planned lunar softlanding of Apollo as follows:

- "Developing and validating the technology for landing softly on the Moon
- Providing data on the compatibility of the Apollo design with conditions encountered on the lunar surface
- Adding to the scientific knowledge of the Moon." [120; para. 1]

Specific objectives

- Perform a soft landing on the Moon within the Apollo zone and east of the Surveyor 1 landing site
- Obtain post-landing television pictures of the lunar surface
- Obtain information on lunar surface bearing strength, radar reflectivity, and thermal properties
- Use the surface sampler to manipulate the lunar surface, and observe the effects with the television camera." [120; para. 1]

Surveyor 4

The Surveyor 4 mission was similar to Surveyor 3, photograph the lunar surface and test the soil for future lunar landing missions of the Apollo program. The Surveyor 4 was equipped as the Surveyor 3 to detect and measure ferrous components in the Moon terrain. The mission was successful, but the communications were abruptly lost before the landing on the Moon. The engineers of the NASA determined that the lander exploded when contact was lost. [51]

Surveyor 5

The Surveyor 5 mission was successful because it obtained data and in-situ composition on the Moon. The spacecraft was the first one to do soil analysis on the Moon. The mission almost failed due to a leak in the spacecraft's system, but fortunately, engineers did land it safely. The spacecraft returned with more than 20,000 photos that were taken during the mission flight, and it was one of the most significant missions and the most successful. The scientific instruments used were "television, Alpha-scattering surface analyzer, and hardness and bearing strength of lunar surface." [82-119; para.1]

The science instruments

TV camera (All Surveyor Spacecraft) "The Surveyor TV camera consisted of a vidicon tube camera aligned 16 degrees from the central axis of the spacecraft. The camera was mounted under a mirror that could be moved in azimuth and elevation. Camera operation was remotely operated from Earth. Frame-by-frame coverage of the lunar surface was obtained over 360 degrees in azimuth.

Alpha-scattering surface analyzer used on Surveyors 5, 6 and 7 was designed to measure the abundances of the major elements of the lunar surface. The instrumentation consisted of six alpha radiation sources (curium 242) and two parallel but independent charged particle detector systems. The two detector systems consisted of a two-sensor unit that measured the energy spectra of the alpha particles scattered from the lunar surface, and the other containing four sensors to detect energy spectra of the protons produced via reactions (alpha and solar wind proton) in the surface material.

Harness and bearing strength of lunar surface experiment were used on the Surveyor 6 and 7. The objective of this experiment was to determine the hardness and bearing strength of the lunar surface by the use of strain gauges, accelerometers, and rate gyros." [96; p. 18]

Surveyor 6

The Surveyor 6 was the first to launch in the surface of the Moon. The spacecraft returned with 30,000 photographs of the vehicle and footprint. It helped scientists to determine the soil and mechanical properties of the lunar terrain. Another objective was to identify the chemical elements in the lunar terrain using the alpha-scattering instrument, obtain arrival "dynamics data, thermal and radar reflectivity data, and conduct a Vernier engine erosion experiment." [81; para. 1]. The instruments used: (1) Imaging system (Visible, geology and morphology; IR spectral – soil/rock composition), (2) Alpha-scattering surface analyzer (same Surveyor 5), and (3) Hardness and bearing strength of lunar surface experiment (same Surveyor 5). The

spacecraft included a TV survey camera mounted "near the top of the tripod and strain gauges, temperature sensors, and other engineering instruments." [118; para. 3]

Surveyor 7

The Surveyor 7 mission focused on scientific investigations. The mission was unique, and the findings with the use of different instruments conducted on the lunar soil made routine findings except for the chemical analysis of the "highland crust showed to have less iron than samples from the lunar maria." [81-1171; para.1]The instruments used in this mission were (a). An imaging system, the (b) Soil mechanics surface sampler was designed to dig, scrape, and trench the Moon terrain and transport the material to take photos and determine its properties (c) Alpha- scattering surface analyzer. It was used on Surveyor 5 and 6, and (d) Hardness and bearing strength of lunar experiment. It was used on Surveyor 6 as well.

Rangers

The Rangers were designed to obtain high-quality photographs of the Moon and send to the Earth where the photos were used for scientific study as well as selecting the best sites for the Apollo Moon missions. The Rangers 1, 2, 3, 4, 5, and 6 had malfunctions in sending clear photographs direct to the Earth. The Rangers 7, 8, and 9 had successful images when sent back to the Earth because Earth-based telescopes made it.

Ranger 1

The Ranger 1 mission was to land and explore the Moon. The vehicle carried different instruments to study the cosmic rays, magnetic fields, and energetic particles. The Ranger 1 had malfunction problems, and a week later, after launch, it burned. "Lyman-alpha telescope, a rubidium vapor magnetometer, electrostatic analyzers, medium-energy range particle detectors, two triple coincidence telescopes, a cosmic-ray integrating ionization chamber, cosmic dust detectors, and solar X-ray scintillation counters" (Williams, 2017; para 2). Scientific Instruments used (1) Lyman-alpha telescope, (2) Magnetometer, (3) Electrostatic analyze. (4) Cosmic ray detector, (5) Cosmic dust detector, and (6) Scintillation counters. [79]

Ranger 2

The Ranger 2 was designed to test flight systems in the future lunar missions but had a malfunction that caused a burning of the spacecraft two days after launch. The scientific instruments used were a Lyman-alpha telescope, Rubidium vapor magnetometer, Electrostatic analyzer, Medium energy particle detectors, Triple coincident telescope, Cosmic ray ion chamber, Cosmic dust detectors, and a Scintillation counter

Ranger 3

The Ranger 3 was built to send photos of the lunar terrain to the Earth stations during 10 minutes of the fight. It deployed some scientific instruments and included a seismometer. It had problems with malfunctions such as increased speeds and other problems. It was unable to enter lunar orbit. [77-114]The scientific instruments used were (a) Imaging system, (b) Gamma ray spectrometer, (c) Radar altimeter, and (d) Seismometer

Ranger 4

Ranger 4 was built to collect data in space and photograph the Moon up close and land on the lunar terrain. The vehicle suffered onboard computer failure; the solar panels could not be deployed and crashed. In a few words, it was unable to complete its objectives. [76-113 The scientific instruments used were the Imaging system, Gamma ray spectrometer, Radar altimeter, and a Seismometer

Ranger 5

The Ranger 5 was designed as the Ranger 4 to collect data, launch and explore the Moon's surface. It had batteries malfunction that caused them to drain eight hours later and left it inoperable. It was nonfunctional but remained in orbit. [75-112] Scientific instruments used were an imaging system, a gamma ray spectrometer, a radar altimeter, and a seismometer

Ranger 6

The Ranger 6 was designed to obtain high-quality photographs of the previous moon impact the Moon terrain. The earlier Rangers missions used other scientific instruments. Ranger 6 known as Block 3 used imaging system. The scientific instrument used was an imaging system

Ranger 7

The Ranger 7 has been successful in its mission, explored the moon, and presaged a new period in the exploration. The future missions were prosperous rather than disasters. Ranger 7 transmitted in 15 minutes more photos, 4316 photographs before it hit the lunar terrain. The scientific instrument used was an imaging system

Ranger 8

The Ranger 8 model was built to accomplish a lunar impact route and send high-resolution photographs from the lunar terrain to the Earth in the final minutes before impact. The vehicle supported six television vidicon cameras, 2 full-scan cameras, and four partial scan cameras to achieve these goals.

"The cameras were prepared in two separate chains, or channels, each self-contained with separate power supplies, timers, and transmitters so as to afford the greatest reliability and probability of obtaining high-quality video pictures. No other experiments were carried on the spacecraft." [111, para. 1]The scientific instrument used was an imaging system

Ranger 9

The Ranger 9 was the last vehicle of these series. It was designed to explore the Moon. It sent high-resolution photographs as the previous models 7 and 8. It carried six television vidicon cameras, 2 full scan cameras, and four partial scan cameras to complete these goals. "The cameras were arranged in two separate chains, or channels, each self-contained with separate power supplies, timers, and transmitters so as to afford the greatest reliability and probability of obtaining high-quality video pictures. No other experiments were carried on the spacecraft." [110; pra.1] The scientific instrument used was an imaging system.

Lunokhod Soviet Moon Landers

The Lunokhod was the first successful Soviet vehicle that landed on the Moon on November 17, 1970. It traveled more than 10 kilometers in 10 months (Howell, 2016). According to David (2010), Lunokhod used an LRO (Lunar Reconnaissance Orbiter) camera to locate "vintage" space hardware crashed on the moon, by the Soviets, in the 1970s, and it was a "boon for the moon." (para. 1) The LROC (Lunar Reconnaissance Orbiter Camera), the Soviet Union's Luna 20 and 24, were located successfully. The Soviet Union sent three robots to the moon that returned as well, it was during the Cold War with the United States, and it was taken as a competition. Some Soviet lunar rovers are known as Lunokhods and included camera eyes of LRO. The Soviet Union had two Lunokhods 1 and 2. [49]

Luna 17/Lunokhod 1

The Luna 17/Lunokhod 1, the rover, was built to travel different locations on the Moon and conduct tests on the lunar soil and surface. The rover sends more than 20,000 TV pictures and more than 200 TV panoramas.

Luna 21/Lunokhod 2

The Lunokhod 2 was developed to land on the Moon, and the objectives were to collect images of the Moon's terrain. Further to examine the ambient environment and perform laser experiments from the Earth, and to employ the scientific instruments like an imaging system, x-ray spectrometer, penetrometer, laser reflector, radiation detectors, x-ray telescope, and an odometer/speedometer.

The Mission of the Chang'e 1

Chang'e 1 was the first Chinese spacecraft to explore the lunar orbit, fly lunar missions, and gain experience for future missions. The primary task was to obtain three-dimensional stereo images of the lunar terrain, analyze the elements of the Moon, evaluate and survey the thickness of the soil and helium three resources and finally, the exploration of the environment between the Moon and Earth. The scientific instruments used were "a stereo camera system to map the lunar surface in visible wavelengths, and interferometer spectrometer imager to obtain multispectral images of the Moon, a laser altimeter to measure the topography, a gamma ray and an X-ray spectrometer to study the overall composition and radioactive components of the Moon, a microwave radiometer to map the thickness of the lunar regolith, and a high energy particle detector and solar wind monitors to collect data on the space environment of the near-lunar region." [100-105; para. 1]

Chang'e 2

The mission of the Chang'e 2 was followed the same mission than Chang'e 1. It was part of the CLEP (Chinese Lunar Exploration Program), and the primary objective was the collection of images in high-

resolution of the lunar terrain. Later, the Chinese will send a Chang'e 3 to land on the Sinus Iridum area in 2013. According to Williams (2017), Chang'e 2 was planned as a backup satellite to the Chang'e 1 (para. 1). Scientific Technologies used:

- "The direct injection of the spacecraft into the lunar-transfer orbit without first settling into an Earth orbit
- Test of the orbital brake technology and capture by the moon at a location 100 km away (100 km lunar orbit insertion)
- Test of the technology on a 100 km x 15 km lunar orbit maneuver and orbit measure
- Capture of high-resolution imagery of the landing area in the Sinus Iridum (Bay of Rainbows, 43°N 31°W), a possible landing site of Chang'e-3.
- Test of the spacecraft by X-band TT&C measurement system
- Demonstrate new technology such as LDPC (Low-density Parity-check Code), high-speed (12 Mbit/s) Lunar-Earth data transmission system, the brand-new landing camera, micro CMOS-camera." [47; para. 1]

Chang'e 3

The Chang'e 3 was the first lander and rover that explored the Moon surface. On December 2013, it landed on the lunar terrain and completed the goal. The previous missions of the Chang'e 1 and Chang'e 2 were similar, and they provided the initial exploration. The Chang'e 1 and Chang'e 2 models helped to pave the way for future missions.

Chang'e 3 Rover

The Chang'e 3 Rover mission was to study the Moon "from its stationary landing platform and with a rover." [106; para. 1] The rover has six wheels and power-driven by solar cells.

Landing System

The landing system, Chang'e 3, used four landing legs with footpads to circumvent sinking into the terrain. The Chinese developed previous, landers to the Moon with a better knowledge of the lunar dust and maximizing stability and minimizing density issues in the landing system. [36; p. 1]

Navigation System

The navigation system is an autonomous landing on the Moon surface without receiving any data from Earth. The Chang'e 3 made an entirely autonomous landing on the Moon while receiving no information or instructions from the Earth. The landing was performed soft on the site, and the equipment had different navigation systems. These navigation systems provided to its central computer accurate altitude and velocity data. [46; p. 7 In the early stages of descent from the orbit, the navigation system platform built in redundancy measure the change of the speed that determines the delta-V target is reached during the engine burn. A Gamma-Ray Altimeter was used to provide range and rate measurements at the final descent, which provides the exact data to the vehicle.

The Apollo Missions

Apollo 1

The goal of the project, as Astronaut Neil Armstrong spoke during interviews, was to land on the Moon and return safely to Earth. It included the technology that meets other interests, at the national level, the achievement of the US in space competition, scientific exploration of the Moon and tested a human presence to work in the lunar environment. In 1967, during the preflight test for Apollo 204 (AS-204), there was a tragedy on the launch pad. NASA scrutinized an investigation of the fire and Apollo was postponed for a year. The missions of AS-201 and AS-202 (Apollo 1 & 2) missions were with the spacecraft aboard; the AS-203 carried the aerodynamic nose cone. [63; para.2]

Apollo 7

The mission of the test flight was to demonstrate the operation of the command and service module, crew performance and supported the crew during the mission and engagement competence.

The Apollo 7 reached the first stage of its journey, in 1968, with an orbital path 227 by 2985 kilometers above Earth (para2). The S-IVB was the second stage, and the lunar spacecraft module adapter panels did not deploy in its totality. The vehicle had different problems in the structure and electrical system. The windows were improperly sealed. The problem was fixed before the advent of Apollo 9.

Apollo 8

The mission of the Apollo 8 was to demonstrate translunar injection, CSM navigation, communication and midcourse corrections, consumable assessment and passive thermal control and test to improve the systems and future lunar operations. The improvement of the inclusion of a high-gain antenna – a four dish unified S-band antenna; it was fruitful and the deployment with the separation as of the third stage. Frank Borman, James Lovell Jr, and William Anders were the astronauts of the Apollo 8

The spacecraft, in the two hours, "50 minutes elapsed time restarted for a five minute a 17-second burn initiating translunar coast" [34; para. 2].

The crew loss of signal at 68 hours, 58 minutes, 45 seconds when Apollo 8 passed behind the moon, and the NASA's three astronauts were the first humans to experience the moon is far side.

Apollo 9

The mission of the spacecraft was the test of the first lunar module (LM) in the Earth orbit. It was the most crucial flight to the moon using the lunar module. The crew members tested the engine of the lunar module during ten days in the Earth orbit. It supported the navigation systems and docking and the backpack life systems also. After the successful orbiting to the moon of the Apollo 8, the mission of the Apollo 9 was ambitious according to Howell (2012).

Apollo 10

Apollo 10 was the first flight of a complete spacecraft to operate around the Moon. The mission objectives were a lunar landing with a separate LM (Lunar Module) and descent to the moon's surface before the rendezvous and docking with the command and CSM (Command Service Module) and about a 70-mile circular lunar orbit. [30]

Apollo 11

The mission objective of Apollo 11 was to perform a crewed lunar landing and return to Earth. The Apollo 11 made scientific exploration using the LM, crew deployment of a TV camera to transmit signals to Earth and experiment with the solar wind composition. Two astronauts sent examples of the lunar surface for return to Earth and used a seismic experiment package and a Laser Ranging Retroreflector. Both took photos and deployed scientific equipment. The LM spacecraft and CSM both had motion picture cameras. The return of the Apollo 11 to the Earth had no problems.

Apollo 12

The objectives of the spacecraft were collecting samples from the terrain of the Moon as well the deployment of some experiments, to work in the Moon's atmosphere, and explore more and obtain photographs.

Apollo 13

The mission had problems, and the crew must return to the Earth. The spacecraft had an explosion in one of the oxygen tanks and had to return to Earth without making a landing.

Apollo 14

The mission was the exploration of the Fra Mauro region and to deploy different scientific instruments and experiments and obtaining high-resolution photographs, investigate the geological surface, and collect material to study as well as tests to determine the effectiveness of S-band signals.

Apollo 15

The mission of the spacecraft was to explore the Moon, gathering information and stay more time in the lunar environment.

Apollo 16

The mission was to land with a crew and return to the Earth and explore those areas that were not explored and collect samples, took photographs and experiments with the ultraviolet camera/spectrograph.

Apollo 17

The mission was to land with humans and walk the Moon terrain, land in the Taurus-Littrow region and obtain photographs, collect information and return to the Earth.

III. Previous and Current Objectives

Surveyors

Williams (2006) explained the objectives of the Surveyors that were the first in the U.S., "to land safely on the Moon" (para. 1). The primary goals of the Surveyors were to obtain close-up images of the lunar terrain and to determine if the surface was safe for manned landings. The Surveyors were equipped with a television camera. "Surveyors 3 and 7 carried a soil mechanics surface sampler scoop, which" excavated ditches and "used for soil mechanics tests. Surveyors 5, 6, and 7 had magnets attached to the footpads and an alpha scattering instrument for chemical analysis of the lunar material" (para. 1)

It was the beginning of the effort for humans to land on the Moon. Currently, the Surveyors are not in use because NASA developed new landers and rovers to land on the Moon and Mars with sophisticated instruments and technology.

Rangers

Williams (2005) discusses in detail the series of the Rangers that were the first to attempt to obtain photography of the lunar terrain very close. They were designed to obtain images from the Moon and send to the Earth. All Rangers were equipped with cameras. In general, the missions had problems or the communication was lost. Presently, they are in the museum as part of the history of the first landers and robots to land soft and obtain images.

Apollo

The Apollo objectives were to land on the Moon and return safely to the Earth. The Astronauts can work on the Moon's surface and environment and implement technology that meets the national interest in space. [63] Today, the Apollos form part of our history, and we can find them in a museum

Lunokhods

The Lunokhods were Russian robot vehicles with eight wheels and controlled by radio wave signals. These vehicles were used to explore the Moon's surface and receive signals from Earth. [3]

Chang'e

The Chang'e 1 was the first Chinese missions to the Moon to obtain experience and evaluate the soil and helium and compare between the Moon and Earth. Later, the Chinese developed a second orbital spacecraft and continued with the lunar mission as made with the first. The first two were orbiters and the third lander and rover. The third carried more equipment to continue to study the Moon. The Yutu rover is powered by solar cells and included sophisticated instruments.

The Chang'e 2 was the next mission to the Moon and tested for future missions. The Chang'e 3 and Yutu was the third mission to the Moon, and its mission was designed to study the Moon with a rover (Yutu).

The Chang'e 4, the CNSA (Chinese National Space Administration lander plans the next mission to the far side of the Moon. The mission will be near the end of 2018, and it has the same instruments as the Chang'e 3 with the different scientific payload. Chang'e 4 will carry eleven instruments and probably will include a rover similar to the Chang'e 3. The lander mass will be about 1200 kg and the rover 140 kg. The Chang'e 4 is based on the Chang'e 2 design and will maintain the mission of communicating between the Earth and the Moon lander. The Chinese mentioned that the South Pole ,Aitken Basin, would be a possible landing site.

The Chang'e 5 Test Vehicle (CE-5 Flight Test Device or Chang'e 5-T1), according to Williams (2017) in its description of the vehicle, it was planned to test and return with a lunar capsule sample. It will do a loop around the Moon and the Earth. This mission is planned to 2017. The purpose of the mission is to demonstrate "hyper-speed semi-ballistic skip reentry technologies" (para. 1). The vehicle mission was in 2014 and tested the atmosphere.

Calandrelli (2016) described that China released color HD photos of the Moon from the latest moon landing. The images were taken by the Yutu rover in the mission of the Chang'e 3.

IV. RPL (Resource Prospector Land)

NASA Mission

A NASA robotic mission has been designed to land and obtain information on Mars. The system involves a prospecting rover, a pallet lander, and a ground control function.

NASA plans to launch in 2020 to Mars to look for water and oxygen. NASA also wants to demonstrate that the Moon has resources outside of the Earth that can be used. NASA wants to prove that humans can live on the Moon and use the resources that it offers. NASA, in this mission, will use a rover with instruments "to drill examples and scan for water vapor and volatiles on the moon."[69; para. 4]

The second experiment will involve NASA's Mars rover, which will launch in 2020. Mars has an ancient ocean, and it has been concluded that there existed habitability and evolution of life like on the Earth. NASA discovered that Mars and the Earth have similar land. In 2016, NASA found a paranormal life that included sculpted images on the rocks and fossils. The 13% of ice caps remain in the Earth in both poles, North and South, today and 87% Ancient Ocean lost to space is abundant in ocean waters and heavy hydrogen. [67]

The design of the robot landers made for the moon is to find the existence of water. The exploration was decided upon because they want to know if the human being can live on the moon.

They found excellent soil, oxygen, and potable water. All these elements are essential or vital for human beings planning to settle in the future as an alternative of the Earth planet.

One of the objectives of the RPL is to transport the rover and land on the moon at one of the moon's poles. The engineers used the LRO (Lunar Reconnaissance Orbiter) and the LCROSS (Lunar Crater Observation and Sensing Satellite). The use of these two elements demonstrated the presence of water ice. [52] The engineers explained the Software Development Plan to use the rover to land on the lunar surface. The RPL will land on the moon for a period up to 7 months using the LOI (Lunar Orbit Insertion).

This project should be possible in the early 2020's. The robot plans are to deploy instruments and locate water, hydrogen, and other volatiles and extract samples.

NASA Vision

NASA has a vision for exploring Mars with humans. NASA plans to explore the Moon before Mars. According to Metzger (2015), both targets have many things in common.

Design robotic lander

NASA works with third party contractors from the government known as CATALYST. CATALYST will facilitate the US commercial robotic delivery capabilities with the following agreements with Astrobotic Technology, Masten Space Systems, and Moon Express. All of them will share different technical areas that facilitate the development of commercial and transportation services development.

Howell, (2014) explains that NASA made advances of human exploration, solar system, asteroids, and Mars. NASA continues developing in the commercial space sector (para. 4). NASA sent robotic missions to the moon to explore the existence of resources like oxygen and water. The LUNAR CATALYST will help with space missions to Mars. NASA will work on this project with commercial U.S. companies that will benefit from the interest to NASA, scientific and academic communities. [70; para. 1]

> *"Commercial robotic lunar lander capabilities could address emerging demand by private customers who wish to conduct activities on the moon and could also enable new science and exploration missions of interest to the larger scientific and academic communities."[1para. 3]*

Commercial Robotic Lander

NASA wants to work on commercial space industry that can enable and develop a robotic lander with commercial entities and other agencies. The robot will expand missions to Mars and targets. There were different technologies and experiments in the International Space Station. NASA wants to investigate those areas that are unknown to humans. NASA can advance commercial efforts to reach the moon.
NASA made previous investments in lander technologies.

A. X-Band (JCS (Johnson Space Center)/MSFC (Marshall Space Flight Center)

The x-band is a radio wave using antennas for example UHF. The traveler communication is done with the orbiters and DNS complete radio waves. It is a common radio wave used for FM stations. The two antennas communicate with the Earth. NASA uses RF and optical techniques for measurements. These measurements are based on the Haystack X-band Radar improved with limited observations compared with

others at the GSSR (Goldstone Solar System Radar). The benefits of the use of these technologies will be to increase the ability to identify and follow the trajectory of orbital debris and smaller objects.

B. Transponder

NASA has two satellites with Amateur Radio transponder payloads, which were chosen for the next or future launches. The transponder is a set of satellite equipment and interconnected units. These units form a communication channel between the antennas (receive and transmit). The expectation of the launches should be taken place in the 2018-2020 years.

The transponder is composed of an input band-limiting device, an input low noise amplifier, a frequency translator, and an output band pass filter. NASA uses a transponder to communicate with satellites in orbit and send back information to Earth. NASA made several tests. There are laser transponders that transfer time amongst distant clocks and indirectly monitor the local gravity at the spacecraft. These were used in lunar and planetary missions where the sub-nanosecond transfer of GPS time to interplanetary spacecraft was needed for improved synchronization of Earth and spacecraft operations. The transponder can serve as an independent self-locking beacon for collocated laser communications systems. [50

Dick et. al.(2008) does experiments and obtains the results and demonstrates design based on the optical transponder architectures that are associated with spectra (i.e., PRRC (Pseudonoradom Range Code) model). The microwave transponder on spacecraft "enable the ultra-accurate capability required by a deep-space navigation and radio science" (p. 2). The transponder is based on an optical PLL (Phase-Locked Loop) scheme and made a good prospect for deep spacecraft. A mission to Mars has used an optical transponder.

The authors, Dick et. al.(2008), showed an example of the application considered for a Mars mission and the farthest distance from the Earth. It has advantages over the current technology, for Doppler.

"For such a mission and base and spacecraft antennas of 1-m and 10-cm diameters, respectively, a requirement of 1 pW received optical power requires a 55-W optical source at each end. A .5-W transmitter is a much more attractive prospect for the spacecraft antenna, calling for operation with received powers of 100 fW or below. We report here experimental results for optical PLL operation that show low cycle-slip rates at optical power levels as low as 40 fW." [50; p 3]

Prochazka, Hamal, and Pershing (2017) describe the laser transponder used for the Mars mission. It was used to provide measurements to the Mars planet with the "decimeter accuracy" (p. 1). The laser transponder was used to detect pulses on Mars as well as "the photon counting detector with nanosecond timing resolution required" (p. 1). On the other hand, Janson and Welle (2013) explains an example of the clear laser communications, the VSOTA (Very Small Optical) TrAnsponder; a system carried on a microsatellite RISESat- downlink-only optical communications. The author concluded that NASA made an effort to validate the missions with different tests and demonstrate components and subsystems that will enable new communications and capabilities on the spacecraft. Dick et. al. (2008) concluded that a new capability with the optical PLL transponder would function even better if it uses a standard pseudo-random range code and better accuracies with Doppler gave stability to it than another scientific instrument.

Prochazka, Hamal, and Pershing (2017) concluded that they developed a solid detector for the proposed Mars laser transponder.

Gather all data for landing missions (Landing systems and sensor) Russia, China (Taiwan).

NASA developed technologies that are used to navigate to the location and have a safe landing and detect hazards during landings throughout the final descent to the terrain. It is one of the most important aspects for future missions to the Moon, Mars, and others to know and locate the high hazardous surface. The new technologies were integrated as a part of the ALHAT (Autonomous Landing and Hazard Avoidance Technology) project. LRC (Langley Research Center) designed three light detection and ranging sensors that can provide the data for a precision landing. It is known as LIDAR.

LIDAR made great improvements over current systems for navigation tasks. The results were accurate, and the precision range of the landing velocity data are critical to the navigation of the lunar vehicles

and made a safe, soft landing. ALHAT's LIDAR impacted the design of the future landing missions with a high potential of helping in the exploration vehicle rendezvous and docking in the reentry to the Earth.

NASA has a record of archived data of missions, research, and programs. NASA developed technologies that are implemented in landing vehicles to verify a safe landing. The technologies applied in the rovers will detect landing hazards during the final descent to the terrain. These technologies will be used for future landing missions to the Moon as well. LaRC designed a LIDAR sensor that helps to get the data for precision landing. The Doppler LIDAR is used to measure the speed and altitude of the vehicle and assist in the landing site chosen. The high-altitude laser altimeter is providing data before the final approach and correcting the trajectory to the landing area

NASA is not secure about the landing missions with China, Taiwan yet. While on the other hand, NASA knows that the Chinese National Space Administration (CNSA) planned, in 2018, to land on the far side of the moon. They also plan to land a traveler on Mars in 2020. Previously, Russia and other nations attempt to land on Mars with no success.

NASA has different developments in communications technology and orbital tracking that form part of the different projects that are used in conjunction with other agencies. The optical communications and navigation deal with other technologies to keep both with a practical and advantageous bandwidth in the optical spectrum.

How can benefit to us as citizens?

The use of robotics and humans will benefit to obtain a high-quality data with better resolution (i.e., cameras) and better and precise landing. NASA uses an extended networking that will increase the availability of data and transfers at the high levels of Earth-based scheduling and scripting. It is possible with the no intervention of a human.

Communications

Rice (2017) assumes that "Lander and Rover communication system is based on the following rules and assumptions:

- Communications system is zero faults tolerant,
- Uses S-band frequency
- DSN tracking (no RF ranging is required post landing
- Communicates via the Deep Space Network
- Relative navigation is handled by Rover (not using RF)
- 100% communications coverage during all critical events" (p. 47)

The spacecraft GNC (Guidance, Navigation, and Control) system needs to maintain suitable control during the subsequent phases:

- "Maintain required attitude and attitude rate during coast from upper stage separation to Solid Rocket Motor (SRM) braking burn.
- Perform up to 3 Trajectory Correction Maneuvers (TCM) during transit to the moon.
- Control the spacecraft during the SRM (STAR-48 B) braking burn
- Maintain attitude and attitude rate during lunar descent coast phase
- Successfully land the spacecraft within 100 meters of the targeted landing site.
- Declare landing and command the shutdown of all thrusters. This could occur at some TBD altitude or once ground contact is confirmed." [92, p. 50]

V. Navigation options to the moon and land

Executive Summary

NASA wants to integrate different navigation options from the Earth to Mars. The goals of communications, navigation, are increased data rates, increased security, and assured data delivery with low latency, autonomous, and a robust networked connectivity during the solar system travel.

NASA has different developments in communications technology and orbital tracking that form part of the different projects done with other agencies. The optical communications and navigation deal with other technologies to keep both with a practical and advantageous bandwidth in the optical spectrum.

How will the exploration benefit humanity?

There are several opportunities to explore space using technologies that benefit Earth. Of course, our curiosity to investigate focused on different approaches such as increasingly complex missions to Mars and beyond.

Veres, Jones, and Jorgenson (2015) explained the PSL (Propulsion System Laboratory) created a continuous cloud of glaciating ice crystals spraying bars, and the duplicated icing was successful and experienced by the Honeywell engine approached during the flight complete ice crystal clouds. Engineering has made tests and concluded that in some part of the parameters have not changed while on the other hand, the engine began to deteriorate and lose control. It happened for the ice accretion in the low-pressure compressor (para. 1). Engineers focus on the improving the efficiency of the ice crystal ingestion on the engine act. The engineers determined that "the increased ice in the low-pressure compressor depends on the concentration of ice crystal ingested, the wet bulb temperature distribution, and the melt radio" (para. 1).

B. GPS (Global Position System) – GSFC (Goddard Space Flight Center)

The execution of a GPS should be implemented to localize **GPS** According to the research investigations, the GPS Satellites and the X-Ray Navigation will provide precise timing beacons that support navigation during the solar system and infrastructure. The experiments will reduce the volume of the system and pointing constraints.

The objectives of the use of the GPS is the transmission and receiving RF communications where the information obtained will induce plasma invasive and a reentering space vehicle. On the other hand, the GPS acts "with accuracies of at least 20 meters." [68; p. 32] ("NASA Technologies Roadmaps," 20, 2017; p. 32). NASA knows that the GPS is used on the Earth, but the GPS built in the Military is more accurate than those developed, to the utilization of the standard user. The most accurate navigation is the DSN (Deep-Space Network) because can determine the position of Mars at 1 km that is the Earth distance and 10 km at Mars distance. In few words, the goals of these technologies will make possible more missions. The use of the GPS has determined its procedure to obtain an accurate landing and deploy of the three or five beacons that will define the position with more exactitude.

GPS Satellites and DSN made advancements in the following areas:

- "Spectrum and power efficient waveform design
- Advance coding schemes
- Adaptive mode control based on mission phases
- Channel and network conditions
- System-wide awareness of cognitive or autonomous behavior,
- Design and validation of space-to-space RF ranging (range, range rate) for rendezvous SWaP and to b compatible for EVA communications system needs." [68; p. 46]

Another important technology that works with the GPS is the X-Ray because it enables the GPS and supports autonomous navigation further than the solar system.

GSFC (Goddard Space Flight Center)

NASA's GSFC plays an important role in all missions as well as on the studies of the atmosphere of MARS.

According to the NASA engineers, there are several breaks in communications during the actual landing systems. The COBALT (Cooperative Blending of Autonomous Landing Technology) project could change that with the cooperation of the STMD (Space Technology Mission Directorate) and the HEOMD

(Human Exploration and Operations Mission Directorate. Bestowing to COBALT, it will reduce the risk in landing and benefit robotic landing in those unreachable areas that human cannot enter. Carson (2017) explains in details about the GPS use with the Xodiac vehicle will collect data. Both are complementing in this task.

C .Pulsars

NICER is known as pulsars. Scientists determine the pulsar's radius, which is a primary vital measurement that they need to understand the interior structure. NICER helps scientist to understand the behaviors of the environment. Then, NICER and GPS can work together because providing precise cosmic clocks and atomic clocks used with the GPS satellites.

D. Beacon

Beacons formed part of the navigation constellation and landing systems resultant from GPS technologies and landing optical goals that are usable for perfect landing. Beacons and optical targets can improve the navigation and be accurate as the GPS and ISS (International Space Station) and docking objectives.

What are the benefits?

Many benefits that beacons offer is the distress signals to passing satellites. Beacons can demonstrate accurate location around 140 meters. The nature of the beacons is to improve and mitigate risks.

E.MAPS (Multi-spacecraft Autonomous Position System)

According to Anzalone and Chuang (2016), MAPS is an integrated system of navigation and communication based on network navigation. "This navigation problem is unique primarily due to the great distances involved and the need for high-accuracy onboard state estimation capability and autonomy. The great distances between assets generate a unique signal environment regarding signal transmission times, power generation, and computational capability onboard the spacecraft" (para. 2).

Both authors, Anzalone and Chuang (2016) explain that MAPS is an innovation that implants navigation information and transmission among assets in the network communication. The packets are transmitting to each asset, and are sending into the message headers that form part of the standards of the CCSDS (Consultative Committee for Space Data System). The point of view of the researcher is the network communication, navigation with the packets are limited to the network because it reduces the load on ground-based navigation systems while on the other hand is improving the estimation capability and precision [5; para. 5]. On the other hand, the question is what could happen if the network is down.

On the other hand, there is an M2M (Machine-to- Machine) development that enables the system to perform a network navigation protocol in different environments. Furthermore, recent information obtained from the NASA Technology Down To Earth (2017), explained the assets are operated precise in GPS in those denied areas that fix the position of the assets and the network architecture is a software update that does not require the use of designed hardware.

Benefits and Applications

Benefits	***Applications***
• ***Versatile***	• *Robotics*
• ***Scalable***	• *Aerospace*
• ***Ease of Use***	• *Wearables*
• ***Precise***	
• ***Emergent***	

If NASA builds, a protocol that creates a decentralized Internet architecture the main question is how far the protocol can maintain into space? The use of the Internet Protocol as, regular communication, between the Earth and the Moon, it will follow the behavior during navigation in space. The navigation in space is feasible to monitor and manipulate the information inside of the spacecraft and instruments.

Some areas are contradictory between the researchers and engineers at Goddard while the JPL researchers found the same obstacles. The problem is the distance delay. The TCP (Transfer Communication Protocol) is not working on the deep-space travel. The remote control is hard to manipulate when there is a 40 minute round trip. [57] It is possible to separate the Internet Protocol (IP) using unreachable Internet to common users. The Internet domain names are not following the standards, use language scripts of the local, and should be a problem with the English language. The Internet is a critical infrastructure for communications, government services and more for every country. The maximum authority in the U.S. government is the ICANN (Internet Corporation for Assigned Names and Numbers).

Returning to the point of view of Anzalone, the potential applications of MAPS is to support the human missions and robotic in space navigation. The benefits are providing a communication network that makes possible "to every communication pass between real-time autonomous and assets." [4 para. 6 & 7]

Optical navigation

The navigation options to the moon and for a soft landing are an excellent option. Optical communication is a form of long distance communication that transmits information. It means sending data across space using lasers instead of radio frequency. [87]

NASA, in 2010, was in the process of the migration of the Ka-band mission as a part of the high data returns from science missions. The Ka-band migrated to optical communication that "Provided access to unregulated spectrum and support the data rates" [93; p. TA05-9]

Landing sensors

A.SPLICE (Safe and Precise Landing Integrated Capabilities Evolution)

The SPLICE is a project to testing landing sensor will not be used earlier on 2020 on the Moon and Mars landing.

B. ALHAT (Landing and Hazard Avoidance Technology*) JSC, LARL, JPL)*

*N*ASA is detecting landing hazards with the new technology. These technologies form part of the ALHAT (Autonomous Landing and Hazard Avoidance Technology) project. The project is in the process of demonstrations in a sequence of flight tests. [76; para. 4] The article explained that the data provided could significantly impact the future of lunar landing and other landing missions. ALHAT Doppler LIDAR is more accurate than the conventional Doppler radar-based sensors that were used in Phoenix Mars Lander and Mars Science Lab.

Congiu (2017) mentions that the terrain on the Moon and Mars is potentially hazardous in many areas. The ALHAT can detect dangerous obstacles (i.e., rocks, holes, and slopes) with its hazard detection system. ALHAT was tested on a helicopter and Morpheus. Morpheus is a land robotic prototype and used with GPS. At this point, the GPS is not available on a planetary lander. It is navigating with sensors only.

According to Carson III, Robertson, Trawny, and Amzajerdian (2015) developed the ALHAT (Autonomous Landing and Hazard Avoidance Technology) to demonstrate the Morpheus rocket-propelled VTB (Vertical Testbed). In 2014, the authors demonstrated the VTB (Vertical Testbed). The ALHAT (Autonomous Landing and Hazard Avoidance Technology) is a sensor that measures the navigation filter employed in the flight-testing with Morpheus and navigation control and subsystem. It will provide a safe and precise landing in future exploration missions. (para. 1).

Carson (2015) explained in depth the ALHAT project and developed the sensors to land the robotic vehicles in any terrain conditions. It is an effort to integrate and test a range of terrestrial vehicles that will be included in the spaceflight applications shortly.(para. 1). To achieve the tests, there is an integration process as well as the verification of the data to evaluate ALHAT (Autonomous Landing and Hazard Avoidance Technology) and GNC (Guidance, Navigation, and Control) performance (para.1). The ALHAT

was tested, especially for the flight test of Morpheus. The tests result successfully demonstrated valuable performance data.

The development of these technologies will expand to future missions and exploration to different locations in dangerous topographies. In 2005, NASA Headquarters commissioned the ALHAT project. The project was concentrated on the objective to obtain an autonomous landing of human or robotic vehicles with precise landing and safety.

Technologies Methods

- TRN (Terrain Relative Navigation) focused on velocimetry, and altimetry long-range. It was not tested yet
- HDS (Hazard Detection System) developed for velocimetry and ranging
- NDL (Doppler LIDAR) developed for velocimetry and ranging
- LAlt (Laser Altimeter) altimetry is the main support over HEOMD (Human Exploration and Operations Mission Directorate)

Sensors and Vehicle Integration

In 2014, ALHAT was a sensor, tested on the Morpheus VTB.

NDL uses FMCW (Frequency Modulated Continuous Wave) it is a technique as well as for detection of velocity data and range which use an optical homodyne.

HDS involves a flash lidar "mounted on a two-axis gimbal, a Northrop Grumman LN200 IMU (Inertial Measurement Unit) and a dedicated CE (Compute Element) and a PDU (Power Distribution Unit) and a battery box." [44; p. 3]

JPL Lessons land on HONEYWELL.

Honeywell has been assigned with high performance and tactical requirements of managed and unmanaged vehicles. The model Honeywell HG8500 Series Radar Altimeter is low cost and is used for tactical targets and remotely piloted vehicles. Below, are listed the two different options of the Honeywell. The tables included will compare both radars.

LaRC (Langley Research Center), JPL (Jet Propulsion Laboratory) Combining LaRC and JPL

LaRC (Langley Research Center) is responsible for the Aerothermodynamics design and analysis of the Mars atmospheric Microprobe. It developed together with JPL (Jet Propulsion Laboratory Combining), JSC (Johnson Space Flight Center), and ALHAT (Autonomous Landing Hazard Avoidance Technology), the HDS (Hardware Description Sheet). Langley developed three sensors:

- Laser Altimeter – measures above the ground and reduce position error
- Flash Lidar generates 3-D terrain images (video) identifies safe landing places
- Doppler Lidar determines the speed and altitude of the spacecraft and navigate and identify safe landing areas

The HDS (Hardware Description Sheet) was developed to conduct tests to validate -hardware implementation and ground verification- "performance abilities and prepare the system for integration and terrestrial flight testing on an HV (Host Vehicle)." [45; para. 2]

The HDS consists of the following:

- Lidar (Light Detection and Ranging)
- FOV (Field of View)
- IMU (Inertial Measurement Unit)
- CE (Compute Element)

The HDS has two main functions:

- GN&C provides locations of safe landing sites
- Provides a subsystem and position measures during the final method to touchdown [43; p. 3]

The HDS has two operational phases, are the following, and occur in the HDP (Hazard Detection Profile)

- HD (10 second period)

- HRN (on board is generated and the DEM (Digital Elevation Model) determine the safe landing sites around 1-hectare area positioned on the ILP (Intended Landing Point) (p. 4)

According to Carson and the scientists involved in the project (2017), Figure 17 explains in detail the operations that consist of providing landing safety and determining the position and terrain features. The HDS algorithm analyzes the HDEM to find a terrain feature. (p. 5).

NDL (Navigation Doppler LIDAR)

Atkinson (2016) explains the system integration for the NDL, which will become a part of NASA payload known as COBALT (CoOperative Blending of Autonomous Landing Technologies). It is a joint development work among different NASA centers JSC (Johnson Space Center), and JPL (Jet Propulsion Laboratory.

The NDL is working as an individual unit with the COBALT flight tests, and it is attached with an LVS. In 2014, it was part of the Morpheus Project, and researchers thought that NDL has the potential and should be considered a sensor for all future missions. Furthermore, NASA developed a filter that fuses the NDL and LVS measures where the LVS was tested and will be used on the Mars 2020 rover. [38]

LVS (Lander Vision System)

The LVS was developed to take pictures of the surface and compare with the present maps. COBALT, LaRC, and JPL are working with the navigation NDL which is ultra precise velocity and measurements, and it is integrated into the LVS for TRN (Terrain Relative Navigation) position.

Lander Vision System (LVS) was designed to be tested on Mars. The Lander Vision System (LVS) is used to detect location relative to landing hazards (i.e., boulders and outcroppings). The LVS mission to Mars will be used to find new discoveries and will be focused on the red planet. [66]

The LVS will be used to pursue new discoveries on Mars that will be planned for 2020 on the red planet.

According to Brown, this rover will be sent to Mars for 2020 to further explore and investigate the planet. The 2020 mission is based on the design MSLR (Mars Science Laboratory Rover), and it is upgraded with sophisticated equipment, and geological instruments will determine the environment, and of course, search for signs of life. On the other hand, the 2020 rover will help the advance of the future human explorers using natural resources of the Red Planet.

What are the objectives of Mars 2020 rover?

- Geological exploration, find evidence relevant to geologic diversity
- Astrobiology determine the viability of an ancient environment, search materials with high biological signature preservation potential, and potential evidence of past life
- Sample Caching - obtain samples and interpret different environments and habitability. Obtain samples, record and, identify the Astrobiology and geologic diversity, and ensure the future needs and choices of NASA
- Preparation for Humans by contributing to the human exploration of Mars and measure the SKG (Strategic Knowledge Gap) for example, oxygen, atmosphere, dust size and morphology and how these can affect human health, validate atmospheric models, use the vehicle to descend to Mars surface

Professor Bell is a principal investigator of the MastCam-Z (2017) and explains that it will help with different Mars 2020 experiments (i.e., identifying rocks and soil). The robot rover can drill rock core and investigate the surface of Mars (para. 14)

C.APL (Applied Physics Lab)-NAV(Navigation) (JHU /APL (Johns Hopkins University Applied Physics Laboratory) –TRN (Terrain Relative Navigation)

The APL (Applied Physics Lab) was established to test a variety of airless bodies that are used in terminal descent (between 30-60 meters). The MSFC (Marshall Space Flight Center tested a lander known as the Mighty Eagle known before as Warm Gas Test Article according to McGee et.al.(2013).
The Mighty Eagle was tested at the end of 2011. It was designed to use as a lander and test activities. Marshall and APL engineers designed the robot lander to use in future exploration of space.

The JHU/APL (Johns Hopkins University Applied Physics Laboratory) developed the SH (SeaHawk), and provided a camera system and used GPS data and provided a real-time tracking of the cameras with the SH-NAV. Figure 34: The APL-NAV has two versions of landers and is the following:

- *SH-NAV (it was designed for an aerial ocean photography project). It is used to make precise calculations of the wind and solar conditions.*
    a. "Provides flight management and navigation capabilities
    b. Allows real-time planning of complex collections of geometries based upon mission geometry and ambient solar wind conditions
    c. Emulates assorted pilot instruments, enabling flight geometry and ambient solar and wind conditions accurately
    d. Can control real-time gimbal tracking
    e. Provides a variety of complex tracking options."[7-8; para. 3]
- *RTV-NAV Adaptation adapted to the aerial LIDAR mapping project.*

a. "Provides flight management and navigation capabilities
b. Provides graphical survey planning for calibration and mapping flights
c. Runs a CDI (Course Direction Indicator) on a video pilot display
d. Controls and configures LIDAR system
e. Monitors and displays LIDAR coverage in real time." [7-8; para. 5]

JHU /APL (Johns Hopkins University Applied Physics Laboratory)

The JHU/APL works in collaboration with the NASA scientists and engineers to plan a space mission. The institution offers an environment where students interact with scientists and engineers, examine instruments, and tour to test facilities while learning the different fields in the space program that NASA offers. NASA has the latest technology and prepares the future missions and scientists and engineers.

.

TRN (Terrain Relative Navigation)

Terrain Relative Navigation (TRN) is an onboard spacecraft GN&C function that creates a location estimate of a spacecraft comparative to a map of a planetary surface. The Terrain Relative Navigation (TRN) measurement sends a signal to communicate to the vehicle its position to the midpoint of the landing, and it is identified on the map before it lands. For example, on Mars, according to Johnson et.al. (2017), it can use diverse "ways depending on the amount of fuel available for a divert"(p. 1)
After the DIMES, (Descendent Image Motion Estimation System for the Mars exploration rovers missions the JPL, TRN research began at that time.

What is the DIMES?

The DIMES is a software package that matches a descendant image and a large orbital image and co-registered digital elevation map that is integrated with a filter – Kalman filter- that fused image measurements. The measurements demonstrated, with inertial data, ten meters landing, with precision at the time of the processing of a sounding rocket data set. ALHATP (Autonomous Landing and Hazard Avoidance Technology Project), and the TRN software was tested off the line. The testing led to a modularization of the TRN software and the capacity of handle illumination changes [59; p. 2]

The processing of the TRN for the Mars landing was taken with a parachute, and it captured the images when descending to compare with the map. It included the IMU data and the LVS diagram
The authors, Johnson et. al. 2017), will continue with the work because they want to eliminate the small bias that invalid TRN runs in the operational moment and the future investigation of the performance of the LVS with EDL

VI. Other all data for landing missions

NASA developed technologies that are used to navigate to the location and have a safe landing and detect hazards during landings throughout the final descent to the terrain. It is one of the most important subjects of research for future missions to the Moon, Mars, and others to know and locate the high hazardous surface conditions and obstacles. The new technologies were integrated as a part of the ALHAT (Autonomous Landing and Hazard Avoidance Technology) project. LRC (Langley Research Center) designed three light detection and ranging sensors that can provide the data and use it to perform a precision landing. It is known as LIDAR.

LIDAR made great improvements over current systems for navigation tasks. The results were accurate, and the precision range of the landing velocity data are critical to the navigation of the lunar vehicles to be able to make a safe, soft landing. ALHAT's LIDAR impacted the design of the future landing missions with a high potential of helping in the exploration vehicle rendezvous and docking in the reentry to the Earth.
.

Potential Problems with Optical Communications

While bandwidth and signal strength are the advantages of optical communication technologies, there are some difficulties that must be addressed. 1) The laser transmitters and receivers must be precisely aligned, or the beams will not hit the targets; either the spacecraft or the ground control center. Depending entirely on lasers could be problematic if the vehicle lost control or were tumbling since the ground control beam could not be received by the tumbling craft in order to stabilize it and aim the system at the ground control once again. 2) Laser light can be obstructed by dust, clouds or debris anywhere along the path of the signal beam because laser communication is strictly line-of-sight. Despite these issues, optical technologies can be used to transmit large amounts of data with minimal data loss and are excellent for the craft to use to send high definition photos and other valuable data sets back to ground stations on Earth.

Conclusions

As a researcher, I found that all technologies can work together, but the problem of the loss of signal between the Earth and the Moon will continue until the engineers find a solution. While artificial intelligence systems (that can recognize hazards and avoid them on their own) are preferable, they are not foolproof, and improvements in human real-time radio control are necessary and possible in the near future. The Resource Prospector Project is working with different commercial and international parties to deliver a robotic lander to the Moon and future Mars terrain. The project is developed to reduce the risks and obtain better results in the design of the landing vehicles, hardware, and software.

Appendix: IMU TABLES (Inertial Measurement Unit)

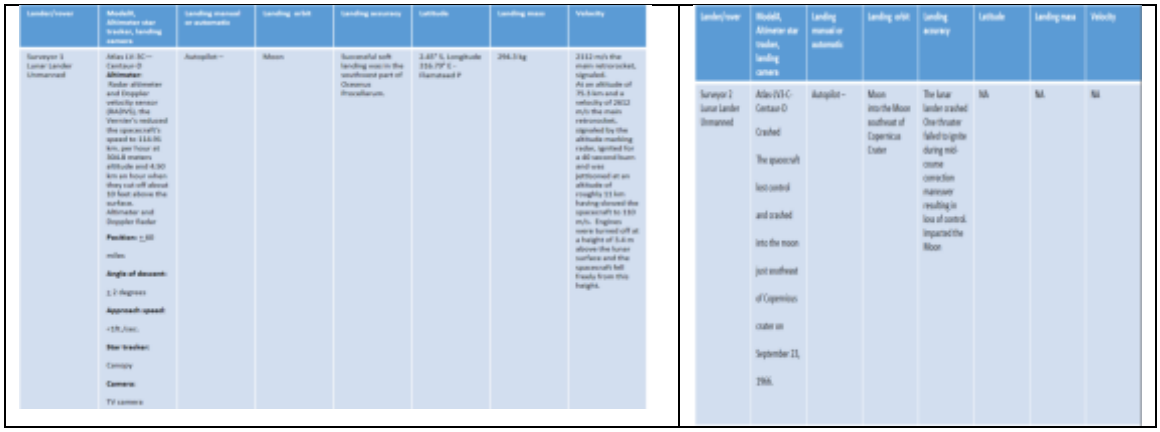

Landing Sensors

Surveyor, Apollo, Lunokhod & Chang'e

Table 1. *Surveyor 1 & 2*

Table 2. *Surveyors 3, 4, 5 & 6*

Lander/rover	Model#, Altimeter star tracker, landing camera	Landing manual or automatic	Landing orbit	Landing accuracy	Latitude	Landing mass	Velocity
Surveyor 7 S-IVB Lunar lander Unmanned	Rocket Atlas SLV-3C Centaur-D Payload: CSM 101 **Altimeter** Doppler and Altimeter radars **RDVS Similar Surveyor 6 Star tracker** Canopus **Landing camera** TV with polarizing filters	Autopilot	Moon - Tycho North Rim	Successful soft lander	Latitude 40.86° S, Longitude 348.53° E -	305.7 kg.	Slow speed about 3 m/s

Table 3. *Surveyor 7*

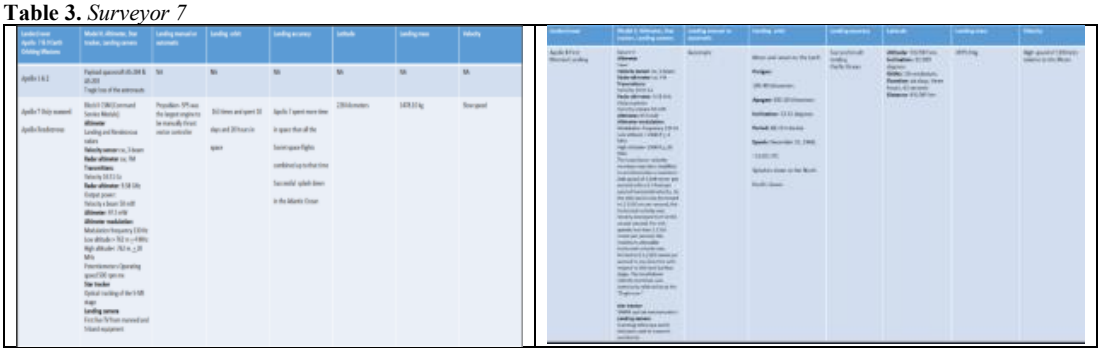

Table 4. *Apollo 1, 2, 7, & 8*

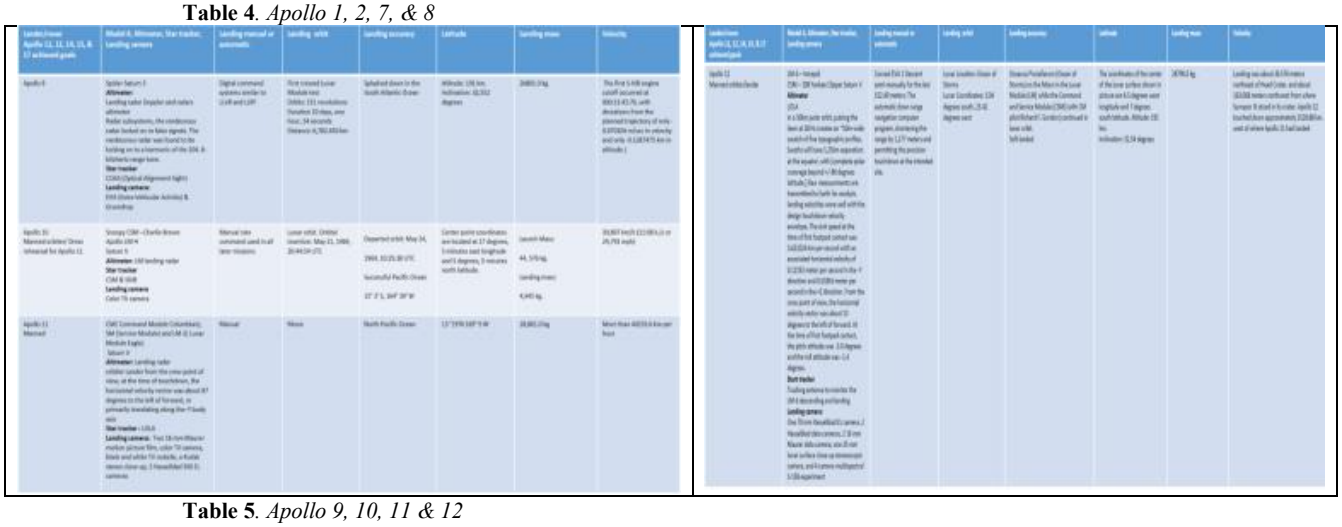

Table 5. *Apollo 9, 10, 11 & 12*

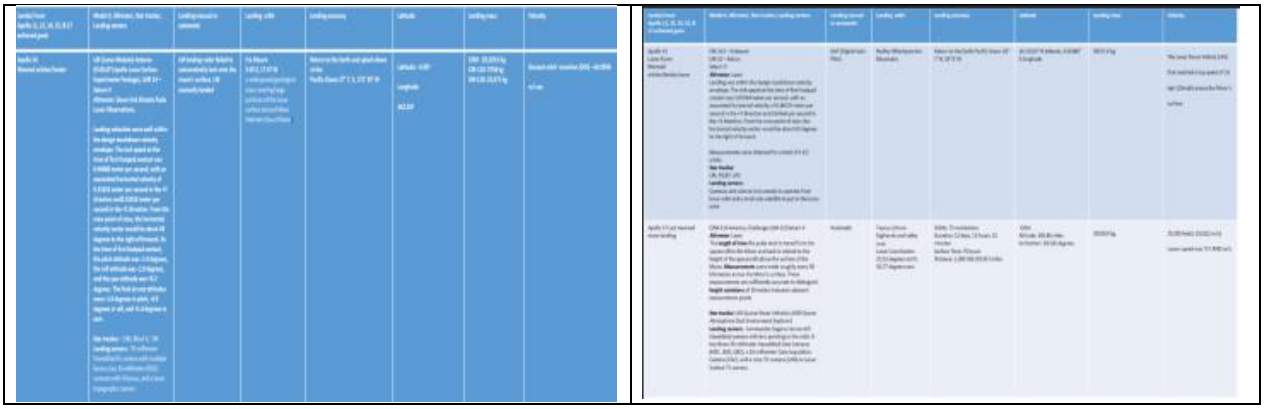

Table 6. *14, 15 & 17*

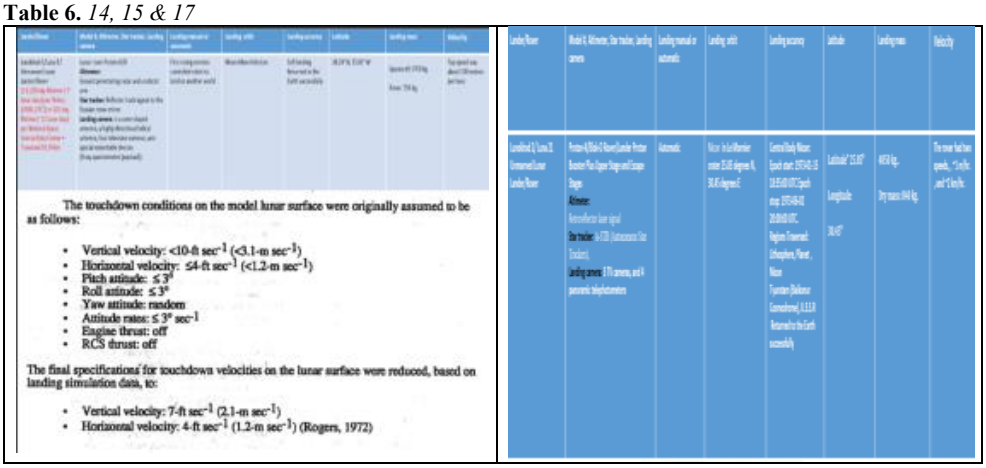

The touchdown conditions on the model lunar surface were originally assumed to be as follows:

- Vertical velocity: <10-ft sec^{-1} (<3.1-m sec^{-1})
- Horizontal velocity: ≤4-ft sec^{-1} (<1.2-m sec^{-1})
- Pitch attitude: ≤ 3°
- Roll attitude: ≤ 3°
- Yaw attitude: random
- Attitude rates: ≤ 3° sec^{-1}
- Engine thrust: off
- RCS thrust: off

The final specifications for touchdown velocities on the lunar surface were reduced, based on landing simulation data, to:

- Vertical velocity: 7-ft sec^{-1} (2.1-m sec^{-1})
- Horizontal velocity: 4-ft sec^{-1} (1.2-m sec^{-1}) (Rogers, 1972)

Table 7. *Lunokhod 1 & 2*

Table 8. *Chang'e 1, 2, & 3*

Acknowledgments

I would like to acknowledge the cooperation with the materials of the scientists that worked on the project ALHAT, JPL, LaRC and JCS to Doctor John M. Carson III (Johnson Space Flight Center), Logan Kennedy (Marshall Space Flight Center), and Dr. Greg Chavers (Marshall Space Flight Center) who made it possible to write this research paper. The knowledge acquired during the Faculty Fellowship at NASA Marshall Flight Space Center is indescribable all knowledge that fits in my profession in Computer Science and Technology as well as in Information Security.

I would like to thank NASA for the opportunity to research this work through the Faculty Fellowship program.

References

1. About Lunar CATALYST (2017). Retrieved from https://www.nasa.gov/lunarcatalyst/

2. Amzajerdian, F., Hines, G. D. Roback, V.E., Petway, L.B., Barnes, B.W., Brewster, P. F., Pierrottet, D.F. and Bulyshev, A. (2015). Advancing Lidar Sensors Technologies for Next Generation Landing Missions. Retrieved from http://hdl.handle.net/2060/20150006846

3. Angelo, Jr., J. A. (2009) THE FACTS ON FILE. SPACE AND ASTRONOMY HANDBOOK. Revised Edition. New York, NY: The Facts On File Inc

4. Anzalone, E. (2015). Space Technology: Game Changing Development Multi-spacecraft Autonomous. Retrieved from https://ntrs.nasa.gov/archive/nasa/casi.ntrs.nasa.gov/20150016173.pdf

5. Anzalone, E. & Chuang, J. (2016). Multi-Spacecraft Autonomous Positioning System/Network-Based Navigation. Retrieved from http://www.techbriefs.com/component/content/article/ntb/tech-briefs/machinery-and-automation/24087

6. Anzalone, E. (2013). Space Technology: Game Changing Development Multi-spacecraft Autonomous Positioning System (MAPS). Retrieved from https://ntrs.nasa.gov/archive/nasa/casi.ntrs.nasa.gov/20150016173.pdf

7. APL-NAV (2014). Retrieved from http://www.jhuapl.edu/OTT/technologies/featuredtech/aplnav/whatis.asp

8. APL-NAV (2014). Retrieved from http://www.lpi.usra.edu/lunar/missions/apollo/apollo_17/photography/http://www.jhuapl.edu/OTT/technologies/featuredtech/aplnav/history.asp

9. Apollo 17: Mission Objective (2011). Retrieved from https://www.nasa.gov/mission_pages/apollo/missions/apollo17.html

10. APOLLO 16 (AS-116): *Landing in the Descartes Highlands*. (2017). Retrieved from https://airandspace.si.edu/explore-and-learn/topics/apollo/apollo-program/landing-missions/apollo16.cfm

11. Apollo 16 16 Mission: Service Operations Overview (2017). Retrieved from https://airandspace.si.edu/explore-and-learn/topics/apollo/apollo-program/landing-missions/apollo16.cfmhttp://www.lpi.usra.edu/lunar/missions/apollo/apollo_16/surface_opp/

12. Apollo 16 Mission (2017), Retrieved from http://www.lpi.usra.edu/lunar/missions/apollo/apollo_16/photography/

13. Apollo 16: *Mission Objective* (2009). Retrieved from https://www.nasa.gov/mission_pages/apollo/missions/apollo16.html

14. Apollo 15 (2017). Retrieved from https://www.nasa.gov/mission_pages/apollo/missions/apollo15.html

15. APOLLO 14 Facts. (2017). Retrieved from https://airandspace.si.edu/explore-and-learn/topics/apollo/apollo-program/landing-missions/apollo14-facts.cfm

16. Apollo 14 Mission (2017). Retrieved from http://www.lpi.usra.edu/lunar/missions/apollo/apollo_14/photography/

17. Apollo 14 Data Collection Results. (2017) retrieved from https://nssdc.gsfc.nasa.gov/nmc/datasetSearch.do?spacecraft=Apollo%2016%20Command%20and%20Service%20Module%20(CSM)

18. APOLLO 13: *Facts* (2017). Retrieved from https://airandspace.si.edu/explore-and-learn/topics/apollo/apollo-program/landing-missions/apollo13-facts.cfm

19. Apollo 13 Mission (2017). Retrieved from http://www.lpi.usra.edu/lunar/missions/apollo/apollo_13/photography/

20. Apollo 13 "Houston, we've had a problem…" (2009). Retrieved from https://www.nasa.gov/mission_pages/apollo/missions/apollo13.html

21. Apollo 13, We Have a Solution: Part 3 (2005). Retrieved from http://spectrum.ieee.org/aerospace/space-flight/apollo-13-we-have-a-solution-part-3

22. Apollo 12 Mission: Landing Site Overview. (2017). Retrieved from http://www.lpi.usra.edu/lunar/missions/apollo/apollo_12/landing_site/

23. Apollo 12 Mission Photography. (2017). Retrieved from http://www.lpi.usra.edu/lunar/missions/apollo/apollo_12/photography/

24. Apollo 12 Mission (2017) Retrieved from http://www.lpi.usra.edu/lunar/missions/apollo/apollo_12/surface_opp/

25. Apollo 12 "The Pinpoint Mission…" (2015). Retrieved from https://www.nasa.gov/mission_pages/apollo/missions/apollo12.html

26. APOLLO 12. *Th e Sixth Mission: The Second Lunar Landing*. (1969). Retrieved from https://history.nasa.gov/SP-4029/Apollo_12a_Summary.htm

27. APOLLO TO THE MOON: *ABOUT THE SPACECRAFT* (2017). Retrieved from https://airandspace.si.edu/exhibitions/apollo-to-the-moon/online/apollo-11/about-the-spacecraft.cfm

28. APOLLO 11 LANDING SITE (2017). Retrieved from https://airandspace.si.edu/explore-and-learn/topics/apollo/apollo-program/landing-missions/apollo11-landing-site.cfm

29. APOLLO 11: The Fifth Mission: The First Lunar Landing. (1969). Retrieved from https://history.nasa.gov/SP-4029/Apollo_11a_Summary.htm

30. Apollo 10 Missions. (2009). Retrieved from https://www.nasa.gov/mission_pages/apollo/missions/apollo10.html

31. APOLLO 10: The Fourth Mission: Testing the LM in Lunar Orbit. (1969). Retrieved from https://history.nasa.gov/SP-4029/Apollo_10a_Summary.htm

32. APOLLO 9 (AS-504). (2017). Retrieved from https://airandspace.si.edu/explore-and-learn/topics/apollo/apollo-program/orbital-missions/apollo9.cfm

33. APOLLO9: *The Third Mission: Testing the LM in Earth Orbit* (1969). Retrieved from https://history.nasa.gov/SP-4029/Apollo_09a_Summary.htm

34. Apollo 8: *Missions* (2009). Retrieved from https://www.nasa.gov/mission_pages/apollo/missions/apollo8.html

35. APOLLO-SOYUZ TEST PROJECT (1975). Retrieved from https://history.msfc.nasa.gov/apollo/docs/Apollo-Soyuz_Press_Kit.pdf

36. Apollo 1: *Apolo 1 Tragedy*. (2017). Retrieved from https://www.nasa.gov/mission_pages/apollo/missions/apollo1.html

37. APOLLO 1 (AS-204): *Disaster on Pad 34.(2017)*. Retrieved from https://airandspace.si.edu/explore-and-learn/topics/apollo/apollo-program/orbital-missions/apollo1.cfm

38. Atkinson, J. (2016). Laser-based Navigation Sensor Could Be Standard for Planetary Landing Missions. Retrieved from NDL works as a standalone unit, but for the COBALT flight tests onboard Xodiac, the NDL will be coupled with a Lander Vision System (LVS) develop by NASA JPL

39. Autonomous Position and Navigation Network (2017). Retrieved from https://techtran.msfc.nasa.gov/patent/MFS-TOPS-64

40. Basilasky, A.T., Abdrakhimov, A.M., Head J.W., Pieters, C.M., Wu, Y. and Xiao, L. (2015). Geologic characteristics of the Luna 17/Lunokhod 1 and Chang'E-3/Yutu landing sites, Northwest Mare Imbrium of the Moon. Retrieved from http://www.planetary.brown.edu/pdfs/5083.pdf

41. Bell, J. Professor. MastCam-Z. (2017) Retrieved from *https://mars.nasa.gov/mars2020/mission/instruments/mastcam-z/)*

42. Browm. D. (2014). NASA Announces Mars 2020 Rover Payload to Explore the Red Planet as Never Before. Retrieved from https://mars.nasa.gov/news/nasa-announces-mars-2020-rover-payload-to-explore-the-red-planet-as-never-before

43. Carson III, J. M. Seubert, C.R., Amazajerdian, F. Bergh, C. Kourchians, A., Restrepo, C. I, Villalpando, C. Y., O'Neal, T.V., Robertson, E. A., Pierrottet, D.F., Hines, G.D., & Garcia, R. (2017). COBALT: Development of a Platform to Flight Test Lander GN&C Technologies on Suborbital Rockets (2017). Retrieved from https://arc.aiaa.org/doi/10.2514/6.2017-1496

44. Carson III, J. M. Robertson, E.A., Pierrottet, D. F., Roback, V. E., Trawny, N., Devolites, H.L., Hart, J., Estes, J.N. and Gadis, G.S. (2015). Preparation and Integration of ALHAT Precision Landing Technology for Morpheus Flight Testing. Retrieved from http://hdl.handle.net/20160/20140009928

45. Carson; J. M., Bailey, E.S., Trawny, N., Johnson, A.E., Roback, V.E, Amzajerdian, F., and Werner R.A. (2013). OPERATIONS CONCEPT, HARDWARE IMPLEMENTATION AND GROUND-TEST VERIFICATION OF A HAZARD DETECTION SYSTEM FOR AUTONOMOUS AND SAFE PRECISION LUNAR LANDING. Document sent by Dr. Carson via email.

46. Chang'e 3 – Mission Overview. (2017). Retrieved from http://spaceflight101.com/change/change-3/

47. Chang'e 2 (2017). Retrieved from https://directory.eoportal.org/web/eoportal/satellite-missions/c-missions/chang-e-2#spacecraft

48. Congiu, S. (2017). ALHAT Detects Landing Hazards on the Surface. Retrieved from https://www.nasa.gov/centers/langley/news/researchernews/rn_ALHAT.html

49. David, L. (2010) NASA Lunar Orbiter Spots Old Soviet Moon Landers. Retrieved from https://www.space.com/8062-nasa-lunar-orbiter-spots-soviet-moon-landers.html

50. Dick, J. Tu, M, Strejakivm D,m Brinbaum, K. & Yu, N. (2008). Optimal Phase Lock at Femtowatt Power Levels for Coherent Optical Deep-Space Transponder. Retrieved from https://tmo.jpl.nasa.gov/progress_report/42-175/175A.pdf

51. Dunfor, B. & Davis, P. (2017) Missions: Surveyor 4.retrieved from https://solarsystem.nasa.gov/missions/surveyor04

52. Duran, S., Chavers, G., Gaspar, T.A., Frederickson, S. Ambrose, R.). (2017). Resource Prospector Lander Software Development Plan. Retrieved from https://sharepoint.msfc.nasa.gov/sites/fppo/FP30/RESOLVE/_layouts/15/WopiFrame2.aspx?sourcedoc=/sites/fppo/FP30/RESOLVE/RESOLVE%20Lander/04.07%20-%20Flight%20Software/SDP/RP_Lander_SDP.docx&action=default

53. Fries, S.D. (2001). NASA Engineers and the Age of Apollo. Retrieved from https://history.nasa.gov/SP-4104.pdf

54. Howell, E. (2016). Lunokhod 1: 1st Successful Lunar Rover. Retrieved from https://www.space.com/35090-lunokhod-1.html

55. Howell, E. (2014). 3 Private Moon Lander Concepts Make NASA's Short List. Retrieved from https://www.space.com/25935-private-moon-landers-nasa-lunar-catalyst.html

56. Howell, E. (2012). Apollo 10: The Lunar Module Flies. Retrieved from https://www.space.com/17616-apollo-10.html

57. Jackson, J. (2005). The Interplanetary Internet: *NASA researchers quarrel over how to network outer space.* Retrieved from http://spectrum.ieee.org/telecom/internet/the-interplanetary-internet

58. Janson, S.W. and Welle, R. P. (2013). The NASA Optical Communication and Sensor Demonstration Program. Retrieved from http://digitalcommons.usu.edu/cgi/viewcontent.cgi?article=2918&context=smallsat

59. Johnson, A.E., Cheng, Y, Montgomery, J., Trawny, N., Tweddle, B. & Zheng, J. (2017). Real-Time Terrain Relative Navigation Test Results from a Relevant Environment for Mars Landing. Retrieved from https://trs.jpl.nasa.gov/bitstream/handle/2014/45631/14-5083_A1b.pdf?sequence=1

60. LePage, A. (2017). Surveyor 2: Things Don't Always Go As Planned. Retrieved from http://www.drewexmachina.com/2017/03/13/surveyor-2-things-dont-always-go-as-planned/

61. Loff, S. & Dunbar, B. (2015). Apollo 11 Mission Overview. Retrieved from https://www.nasa.gov/mission_pages/apollo/missions/apollo11.html

62. Loff, S. (2017). Looking Back: *Dr. George Carruthers and Apollo 16 Far Ultraviolet Camera/Spectrograph*.Retrieved from https://www.nasa.gov/image-feature/looking-back-dr-george-carruthers-and-apollo-16-far-ultraviolet-cameraspectrograph

63. Loff, S. (2015). Apollo Missions. Retrieved from https://www.nasa.gov/mission_pages/apollo/missions/index.html

64. Logan Jr. R. T. (2016) Ruggedized Photonic Transceivers for Spacecraft Datalinks. Retrieved from datalinks and under his permission made possible to help in the research investigation http://spacewire.esa.int/content/Home/HomeIntro.php
DOI: 10.1109/SpaceWire.2016.7771598Mohon, L (2017).

65. McGee, T., J. Artis, D. T. Cole, D. Eng, C. Reed, M. Hannan, D. G. Chavers, L. Kennedy, J. Moore & C. Stemple. 2012. "Mighty Eagle: The Development and Flight Testing of an Autonomous Robotic Lander Test Bed," Johns Hopkins APL Technical Digest, Volume 32, Number 3, December 2013.

66. Murphy, M (2014). Fresh Eyes on Mars: *Mars 2020 Lander Vision System Tested through NASA's Flight Opportunities Program.* Retrieved from https://www.nasa.gov/centers/armstrong/features/fresh_eyes_on_mars.html)

67. NASA Goddards (2016). Mars Ancient Ocean. Retrieved from https://www.youtube.com/watch?v=oC31pqk9sak

68. NASA Technologies Roadmaps: TA5: Communication, Navigation, and Orbital Debris Tracking and Characterization Systems (2015). Retrieved from https://www.nasa.gov/sites/default/files/atoms/files/2015_nasa_technology_roadmaps_ta_5_communication_and_navigation_final.pdf

69. NASA make water on Moon and oxygen on Mars (2014). Retrieved from http://www.ndtv.com/world-news/nasa-to-make-water-on-moon-and-oxygen-on-mars-549294

70. NASA Selects Partners for U.S. Commercial Lander Capabilities. (2014) Retrieved from https://www.nasa.gov/press/2014/april/nasa-selects-partners-for-us-commercial-lander-capabilities/

71. Nelson, J. (2017). Mission to Moon Ranger 9. Retrieved from https://www.jpl.nasa.gov/missions/ranger-9/

72. Nelson, J. (2017). Mission to Moon Ranger 8. Retrieved from https://www.jpl.nasa.gov/missions/ranger-8/

73. Nelson, J. (2017). Mission to Moon Ranger 7. Retrieved from https://www.jpl.nasa.gov/missions/ranger-7/

74. Nelson, J. (2017). Mission to Moon Ranger 6. Retrieved from https://www.jpl.nasa.gov/missions/ranger-6/

75. Nelson, J. (2017) Mission to Moon Ranger 5. Retrieved from https://www.jpl.nasa.gov/missions/ranger-5/

76. Nelson, J. (2017) Mission to Moon Ranger 4; Retrieved from https://www.jpl.nasa.gov/missions/ranger-4/

77. Nelson, J. (2017) Mission to Moon: Ranger 3. Retrieved from https://www.jpl.nasa.gov/missions/ranger-3/

78. Nelson, J. (2017) Mission to Moon: Ranger 2. Retrieved from https://www.jpl.nasa.gov/missions/ranger-2/

79. Nelson, J. (2017) Mission to Moon: Ranger 1 Retrieved from https://www.jpl.nasa.gov/missions/ranger-1/

80. Nelson, J. (2017). Missions to Moon: *Surveyor*. Retrieved from https://www.jpl.nasa.gov/missions/surveyor-1/

81. Nelson, J. (2017). Missions to Moon: Surveyor 7. Retrieved from https://www.jpl.nasa.gov/missions/surveyor-7/

82. Nelson, J. (2017) Mission to Moon: Surveyor 5. Retrieved from https://www.jpl.nasa.gov/missions/surveyor-5/

83. Nelson, J. (2017) Missions to Moon Surveyor 4. Retrieved from https://www.jpl.nasa.gov/missions/surveyor-4/

84. Nelson, J. (2017). Missions to Moon Surveyor 2. Retrieved from https://www.jpl.nasa.gov/news/news.php?feature=6523

85. Nelson, J. (2017)Mission to Moon Surveyor 1. Retrieved from https://www.jpl.nasa.gov/missions/surveyor-1/

86. Optical Communications (2014). Retrieved from https://www.nasa.gov/directorates/heo/scan/engineering/technology/txt_opticalcomm_start.html

87. Optical Communication (2012). Retrieved from https://www.nasa.gov/directorates/heo/scan/engineering/technology/txt_opticalcomm.html

88. Phillips, T. (2005). En Route to Mars, the Moon. Retrieved from https://www.nasa.gov/vision/universe/solarsystem/18mar_moonfirst.html

89. Project Apollo 7 (1968) Retrieved from https://history.nasa.gov/alsj/a410/A07_PressKit.pdf

90. Procharzka, I. Hamal, L & Pershing=, S. M. (2017). Solid State Detector Package for the Mars Laser Transponder. Retrieved from https://www.researchgate.net/profile/Ivan_Prochazka/publication/229008212_Solid_state_detector_package_for_the_Mars_laser_transponder/links/0912f51126238d3760000000/Solid-state-detector-package-for-the-Mars-laser-transponder.pdf

91. Pyle, R. (2016). Fifty Years of Moon Dust: Surveyor 1 was a Pathfinder for Apollo. Retrieved from https://www.jpl.nasa.gov/news/news.php?feature=6523f

92. Rice, J. S. (2017). NASA-TBD Lander Design Data Book. Retrieved from https://sharepoint.msfc.nasa.gov/sites/fppo/FP30/RESOLVE/_layouts/15/WopiFrame.aspx?sourcedoc=/sites/fppo/FP30/RESOLVE/RESOLVE%20Lander/02%20-%20Lander%20Systems%20Engineering/Data%20Book/Integrated%20Data%20Book-Taiwan.docx&action=default

93. Rush, J., Israel, D., Ramos, C. Deutsch, L.. Dennehy, N. & Seibert, M. (2010). DRAFT Communication And Navigation Systems Roadmap: *TECHNOLOGY AREA 05*. Retrieved from https://www.nasa.gov/pdf/501623main_TA05-CommNav-DRAFT-Nov2010-A.pdf

94. Ryba, J.(2009). Apollo 7: Mission Objectives. Retrieved from https://www.nasa.gov/mission_pages/apollo/missions/apollo7.html

95. Sensors Advance Lunar Landing Project (2017) Retrieved from https://www.nasa.gov/exploration/home/alhat-project.html

96. SP 200: *Space Exploration Tools*. (2017). Retrieved from http://pages.erau.edu/~ericksol/courses/sp200/exploration_tools.html

97. Taylor, J., Sakamota, L. & Jen Wong, -C (2002). Cassini Orbiter/Huygens Probe Telecommunications. Retrieved from https://descanso.jpl.nasa.gov/DPSummary/Descanso3--Cassini2.pdf

98. The Legend of Chang E. (2017). Retrieved from http://www.moonfestival.org/the-legend-of-chang-e.html

99. This Week in NASA History: *Apollo AS-203 Launches—July 5, 1966.* Retrieved from https://www.nasa.gov/centers/marshall/history/this-week-in-nasa-history-apollo-as-203-launches-july-5-1966.html

100. Wessen, A. (2017). Chang'e 1: In Depth. Retrieved from https://solarsystem.nasa.gov/missions/change1/indepth

101. Wessen, A. (2017). Luna 17?Lunokhod 1: In Depth. Retrieved from https://solarsystem.nasa.gov/missions/luna_17/indepth

102. Wessen, A. (2017). Luna 21/Lunokhod 2: In Depth. Retrieved from https://solarsystem.nasa.gov/missions/luna_21/indepth

103. Wilson, J. (2015). NASA History Overview. Retrieved from https://www.nasa.gov/content/nasa-history-overview

104. Williams, D. R. (2017). Apollo 17 Command and Service Module (CSM). Retrieved from https://nssdc.gsfc.nasa.gov/nmc/masterCatalog.do?sc=1972-096A

105. Williams, D.R. (2017) Chang'e 5-T1. Retrieved from https://nssdc.gsfc.nasa.gov/nmc/spacecraftDisplay.do?id=2014-065A

106. Williams, D.R. (2017). Chang'e 1. Retrieved from https://nssdc.gsfc.nasa.gov/nmc/spacecraftDisplay.do?id=2007-051A

107. Williams, D. R. (2017). Chang'e 3 Rover. Retrieved from https://nssdc.gsfc.nasa.gov/nmc/spacecraftDisplay.do?id=2013-070C

108. Williams, D. R. (2016). Chronology of Lunar and Planetary Exploration. Retrieved from https://nssdc.gsfc.nasa.gov/planetary/chronology.html#2015

109. Williams, D. R. (2017). Luna 21?Lunokhod 2. Retrieved from https://nssdc.gsfc.nasa.gov/nmc/spacecraftDisplay.do?id=1973-001ALuno

110. Williams, D.R. (2017). Ranger 6. Retrieved from https://nssdc.gsfc.nasa.gov/nmc/spacecraftDisplay.do?id=1964-007A

111. Williams, D.R. (2017) Ranger 9. Retrieved from https://nssdc.gsfc.nasa.gov/nmc/spacecraftDisplay.do?id=1965-023A

112. Williams, D.R. (2017) Ranger 8. Retrieved from https://nssdc.gsfc.nasa.gov/nmc/spacecraftDisplay.do?id=1965-010A

113. Williams, D. R. (2017). Ranger 5. Retrieved from https://nssdc.gsfc.nasa.gov/nmc/spacecraftDisplay.do?id=1962-055A

114. Williams , D.R. (2017). Ranger 4. Retrieved from https://nssdc.gsfc.nasa.gov/nmc/spacecraftDisplay.do?id=1962-012A

115. Williams, D.R. (2017). Ranger 3. Retrieved from https://nssdc.gsfc.nasa.gov/nmc/spacecraftDisplay.do?id=1962- 001A

116. Williams, D.R. (2017). Ranger 2. Retrieved from https://nssdc.gsfc.nasa.gov/nmc/spacecraftDisplay.do?id=1961-032A

117. Williams, D.R. (2017). Ranger 1. Retrieved from https://nssdc.gsfc.nasa.gov/nmc/spacecraft

118. Williams, D.R. (2017). Surveyor 7. Retrieved from https://nssdc.gsfc.nasa.gov/nmc/spacecraftDisplay.do?id=1968-001A

119. Williams, D.R. (2017. Surveyor 6. Retrieved from https://nssdc.gsfc.nasa.gov/nmc/spacecraftDisplay.do?id=1967-112A

120. Williams, D.R. (2017) Surveyor 5. Retrieved from https://nssdc.gsfc.nasa.gov/nmc/spacecraftDisplay.do?id=1967-084A

121. Williams, D.R. (2017). Surveyor 3. Retrieved from https://nssdc.gsfc.nasa.gov/nmc/spacecraftDisplay.do?id=1967-035A

122. Williams, D.R. (2017) Surveyor 1. Retrieved from https://nssdc.gsfc.nasa.gov/nmc/masterCatalog.do?sc=1966-045A

123. Williams, D. R. (2006). Surveyors (1966-1968). Retrieved from https://nssdc.gsfc.nasa.gov/planetary/lunar/surveyor.html

Application of Temperature-Controlled Thermal Atomization for Printing Electronics in Space

Chih-Hao Wu[1] and Furman V. Thompson[2]
NASA Marshall Space Flight Center, Huntsville, AL, 35812

Additive Manufacturing (AM) is a technology that builds three dimensional objects by adding material layer-upon-layer throughout the fabrication process. The Electrical, Electronic and Electromechanical (EEE) parts packaging group at Marshall Space Flight Center (MSFC) is investigating how various AM and 3D printing processes can be adapted to the microgravity environment of space to enable on demand manufacturing of electronics. The current state-of-the art processes for accomplishing the task of printing electronics through non-contact, direct-write means rely heavily on the process of atomization of liquid inks into fine aerosols to be delivered ultimately to a machine's print head and through its nozzle. As a result of cumulative International Space Station (ISS) research into the behaviors of fluids in zero-gravity, our experience leads us to conclude that the direct adaptation of conventional atomization processes will likely fall short and alternative approaches will need to be explored. In this report, we investigate the development of an alternative approach to atomizing electronic materials by way of thermal atomization, to be used in place of conventional aerosol generation and delivery processes for printing electronics in space.

I. Introduction

In addition to the numerous historically established technology accomplishments, there are four major research thrust areas of engineering and science developments at National Aeronautics and Space Administration (NASA) and Marshall Space Flight Center (MSFC) that draw the world's attention: Propulsion, Friction Stir Welding, CubeSats and Additive Manufacturing. In the field of Additive Manufacturing technology, the most current and established practices are implementing plastic Fused Deposition Modeling (FDM) and selective laser melting (SLM) based Additive Manufacturing processes for the generation of plastic and metal parts discretely. The Marshall team in collaboration with various other NASA centers is primarily focusing on using this AM technology to create functional electronic parts, giving birth to a focus area defined as Additive Electronics Manufacturing (AEM). The purpose of this area is to foster the capability to produce on-demand self-sustaining electronic/avionics parts that could be used for ISS research and/or onboard deep space exploration vehicles such as Space Launch System (SLS) and Orion. To accomplish this objective, Marshall is investigating, improving, and developing various terrestrial printing technologies and adapting them for use in microgravity. One of the most common practices utilized on electronics printers and spray deposition systems today is pneumatic or ultrasonic atomization. While these systems and processes reign supreme in a terrestrial environment, we predict that their performance will be limited due to lessons learned from ISS research over the years about the physics of fluids in microgravity. For the sake of this report Aerosol Jet Technology was investigated as a candidate process to baseline predictions going forward. Aerosol Jet® (AJ) printing is capable of printing fine, scalable, controlled depositions of conductive nano-particle fluid inks to create functional, geometrically complex, and robust avionics parts. In this report, we focus on the development of a novel approach for the aerosol mist generation of conductive ink and non-conductive ink utilizing a localized heating element through a conventional vaping device.

II. The Description of Different Atomization Processes of Aerosol Jet® Printing

NASA MSFC has an Optomec Aerosol Jet® Deposition System 300 as shown in Figure 1. This machine is capable of generating aerosol mist that contains functional electronic material inks to deposit onto various substrates to produce functional electronic parts. Currently, there are two major methods within this system to generate aerosol mist: a pneumatic atomization process and an ultrasonic atomization process. In the text to follow, we will give a brief

[1] Summer Faculty Fellow, EEE Parts Packaging (ES43), NASA MSFC, Harding University.
[2] Focus Area Champion, EEE Parts Packaging (ES43), Huntsville, AL, 35812, NASA MSFC.

description of each atomization process. Furthermore, we will introduce the development of an alternative approach for mist generation of conductive and non-conductive ink through a localized heating element of a conventional vaping device.

Figure 1. Optomec Aerosol Jet® printer 300 (AJ 300) Series Located at MSFC

(a) The Pneumatic Atomization Process method

The NASA MSFC Aerosol Jet® printer (AJ 300) has traditionally used a pneumatic atomization process. The mist generation is accomplished by supplying external air pressure to an atomizing reservoir known as the pneumatic atomizer. Within the reservoir the device that performs the atomization functions by blowing the externally supplied air at high speed across the top of an open vertical channel that is submerged in the liquid. This high speed air blowing past the top of the submerged channel satisfies Bernoulli's principle creating a high velocity low pressure condition at the top of the channel and a low velocity high pressure condition at the bottom of the channel where the liquid ink exists. Fluid inks in this case flow from high to low pressure resulting in ink materials of low to high viscosity (0-1000 c.P.) to be drawn up the channel and atomized as they converge with the high velocity air moving across the top of the channel. The aerosol mist that is generated continues to expand until it completely fills the open volume within the atomizer reservoir and exits through the output port on to the next stage in printing. From this point in the process we can predict that under microgravity conditions of no hydrostatic pressure, buoyancy, and weight the fluid in the reservoir will not be contained and will not remain in continuous contact with the atomizer device. It is likely that the fluid will have no separation and exist as a single large body moving around within the open volume of the container. Potentially this single body of fluid could migrate and contact the output port and be pushed out of the reservoir completely from the rising air pressure and bypass atomization all together. This would decrease the overall continuous print consistency. Therefore, modification to this configuration or alternative means to atomize the liquid inks for delivery to the next stage in printing must be investigated.

(b) The Ultrasonic Atomization Process method

The process involving ultrasonic atomization for the AJ 300 is to utilize ultrasonic waves to aerosolize the conductive nanoparticle ink material. The limitation to this atomization process is the low viscosities of the ink material that could be used in the aerosolizing process. The typical viscosity value for ultrasonic atomization is usually 20 c.P. or less, which is fairly low in comparison to pneumatic atomization. In many aerospace printed electronics applications where the parts require higher concentration of metal content, this is not ideal.

In this atomization process, the conductive ink has been injected into an atomization vial and positioned over a transducer. The principle is that the transducer produces a sound wave that vibrates at ultrasonic frequencies. This high-energy ultrasonic wave then generates small perturbations to break up small droplets from the ink surface. For the best practice to generate efficient atomization, the use of a coupling fluid (usually temperature controlled deionized water) facilitates the transfer of ultrasonic energy from the transducer to the atomization vial in contact with the material. As the small aerosol droplets are ejected from the surface of the ink and fill the ultrasonic glass reservoir a glass tube provides a direct exit path from the vial to the print head for deposition. The configuration of this ultrasonic atomization system works well in laboratory environments on earth but presents fundamental challenges in microgravity. Again at this point we can predict that technical modification or alternative atomization techniques will need to be explored to enable this technology for use in microgravity.

III. The Development of an Alternative Atomization Process for Microgravity

As a result of years of research in fluid science in both standard gravity and microgravity environments, basic phenomena can be used to anticipate the systems that will need to be developed to enable the production of fluid based electronics in space processing. One of the shared advantages that microgravity provides that is also available on earth is the principle of capillary action. In this work, capillary action is used as a means to wick/draw up the fluid ink from a sealed reservoir creating a more controllable delivery mechanism than the reservoirs mentioned previously. The ink can be trapped and packaged in a sealed reservoir that only allows the fluid to escape by means of capillary action through a custom designed wick of varying materials. In this proposed thermal atomization system the fluid is wicked out of the reservoir and delivered to the surface of metal coils to be atomized. The metal coils are wrapped around the wick and are heated by a temperature controlled power supply. When the temperature of the coils approach the boiling point of the solvent and liquid binders in the inks, they begin to atomize and expand freely, thereby creating an alternative thermal atomization process to generate mist for printing. This thermal wicking system serves as the foundation for the first step in enabling an alternative atomization process in microgravity.

The Description of the device

(1) Power Supply

We purchased a commercial product (SMOK OSUB 40W 1350mAh) as the power supply for the atomization process. The particular power supply model is shown in Figure 2. This is a OSUB Mod, which is a medium size power supply marketed for commercial vaping devices. In our experiments, the power usage was set to 27.5 watts. In addition, the supply has an adjustable temperature, micro USB port and OLED display for ergonomic purposes. The OSUB Mod supply has dimensions of 75 mm in depth, 25 mm in height and 54.5 mm in width. The temperature range is between 200 degrees and 600 degrees Fahrenheit and the voltage range is between 0.8V to 9.0V.

Figure 2. The Power Supply purchased for the thermal atomization process

(2) Rebuildable Dripping Atomizer (RDA)

The HCigar Legend V2 RDA was chosen and recommended by the vape shop experts as being ideal for this experiment. As seen in Figure 3, the RDA was chosen to provide an open platform where custom coils and wicks could be designed and built enabling virtually unlimited configurations of the atomizer setup.

Figure 3. The RDA purchased for the thermal atomization process

The RDA was manufactured from 304 stainless steel, Delrin insulator and O-rings, and solid copper pins. It has dimensions of 22 mm in depth, 46 mm in height and 22 mm in width. The total product weight for the RDA is 48 grams. It has a removable SS 510 drip tip and finned top design. It also has deep juice well and 510 threading connection. It processes adjustable 510 copper center screw and 22 mm overall diameter. Large air flow options allow for our dual coil setup and wide range air flow from low volume to massive intake volume, as in our case, was needed. Huge holes cross drilled through the post allow for flexible coil building, using a variety of wire gauges and creative building techniques. As can be seen in Figure 4, we build our two coils using Kanthal wires, carefully constructed so that the actual wires were not touching each other to avoid an electrical short circuit.

Figure 4. The Internal structure of the RDA for the thermal atomization process

(3) The resistive coil

Figure 5. The conventional pre-made resistive coil for the RDA of the thermal atomization process

The design of the temperature control atomizing device involved optimizations of the following parameters: temperature coefficient of the wire, power consumption of the module, and coil resistance. The electrical temperature coefficient describes the change of resistance with respect to a temperature change. The higher the wire resistance temperature coefficient, the higher the accuracy of the temperature control. In our current experiment, the design concept for the development of a novel approach for mist generation of conductive ink and non-conductive ink through a localized heating element of a vaping device, we focused on using “Kanthal” wire, shown in Figure 6.

Figure 6. The Kanthal wire used to build a custom resistive coil of the RDA

We use Kanthal wire because it has low relative resistance change over increased temperature. This particular characteristic provides us a constant flow of aerosol. To enable an accurate temperature measurement, precise measurement of resistance is necessary. The power setting with temperature control enabled defines the maximum power that the temperature algorithm may apply to the coil. This is only true during the heat up phase at the beginning of the mist generation until the temperature has reached the set point. In general, in order to create a large amount of aerosol mist, the design concept adopted was to use thick wire and a high power setting.

(4) The wicking material

The wicking materials we experimented with are: Traditional cotton, Japanese Rayon cotton, and Silica, as illustrated in Figure 7 (a) (b) and (c). The silica wick is an amorphous material and has a dry burn characteristic. For the purpose of aerosol generation of the final conductive ink material, this wick proved superior to the conventional wicking material used for vaping, such as cotton. Silica wick is a mineral wick which does not break down like organic material. Our initial experiments using a cotton wick with conductive silver ink demonstrated that the cotton sintered with nanoparticle ink due to heat and became conductive, halting the atomization process.

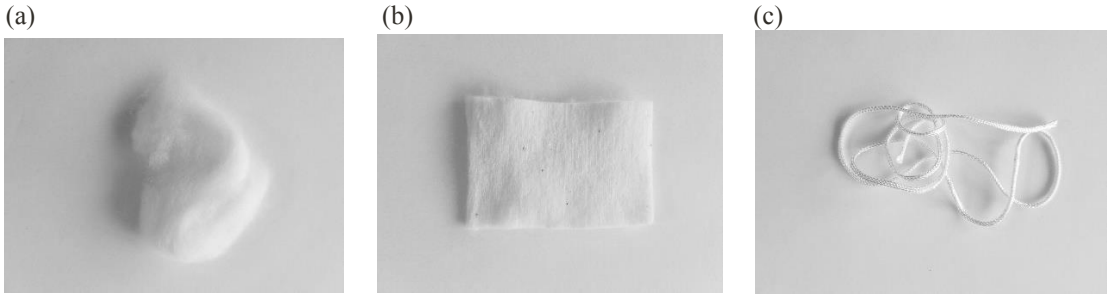

Figure 7. (a) Traditional Cotton (b) Japanese Rayon cotton and (c) Silica Wick

(5) The fluid to be aerosolized

We experimented with thermal atomization of vegetable glycerin, polyimide and conductive silver ink as illustrated in Figure 8 (a) (b) and (c).

Figure 8. (a) Vegetable Glycerin (b) Nexolve® Polyimide and (c) Novacentrix® Conductive Ink

The boiling point for vegetable glycerin is between 188-190 degree Celsius. For the conventional vaping process, the chemical reaction is an incomplete combustion reaction. In a commercially available vaporizer, the concepts are to combine vegetable glycerin and flavor molecule into the vapor phase. In our experiment, we use USP-Kosher, food grade, non-GMO, palm derived pure vegetable glycerin with 1.7% minimum purity, and with no added flavor. The vapor phase serves as the aerosol droplet we are attempting generate. We use glycerin for a proof of concept to validate the functionality of our custom made Kanthal wire and silica wick. We then use the same device on polyimide fluid and finally conductive nanoparticle ink fluid. We begin this task by heating up a very high-temperature resistor coil. The general principle of thermal atomization is that heat transfer happens quickly and a large amount of liquid will be vaporized. One potential problem is that the high temperature heat source in the presence of oxygen can result in at least some of the liquid reaching combustion temperature instead of just vaporizing. Hydrocarbons in the vegetable glycerin molecule are partially oxidized. If the combustion process is complete, then only water and carbon dioxide will be the end product. When the combustion is incomplete, formaldehyde and acetaldehyde are formed.

We next attempted the thermal atomization of Polyimide using our thermal wick. The Polyimide material we use to atomize is Nexolve® CP1 Polyimide, a high performance material which has been widely used in display technology, space structures, thermal insulation and advanced composites. This material provides superior physical and electrical properties over a wide range of temperature and in a number of harsh environments. The polyimide liquid is shown in Figure 8 (b). The Nexolve® CP1 we are using is available in the form of continuous rolls, sprayable resin, castable resin, raw powder and optical film. We chose the sprayable resin with NMP solvent. Our polyimide CP1 Fluid has 6.06% solid loading and viscosity of 78 c.P. The conductive ink we used is from Novacentrix® Metalon® HPS 030-AE1. It is a water-based aerosol sprayable silver flake ink with viscosity between 130-180 c.P. and specific gravity of about 2.0. The silver content is 55% by weight. Figure 8 (c) shows Novacentrix® Metalon® HPS 030-AE1.

(6) Experimental Results

We were able to generate the aerosol mist using all three of the candidate materials: vegetable glycerin, polyimide and conductive ink. Figure 9 illustrates the aerosol generation of (a) conventional vegetable glycerin (b) polyimide and (c) conductive ink.

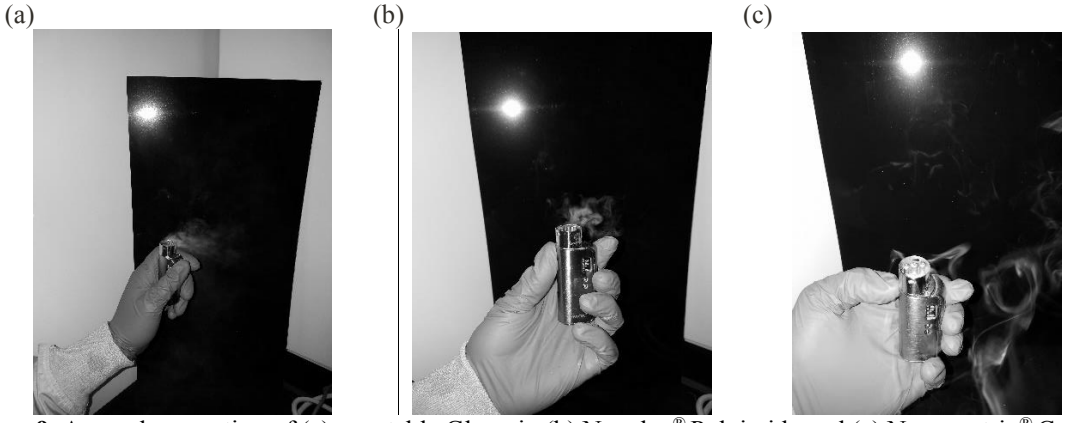

Figure 9. Aerosol generation of (a) vegetable Glycerin (b) Nexolve® Polyimide and (c) Novacentrix® Conductive Ink

III. Prediction of Fluid Behavior in Microgravity

Microgravity is defined as the acceleration conditions that exist on a reference frame in which the Earth's gravitational force is almost entirely balanced by the inertial force. The peculiar behavior of fluids in a microgravity environment motivate numerous Material Science and Life Science experiments in orbit. A number of basic phenomena may be identified which have a direct and/or indirect influence on the fluid behavior, and which could be exploited to improve a number of space processes (Monti and Savino 1997) as illustrated in following Table 1. [6]

Basic Phenomena in zero-g	Consequences in fluid phases	Utilization in space processing
No hydrostatic pressure	Large Interfaces, Large drops, Large liquid bridges Constant pressure in liquid specimens	Containerless processing, Undercooling in drops, Critical point experiment
No buoyancy	No separation between Phases or components	Metal synthesis, Miscibility gap
No natural convection (thermal/concentration)	Purely diffusive processes in the presence of temperature and/or concentration gradients	Growth from melts, from solution, as well as vapor, Precise measurement of fluid properties, Combustion, Dendrite growth
Reduced importance of gravitational effects	Separation effects due to: Marangoni flow, Thermal radiation forces Electromagnetic forces, wetting	Bubble/drops Marangoni migration, boiling, Bubble measurement, Floating zone refining
No weight		Large, soft crystal growth, large fractal structures, Arrogates of cosmic dust

Table 1 The role of fluid behavior in physical science experiment [6]

IV. Conclusion

We presume that ink reservoirs that are open and do not confine the liquid to stay in contact with the atomizer or fluid delivery mechanism will be ineffective in microgravity. The use of pressurized cartridges or capillary action based material delivery techniques will function as feasible alternatives. Further research is required to better understand the separation effects of liquid inks and their surface interactions during processes such as ultrasonic, pneumatic, and thermal atomization. Systems that direct and consolidate the mist after atomization will also need to be investigated to prove that the fundamental mechanisms they rely on are still functional in a microgravity setting. An overarching goal of this work is to serve as a starting point, forming a foundation for future applied research that will enable in-space manufacturing of electronics in a greater capacity.

The purpose of this project was not to rule out the possibility of using pneumatic and ultrasonic atomization based deposition systems in space, but to shed light on the need for alternative approaches to atomize and manipulate materials in future in-space manufacturing (ISM) processes. Enabling the capability to produce electronics on demand in space will reap enormous benefits that will enable NASA to explore in ways that were not previously possible. The potential new space-based electronics/avionics products will be in a class of their own and will serve to support the extraterrestrial technology markets of tomorrow. If these processes and technologies are supported in the early stages the potential payoff could enable a standard of living in space and on earth that would support longer duration deep space exploration, habitation, and sustainability.

Acknowledgments

I appreciate the opportunity to work with my mentor Furman Thompson and thank him for his excellent guidance, motivation and support.

References

[1]Snyder, M. P., Dunn, J. J., Gonzales, E. G., "Effect of Microgravity on Extrusion Based Additive Manufacturing", *American Institute of Aeronautics and Astronautics Space 2013 Conference and Exposition,* San Diego, CA. September 10-12, 2013.

[2]Sunol, F., Gonzalez-Cinca, R., Liquid Jet Breakup and Subsequent Droplet Dynamics Under Normal Gravity and in Microgravity Conditions. *Physics of Fluids 2, 077102.* (2015).

[3]Gibson, I., *Additive Manufacturing Technologies*, 2nd edition, Springer, New York, 2015.

[4]Prater, T. J., Bean, Q. A., Beshears, R. D., Rolin, T. D., Werkheiser, N. J., Ordonez, E. A., Ryan, R. M., Ledbetter, F. E., "Summary Report on Phase I Results From 3D Printing in Zero-G Technology Demonstration Mission, Volume I, NASA/TP-2016-219101, Marshall Space Flight Center, Huntsville, Alabama.

[5]Aerosol Jet and Optomec are trademark of Optomec, Inc.

[6]Monti, R., Physics of Fluid in Microgravity, Taylor and Francis, New York, 2001.

[7]Lappa, M., Fluids, Materials & Microgravity-Numerical Techniques and Insights into Physics, Elsevier, Oxford, 2004.

Composite Payload Attach Fitting

2017 NASA Marshall Space Flight Center
Summer Faculty Fellowship Final Report

Charles Yang[1]
Wichita State University, Wichita, KS 67260

Justin R. Jackson[2] *and* William E. Guin[3]
NASA Marshall Space Flight Center, Huntsville, AL 35811

A composite Payload Attach Fitting (PAF) is being designed and fabricated at NASA Marshall Space Flight Center for the Block 1B heavy-lift Space Launch System (SLS). Functions as the primary structural interface between the payload and the body of the lunch vehicle, the PAF is a cone-shaped structure of about 25 feet in diameter, 11 feet in length, and consists of eight longitudinal segments of curved composite honeycomb sandwich panels. The PAF is connected to the payload at the forward end and to the body of the launch vehicle at the aft end by metal clevis fittings. The objectives of this study are to analyze the internal and support forces of the PAF under axial and pressure loads, analyze the pinned joint strength of the composite honeycomb sandwich panels, and analyze/design test configurations of the metal fittings. The results show that the stress due to bending moment in the PAF at the forward end is comparable in magnitude to the stress due to membrane force. The reaction moment at the forward end also has a large magnitude which should not be overlooked when designing the fitting and the joint. The simple formula using the projected bearing area of the pin hole and the assumption of a uniform bearing stress predicts the pin-bearing capacity of the composite honeycomb sandwich panels reasonably well based on the limited test data.

Nomenclature

d	=	diameter of fastener
F	=	applied force
F_{failure}	=	applied force at failure
$F_{\text{f,test}}$	=	test data of applied force at failure
h	=	thickness of the PAF composite honeycomb sandwich panel
$RF1$	=	reaction force in the meridional direction
$RF2$	=	reaction force in the hoop direction
$RM3$	=	reaction moment about the hoop direction
$SF1$	=	membrane force per unit width in the meridional direction
$SF2$	=	membrane force per unit width in the hoop direction
$SM1$	=	bending moment per unit width about the hoop direction
$SM2$	=	bending moment per unit width about the meridional direction
t	=	thickness of composite laminate
z	=	coordinate in the transverse direction with the origin at the mid-plane
σ_{11}	=	membrane stress in the meridional direction
σ_{22}	=	membrane stress in the hoop direction
$\sigma_{\text{c,allowable}}$	=	allowable compressive stress of composite laminate

[1] Professor, Department of Aerospace Engineering, MSFC Faculty Fellow
[2] Materials Engineer, EM 42, MSFC Collaborator
[3] Materials Engineer, EM 42

I. Introduction

Due to the high strength-to-weight ratio compared to traditional metallic materials, advanced composite materials have gained attention from aircraft/spacecraft designers in the past decades. Research and development efforts as well as experience have gradually pushed the applications of advanced composite materials from secondary, non-essential parts such as cosmetic aircraft interior panels to primary load-carrying structures such as the all-composite fuselage of Boeing 787 and Airbus A350, just to name a few. NASA's intension to take advantage of the benefits from advanced composite materials can be seen from the Composite Crew Module (CCM) constructed from 2006 for the Constellation Program Crew Exploration Vehicle. Even though the CCM was not actually adopted for any space exploration projects, the technologies industry gained have assisted in future composites applications.

NASA's current heavy-lift Space Launch System program is aiming at sending astronauts and/or payloads to cis-lunar space as well as to Mars and other deep-space destinations in the 2020s. Part of the new flight hardware development of the SLS program is the honeycomb sandwich composite Payload Attach Fitting (PAF). As shown in Fig. 1, the PAF is a cone-shaped structure used to connect the payload to the body of the launch vehicle. The main function of the PAF is to support the weight and inertia force during launch and deployment of the payload. Based on the current design, the forward end of the PAF is about 60 inches in diameter while the aft diameter is about 320 inches. The PAF is fabricated by automated fiber placement process and each one-eighth of the PAF is laid-up and autoclave cured individually. The eight segments are then joined with a double-lap configuration in the longitudinal direction to complete the PAF. The PAF is joined to the payload on the forward end and to the launch vehicle body on the aft end via metal fittings. Figure 2 shows the schematic of a metal clevis fitting at the forward end.

The purpose of this study is threefold: (1) obtain the internal and support forces of the PAF for the design of longitudinal joints within the PAF and for the design of the metal fittings, (2) predict the pin-bearing capacity of the composite honeycomb sandwich panel, and (3) analyze/design the test specimen for the metal clevis joints.

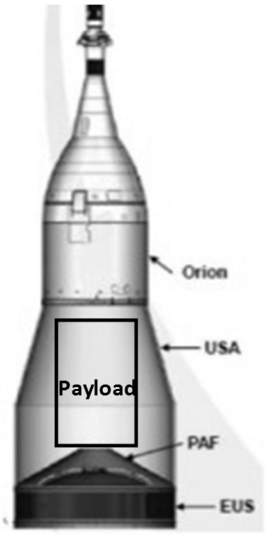

Figure 1. Location of PAF.

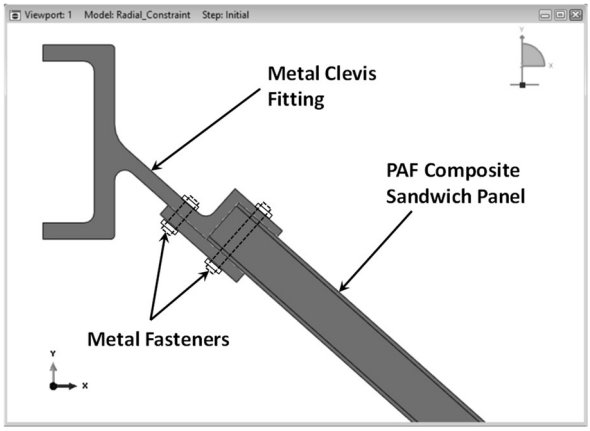

Figure 2. Metal clevis fitting.

II. Payload Attach Fitting's Internal and Support Forces

In order to design the longitudinal joints of the eight PAF segments, the internal section forces and bending moments of the PAF were calculated using the finite element method. The reaction forces from the supports were determined for designing the joints between the PAF and the payload and the body of the launch vehicle. The commercial finite element software Abaqus was used for this purpose. Figure 3 shows the geometry of the PAF with a distributed downward force applied at the forward end and a pressure load applied on the outer surface of the PAF. Two-dimension axisymmetric shell elements were used in the finite element model to determine the internal and reaction forces of the PAF under an axial or pressure load. In the finite element model, the forward end was

constrained for displacement in the radial direction and for rotation about the hoop direction. The aft end was constrained for displacements in the radial and axial directions and rotation about the hoop direction.

Figures 4 and 5 show the membrane (in-plane) force and bending moment distributions, respectively, along the meridional direction under an axial force of 1,000 lb/in applied at the forward end. *SF*1 and *SF*2 are the membrane forces per unit width in the meridional and hoop directions, respectively, and *SM*1 and *SM*2 are the bending moment per unit width about the hoop and meridional directions, respectively. These forces are related to the in-plane stresses as

$$(SF1, SF2) = \int_{-h/2}^{h/2} (\sigma_{11}, \sigma_{22}) dz \quad (1)$$

$$(SM1, SM2) = \int_{-h/2}^{h/2} (\sigma_{11}, \sigma_{22}) z dz \quad (2)$$

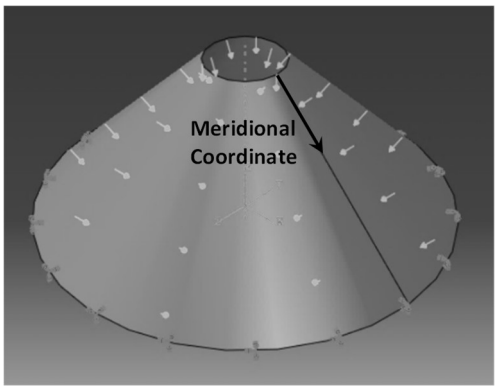

Figure 3. PAF geometry, applied loads, and meridional coordinate.

where σ_{11} and σ_{22} are the membrane stresses in the meridional and hoop directions, respectively, z is the coordinate in the transverse direction of the PAF sandwich panel and has its origin at the mid-plane, and h is the thickness of the PAF sandwich panel.

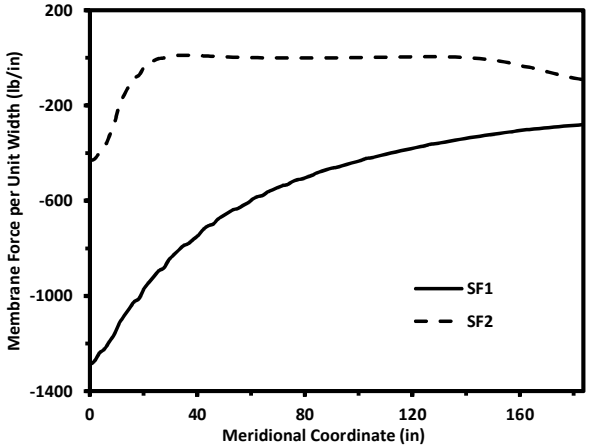

Figure 4. Membrane force distributions of PAF under 1,000 lb/in line load.

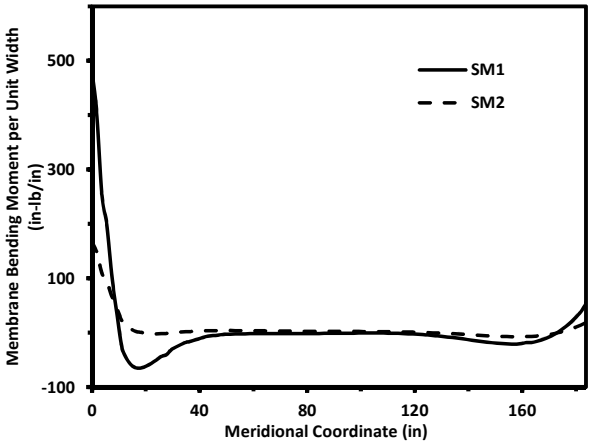

Figure 5. Bending moment distributions of PAF under 1,000 lb/in line load.

The membrane force and bending moment distributions in Figs. 6 and 7, respectively, were obtained under a 0.1 psi pressure load on the PAF surface. The origin of the meridional coordinate used in Figs. 4-7 is located at the forward end as shown in Fig. 3. As can be seen from the results, when an axial force of 1,000 lb/in is applied at the forward end, the maximum *SM*1, which is located at the forward end, has a magnitude of 480 in-lb/in. This bending moment translates to a maximum bending stress which is 68% of the normal stress due to the membrane force *SF*1 at the same location if the PAF consists of a 1-inch core and two 13-ply facesheets. The percentage increases to 88% if a 3/4-inch core is used. Similarly, the bending stress due to *SM*2 at the forward end is 71% of the normal stress due to *SF*2 for a 1-inch core and 91% for a 3/4-inch core. The membrane force and bending moment of the PAF due to surface pressure are very small compared to those caused by axial force, as long as both the pressure and axial force are of the same orders of magnitude as described.

Table 1 lists the reaction forces at the forward and aft supports when the PAF is under a distributed load at the forward end or a pressure load at the PAF surface. *RF*1 and *RF*2 are the reaction forces in the meridional and hoop directions, respectively, and *RM*3 is the reaction moment about the hoop direction. Attention needs to be paid to the large reaction moment at the forward end when the axial load is applied. Because all the finite element models are linear, the results shown can be scaled proportionally according to the magnitude of any applied axial or pressure loads. Superposition of results due to any combinations of axial and pressure loads is also appropriate.

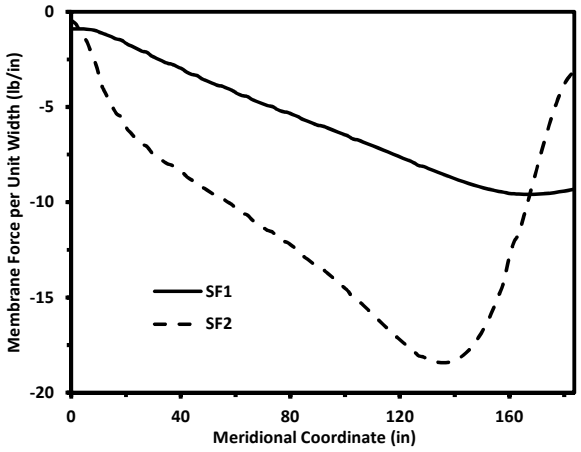

Figure 6. Membrane force distributions of PAF under 0.1 psi pressure load.

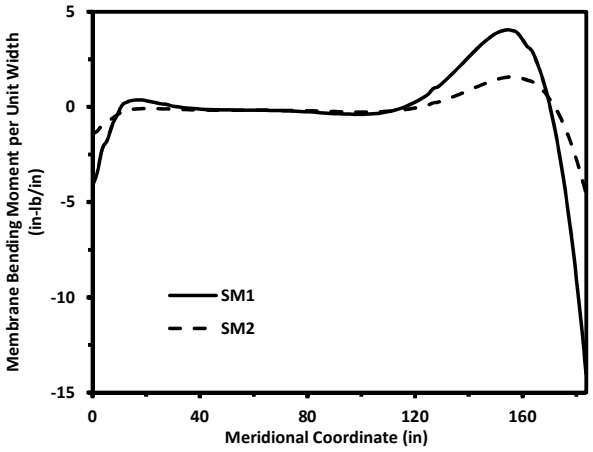

Figure 7. Bending moment distributions of PAF under 0.1 psi pressure load.

Table 1. Reaction forces from the support of PAF under different loads.

Applied Load	Forward End			Aft End		
	*RF*1 (lb/in)	*RF*2 (lb/in)	*RM*3 (in-lb/in)	*RF*1 (lb/in)	*RF*2 (lb/in)	*RM*3 (in-lb/in)
1,000 lb/in Line Load at Forward End	849	0	-575	-203	193	62
0.1 psi Pressure on PAF Surface	1.29	0	4.95	-5.40	7.74	-15.4

III. Pinned Joint Failure Load of Composite Honeycomb Sandwich Panels

There has not been much research work conducted on pin-bearing or bolt-bearing damage of composite honeycomb sandwich panels even though pin- and bolt-bearing damage on solid composite laminates have been studied in depth [1-14]. Assume the honeycomb core in a composite sandwich panel does not take significant bearing load, the two composite facesheets of the sandwich panel are bearing all the load transferred in a pinned joint. Therefore, the pin-bearing capacity of the facesheets which are two solid composite laminates is used to determine the load carrying capacity of the pinned joints of composite honeycomb sandwich panels.

One of the most significant works found in the literature on pin- and bolt-bearing damage on solid composite laminates was conducted by Hung and Chang in 1996 [13]. They developed an Abaqus finite element user subroutine based on progressive damage models of composite laminates, including matrix compression failure and fiber compression/shear failure, to analyze the bearing failures and to predict the load carry capacities of pinned and bolted joints of T800H/3900-2 carbon/epoxy composite laminates. Their results showed good correlations with test data. On the other hand, the NASA Technical Memorandum published by Chamis [14] in 1988 suggests a simplified equation for estimating the load carry capacity of a pinned or bolted joint against bearing failure as

$$F_{failure} = \sigma_{c,allowable} dt \tag{3}$$

where F_{failure} is the applied compressive force at bearing failure, $\sigma_{\text{c,allowable}}$ is the allowable compressive stress of the composite laminate, d is the fastener diameter, and t is the laminate thickness.

Without being able to run Hung and Chang's Abaqus subroutine to simulate progressive damage of composite laminate under bearing loads, an attempt was made to verify the effectiveness of Eq. (3) using Hung and Chang's data [13] which includes the moduli and failure parameters of T800H/3900-2 unitape as well as test data of the pin-bearing strength of $[(0/90)_6]_s$ cross-ply and $[(90/45/-45/0)_3]_s$ quasi-isotropic laminates. In order to determine $\sigma_{c,allowable}$ of the two composite laminates, finite element models of a square composite panel were constructed using the commercial finite element software MSC Patran/Nastran which features Tsai-Hill and Tsai-Wu first-ply failure

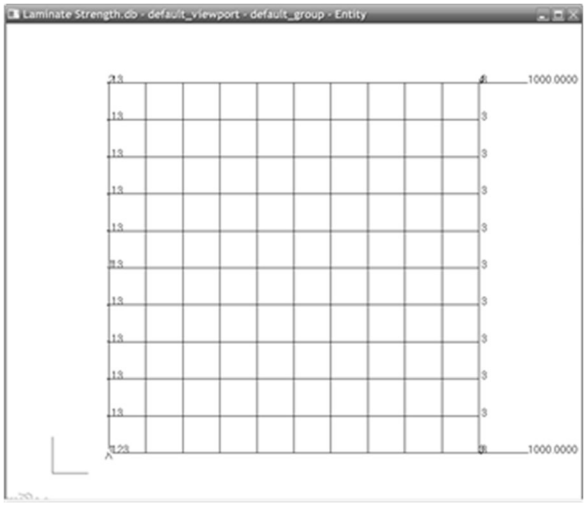

Figure 8. MSC Patran/Nastran model of a square laminate.

criteria. The finite element model of 10×10 two-dimensional composite shell elements, as shown in Fig. 8, with *x*-directional constraint on the left edge and a line load on the right edge was used for this purpose. Another finite element model was used to determine the maximum contact stress to be 1.4 times the average compressive stress (*F*/*dt*) at the bearing area of a pin-loaded hole on a composite laminate. Therefore, if stress concentration is considered, Eq. (3) is revised as

$$F_{failure} = \frac{\sigma_{c,allowable} dt}{1.4} \tag{4}$$

Table 2 lists the predicted $F_{failure}$ with and without the stress concentration factor of 1.4 and the test data with d = 0.25 inch and t = 0.15504 inch. It is noticed that

(1) Tsai-Hill and Tsai-Wu criteria predicted different plies for the first failure occurrence of the quasi-isotropic laminate.

(2) Both Tsai-Hill and Tsai-Wu criteria overestimated the pin-bearing capacity of the cross-ply laminate while both underestimated the pin-bearing capacity of the quasi-isotropic laminate. This was mainly because Tsai-Hill and Tsai-Wu criteria predict only the damage initiation of the laminate without considering damage progression.

(3) Even though the cross-ply laminate is stiffer and stronger than the quasi-isotropic laminate, its pin-bearing capacity is lower than the quasi-isotropic laminate. It is mainly because bearing damage is the result of compression failure due to concentrated bearing load. Compression failure initiates from the contact surface but the subsequent formation of shear crack and delamination is the major characteristic of bearing failure. The ±45-deg plies in the quasi-isotropic laminate inhibited/reduced the shear crack propagation which resulted in a higher bearing capacity of the laminate.

Table 2. Pin-bearing failure of T800H/3900-2 carbon/epoxy composite laminates.

Laminate	Laminate Failure Criterion	MSC Patran/Nastran		Predicted $F_{failure}$ Eq. (3) (lb)	Predicted $F_{failure}$ Eq. (4) (lb)	Test Data $F_{failure}$ (lb) [13]
		$\sigma_{c,allowable}$ (ksi)	Ply Failed First (deg)			
$[(0/90)_6]_s$	Tsai-Hill	118	0	4,574	3,267	3,100
	Tsai-Wu	136	0	5,271	3,765	
$[(90/45/-45/0)_3]_s$	Tsai-Hill	49.2	45	1,906	1,361	3,867
	Tsai-Wu	57.4	0	2,225	1,589	

As mentioned previously, there is no test data or analysis can be found in the literature regarding pin-bearing bearing, bolt-bearing failure, or pinned and bolted joints of composite honeycomb sandwich panels. In order to obtain preliminary information on pinned joint of the PAF composite panels, five specimens of pinned joint of composite honeycomb sandwich panels with 11-ply facesheets were tested at the NASA MSFC facility. Figure 9 shows the test setup. Assume that the honeycomb has no contribution to the bearing strength of the sandwich panel,

the pin-bearing strength of the sandwich panel was calculated based on the bearing strength of the two facesheets. The same procedures used to analyze the pin-bearing strength of T800H/3900-2 carbon/epoxy solid composite laminates were followed to analyze the pinned joint of the sandwich panel. Table 3 lists the calculated $\sigma_{allowable}$ as percentage of the average test result from the five specimens. Despite the fact that the two simple equations either over or underestimated the pinned joint strength of T800H/3900-2 carbon/epoxy solid composite laminates, Eq. (3) actually predicted the pinned joint strength of NASA composite honeycomb sandwich panel within 20% deviation from the test data. This is probably due to the particular stacking sequence used in the facesheets of NASA PAF sandwich panels. A more sophisticated model is deemed necessary to be able to predict the pinned joint failure load of composite honeycomb sandwich panels.

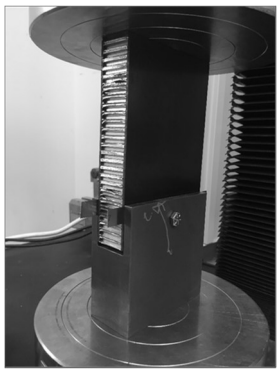

Figure 9. Pinned joint test setup.

Table 3. Pinned joint strength of NASA composite honeycomb sandwich panels.

Laminate Failure Criterion	Predicted $F_{failure}/F_{f,test}$ Eq. (3) (%)	Predicted $F_{failure}/F_{f,test}$ Eq. (4) (%)	Test Data $F_{f,test}/F_{f,test}$ (%)
Tsai-Hill	102	73.2	100
Tsai-Wu	117	83.9	

IV. Design and Analysis of the Clevis Joint between the PAF and Payload

The current joining method between the PAF and the payload and the body of the launch vehicle is to use clevis type of circular metal fittings as shown in Fig. 2. The PAF panel is pinned to the metal fittings. Based on the design, all the load transfer between the PAF and the fittings is through the pins. Because the reaction forces are much larger at the forward end than at the aft end, the design of the PAF composite panel and pinned joint is emphasized for the forward end.

A. Adding a Fabric Ply for Pinned Joints

In order to increase the pin-bearing capacity of the sandwich panel at the forward clevis joint, it is proposed to add a ±45-deg cross-ply fabric composite layer to each of the two facesheets of the PAF panel at the forward end as shown in Fig. 10. Even though the ±45-deg fabric ply has little contribution to the stiffness and strength of the PAF sandwich panel in either the meridional or hoop direction, it can significantly increase the pin-bearing capacity of the facesheets based on Hung and Chang's study [13]. However, the length (as shown in Fig. 10) of the added ply is to be determined.

As shown in Fig. 10, when a downward force is apply at the top of the main laminate, a portion of the force is transferred from the main laminate to the added fabric ply and a portion of the transferred force is supported by the fastener. The load transfer between the main laminate and the added fabric ply

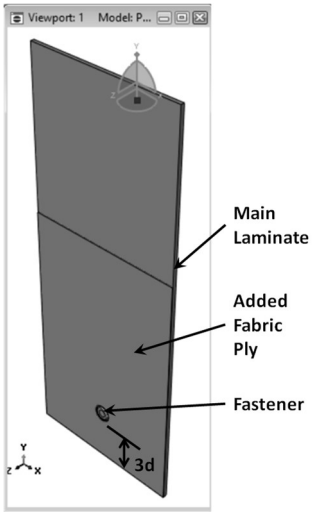

Figure 10. Finite element model of pinned joint with an added fabric ply.

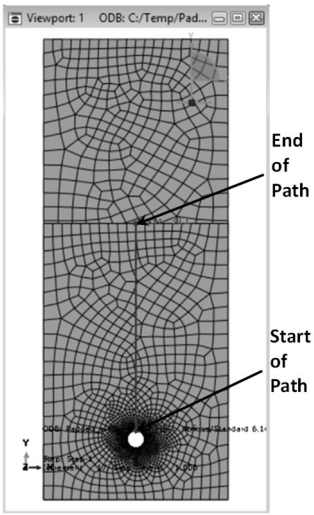

Figure 11. Finite element mesh and path definition.

is via shear. Due to the load eccentricity and the subsequent rotation of the added fabric ply, there also exists a peel stress at the vicinity of the upper end of the added ply and around the fastener hole. The added ply needs to be long enough to ensure a proper load transfer between the main laminate and the added ply. Therefore, three-dimensional finite element models were constructed using Abaqus, as shown in Fig. 11, to investigate the influence of the length of the added fabric ply on the maximum shear and peel stresses at the interface between the main laminate and the added fabric ply. The finite element models used 8-noded three-dimensional solid elasticity brick elements with lumped 13-ply PAF facesheet laminate moduli for the main laminate. Six elements were used in the thickness direction of the main laminate and two elements were used for the added fabric ply. The main laminate was four inches wide and ten inches long while the added fabric ply had the same width and a varying length from three to six inches. The diameter of the fastener d was 3/8 inch and the edge distance of the hole, as shown in Fig. 10, was 3d. The steel fastener was fixed for its center half of the diameter and a total force of 3,200 lb was applied at the top of the main laminate as a uniform pressure. The back side of the main laminate was constrained for displacement in the out-of-plan direction.

Figures 12 and 13 show the interfacial shear and peel stress distributions between the added fabric ply and the main laminate along the path shown in Fig. 11. As can be seen, the maximum interfacial shear stress occurred around the fastener hole and the shear stress remained almost 0 at most of the area between the fastener hole and the upper edge of the added fabric ply. The maximum interfacial shear stress of the 6-in., 5-in., 4-in., and 3-in. long added fabric plies along the path were 2,889 psi, 3,036 psi, 2,907 psi, and 3,073 psi, respectively, which reflects a 6.4% increase from a 6-in. to 3-in. long fabric ply. Figure 14 shows the comparison of the maximum overall (not restricted on the path) interfacial shear and peel stresses of the added fabric ply among the four different lengths. As can be seen, the difference is very minimal. Because of the low stiffness of the added fabric ply in the load direction, the amount of force carried by the fabric ply was small. This resulted in low interfacial shear and peel stresses. Again, the purpose for the added fabric ply is not to alleviate the bearing stress but to increase the pin-bearing capacity at the fastener holes. In conclusion, the added fabric ply does not need to be long (in the load direction) to achieve its objective.

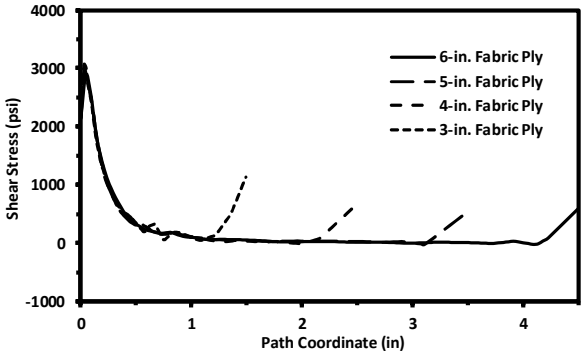

Figure 12. Interfacial shear stress distributions.

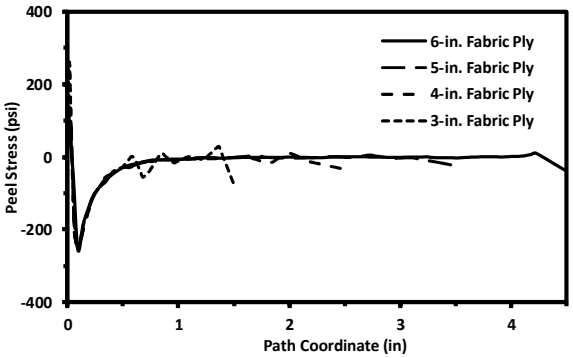

Figure 13. Interfacial peel stress distributions.

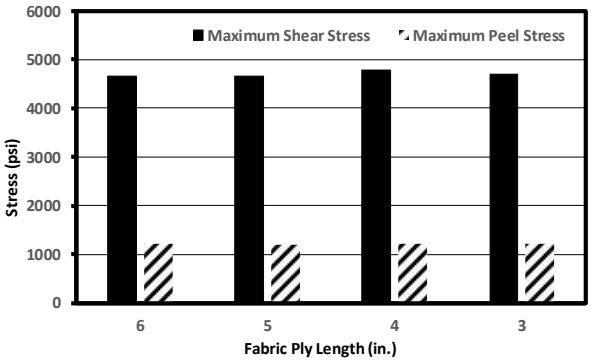

Figure 14. Overall maximum shear and peel stresses of added fabric ply.

B. Length of Clevis Joint Test Specimen

A test plan is being written for the clevis joint. Because the specimen will be under compression, it is desired to shorten the specimen to avoid buckling but the specimen needs to be long enough to avoid uneven stress at the end in contact with the load platen. A two-dimensional finite element model was constructed using the lumped mechanical properties of the facesheet laminate and two 0.25-inch steel pins. Four-noded two-dimensional plane-stress solid elasticity elements were used for this purpose. As shown in Fig. 15, the fastener distance, from center to center, is 2 inches, the panel width is 3.75 inches, and the edge distance at the bottom of the panel is 0.5 inch. The full length of the panel is 15 inches while Fig. 14 shows only the 25% of panel from the bottom edge. Fixed boundary conditions were applied at the central 0.15-inch diameter circle of each of the two steel pins. A total downward force of 3,825 lb was applied at the top of the panel as a uniform pressure. It was found that at 4 inches from the bottom of the panel, the stress variation across the width is less than 3.1% which indicates an acceptable specimen length.

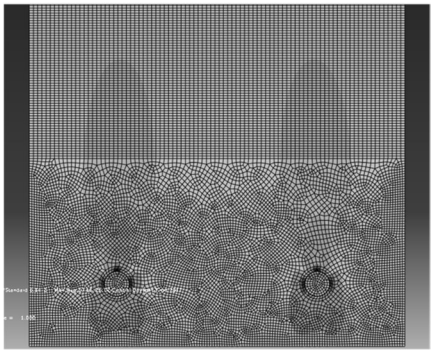

Figure 15. Finite element mesh for stress distribution of a pinned joint.

C. Bending/Rotation of Test Specimen due to Eccentricity

During the design of the test specimen/configuration of the pinned joint between the PAF composite sandwich panel and the aluminum clevis fitting, as shown in Fig. 16, a concern was raised regarding the rotation of the specimen caused by the load/support eccentricity. In order to determine the rotation of the specimen, a two-dimensional finite element model was constructed using Abaqus with plane-strain solid elasticity elements. As shown in Fig. 16, the panel was 8 inches in length and a total downward force of 700 lb was applied on the four nodes at the top of the two facesheets. A fixed-end boundary condition was applied at the bottom surface of the fitting. The results showed a maximum horizontal displacement of 0.12 inch at the top of the panel due to rotation. This small horizontal displacement eliminated the concern that the specimen might slip off from the load platen at the top due to rotation in the test.

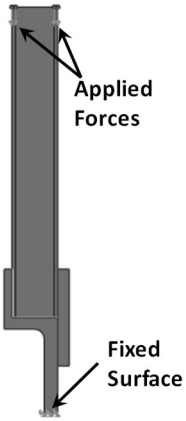

Figure 16. Clevis joint test specimen

V. Conclusion

The use of advanced composite materials for the PAF of NASA's SLS is a significant undertaking. Test data is to be relied on for the design of all components of the new composite PAF. Analytical tools and modeling not only assist in the design process but also ensure cost effectiveness of experimental work. The studies documented in this report demonstrate examples of such practice. A more sophisticated analytical/numerical methodology/model is deemed necessary in order to predict the load carrying capacity of pinned joints of composite honeycomb sandwich panels.

Acknowledgments

The first author of this report would like to express his appreciation to the Marshall Space Flight Center Faculty Fellowship Program Director, Dr. Frank Six, and all the coordinators including Dr. Gerald Karr, Rachael Damiani, Mona Miller, and Katie Hayden, for providing this unique opportunity to work with NASA researchers in a NASA environment. A special gratitude he gives to the MSFC Collaborator, Justin Jackson, and Dr. William Guin. They

have spent time and efforts to make this Fellowship meaningful and fruitful. Many thanks also go to Stephen Richardson, Robert Wingate, and Dawn Phillips for their tremendous help.

References

[1]Thoppul, S. D., Finegan, J., and Gibson, R. F., "Mechanics of Mechanically Fastened Joints in Polymer–Matrix Composite Structures – A review," *Composites Science and Technology,* Vol. 69, 2009, pp. 301-329.

[2]Xiao, Y., and Ishikawa, T., "Bearing Strength and Failure Behavior of Bolted Composite Joints (part I: Experimental Investigation)," *Composites Science and Technology,* Vol. 65, 2005, pp. 1022-1031.

[3]Xiao, Y., and Ishikawa, T., "Bearing Strength and Failure Behavior of Bolted Composite Joints (part II: Modeling and Simulation)," *Composites Science and Technology,* Vol. 65, 2005, pp. 1032-1043.

[4]Camanho, P. P., and Lambert, M., "A Design Methodology for Mechanically Fastened Joints in Laminated Composite Materials," *Composites Science and Technology,* Vol. 66, 2006, pp. 3004-3020.

[5]Broughton, W. R., Crocker, L. E., and Gower, M. R. L., "Design Requirements for Bonded and Bolted Composite Structures," NPL Report MATC(A)65, January 2002.

[6]İçten, B. M., and Sayman, O., "Failure Analysis of Pin-Loaded Aluminum–Glass–Epoxy Sandwich Composite Plates," *Composites Science and Technology,* Vol. 63, 2003, pp. 727-737.

[7]Shokrieh, M. M., "Failure of Laminated Composite Pinned Connections," Master's Thesis, Dept. of Mechanical Engineering, McGill Univ., Montreal, Canada, 1991.

[8]Zhou Y., Fei, Q., and Tao, J., "Profile design of loaded pins in composite single lap joints: From circular to non-circular," *Results in Physics*, Vol. 6, 2016, pp. 471-480.

[9]Okutan, B., and Karakuzu, R., "The Failure Strength For Pin-loaded Multi-directional Fiber-glass Reinforced Epoxy Laminate," *Journal of Composite Materials*, Vol. 36, No. 24, 2002, pp. 2695-2712.

[10]Okutan, B., and Karakuzu, R., "The strength of pinned joints in laminated composites," *Composites Science and Technology,* Vol. 63, 2003, pp. 893-905.

[11]Lessard, L. B., and Shokrieh, M. M., "Two-Dimensional Modeling of Composite Pinned-Joint failure ," *Journal of Composite Materials*, Vol. 29, No. 5, 1995, pp. 671-697.

[12]Wang, H. S., Hung, C. L., and Chang, F. K., "Bearing Failure of Bolted Composite Joints. Part I: Experimental Characterization," *Journal of Composite Materials*, Vol. 30, No. 12, 1996, pp. 1284-1313.

[13]Hung, C. L. and Chang, F. K., "Bearing Failure of Bolted Composite Joints. Part II: Model and Verification," *Journal of Composite Materials*, Vol. 30, No. 12, 1996, pp. 1359-1400.

[14]Chamis, C. C., "Simplified Procedures for Designing Composite Bolted Joints," NASA Technical Memorandum 100281, 1988.

Properties, propagation, and excitation of EMIC waves observed by MMS: A case study

Jichun Zhang[1] and Victoria N. Coffey[2]
University of New Hampshire 1, Durham, NH 03824
NASA Marshall Space Flight Center 2, Huntsville, AL 35812

Michael O. Chandler[2], Scott A. Boardsen[3], Anthony A. Saikin[1], Emily M. Mello[1], Christopher T. Russell[4], Roy B. Torbert[1], Stephen A. Fuselier[5], Barbara L. Giles[3], and Daniel J. Gershman[3]
NASA Goddard Space Flight Center 3, Greenbelt, MD 20771
UCLA, Los Angeles 4, CA 951567
Southwest Research Institute 5, San Antonio, TX 78238

Abstract

Electromagnetic ion cyclotron (EMIC) waves (0.1-5 Hz) play an important role in particle dynamics in the Earth's magnetosphere. EMIC waves are preferentially excited in regions where hot anisotropic ions and cold dense plasma populations spatially overlap. While the generation region of EMIC waves is usually on or near the magnetic equatorial plane in the inner magnetosphere, EMIC waves have both equatorial and off-equator source regions on the dayside in the compressed outer magnetosphere. Using field and plasma measurements from the Magnetospheric Multiscale (MMS) mission, we perform a case study of EMIC waves and associated local plasma conditions observed on 19 October 2015. From 0315 to 0810 UT, before crossing the magnetopause into the magnetosheath, all four MMS spacecraft detected long-lasting He^+-band EMIC wave emissions around local noon (MLT = 12.7 – 14.0) at high L-shells (L = 8.8 – 15.2) and low magnetic latitudes (MLAT = -21.8º – -30.3º). Energetic (> 1 keV) and anisotropic ions were present throughout this event that was in the recovery phase of a weak geomagnetic storm (min. *Dst* = -48 nT at 1000 UT on 18 October 2015). The testing of linear theory suggests that the EMIC waves were excited locally. Although the wave event is dominated by small normal angles, its polarization is mixed with right- and left-handedness and its propagation is bi-directional with regard to the background magnetic field. The short inter-spacecraft distances (as low as ~15 km) of the MMS mission make it possible to accurately determine the k vector of the waves using the phase difference technique. Preliminary analysis finds that the k vector magnitude, phase speed, and wavelength of the 0.3-Hz wave packet at 0453:55 UT are 0.005 km^{-1}, 372.9 km/s, and 1242.9 km, respectively.

---

[1] Research Associate Professor, Department of Physics, Space Science Center, University of New Hampshire.
[2] Research Scientist, Natural Environments, EV44 Huntsville AL 35812, NASA Marshall Space Flight Center.
[3] Research Scientist, Natural Environments, EV44 Huntsville AL 35812, NASA Marshall Space Flight Center.
[4] Research Scientist, Goddard Planetary Heliophysics Institute, College Park MD 20742, University of Maryland.
[5] Graduate Student Research Assistant, Department of Physics, 8 College Road, Durham, NH 03824, Space Science Center.
[6] Research Assistant, Department of Physics, 8 College Road, Durham, NH 03824, Space Science Center.
[7] Professor, Department of Earth, Planetary, and Space Sciences, 595 Charles Young Drive East, Los Angeles, CA 90095, Institute of Geophysics and Planetary Physics.
[8] Professor, Department of Physics, 8 College Road, Durham, NH 03824, Space Science Center.
[9] Executive Director, Space Science Department, 6220 Culebra Road, San Antonio, TX 78238, Southwest Research Institute.
[10] Associate Chief, Geospace Physics Laboratory, 6730 Greenbelt MD 20771, NASA Goddard Space Flight Center.
[11] Research Scientist, Goddard Planetary Heliophysics Institute, College Park MD 20742, University of Maryland.

I. Introduction

Electromagnetic ion cyclotron (EMIC) waves, typically in the frequency range of 0.1-5 Hz, are called Pc 1-2 pulsations when seen on the ground. They are normally excited by a temperature anisotropic ($T_\perp > T_\parallel$) distribution of hot (~1-100 keV) ions. [2-4] Under a dipole-like magnetic field configuration in the Earth's inner magnetosphere (see Fig. 1), the excitation region of EMIC waves is usually on or near the magnetic equatorial plane, [5, 6] where the magnetic energy per particle is lower and thus the growth rate of waves is larger due to the greater plasma density and weaker magnetic field strength. [2] EMIC waves are preferentially generated in regions where hot anisotropic ions and cold dense plasma populations spatially overlap (Fig. 2). [7-10] In the terrestrial inner magnetosphere, these ion populations can commonly be found where the ring current overlaps the outer plasmasphere and plasmapause [4, 11, 12] and the "edges" of plasmaspheric drainage plumes. [5, 13, 14] A significant population of hot anisotropic H^+ can also be created on the dayside outer magnetosphere through the drift-shell splitting, [15, 16] the Shabansky orbits (a non-energization mechanism), [17, 18] or during a magnetospheric compression, which is often driven by a sudden, large increase in the solar wind dynamic pressure (*Pdyn*). [19-23] Because of the dayside geomagnetic field compression in the outer magnetosphere by *Pdyn*, local minimum *B* regions can be formed off the magnetic equator in the dayside magnetosphere (see Fig. 2). [1] EMIC waves excited near the off-equator minimum *B* regions have been investigated in recent theoretical work, [18, 23] followed by observational evidence. [24-26] Due to the distortion of the geomagnetic field from a simple dipole field and the spatial extent of EMIC wave source regions, EMIC waves and the associated plasma conditions have not been fully understood in the outer magnetosphere.

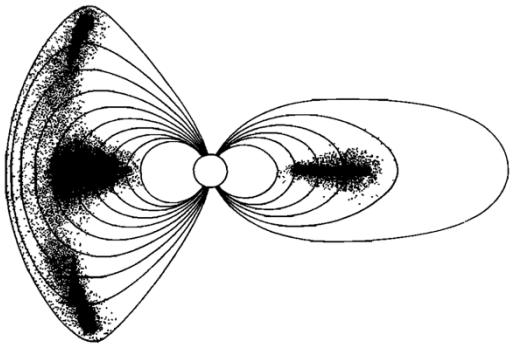

Figure 1. Schematic sketch of chorus/EMIC wave excitation regions, denoted by dots, on the noon-midnight meridian plane. [1]

As displayed in the lower part of Fig. 2, the excited EMIC waves can result in the energization and loss of magnetospheric particles. [2, 27-30] Through resonant wave-particle interactions, EMIC waves are able to accelerate cold ions into the thermal (~1eV – 1 keV) energy range in the direction perpendicular to the ambient magnetic field [27-29, 31, 32] and cause the pitch angle scattering loss of hot ions in the ring current. [33-35] Particularly, previous studies [30, 36-47] have confirmed that EMIC waves can also resonantly interact with relativistic electrons and result in pitch angle scattering of the electrons.

Newly excited EMIC waves are often transverse and left-hand polarized, consistent with the direction of ion gyration in the magnetic field. [2] After being generated, EMIC waves can be guided along the magnetic field lines and propagate from the source region to other magnetic latitudes (MLATs). In the case of the equatorial source region, they propagate from the equatorial plane to higher MLATs. Using the Combined Release and Radiation Effects Satellite (CRRES) electric and magnetic field data (covering only MLT = 1400 – 1800), *Loto'aniu et al.* [6] found that the directions of the energy propagation (i.e., Poynting vector) of EMIC waves are unidirectional when |MLAT| > 11° but they are bidirectional in the MLAT range of [-11°, 11°] in the inner magnetosphere. *Khazanov et al.* [48] claimed that most unidirectional events were indeed detected beyond the range of MLAT = [-18°**,** 18°**]** due to data gaps in the statistical study by *Loto'aniu et al.* [6] Depending on their frequency with respect to the local ion gyrofrequencies such as f_{He+}, some waves are well guided along the field lines and can generally propagate to the ground. [49] Some waves may even experience a polarization reversal where the wave frequency *f* is equal to the crossover frequency f_{co} during their higher-latitude propagation and then be reflected where *f* equals the bi-ion hybrid frequency f_{bi} at an even higher latitude. [49] As a result, their polarization is crossed over from a left-hand to a right-

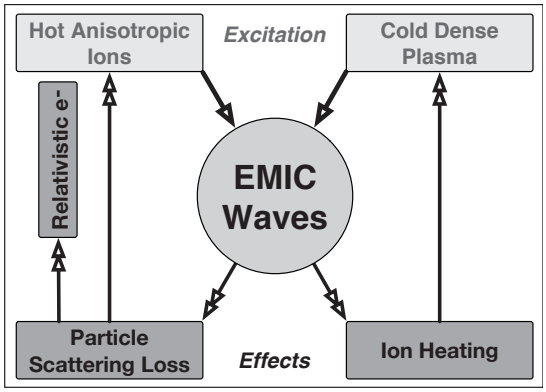

Figure 2. A schematic diagram depicting the excitation and effects of EMIC waves. The overlapping of hot anisotropic ions and cold dense plasma result in the generation of EMIC waves, and EMIC waves in turn cause the ion heating of the cold dense plasma and the pitch angle scattering of both relativistic electrons (e^-) and hot ions through resonant wave-particle interactions.

hand or linear mode. These waves could undergo multiple equatorial crossings along magnetic flux tubes without a large radial or azimuthal drift. Because of their successive passes through the equatorial wave growth region, the waves are expected to be drastically amplified by continuing to obtain energy from the energetic protons. [49, 50] Nevertheless, *Horne and Thorne* [51] found that, in the absence of density gradients, significant wave amplifications can only occur on the first equatorial pass because wave normal angles become large after the initial pass. *Horne and Thorne* [52] concluded that wave damping by thermal heavy ions also makes it impossible for the same EMIC wave packet to bounce through its source region multiple times. But, a consensus about the wave propagation and reflection has not been reached. [48, 50, 53]

In this study, using *in situ* field and plasma measurements from the Magnetospheric Multiscale (MMS) mission, we perform a case study of EMIC waves and associated local plasma conditions in the outer magnetosphere on 19 October 2015. The concentration of our current work is on the wave properties, propagation, excitation, and the calculation of wave **k** vector at one time point. The current investigation is also a follow-up to our recently published case and statistical studies of EMIC waves detected by Van Allen Probes [4, 54-56] in the inner magnetosphere and by Cluster [26, 28, 57-59] in a polar orbit.

This paper is organized as follows: after the introduction (current section), we describe MMS instrumentation in Section 2. Section 3 presents results from the case study of the EMIC wave event. Conclusions and future work are discussed in Section 4.

II. MMS Instrumentation

The MMS mission [60] has four identical spacecraft, which were launched into 24-hour period, highly elliptical, near-equatorial orbits on 12 March 2015. The MMS spacecraft are positioned in a tetrahedron formation of variable inter-spacecraft distances from tens to hundreds of kilometers. Multiple instruments onboard each MMS spacecraft measure and derive a variety of parameters from plasma particles and magnetic and electric fields.

In this study, the high-resolution field measurements are used to obtain wave frequency spectrums utilizing the Fast Fourier Transform (FFT) technique. Magnetic field (8 or 15 Hz) and electric field (33 Hz) data are obtained from the Fluxgate Magnetometers (FGMs) [61] and the spin-plane double-probe electric-field sensors (EDPs) in the FIELDS instrument suite, respectively. [62] MMS FIELDS includes a sensor suite consisting of two axial and four spin-plane double-probe electric-field sensors, two flux-gate magnetometers, a search-coil magnetometer, and two electron drift instruments onboard each MMS spacecraft. These instruments measure the DC magnetic field with a resolution of 10 ms, the DC electric field with a resolution of 1 ms, electric plasma waves to 100 kHz, and magnetic plasma waves to 6 kHz.

Plasma data are from the Fast Plasma Investigation (FPI) [63] and the Hot Plasma

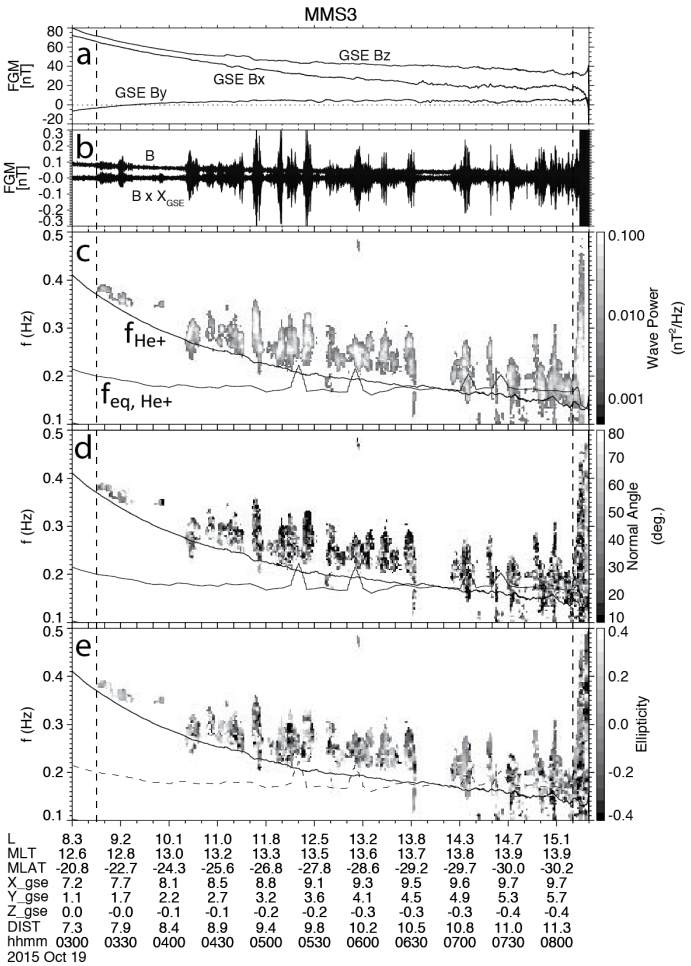

Figure 3. (a) Three measured high-resolution magnetic field components in the geocentric solar ecliptic (GSE) coordinates, (b) waveforms in the field-aligned coordinates (FAC) after the ambient magnetic field is filtered out, and (c) frequency-UT spectrograms of wave power, (d) normal angle, and (e) ellipticity (<0, L-mode; >0, R-mode). The vertical dashed lines indicate the start and end times of the wave event. The solid/dashed traces in Panels c-e represent local/equatorial He^+ gyrofrequencies $f_{He+}/f_{eq,He+}$.

Composition Analyzer (HPCA). [64] FPI includes four dual electron spectrometers (DES) and four dual ion spectrometers (DIS) on each of the four spacecraft. When measurements from the two sets of four dual-spectrometers are combined, FPI can provide the velocity-space distribution of electrons and ions from 10 eV to 30 keV with a time resolution of 30 and 150 ms, respectively. One HPCA on each spacecraft measures the composition-resolved velocity-space distribution of ions from 1 eV to 40 keV with a time resolution of 10–15 s.

III. EMIC wave event on 19 October 2015

A. Field Data and Wave Activity

Figure 3 demonstrates high-resolution magnetic field data measured by MMS/FGM from 0300 to 0820 UT on 19 October 2015 and their results from the FFT analysis, using 1024 time points and a step length of 32 points. The magnetic field data are first converted into field-aligned coordinates (FAC) and then the FFT spectral analysis [65] is applied to obtain waveforms, wave power, normal angle, and ellipticity (<0, L-mode; >0, R-mode) for the EMIC wave event. When wave powers (Fig. 3c) are less than 0.002 nT^2/Hz, data points are removed from the spectrogram plots shown in Figs. 3c-e. The EMIC wave event is labeled with the two vertical dashed lines, starting at 0315 and lasting for 4 hours 55 minutes. The event exhibits multiple shorter-period wave activity in the frequency ranges mostly above f_{He+}, i.e., in the H^+ band. The wave event is dominated by small normal angles, and its polarization is mixed with right- and left-handedness. All four MMS spacecraft detected the long-lasting EMIC wave emissions in the same UT time period. The EMIC waves were around local noon (MLT = 12.7 – 14.0), at high L-shells (L = 8.8 – 15.2), and at low magnetic latitudes (MLAT = -21.8 – -30.3°).

Figure 4 shows the X and Y components of wave electric and magnetic fields, the Z component of wave Poynting vector spectrograms (S_z), and angles (*AngBS*) between the background magnetic field and the Poynting vector on MMS3 during the EMIC wave event. We obtain the waveform data by applying a 0.1- to 0.5-Hz band-pass filter to both the *in situ* FGM magnetic field measurements and EDP electric field measurements, after they are transferred into the local field-aligned coordinate system. The transverse (i.e., X and Y) components of electric and magnetic fields are used to compute S_z with the following formula: [6]

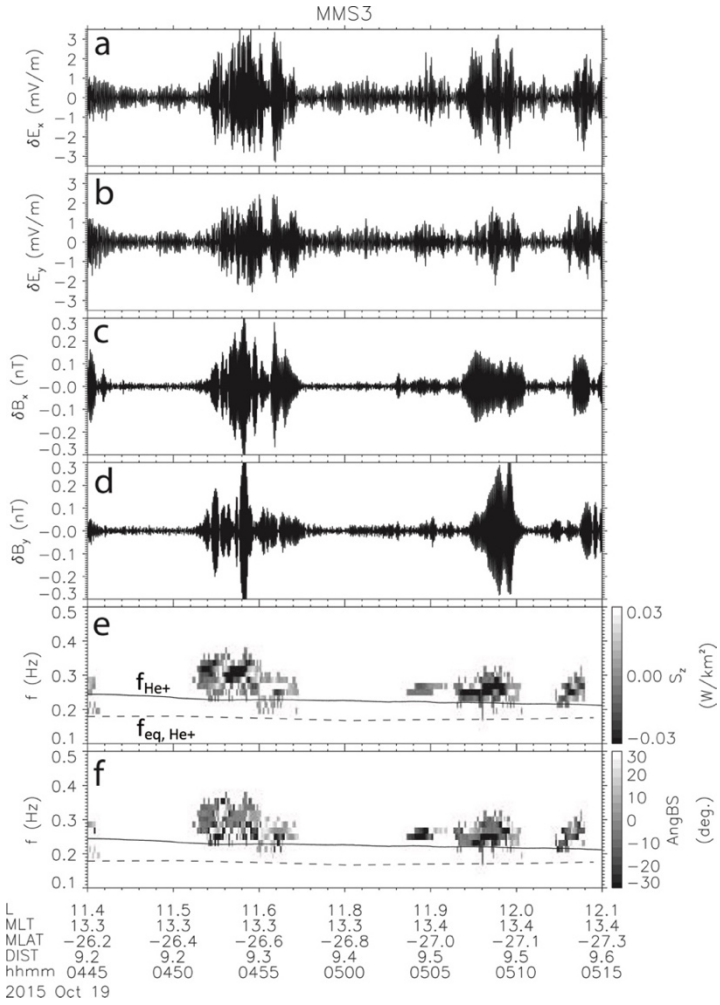

Figure 4. Wave fields and Poynting vector on MMS3 during 0445 – 0515 UT, 19 October 2015. From top to bottom, the panels show wave electric field components (δE_x and δE_y), wave magnetic field components (δB_x and δB_y), Poynting vector Z component (S_z), and the angles (*AngBS*) of the background magnetic field and the Poynting vector. The data are transferred into the local field-aligned coordinate system: Z is along the magnetic field, $Y=Z\times X_{GSE}$, and $X=Y\times Z$, which completes the right-hand system. The solid/dashed traces in Panels e-f represent the local/equatorial He^+ gyrofrequencies $f_{He+}/f_{eq,He+}$.

$$\mathbf{S} = \frac{1}{4\mu}(\delta\mathbf{E}^* \times \delta\mathbf{B} + \delta\mathbf{E} \times \delta\mathbf{B}^*) \quad (1)$$

where **S** is the wave Poynting vector spectrograms, **δE** and **δB** are the complex spectral matrices of the wave fields, and **δE*** and **δB*** are their conjugate matrices. The wave Poynting vector points the propagation direction of the wave energy, same as that of the wave group velocity $\mathbf{V_g}$. In the event, the peak value of δE_x (δE_y) is 3.5 (-2.6) mV/m, and the maximum magnitude of δB_x and δB_y is 0.3 (0.3) nT. To highlight the sign change in S_z, S_z is plotted in a narrow range, i.e., [-0.03, 0.03] W/km^2, and all its values are marked as NaN when they are $\leq 3\times10^{-4}$ W/km^2. The minimum (maximum) value of S_z is -0.25 (1.19) W/km^2 during the plotting period. The energy propagation of the EMIC waves is bi-directional with regard to the ambient magnetic field. This indicates the local excitation of the wave activity. Later in the paper, we will further test whether local plasma conditions are associated with the generation of the waves.

B. Solar Wind and Geomagnetic Conditions

From top to bottom, Fig. 5 shows the solar wind bulk flow speed *Vsw*, plasma number density *Nsw*, dynamic pressure *Pdyn*, interplanetary magnetic field (IMF) magnitude *B*, IMF z-component B_z, *AE, Kp*, and *Dst* and *Dst** (in the same panel), respectively. The plotting time period is 3.5 days from 0000 UT, 17 October 2015. *Dst** is the *Pdyn*-corrected *Dst*, which does not include the contribution of the magnetopause currents to disturbances in the geomagnetic field. $Dst^*=Dst-7.26Pdyn^{1/2}+11$ nT. [66] The solar wind plasma/IMF data are in 1-minute resolution and obtained from the High Resolution OMNI (HRO) database, which is contained in NASA/GSFC's Space Physics Data Facility's OMNIWeb service. This service provides solar wind data propagated to the Earth's bow shock nose using the minimum variance analysis (MVA) technique. [67-69] Similar to Fig. 3, the vertical dashed lines indicate the duration of the EMIC wave event.

The EMIC wave event occurred in the middle recovery phase of a moderate geomagnetic storm that has maximum *AE* = 1400, maximum *Kp* = 4, and minimum *Dst** = -51.5 nT at 0900 UT, 18 October 2015. The minimum *Dst** is denoted with the vertical dotted line in Fig. 5. The intensity of the storm is consistent with the levels of disturbances in solar wind plasma and IMF, particularly the magnitude and duration of the southward IMF B_z.

C. Plasma Observations and Comparison with Linear Theory

To quantitatively evaluate conditions for the excitation of the EMIC waves, we test the linear theory of the EMIC instability with local

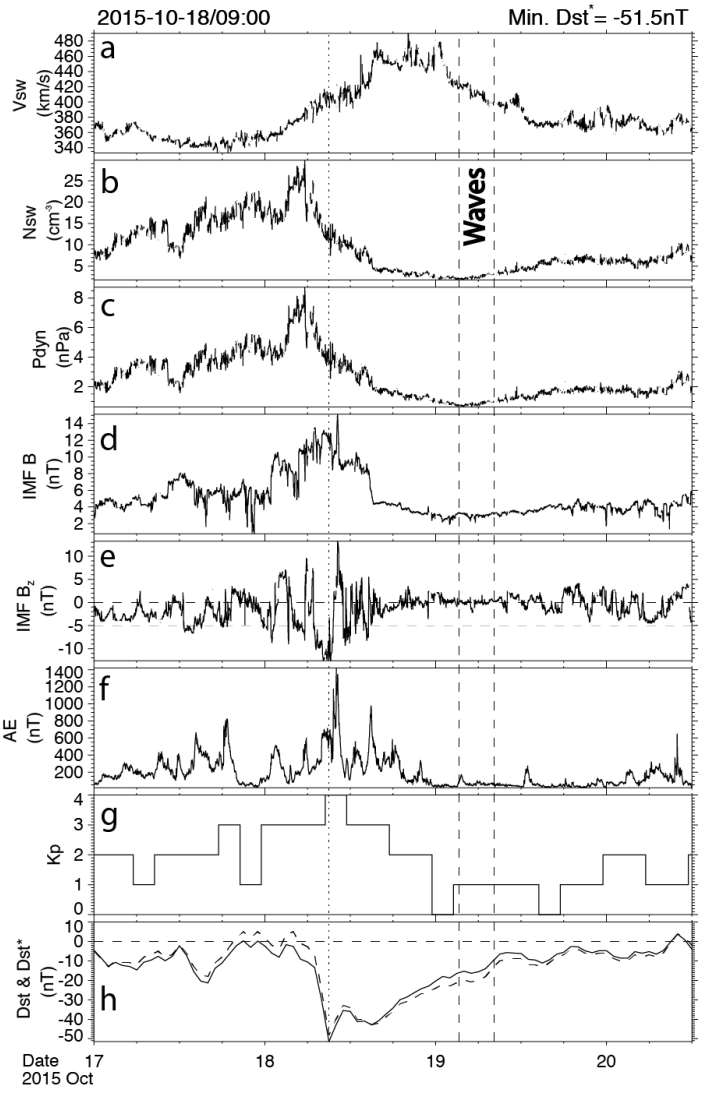

Figure 5. Solar wind plasma, IMF, and geomagnetic indices during the EMIC wave event: 0000 UT, 17 October to 1200 UT, 20 October 2015. Shown from top to bottom are solar wind bulk flow speed *Vsw*, plasma number density *Nsw*, dynamic pressure *Pdyn*, IMF *B*, IMF B_z, *AE*, *Kp*, and *Dst overplotted with *Dst*. The vertical dashed lines indicate the time periods of the wave activity, and the vertical dotted lines denote the time of min. *Dst**. In (e), the horizontal dashed lines indicate the values of 0 and −5 nT, respectively. In (h), the horizontal dashed lines mark the zero value.**

magnetic field and plasma parameters, which are derived from the H^+ energy and pitch angle (PA) fluxes. Based on linear theory, EMIC wave activity can occur only if $\Sigma_h > S_h$. [70] S_h is the EMIC instability threshold,

$$S_h = \sigma_0 + \sigma_1 \ln(\frac{n_{hp}}{n_e}) + \sigma_2 [\ln(\frac{n_{hp}}{n_e})]^2, \quad (2)$$

where σ_0 = 0.429, σ_1 = 0.124, and σ_2 = 0.0118. These constants are given in Ref. 71, obtained by assuming the wave growth rate is 0.001 and fitting linear theory results to LANL Magnetospheric Plasma Analyzer (MPA) observations at geosynchronous orbit. n_{hp} ("hp" denotes hot protons) is the density of hot (e.g., >1 keV) H^+ and n_e is the total electron density. Σ_h is the observational EMIC growth parameter,

$$\Sigma_h = (\frac{T_\perp}{T_\parallel} - 1)\beta_{\parallel h}^{\alpha_h}, \quad (3)$$

where

$$\beta_{\parallel h} = 2\mu_0 n_{hp} k T_\parallel / B^2 \quad (4)$$

$$\alpha_h = a_0 - a_1 \ln(\frac{n_{hp}}{n_e}) - a_2 [\ln(\frac{n_{hp}}{n_e})]^2 \quad (5)$$

and a_0 = 0.409, a_1 = 0.0145, and a_2 = 0.00028. [71] $T_\perp$ ($T_\parallel$) is the temperature perpendicular (parallel) to the background magnetic field, $T_\perp / T_\parallel - 1$ is the temperature anisotropy, and B is the magnetic field magnitude.

MMS measured the plasma and magnetic field parameters for the EMIC wave event, which allows us to test the threshold of the EMIC instability for the observed conditions. Fig. 6 shows several associated parameters from MMS3 from 0240 – 0845 UT on 19 October 2015: HPI-DIS ion flux spectrograms, HPCA H^+ flux spectrograms, temperature anisotropy for >1 keV H^+, $A_{hp} = T_\perp / T_\parallel - 1$, n_{hp} for >1 keV H^+, n_e, $|B|$, $\beta_{\parallel h}$ for >1 keV H^+, Σ_h, S_h, and the difference between Σ_h and S_h. The H^+ moments ($T_\perp$, $T_\parallel$, and n_{hp}) are calculated with H^+ 3-D distributions measured by HPCA over all energy channels. Again, the start and end time of the wave events are denoted

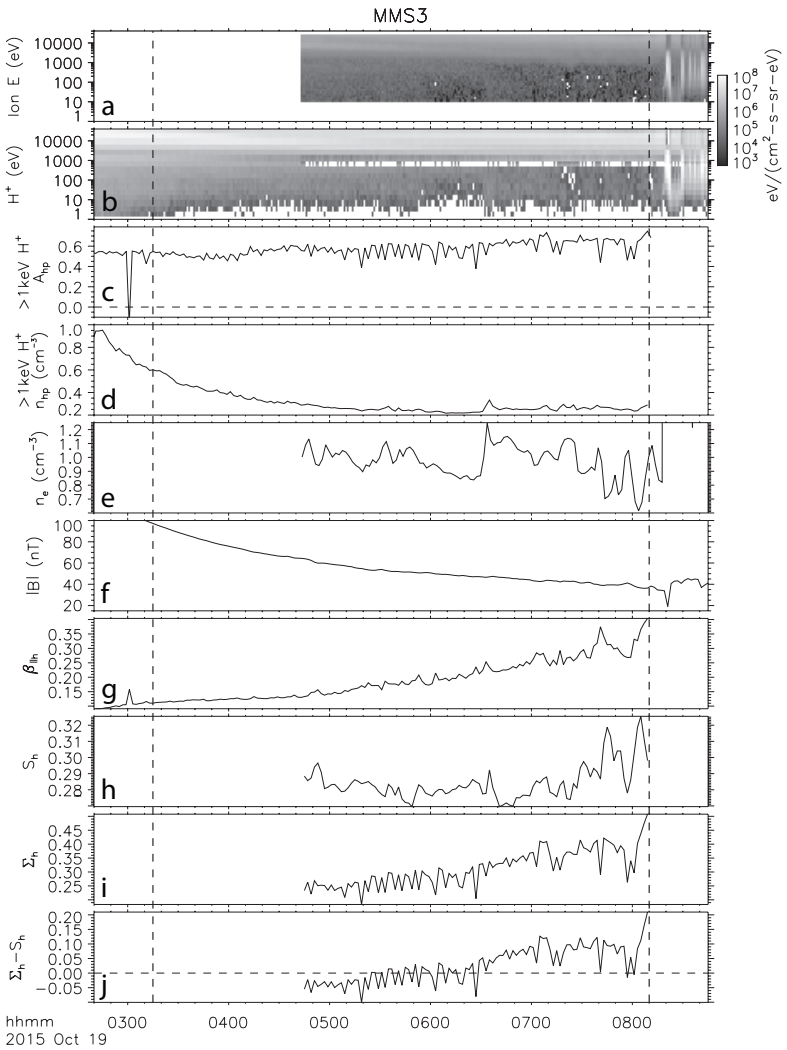

Figure 6. EMIC instability related parameters on MMS3 from 0240 – 0845 UT on 19 October 2015. From top to bottom, the panels show HPI-DIS ion energy-UT flux spectrograms, HPCA H^+ energy-UT flux spectrograms, hot-proton (>1 keV) temperature anisotropy ($A_{hp} = T_\perp / T_\parallel - 1$), hot-proton density ($n_{hp}$), electron density ($n_e$), magnetic field magnitude ($|B|$), hot-proton parallel plasma beta ($\beta_{\parallel h}$), the observational EMIC wave growth parameter (Σ_h), the theoretical EMIC instability parameter (S_h), and their difference ($\Sigma_h - S_h$). The vertical dashed lines indicate the start and end times of the wave event. In Figs. 6c and 6j, the horizontal dashed line marks the value of 0.

by the pair of the vertical dashed lines. In Figs. 6c-6j, the critical value of zero is marked with the horizontal dashed lines. n_e is the total electron density by DES with a multiplication factor of 1.2 (suggested by S. A. Boardsen). This factor is estimated by comparing the difference between the measured total DES n_e and electron density derived from the frequencies of MMS-detected upper hybrid waves.

As shown in Figs. 6a-6b, energetic (> 1 keV) ions are present throughout the EMIC wave event. A_{hp} is moderately high during the wave event, with the maximum average value at 0.75. The n_{hp} average is ~0.3 cm^{-3} during the periods of the waves. The wave event occurred at low MLATs, close to local minimum $|B|$ regions (i.e., on the magnetic equatorial plane). The average of $|B|$ is ~60 nT. In contrast to n_{hp} and $|B|$, $\beta_{\|h}$ keeps increasing from the beginning of the wave event, peaking at 0.4 in the end. While Σ_h -S_h (varying as Σ_h) is not always >0 during the EMIC wave activity, the average of Σ_h -S_h exceeds 0 and is clearly elevated closer to the end of the wave event. It reaches a positive value as high as 0.22 in the end.

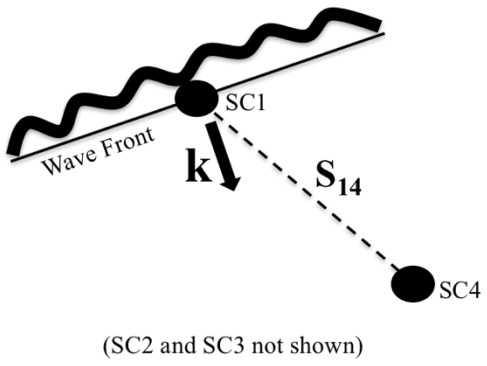

Figure 7. A schematic diagram of the EMIC wave packet at ~0453:55 UT on 19 October 2015, which arrived first at SC1 and then at the other three spacecraft (only SC4 shown) at later times.

D. Wave k Vector

As long as the spatial configuration of the four MMS spacecraft is such that the so-called "spatial aliasing" [72] can be avoided, multipoint measurements of the spacecraft can make it possible to determine wave vector **k**.[73-76] For instance, using high-resolution EDP electric field measurements from the four MMS spacecraft during the 19 October 2015 event, we can determine **k** and thus several other important wave parameters of the wave activity. [76] Figure 7 illustrates the arrival of the EMIC wave packet (f = 0.3 Hz) at ~0453:55 UT first at MMS1 (SC1) and then at MMS2 (SC2), MMS4 (SC4), and MMS3 (SC3) with a time delay of 0.031 s (dt_{12}), 0.047 s (dt_{14}), and 0.054 s (dt_{13}), respectively. The wave phase velocity $\mathbf{V_p}$ can be found by solving

$$\mathbf{S_{1i}} \cdot \frac{\mathbf{V_p}}{{V_p}^2} = dt_{1i} \qquad (6)$$

where i = 2, 3, and 4 and $\mathbf{S_{1i}}$ is the distance vector between SC1 and the other spacecraft. In the geocentric solar ecliptic (GSE) coordinates, $\mathbf{V_p}$ = (43.3, 360.8, 83.3) km/s. Therefore, the wavelength $\lambda = \mathbf{S_{1i}} \cdot \mathbf{n_{v_p}}/(f dt_{1i})$ = 1242.9 km, $|\mathbf{k}| = 2\pi/\lambda$ = 0.005 km^{-1} ($\mathbf{k}$ has the same direction as $\mathbf{V_p}$), phase speed V_p = λf = 372.9 km/s, and the angle between $\mathbf{k}$ and magnetic field $\Psi = \cos^{-1}(\mathbf{n_{v_p}} \cdot \mathbf{b})$ = 71.5°. During the period, the four spacecraft had a separation distance of 15.8 – 19.3 km and travelled at a speed of 2.0 km/s. The DIS plasma bulk flow speed is ~30 km/s, much smaller than V_p. This preliminary analysis suggests the validity of the assumption of the temporal stationarity and spatial homogeneity of the MMS plasma data.

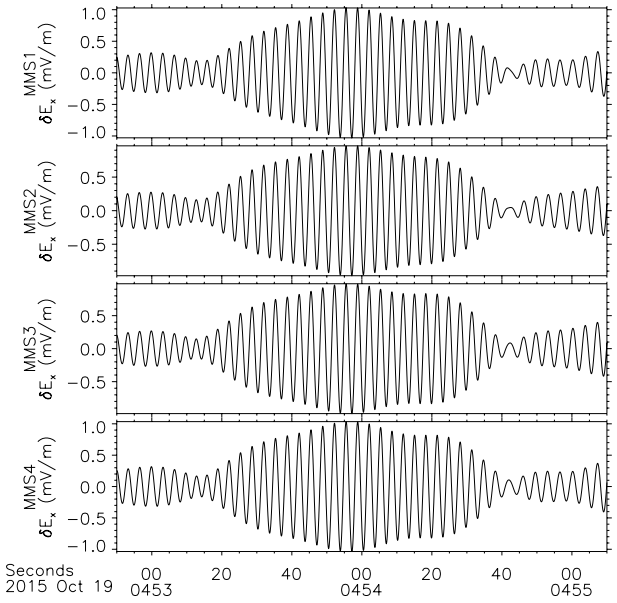

Figure 8. Wave electric field forms on four MMS spacecraft during 0452:50 – 0455:10 UT, 19 October 2015. From top to bottom, the panels show wave electric field component δE_x on MMS1, MMS2, MMS3, and MMS4. The data are transferred into the local field-aligned coordinate system: Z is along the magnetic field, Y=Z×X_{GSE}, and X =Y×Z, which completes the right-hand system.

IV. Conclusions and Future Work

Using MMS field and plasma measurements, we performed a case study of EMIC waves and associated local plasma conditions observed on 19 October 2015. It is suggested that the long-lasting EMIC waves were excited locally. Short inter-spacecraft distances of the MMS mission make it possible to accurately determine the **k** vector of EMIC waves using the phase difference technique. This study helps us better understand several aspects of EMIC waves, e.g., off-equator source regions and wave propagation path and reflection, which still remain under debate or not well explored. [48, 50, 53, 77] The present investigation also extends EMIC wave studies with observations from the inner magnetosphere (e.g., Van Allen Probes) [4, 54-56] or a polar orbit (e.g., Cluster) [26, 28, 57-59] to the low-latitude outer magnetosphere (MMS).

Future work, following the current study, includes 1) to obtain a dispersion relation of EMIC waves by calculating the wave **k** vector as a function of wave frequency, 2) to examine EMIC wave activity in the global magnetosphere by combing observations from other space missions, e.g., Van Allen Probes, THEMIS, and Cluster, and 3) to extend this case study to a statistical study.

Acknowledgments

This work was supported by the 2017 NASA Marshall Faculty Fellowship Program. Work at UNH was also supported by NASA under grant numbers NNX11AO82G and NNX13AE23G. The authors thank the MMS team for their data and software. N. A. Tsyganenko of University of St.-Petersburg in Russian Federation and H. Korth of JHU/APL provided the Tsyganenko magnetic field model and the IDL/Geopack module for magnetic field tracings to calculate the equatorial He^+ gyrofrequencies. Solar wind plasma/IMF data and the geomagnetic indices were obtained from the GSFC/SPDF OMNIWeb interface at http://omniweb.gsfc.nasa.gov.

References

[1]Tsurutani, B. T., and Smith, E. J. "Two types of magnetospheric ELF chorus and their substorm dependences," *Journal of Geophysical Research-Space Physics* Vol. 82, No. 32, 1977, pp. 5112-5128.
doi: 10.1029/JA082i032p05112

[2]Kennel, C. F., and Petschek, H. E. "Limit on stably trapped particle fluxes," *Journal of Geophysical Research* Vol. 71, No. 1, 1966, pp. 1-&.
doi: 10.1029/JZ071i001p00001

[3]Anderson, B. J., Denton, R. E., Ho, G., Hamilton, D. C., Fuselier, S. A., and Strangeway, R. J. "Observational test of local proton cyclotron instability in the Earth's magnetosphere," *Journal of Geophysical Research-Space Physics* Vol. 101, No. A10, 1996, pp. 21527-21543.
doi: 10.1029/96JA01251

[4]Zhang, J. C., Saikin, A. A., Kistler, L. M., Smith, C. W., Spence, H. E., Mouikis, C. G., Torbert, R. B., Larsen, B. A., Reeves, G. D., Skoug, R. M., Funsten, H. O., Kurth, W. S., Kletzing, C. A., Allen, R. C., and Jordanova, V. K. "Excitation of EMIC waves detected by the Van Allen Probes on 28 April 2013," *Geophysical Research Letters* Vol. 41, No. 12, 2014, pp. 4101-4108.
doi: 10.1002/2014GL060621

[5]Fraser, B. J., and Nguyen, T. S. "Is the plasmapause a preferred source region of electromagnetic ion cyclotron waves in the magnetosphere?," *Journal of Atmospheric and Solar-Terrestrial Physics* Vol. 63, No. 11, 2001, pp. 1225-1247.
doi: 10.1016/S1364-6826(00)00225-X

[6]Loto'aniu, T. M., Fraser, B. J., and Waters, C. L. "Propagation of electromagnetic ion cyclotron wave energy in the magnetosphere," *Journal of Geophysical Research-Space Physics* Vol. 110, No. A07214, 2005.
doi: 10.1029/2004JA010816

[7]Pickett, J. S., Grison, B., Omura, Y., Engebretson, M. J., Dandouras, I., Masson, A., Adrian, M. L., Santolik, O., Decreau, P. M. E., Cornilleau-Wehrlin, N., and Constantinescu, D. "Cluster observations of EMIC triggered emissions in association with Pc1 waves near Earth's plasmapause," *Geophysical Research Letters* Vol. 37, No. L09104, 2010.
doi: 10.1029/2010GL042648

[8]Jordanova, V. K., Farrugia, C. J., Thorne, R. M., Khazanov, G. V., Reeves, G. D., and Thomsen, M. F. "Modeling ring current proton precipitation by electromagnetic ion cyclotron waves during the May 14-16, 1997, storm," *Journal of Geophysical Research-Space Physics* Vol. 106, No. A1, 2001, pp. 7-22.
doi: 10.1029/2000JA002008

[9]Lin, R. L., Zhang, J. C., Allen, R. C., Kistler, L. M., Mouikis, C. G., Gong, J. C., Liu, S. Q., Shi, L. Q., Klecker, B., Sauvaud, J. A., and Dunlop, M. W. "Testing linear theory of EMIC waves in the inner magnetosphere: Cluster observations," *Journal of Geophysical Research-Space Physics* Vol. 119, No. 2, 2014, pp. 1004-1027.
doi: 10.1002/2013JA019541

[10]Allen, R. C., Zhang, J.-C., Kistler, L. M., Spence, H. E., Lin, R.-L., Klecker, B., Dunlop, M. W., Andre, M., and Jordanova, V. K. "A statistical study of EMIC waves observed by Cluster: 2. Associated plasma conditions," *Journal of Geophysical Research-Space Physics* Vol. 121, 2016.

doi: 10.1002/2016JA022541
[11]Criswell, D. R. "Pc 1 micropulsation activity and magnetospheric amplification of 0.2- to 5.0-Hz hydromagnetic waves," *Journal of Geophysical Research* Vol. 74, No. 1, 1969, pp. 205-&.
doi: 10.1029/JA074i001p00205
[12]Thorne, R. M., and Horne, R. B. "Modulation of electromagnetic ion cyclotron instability due to interaction with ring current O+ during magnetic storms," *Journal of Geophysical Research-Space Physics* Vol. 102, No. A7, 1997, pp. 14155-14163.
doi: 10.1029/96JA04019
[13]Anderson, B. J., Erlandson, R. E., and Zanetti, L. J. "A statistical study of Pc 1-2 magnetic pulsations in the equatorial magnetosphere, 1. Equatorial occurrence distributions," *Journal of Geophysical Research-Space Physics* Vol. 97, No. A3, 1992, pp. 3075-3088.
doi: 10.1029/91JA02706
[14]Morley, S. K., Ables, S. T., Sciffer, M. D., and Fraser, B. J. "Multipoint observations of Pc1-2 waves in the afternoon sector," *Journal of Geophysical Research-Space Physics* Vol. 114, No. A09205, 2009, pp. -.
doi: 10.1029/2009JA014162
[15]Sibeck, D. G., Mcentire, R. W., Lui, A. T. Y., Lopez, R. E., and Krimigis, S. M. "Magnetic field drift shell splitting: Cause of unusual dayside particle pitch angle distributions during storms and substorms," *Journal of Geophysical Research-Space Physics* Vol. 92, No. A12, 1987, pp. 13485-13497.
doi: 10.1029/JA092ia12p13485
[16]Takahashi, K., Anderson, B. J., Ohtani, S.-I., Reeves, G. D., Takahashi, S., Sarris, T. E., and Mursula, K. "Drift-shell splitting of energetic ions injected at pseudo-substorm onsets," *Journal of Geophysical Research-Space Physics* Vol. 102, No. A10, 1997, pp. 22117–22130.
doi: 10.1029/97JA01870
[17]Shabansky, V. P. "Some Processes in Magnetosphere," *Space Science Reviews* Vol. 12, No. 3, 1971, pp. 299-418.
doi: 0.1007/Bf00165511
[18]McCollough, J. P., Elkington, S. R., and Baker, D. N. "The role of Shabansky orbits in compression-related electromagnetic ion cyclotron wave growth," *Journal of Geophysical Research-Space Physics* Vol. 117, No. A01208, 2012.
doi: 10.1029/2011JA016948
[19]Anderson, B. J., and Hamilton, D. C. "Electromagnetic ion cyclotron waves stimulated by modest magnetospheric compressions," *Journal of Geophysical Research-Space Physics* Vol. 98, No. A7, 1993, pp. 11369-11382.
doi: 10.1029/93JA00605
[20]Usanova, M. E., Mann, I. R., Rae, I. J., Kale, Z. C., Angelopoulos, V., Bonnell, J. W., Glassmeier, K. H., Auster, H. U., and Singer, H. J. "Multipoint observations of magnetospheric compression-related EMIC Pc1 waves by THEMIS and CARISMA," *Geophysical Research Letters* Vol. 35, No. 17, L17S25, 2008, pp. -.
doi: 10.1029/2008GL034458
[21]Usanova, M. E., Mann, I. R., Kale, Z. C., Rae, I. J., Sydora, R. D., Sandanger, M., Soraas, F., Glassmeier, K. H., Fornacon, K. H., Matsui, H., Puhl-Quinn, P. A., Masson, A., and Vallieres, X. "Conjugate ground and multisatellite observations of compression-related EMIC Pc1 waves and associated proton precipitation," *Journal of Geophysical Research-Space Physics* Vol. 115, No. A07208, 2010, pp. -.
doi: 10.1029/2009JA014935
[22]Winglee, R. M., Chua, D., Brittnacher, M., Parks, G. K., and Lu, G. "Global impact of ionospheric outflows on the dynamics of the magnetosphere and cross-polar cap potential," *Journal of Geophysical Research-Space Physics* Vol. 107, No. 1237, 2002.
doi: 10.1029/2001JA000214
[23]McCollough, J. P., Elkington, S. R., Usanova, M. E., Mann, I. R., Baker, D. N., and Kale, Z. C. "Physical mechanisms of compressional EMIC wave growth," *Journal of Geophysical Research-Space Physics* Vol. 115, No. A10214, 2010.
doi: 10.1029/2010JA015393
[24]Liu, Y. H., Fraser, B. J., and Menk, F. W. "Pc2 EMIC waves generated high off the equator in the dayside outer magnetosphere," *Geophysical Research Letters* Vol. 39, No. L17102, 2012.
doi: 10.1029/2012GL053082
[25]Liu, Y. H., Fraser, B. J., Menk, F. W., Zhang, J.-C., Kistler, L. M., and Dandouras, I. "Correction to "Pc2 EMIC waves generated high off the equator in the dayside outer magnetosphere"," *Geophysical Research Letters* Vol. 40, 2013, pp. 1950-1951.
doi: 10.1002/grl.50283
[26]Allen, R. C., Zhang, J.-C., Kistler, L. M., Spence, H. E., Lin, R.-L., Dunlop, M. W., and Andre, M. "Multiple bidirectional EMIC waves observed by Cluster at middle magnetic latitudes in the dayside magnetosphere," *Journal of Geophysical Research-Space Physics* Vol. 118, No. 10, 2013, pp. 6266-6278.
doi: 10.1002/jgra.50600
[27]Zhang, J.-C., Kistler, L. M., Mouikis, C. G., Dunlop, M. W., Klecker, B., and Sauvaud, J.-A. "A case study of EMIC-wave associated He+ energization in the outer magnetosphere: Cluster and Double Star 1 observations," *Journal of Geophysical Research-Space Physics* Vol. 115, No. A06212, 2010.
doi: 10.1029/2009JA014784
[28]Zhang, J. C., Kistler, L. M., Mouikis, C. G., Klecker, B., Sauvaud, J. A., and Dunlop, M. W. "A statistical study of EMIC wave-associated He+ energization in the outer magnetosphere: Cluster/CODIF observations," *Journal of Geophysical Research-Space Physics* Vol. 116, No. A11201, 2011.

doi: 10.1029/2011JA016690
[29]Young, D. T., Perraut, S., Roux, A., Devilledary, C., Gendrin, R., Korth, A., Kremser, G., and Jones, D. "Wave-particle interactions near ΩHe+ observed on GEOS 1 and 2, 1. Propagation of ion cyclotron waves in He+-rich plasma," *Journal of Geophysical Research-Space Physics* Vol. 86, No. A8, 1981, pp. 6755-6772.
doi: 10.1029/JA086iA08p06755
[30]Zhang, J., Halford, A. J., Saikin, A. A., Huang, C.-L., Spence, H. E., Larsen, B. A., Reeves, G. D., Millan, R. M., Smith, C. W., Torbert, R. B., Kurth, W. S., Kletzing, C. A., Blake, J. B., Fennel, J. F., and Baker, D. N. "EMIC waves and associated relativistic electron precipitation on 25–26 January 2013," *Journal of Geophysical Research: Space Physics*, 2016, pp. n/a-n/a.
doi: 10.1002/2016JA022918
[31]Gendrin, R., and Roux, A. "Energization of helium ions by proton-induced hydromagnetic-waves," *Journal of Geophysical Research-Space Physics* Vol. 85, No. A9, 1980, pp. 4577-4586.
doi: 10.1029/JA085iA09p04577
[32]Fuselier, S. A., and Anderson, B. J. "Low-energy He+ and H+ distributions and proton cyclotron waves in the afternoon equatorial magnetosphere," *Journal of Geophysical Research-Space Physics* Vol. 101, No. A6, 1996, pp. 13255-13265.
doi: 10.1029/96JA00292
[33]Jordanova, V. K., Farrugia, C. J., Quinn, J. M., Thorne, R. M., Ogilvie, K. W., Lepping, R. P., Lu, G., Lazarus, A. J., Thomsen, M. F., and Belian, R. D. "Effect of wave-particle interactions on ring current evolution for January 10-11, 1997: Initial results," *Geophysical Research Letters* Vol. 25, No. 15, 1998, pp. 2971-2974.
doi: 10.1029/98GL00649
[34]Fok, M. C., Kozyra, J. U., Nagy, A. F., Rasmussen, C. E., and Khazanov, G. V. "Decay of equatorial ring current ions and associated aeronomical consequences," *Journal of Geophysical Research-Space Physics* Vol. 98, No. A11, 1993, pp. 19381-19393.
doi: 10.1029/93JA01848
[35]Kozyra, J. U., Fok, M. C., Sanchez, E. R., Evans, D. S., Hamilton, D. C., and Nagy, A. F. "The role of precipitation losses in producing the rapid early recovery phase of the Great Magnetic Storm of February 1986," *Journal of Geophysical Research-Space Physics* Vol. 103, No. A4, 1998, pp. 6801-6814.
doi: 10.1029/97JA03330
[36]Thorne, R. M., and Kennel, C. F. "Relativistic electron precipitation during magnetic storm main phase," *Journal of Geophysical Research* Vol. 76, No. 19, 1971, pp. 4446-&.
doi: 10.1029/JA076i019p04446
[37]Jordanova, V. K., Albert, J., and Miyoshi, Y. "Relativistic electron precipitation by EMIC waves from self-consistent global simulations," *Journal of Geophysical Research-Space Physics* Vol. 113, No. A00A10, 2008.
doi: 10.1029/2008JA013239
[38]Loto'aniu, T. M., Thorne, R. M., Fraser, B. J., and Summers, D. "Estimating relativistic electron pitch angle scattering rates using properties of the electromagnetic ion cyclotron wave spectrum," *Journal of Geophysical Research-Space Physics* Vol. 111, No. A04220, 2006.
doi: 10.1029/2005JA011452
[39]Summers, D., and Thorne, R. M. "Relativistic electron pitch-angle scattering by electromagnetic ion cyclotron waves during geomagnetic storms," *Journal of Geophysical Research-Space Physics* Vol. 108, No. A4, 1143, 2003, pp. -.
doi: 10.1029/2002JA009489
[40]Meredith, N. P., Thorne, R. M., Horne, R. B., Summers, D., Fraser, B. J., and Anderson, R. R. "Statistical analysis of relativistic electron energies for cyclotron resonance with EMIC waves observed on CRRES," *Journal of Geophysical Research-Space Physics* Vol. 108, No. A6, 1250, 2003, pp. -.
doi: 10.1029/2002JA009700
[41]Miyoshi, Y., Sakaguchi, K., Shiokawa, K., Evans, D., Albert, J., Connors, M., and Jordanova, V. "Precipitation of radiation belt electrons by EMIC waves, observed from ground and space," *Geophysical Research Letters* Vol. 35, No. L23101, 2008.
doi: 10.1029/2008GL035727
[42]Rodger, C. J., Raita, T., Clilverd, M. A., Seppala, A., Dietrich, S., Thomson, N. R., and Ulich, T. "Observations of relativistic electron precipitation from the radiation belts driven by EMIC waves," *Geophysical Research Letters* Vol. 35, No. L16106, 2008.
doi: 10.1029/2008GL034804
[43]Blum, L. W., Schiller, Q., Li, X., Millan, R., Halford, A., and Woodger, L. "New conjunctive CubeSat and balloon measurements to quantify rapid energetic electron precipitation," *Geophysical Research Letters* Vol. 40, No. 22, 2013, pp. 5833-5837.
doi: 10.1002/2013GL058546
[44]Li, Z., Millan, R. M., and Hudson, M. K. "Simulation of the energy distribution of relativistic electron precipitation caused by quasi-linear interactions with EMIC waves," *Journal of Geophysical Research-Space Physics* Vol. 118, No. 12, 2013, pp. 7576-7583.
doi: 10.1002/2013JA019163
[45]Li, Z., Millan, R. M., Hudson, M. K., Woodger, L. A., Smith, D. M., Chen, Y., Friedel, R., Rodriguez, J. V., Engebretson, M. J., Goldstein, J., Fennell, J. F., and Spence, H. E. "Investigation of EMIC wave scattering as the cause for the BARREL 17 January 2013 relativistic electron precipitation event: A quantitative comparison of simulation with observations," *Geophysical Research Letters* Vol. 41, No. 24, 2014, pp. 8722-8729.
doi: 10.1002/2014GL062273

[46]Hendry, A. T., Rodger, C. J., Clilverd, M. A., Engebretson, M. J., Mann, I. R., Lessard, M. R., Raita, T., and Milling, D. K. "Confirmation of EMIC wave-driven relativisticelectron precipitation," *J. Geophys.Res. Space Physics* Vol. 121, 2016.
doi: 10.1002/2015JA022224

[47]Rodger, C. J., Hendry, A. T., Clilverd, M. A., Kletzing, C. A., Brundell, J. B., and Reeves, G. D. "High-resolution in situ observations of electron precipitation-causing EMIC waves," *Geophysical Research Letters* Vol. 42, No. 22, 2015, pp. 9633-9641.
doi: 10.1002/2015gl066581

[48]Khazanov, G. V., Gamayunov, K. V., Gallagher, D. L., and Kozyra, J. U. "Reply to comment by R. M. Thorne and R. B. Horne Khazanov et al. [2002] and Khazanov et al. [2006]," *Journal of Geophysical Research-Space Physics* Vol. 112, No. A12215, 2007.
doi: 10.1029/2007JA012463

[49]Rauch, J. L., and Roux, A. "Ray tracing of ULF waves in a multicomponent magnetospheric plasma: Consequences for the generation mechanism of ion cyclotron waves," *Journal of Geophysical Research-Space Physics* Vol. 87, No. A10, 1982, pp. 8191-8198.
doi: 10.1029/JA087iA10p08191

[50]Khazanov, G. V., Gamayunov, K. V., Gallagher, D. L., and Kozyra, J. U. "Self-consistent model of magnetospheric ring current and propagating electromagnetic ion cyclotron waves: Waves in multi-ion magnetosphere," *Journal of Geophysical Research-Space Physics* Vol. 111, No. A10202, 2006.
doi: 10.1029/2006JA011833

[51]Horne, R. B., and Thorne, R. M. "On the preferred source location for the convective amplification of ion cyclotron waves," *Journal of Geophysical Research-Space Physics* Vol. 98, No. A6, 1993, pp. 9233-9247.
doi: 10.1029/92JA02972

[52]Horne, R. B., and Thorne, R. M. "Wave heating of He+ by electromagnetic ion cyclotron waves in the magnetosphere: Heating near the H+-He+ bi-ion resonance frequency," *Journal of Geophysical Research-Space Physics* Vol. 102, No. A6, 1997, pp. 11457-11471.
doi: 10.1029/97JA00749

[53]Thorne, R. M., and Horne, R. B. "Comment on Khazanov et al. [2002] and Khazanov et al. [2006]," *Journal of Geophysical Research-Space Physics* Vol. 112, No. A12214, 2007.
doi: 10.1029/2007JA012268

[54]Saikin, A. A., Zhang, J. C., Allen, R. C., Smith, C. W., Kistler, L. M., Spence, H. E., Torbert, R. B., Kletzing, C. A., and Jordanova, V. K. "The occurrence and wave properties of H+-, He+-, and O+-band EMIC waves observed by the Van Allen Probes," *Journal of Geophysical Research-Space Physics* Vol. 120, No. 9, 2015, pp. 7477-7492.
doi: 10.1002/2015JA021358

[55]Saikin, A. A., Zhang, J. C., Smith, C. W., Spence, H. E., Torbert, R. B., and Kletzing, C. A. "The dependence on geomagnetic conditions and solar wind dynamic pressure of the spatial distributions of EMIC waves observed by the Van Allen Probes," *Journal of Geophysical Research: Space Physics* Vol. 121, No. 5, 2016, pp. 4362-4377.
doi: 10.1002/2016JA022523

[56]Zhang, J. C., Halford, A. J., Saikin, A. A., Huang, C. L., Spence, H. E., Larsen, B. A., Reeves, G. D., Millan, R. M., Smith, C. W., Torbert, R. B., Kurth, W. S., Kletzing, C. A., Blake, J. B., Fennel, J. F., and Baker, D. N. "EMIC waves and associated relativistic electron precipitation on 25-26 January 2013," *Journal of Geophysical Research-Space Physics* Vol. 121, No. 11, 2016, pp. 11086-11100.
doi: 10.1002/2016ja022918

[57]Allen, R. C., Zhang, J. C., Kistler, L. M., Spence, H. E., Lin, R. L., Klecker, B., Dunlop, M. W., André, M., and Jordanova, V. K. "A statistical study of EMIC waves observed by Cluster: 1. Wave properties," *Journal of Geophysical Research: Space Physics* Vol. 120, No. 7, 2015, pp. 5574-5592.
doi: 10.1002/2015JA021333

[58]Allen, R. C., Zhang, J. C., Kistler, L. M., Spence, H. E., Lin, R. L., Klecker, B., Dunlop, M. W., André, M., and Jordanova, V. K. "A statistical study of EMIC waves observed by Cluster: 2. Associated plasma conditions," *Journal of Geophysical Research: Space Physics* Vol. 121, No. 7, 2016, pp. 6458-6479.
doi: 10.1002/2016JA022541

[59]Zhang, J. C., Kistler, L. M., Mouikis, C. G., Dunlop, M. W., Klecker, B., and Sauvaud, J. A. "A case study of EMIC wave-associated He plus energization in the outer magnetosphere: Cluster and Double Star 1 observations," *Journal of Geophysical Research-Space Physics* Vol. 115, No. A06212, 2010.
doi: 10.1029/2009JA014784

[60]Burch, J. L., Moore, T. E., Torbert, R. B., and Giles, B. L. "Magnetospheric Multiscale Overview and Science Objectives," *Space Science Reviews* Vol. 199, No. 1-4, 2016, pp. 5-21.
doi: 10.1007/s11214-015-0164-9

[61]Russell, C. T., Anderson, B. J., Baumjohann, W., Bromund, K. R., Dearborn, D., Fischer, D., Le, G., Leinweber, H. K., Leneman, D., Magnes, W., Means, J. D., Moldwin, M. B., Nakamura, R., Pierce, D., Plaschke, F., Rowe, K. M., Slavin, J. A., Strangeway, R. J., Torbert, R., Hagen, C., Jernej, I., Valavanoglou, A., and Richter, I. "The Magnetospheric Multiscale Magnetometers," *Space Science Reviews* Vol. 199, No. 1-4, 2016, pp. 189-256.
doi: 10.1007/s11214-014-0057-3

[62]Torbert, R. B., Russell, C. T., Magnes, W., Ergun, R. E., Lindqvist, P. A., LeContel, O., Vaith, H., Macri, J., Myers, S., Rau, D., Needell, J., King, B., Granoff, M., Chutter, M., Dors, I., Olsson, G., Khotyaintsev, Y. V., Eriksson, A., Kletzing, C. A., Bounds, S., Anderson, B., Baumjohann, W., Steller, M., Bromund, K., Le, G., Nakamura, R., Strangeway, R. J., Leinweber, H. K., Tucker, S., Westfall, J., Fischer, D., Plaschke, F., Porter, J., and Lappalainen, K. "The FIELDS Instrument Suite on MMS: Scientific Objectives, Measurements, and Data Products," *Space Science Reviews* Vol. 199, No. 1-4, 2016, pp. 105-135.
doi: 10.1007/s11214-014-0109-8

[63]Pollock, C., Moore, T., Jacques, A., Burch, J., Gliese, U., Saito, Y., Omoto, T., Avanov, L., Barrie, A., Coffey, V., Dorelli, J., Gershman, D., Giles, B., Rosnack, T., Salo, C., Yokota, S., Adrian, M., Aoustin, C., Auletti, C., Aung, S., Bigio, V., Cao, N., Chandler, M., Chornay, D., Christian, K., Clark, G., Collinson, G., Corris, T., De Los Santos, A., Devlin, R., Diaz, T., Dickerson, T., Dickson, C., Diekmann, A., Diggs, F., Duncan, C., Figueroa-Vinas, A., Firman, C., Freeman, M., Galassi, N., Garcia, K., Goodhart, G., Guererro, D., Hageman, J., Hanley, J., Hemminger, E., Holland, M., Hutchins, M., James, T., Jones, W., Kreisler, S., Kujawski, J., Lavu, V., Lobell, J., LeCompte, E., Lukemire, A., MacDonald, E., Mariano, A., Mukai, T., Narayanan, K., Nguyan, Q., Onizuka, M., Paterson, W., Persyn, S., Piepgrass, B., Cheney, F., Rager, A., Raghuram, T., Ramil, A., Reichenthal, L., Rodriguez, H., Rouzaud, J., Rucker, A., Saito, Y., Samara, M., Sauvaud, J. A., Schuster, D., Shappirio, M., Shelton, K., Sher, D., Smith, D., Smith, K., Smith, S., Steinfeld, D., Szymkiewicz, R., Tanimoto, K., Taylor, J., Tucker, C., Tull, K., Uhl, A., Vloet, J., Walpole, P., Weidner, S., White, D., Winkert, G., Yeh, P. S., and Zeuch, M. "Fast Plasma Investigation for Magnetospheric Multiscale," *Space Science Reviews* Vol. 199, No. 1-4, 2016, pp. 331-406.
doi: 10.1007/s11214-016-0245-4

[64]Young, D. T., Burch, J. L., Gomez, R. G., De Los Santos, A., Miller, G. P., Wilson, P., Paschalidis, N., Fuselier, S. A., Pickens, K., Hertzberg, E., Pollock, C. J., Scherrer, J., Wood, P. B., Donald, E. T., Aaron, D., Furman, J., George, D., Gurnee, R. S., Hourani, R. S., Jacques, A., Johnson, T., Orr, T., Pan, K. S., Persyn, S., Pope, S., Roberts, J., Stokes, M. R., Trattner, K. J., and Webster, J. M. "Hot Plasma Composition Analyzer for the Magnetospheric Multiscale Mission," *Space Science Reviews* Vol. 199, No. 1-4, 2016, pp. 407-470.
doi: 10.1007/s11214-014-0119-6

[65]Anderson, B. J., Denton, R. E., and Fuselier, S. A. "On determining polarization characteristics of ion cyclotron wave magnetic field fluctuations," *Journal of Geophysical Research-Space Physics* Vol. 101, No. A6, 1996, pp. 13195-13213.
doi: 10.1029/96JA00633

[66]O'Brien, T. P., and McPherron, R. L. "An empirical phase space analysis of ring current dynamics: Solar wind control of injection and decay," *Journal of Geophysical Research-Space Physics* Vol. 105, No. A4, 2000, pp. 7707-7719.
doi: 10.1029/1998JA000437

[67]Weimer, D. R. "Correction to "Predicting interplanetary magnetic field (IMF) propagation delay times using the minimum variance technique"," *Journal of Geophysical Research-Space Physics* Vol. 109, No. A12104, 2004, p. 1.
doi: 10.1029/2004JA010691

[68]Weimer, D. R., and King, J. H. "Improved calculations of interplanetary magnetic field phase front angles and propagation time delays," *Journal of Geophysical Research-Space Physics* Vol. 113, No. A01105, 2008, p. 14.
doi: 10.1029/2007JA012452

[69]Weimer, D. R., Ober, D. M., Maynard, N. C., Collier, M. R., McComas, D. J., Ness, N. F., Smith, C. W., and Watermann, J. "Predicting interplanetary magnetic field (IMF) propagation delay times using the minimum variance technique," *Journal of Geophysical Research-Space Physics* Vol. 108, No. A1, 2003, p. 12.
doi: 10.1029/2002JA009405

[70]Gary, S. P., Moldwin, M. B., Thomsen, M. F., Winske, D., and McComas, D. J. "Hot proton anisotropies and cool proton temperatures in the outer magnetosphere," *Journal of Geophysical Research-Space Physics* Vol. 99, No. A12, 1994, pp. 23603-23615.
doi: 10.1029/94JA02069

[71]Blum, L. W., MacDonald, E. A., Gary, S. P., Thomsen, M. F., and Spence, H. E. "Ion observations from geosynchronous orbit as a proxy for ion cyclotron wave growth during storm times," *Journal of Geophysical Research-Space Physics* Vol. 114, No. A10214, 2009.
doi: 10.1029/2009JA014396

[72]Chanteur, G. "Spatial interpolation for four spacecraft: Theory," *Analysis Methods for Multi-Spacecraft Data*. Vol. SR-001 (Electronic edition 1.1), ESA Publications Division, 2000, pp. 349-370.

[73]Pinçon, J. L., and Lefeuvre, F. "Local characterization of homogeneous turbulence in a space plasma from simultaneous measurements of field components at several points in space," *Journal of Geophysical Research-Space Physics* Vol. 96, No. A2, 1991, pp. 1789-1802.
doi: 10.1029/90JA02183

[74]Motschmann, U., Woodward, T. I., Glassmeier, K. H., Southwood, D. J., and Pincon, J. L. "Wavelength and direction filtering by magnetic measurements at satellite arrays: Generalized minimum variance analysis," *Journal of Geophysical Research-Space Physics* Vol. 101, No. A3, 1996, pp. 4961-4965.
doi: 10.1029/95JA03471

[75]Neubauer, F. M., and Glassmeier, K. H. "Use of an array of satellites as a wave telescope," *Journal of Geophysical Research-Space Physics* Vol. 95, No. A11, 1990, pp. 19115-19122.
doi: 10.1029/JA095iA11p19115

[76]Glassmeier, K. H., Motschmann, U., Dunlop, M., Balogh, A., Acuna, M. H., Carr, C., Musmann, G., Fornacon, K. H., Schweda, K., Vogt, J., Georgescu, E., and Buchert, S. "Cluster as a wave telescope - first results from the fluxgate magnetometer," *Annales Geophysicae* Vol. 19, No. 10-12, 2001, pp. 1439-1447.
doi: 10.5194/angeo-19-1439-2001

[77]Khazanov, G. V., Gamayunov, K. V., Jordanova, V. K., and Krivorutsky, E. N. "A self-consistent model of the interacting ring current ions and electromagnetic ion cyclotron waves, initial results: Waves and precipitating fluxes," *Journal of Geophysical Research-Space Physics* Vol. 107, No. A6, 2002.
doi: 10.1029/2001JA000180

APPENDIX A— NASA MARSHALL SPACE FLIGHT CENTER FACULTY FELLOWSHIP PROGRAM ANNOUNCEMENT

MARSHALL FACULTY FELLOWSHIP PROGRAM

JUNE 5, 2017 – AUGUST 11, 2017

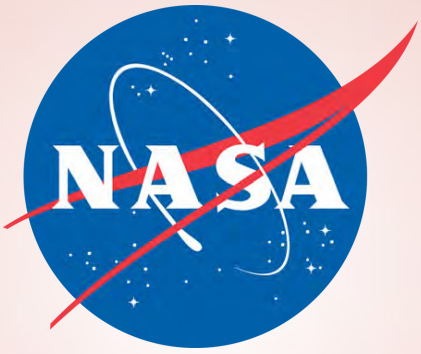

Application Deadline February 22, 2017

- The Marshall Space Flight Center is offering Faculty Fellowships for qualified STEM faculty at U.S. colleges and universities to conduct research with NASA colleagues during a ten-week residential program in Huntsville, Alabama.
- Faculty Fellows will receive stipends of $15,000 (Assistant Professor, Research Faculty), $17,000 (Associate Professor), or $19,000 (Professor).
- A relocation allowance of $1,500 will be provided to those fellows who live more than fifty miles from MSFC and a $500 travel supplement for one round-trip.
- Applicants must be U.S. citizens who hold full-time teaching or research appointments at accredited U.S. universities or colleges.
- During the ten-week program, fellows are required to conduct their research on-site at the Marshall Space Flight Center.

Women and under-represented minorities, and persons with disabilities are encouraged to apply.

APPENDIX B—NASA MARSHALL SPACE FLIGHT CENTER FACULTY FELLOWSHIP PROGRAM DESCRIPTION

Program Description

- The Marshall Faculty Fellowship program is a residential research experience. Fellows are required to conduct their research, during the ten-week program, on-site at the Marshall Space Flight Center.
- Participants cannot receive remuneration from other entities or other programs or other university or government sources during the Faculty Fellowship 10-week period.
- An oral presentation by the Fellow to the Marshall group with which s/he has been affiliated is required, near the end of the fellowship period.
- A written final report is required at the end of the Fellowship.
- A written evaluation of the program by the Fellow is expected at the end of the Fellowship.

Eligibility

- US citizen
- Full time teaching or research appointment at accredited US university or college.
- Fellowship is awarded for one summer period, but Fellow may apply again for a second year.
- Women, under-represented minorities, and persons, with disabilities are encouraged to apply.

Selection

The applications selected to be Faculty Fellows will be chosen by the Marshall group which has been assigned the area of investigation (concentration) chosen by the applicant.

Marshall Collaborator

A Marshall Collaborator will be identified to serve as the co-investigator and day-to-day contact. At the end of the ten-week period, the Faculty Fellow and the Marshall Collaborator will prepare a white paper summarizing the summer effort, including results and recommending follow-up work.

Compensation

Stipends for Faculty Fellows are set as follows for the 10-week period:

Assistant Professors and Research Faculty	$15,000
Associate Professors	$17,000
Professors	$19,000

A relocation allowance of $1,500 will be provided to fellows who live more than fifty miles from the Marshall Center.

A travel supplement of $500 will be provided to those fellows receiving the relocation allowance.

REPORT DOCUMENTATION PAGE

Form Approved
OMB No. 0704-0188

1. REPORT DATE *(DD-MM-YYYY)*	2. REPORT TYPE	3. DATES COVERED *(From - To)*
01–12–2017	Technical Memorandum	

4. TITLE AND SUBTITLE

Marshall Space Flight Center Faculty Fellowship Program

5a. CONTRACT NUMBER

5b. GRANT NUMBER

5c. PROGRAM ELEMENT NUMBER

6. AUTHOR(S)

N.F. Six, Program Director and R. Damiani, Compiler*

5d. PROJECT NUMBER

5e. TASK NUMBER

5f. WORK UNIT NUMBER

7. PERFORMING ORGANIZATION NAME(S) AND ADDRESS(ES)

George C. Marshall Space Flight Center
Huntsville, AL 35812

8. PERFORMING ORGANIZATION REPORT NUMBER

M–1451

9. SPONSORING/MONITORING AGENCY NAME(S) AND ADDRESS(ES)

National Aeronautics and Space Administration
Washington, DC 20546–0001

10. SPONSORING/MONITOR'S ACRONYM(S)

NASA

11. SPONSORING/MONITORING REPORT NUMBER

NASA/TM—2017–219848

12. DISTRIBUTION/AVAILABILITY STATEMENT

Unclassified-Unlimited
Subject Category 31
Availability: NASA STI Information Desk (757–864–9658)

13. SUPPLEMENTARY NOTES

Prepared by the Academic Affairs Office, Office of Human Capital
*The University of Alabama in Huntsville

14. ABSTRACT

Faculty Fellows at the Marshall Space Flight Center conducted propulsion research on low power arcjets and the electric sail concept; materials investigations of Martian and lunar regolith, friction stir welding, radiation degradation, thermal atomization, composites and high performance polymers. Four studies involved instrumentation: variable conductance heat pipes, neutrino detection, and remote sensing. Additional research included fluid dynamics, software development, life support, systems analysis, spacecraft landing systems, and magnetospheric plasmas.

15. SUBJECT TERMS

Space transportation, spacecraft propulsion, materials engineering, instrumentation, wireless communications, fluid dynamics, life support, space science

16. SECURITY CLASSIFICATION OF:			17. LIMITATION OF ABSTRACT	18. NUMBER OF PAGES	19a. NAME OF RESPONSIBLE PERSON
a. REPORT	b. ABSTRACT	c. THIS PAGE			STI Help Desk at email: help@sti.nasa.gov
U	U	U	UU	240	19b. TELEPHONE NUMBER *(Include area code)* STI Help Desk at: 757–864–9658

National Aeronautics and
Space Administration
IS02
George C. Marshall Space Flight Center
Huntsville, Alabama 35812